

## **General Disclaimer**

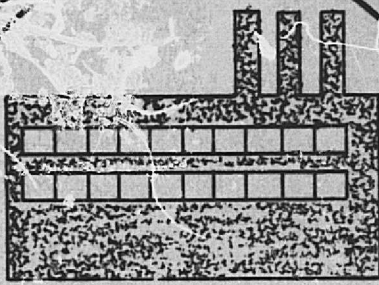
### **One or more of the Following Statements may affect this Document**

- This document has been reproduced from the best copy furnished by the organizational source. It is being released in the interest of making available as much information as possible.
- This document may contain data, which exceeds the sheet parameters. It was furnished in this condition by the organizational source and is the best copy available.
- This document may contain tone-on-tone or color graphs, charts and/or pictures, which have been reproduced in black and white.
- This document is paginated as submitted by the original source.
- Portions of this document are not fully legible due to the historical nature of some of the material. However, it is the best reproduction available from the original submission.

# REMOTE SENSING LABORATORY

E7.6-10369

NASA CR-  
147719



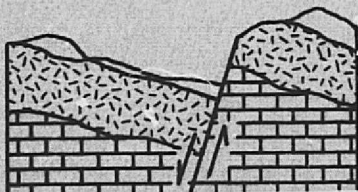
## FINAL REPORT CONTRACT: NAS 9-13298

December, 1975

R. S. Houston

R. W. Marrs

L. E. Borgman



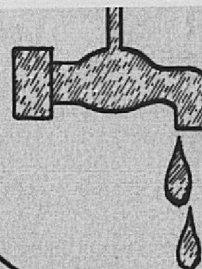
(E76-10369) MULTIDISCIPLINARY STUDY ON  
WYOMING TEST SITES FINAL REPORT (WYOMING  
UNIV.) 219 P HC \$7.75 CSCL 08F

N76-25615

UNCLAS  
00369

G3/43

University  
of Wyoming



TYPE III FINAL REPORT

on

MULTIDISCIPLINARY STUDY ON WYOMING TEST SITES

By: R. S. Houston, R. W. Marrs, and L. E. Borgman

With Contributions From: D. L. Blackstone, Jr., K. G. Downing,  
J. Earle, N. Froman, R. C. Gordon,  
B. Kaminsky, K. E. Kolm, B. J. Tomes,  
J. Vietti and D. M. Worrall

Department of Geology  
University of Wyoming  
Laramie, Wyoming 82071

Original photography may be purchased from:  
EROS Data Center  
10th and Dakota Avenue  
Sioux Falls, SD 57198

**ORIGINAL CONTAINS  
COLOR ILLUSTRATIONS**

December, 1975

Prepared for:  
NASA/JOHNSON SPACE CENTER  
HOUSTON, TEXAS 77058

TECHNICAL REPORT STANDARD TITLE PAGE

1. Report No.	2. Government Accession No.	3. Recipient's Catalog No.	
4. Title and Subtitle TYPE III FINAL REPORT on MULTIDISCIPLINARY STUDY OF WYOMING TEST SITES		5. Report Date December, 1975	6. Performing Organization Code
7. Author(s) R. S. Houston, R. W. Marrs		8. Performing Organization Report No.	
9. Performing Organization Name and Address Department of Geology University of Wyoming Laramie, Wyoming 82071		10. Work Unit No.	11. Contract or Grant No. NAS 9-13298
12. Sponsoring Agency Name and Address NASA/JOHNSON SPACE CENTER Houston, Texas 77058		13. Type of Report and Period Covered Final Report	
14. Sponsoring Agency Code			
15. Supplementary Notes			
16. Abstract (see following page)			
17. Key Words (Selected by Author(s)) Evaluation and Comparison, S-190A, S-190B, S-192, Geology Land-use, Geo- hydrology, Range Management		18. Distribution Statement	
19. Security Classif. (of this report) unclassified	20. Security Classif. (of this page) unclassified	21. No. of Pages 168	22. Price*

\*For sale by the Clearinghouse for Federal Scientific and Technical Information, Springfield, Virginia 22151.

Figure 2. Technical Report Standard Title Page



## ABSTRACT

Ten EREP data passes over the Wyoming test site provided excellent S-190A and S-190B coverage and some useful S-192 imagery. These data were employed in an evaluation of the EREP imaging sensors in several earth resources applications. Planned evaluations of the S-191 sensor were not completed because of the poor quality of the S-191 data.

Boysen Reservoir and Hyattville were selected as test areas for band-to-band comparison of the S-190 and S-192 sensors and for evaluation of the image data as tools for general geologic mapping. Photo-geologic maps compiled from each band of the S-190A photography and from the S-190B photography demonstrate that the spatial resolution of the film products is the dominant control governing the utility of the photography.

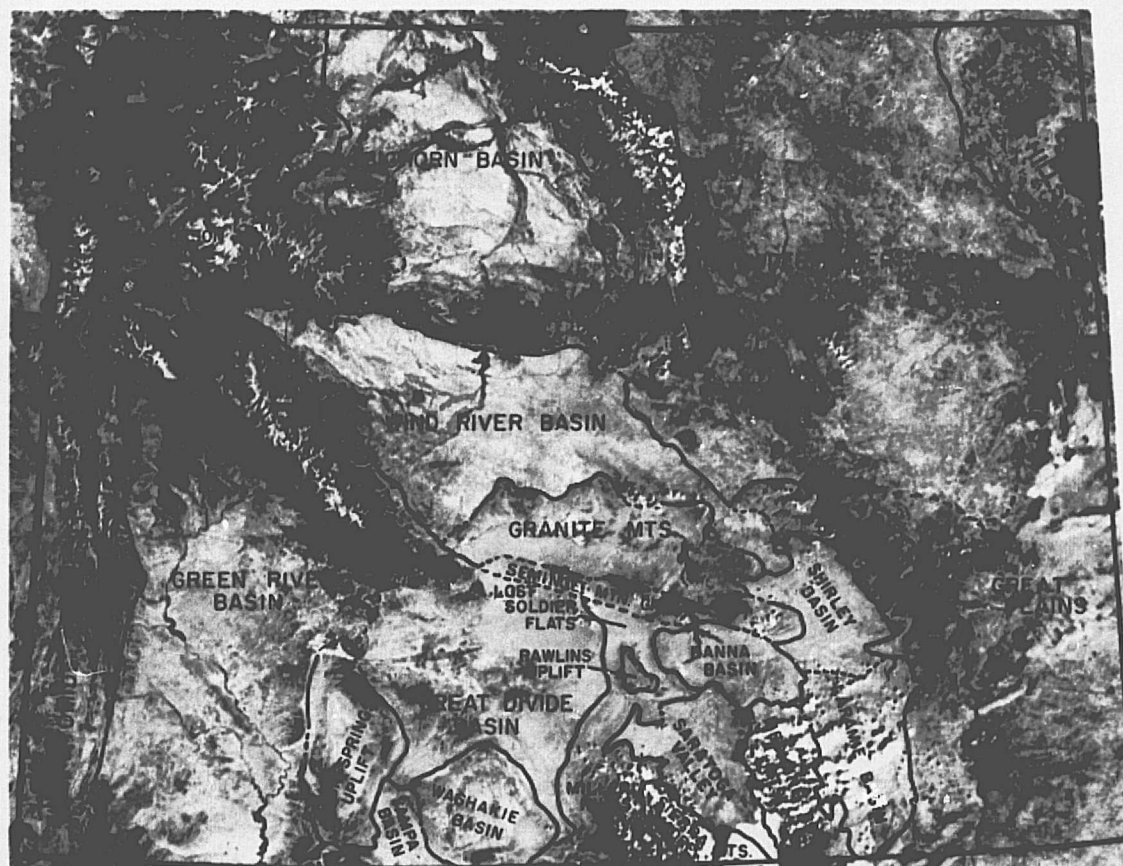
Contrast measurements were made from the S-192 image data for a typical sequence of sedimentary rocks. Histograms compiled from these measurements show that near infrared S-192 bands provide the greatest amount of contrast between geologic units. This result is attributed mostly to the natural "contrast stretching" which arises from the higher reflectance of most rocks in infrared bands.

Comparison was also made between LANDSAT imagery and S-190B and aerial photography for regional land-use mapping. In this work the Skylab S-190B photography was found far superior to the color-composite LANDSAT imagery and was almost as effective as the 1:120,000-scale aerial photography. The EREP photography was used successfully in a number of more specialized geologic applications. Interpretation of the EREP photography provided a valuable assist to LANDSAT imagery in compiling a complete "linear features" map of Wyoming used in a study of regional tectonics. The use of the Skylab data was particularly instrumental in removing the "sun-angle bias" which was introduced from the interpretations of LANDSAT imagery.

A similar map of linear elements prepared from LANDSAT and EREP imagery of the southwestern Bighorn Mountains provided an important aid in defining the relationship between fracture and groundwater movement through the Madison aquifer.

The Skylab S-190A and S-190B photography was found very useful in mapping of land-forms and vegetation. The Skylab photography is now being used as a mapping base for compilation of regional land-forms, vegetation, and land-use maps of the entire Powder River Basin.

Computer analyses of Skylab S-192 data were used as a quantitative test of the relative contrast values measured from S-192 imagery. These measurements confirm the conclusion that the near infrared bands provide the highest reflectance contrast between lithologic units. Q-mode pattern recognition was also found promising for enhancement of certain lithologic and vegetative contrasts.



Color composite LANDSAT mosaic of Wyoming showing the major physiographic and geomorphic provinces.

## PREFACE

The Wyoming EREP investigation represents the second half of a comprehensive evaluation of earth resources satellite data for a variety of earth resource applications, including geology, hydrology, land-use, and range management. The initial portion of the study (funded under contract NAS 5-21799) comprised an evaluation of the LANDSAT satellite data and was completed in January, 1975. This final portion of this study comprises an evaluation of its EREP S-190 and S-192 data and a comparison of the Skylab data with LANDSAT imagery and high-altitude aerial photography.

Early success with some earth resources applications of the Skylab data have already precipitated operational applications of the data to resource problems. However, the major value of the Skylab EREP sensors may be the comparative determinations which offer insight into essential parameters required of an operational earth resources satellite program.

## TABLE OF CONTENTS

	Page
INTRODUCTION AND OBJECTIVES . . . . .	1
PERSONNEL . . . . .	1
DESCRIPTION OF THE TEST SITES . . . . .	7
APPROACH . . . . .	9
RESULTS OF INTERPRETATIONS OF SKYLAB DATA . . . . .	9
General Resource Applications . . . . .	9
Geology . . . . .	11
General Geologic Mapping . . . . .	12
Tectonics . . . . .	24
Geomorphology and Landforms . . . . .	36
Land-use and Environment . . . . .	38
Hydrology . . . . .	46
Crops and Range . . . . .	48
Mineral Exploration and Economic Geology . . . . .	52
Construction Materials . . . . .	62
Mineralization and Alteration . . . . .	62
Comparative Studies . . . . .	64
Comparisons in the Boysen Test Area . . . . .	70
Description of the Test Area . . . . .	70
Geologic Mapping Using S-190A Photography . . . . .	72
Comparisons of Skylab, LANDSAT and Aircraft Imagery for General Geologic Mapping in the Horn Area . . . . .	94
Evaluation of S-192 Imagery of the Hyattville Area . . . . .	102

Qualitative evaluation . . . . .	103
Quantitative image evaluations . . . . .	108
Digital evaluation of S-192 data . . . . .	117
Tape read problems . . . . .	118
Alphanumeric maps . . . . .	120
Pair-wise visual clustering. . . . .	120
R-Mode factor studies . . . . .	124
Q-Mode factor studies . . . . .	126
Additional comments on Q-Mode analysis . . . . .	136
The Q-Mode computer algorithm . . . . .	137
COST/BENEFIT ESTIMATES . . . . .	138
SUMMARY OF SIGNIFICANT RESULTS . . . . .	140
SELECTED REFERENCES . . . . .	144
APPENDICES . . . . .	147
Appendix A . . . . .	149
Appendix B: FACTOR ANALYSIS FOR LARGE DATA SETS . . . . .	150
Summary of factor analysis procedure . . . . .	151
Generalized R- and Q-mode analysis . . . . .	152
Interrelations between generalized R- and Q-mode analysis. . . . .	152
Application of the interrelation . . . . .	154

## LIST OF FIGURES

	Page
Figure 1. Index maps showing Skylab groundtrack pattern and S-190A coverage of Wyoming. . . . .	2
Figure 2. Index map showing high-altitude air photo coverage of Wyoming flown by NASA aircraft. Missions 248 and 310 were flown in support of the EREP investigation. . . . .	5
Figure 3. Wyoming stratigraphic nomenclature chart. . . . .	13
Figure 4. Skylab S-190A image of the Wyoming Thrust Belt, the Green River Basin, and the Wind River Mountains. . . . .	15
Figure 5. Geologic photo interpretation of the Green River Basin, Wyoming; interpreted from EREP S-190A photo 41-204. . . . .	16
Figure 6. Outcrop map of the Black Hills/Powder River Basin area of north-east Wyoming (interpreted from Skylab, S-190B, color photograph 81-153). . . . .	18
Figure 7. Halftone reproduction of Skylab S-190B color photograph. The area shown is a portion of the Powder River Basin lying immediately west of the Black Hills. . . . .	19
Figure 8a. Photogeologic map of the Sheep Mountain area near Greybull, Wyoming, interpreted from Skylab S-190A photography. . . . .	21
Figure 8b. 1:125,000-scale field geologic map of the Sheep Mountain area near Greybull, Wyoming. . . . .	21
Figure 9a. Geologic map of Precambrian units in the Owl Creek Mountains of Wyoming. . . . .	23
Figure 9b. Photogeologic map of the Owl Creek greenstone belt as interpreted from Skylab, S-190B photography. . . . .	23
Figure 9c. Reconnaissance geologic map of the eastern Owl Creek greenstone belt. . . . .	23



Figure 10.	Oblique photograph of snow-covered northwest Wyoming taken by Skylab astronauts on Skylab mission 4. . . . .	26
Figure 11.	Photolinear features interpreted from the Skylab 70mm oblique photo. . . . .	27
Figure 12.	Skylab hand-held oblique photo rectified to allow correlation with vertical photography and base maps. . . . .	28
Figure 13.	Linear features map prepared from rectified oblique photograph. . . . .	29
Figure 14.	Comparison of linear features mapped using LANDSAT MSS images and Skylab S-190B photographs of the Wind River Mountains test site. . . . .	30
Figure 15.	Map of all linear elements detected on LANDSAT images of the Wind River Mountains. . . . .	32
Figure 16.	Map of all linear elements detected on Skylab S-190A photography of the Wind River Mountains test site. . . . .	33
Figure 17.	Photo linear elements interpreted from Skylab imagery. . . . .	34
Figure 18a.	Enlargement of Skylab S-190B image showing the Wyodak coal mine near Gillette, Wyoming. . . . .	40
Figure 18b.	Interpreted isodensity contour map compiled from an isodensitracing of the S-190B photograph. . . . .	40
Figure 19.	Index map of Wyoming showing the location of the reference site (arrow) and the area mapped from Skylab photography (shaded area) (after Koim, 1975a). . . . .	42
Figure 20.	Enlarged S-190B photograph showing the location of the AMAX, Belle Ayre reference site. . . . .	43
Figure 21.	Seleniferous soils mapped from Skylab S-190B photography of the AMAX, Belle Ayre reference site. . . . .	44
Figure 22.	Seleniferous soils, outcrops, and plant indicators in the Lower Tertiary Wasatch Formation, mapped from field observations on aerial photography. . . . .	45

Figure 23.	Skylab S-190A photograph (track 5, pass 10, frame 228, June 12, 1973) showing the Medicine Lodge study area along the west flank of the Bighorn Mountains. . . . .	47
Figure 24.	Major and minor linear features of the Bighorn Mountains and detail maps for two areas within the Medicine Lodge test area. . . . .	49
Figure 25a.	Geologic map compiled by Darton (1906). . . . .	50
Figure 25b.	Darton's geologic map updated and geographically corrected using Skylab photography. . . . .	50
Figure 26.	Portion of Skylab S-190B photograph showing the Riverton agricultural area (S-190B, track 62, pass 4, August 5, 1973). . . . .	51
Figure 27.	Crop and agricultural use map of the Riverton area interpreted from Skylab S-190B photography. . . . .	53
Figure 28.	Detailed crop map for a portion of the Riverton agricultural area. Interpreted from Skylab S-190B photography (Fig. 26). . . . .	54
Figure 29.	Location of Baggs study site. . . . .	55
Figure 30a.	Range vegetation map developed from LANDSAT-1 imagery of the Baggs test site. . . . .	56
Figure 30b.	Range vegetation map developed from LANDSAT-1 imagery of the Baggs test site. . . . .	57
Figure 31a.	Range vegetation map interpreted from Skylab photographs of the Baggs test site. . . . .	58
Figure 31b.	Range vegetation map from Skylab photographs of the Baggs test site. . . . .	59
Figure 32a.	Range vegetation map of the Baggs test area compiled from low-level aerial photography supplemented with ground reconnaissance. . . . .	60
Figure 32b.	Range vegetation map of the Baggs test area compiled from low-level aerial photography supplemented with ground reconnaissance. . . . .	61
Figure 33.	Map of baked shale outcrops in the Powder River Basin of northeast Wyoming interpreted from Skylab S-190B color photography. . . . .	63

Figure 34.	Skylab S-190A photograph of the Absaroka Range and Beartooth Mountains, Wyoming and Montana. . . . .	.65
Figure 35.	Comparison of alteration zones mapped by two interpreters from EREP S-190A image 15-225 of the Absaroka and Beartooth Mountains. . . . .	66
Figure 36.	Alteration map interpreted from LANDSAT color composite image 1047-17182. . . . .	.67
Figure 37.	Area of alteration mapped from Skylab S-190A color infrared photograph. . . . .	68
Figure 38.	Map showing the extent of known uranium alteration in the southern Powder River Basin. . . . .	.69
Figure 39.	Index map showing the location of the Boysen test area and the Hyattville test area. . . . .	.71
Figure 40.	Comparison of S-190A bands and S-190B photography for a small part of the Boysen area. Resolution differences are readily apparent in these enlargements. . . . .	74
Figure 41.	Field scene showing a typical pediment surface in the Boysen area. . . . .	.77
Figure 42.	Comparison of LANDSAT color composite imagery (left) and Skylab S-190A color infrared photography (right) showing the marked difference in presentation of Tertiary red beds on the LANDSAT and Skylab imagery. . . . .	.80
Figure 43.	Field scenes comparing the relatively pale Tertiary red beds to the orange-red Permo-Triassic red beds. . . . .	.82
Figure 44.	Comparison of LANDSAT color composite imagery and Skylab color infrared photography of an area in which the Thermopolis and Mowry shales are used as a geologic marker unit. . . . .	.83
Figure 45.	Spectral reflectance curves for Wyoming rocks. . . . .	84
Figure 46.	Spectral sensitivity curves for Kodak color infrared film (2443). . . . .	86

Figure 47.	Field scene showing the peculiar distribution of sagebrush on outcrops of the Cody Shale. . . . .	91
Figure 48.	A detailed geologic interpretation of an area near Thermopolis, Wyoming . . . . .	93
Figure 49.	Reconnaissance geologic map of a small area near Thermopolis, Wyoming. The enlarged S-190B photography was used as a mapping base. . . . .	95
Figure 50.	Index map showing the location of the three areas mapped from Skylab, ERTS (LANDSAT), and aerial photography. . . . .	97
Figure 51.	Skylab S-190B photograph of the Horn area (Skylab Mission 2, pass 10, frame 146, June 13, 1973). . . . .	98
Figure 52.	Reconnaissance geologic map of the Horn area, from Skylab S-190B and S-190A photography. . . . .	99
Figure 53.	Photogeologic map of the Horn area prepared from color infrared aerial photography (NASA Mission 72-138, September 10, 1972). . . . .	100
Figure 54.	Field geologic map of the Horn area (after Hose, 1955 and Richardson, 1950). . . . .	101
Figure 55.	Skylab S-192 imagery of the Hyattville area. . . . .	104
Figure 56.	Spectral reflectance curves for some common rocks. . . . .	106
Figure 57.	Photograph of the Spatial Data video analysis system used in making density measurements from the Skylab S-192 imagery. . . . .	110
Figure 58.	Histograms showing relative opacity and contrast of each S-192 image for fifteen lithologic units cropping out in the Hyattville test area. . . . .	112
Figure 59.	Summary histograms comparing total band-to-band contrasts for all fifteen lithologic units. . . . .	113
Figure 60.	Histograms summarizing image opacities measured for each unit on each of the twelve available S-192 bands. . . . .	114

- Figure 61. Diazo composite of "best" S-192 bands selected from densitometric measurements. . . . .116
- Figure 62. Alphanumeric pattern map of the Hyattville test area. Values plotted were computed via Q-mode pattern recognition. All points are scaled according to their component (weight) relative to Factor 2. . . . . 131
- Figure 63. Alphanumeric pattern map of the Hyattville test area. Values plotted were computed via-mode pattern recognition. All points are scaled according to their component (weight) relative to Factor 3. . . . .132
- Figure 64. S-190A color photograph of the Hyattville test area (track 5, pass 10, roll 16, frame 228, June 13, 1973). . . . .134
- Figure 65. Topographic map of the Hyattville test area (A.M.S., 1:250,000-scale, Sheridan two-degree sheet). Map area corresponds to region covered by color photograph (Fig. 64). Area outlined corresponds to region of figures 62 and 63 analyzed by computer. . . . 135

# LIST OF PLATES

Plate 1.	Land-use in the Moorcroft/Keyhole area interpreted from LANDSAT imagery. . . . .	pocket
Plate 2.	Land-use in the Moorcroft/Keyhole area interpreted from Skylab S-190B photography . . . .	pocket
Plate 3.	Land-use in the Moorcroft/Keyhole area interpreted from high-altitude aerial photography and field checked . . . . .	pocket
Plate 4.	LANDSAT image 1353-1718, Moorcroft/Keyhole area. . . . .	pocket
Plate 5.	Skylab photograph of the Moorcroft/Keyhole area. . . . .	pocket
Plate 6.	High-altitude aerial photograph of the Moorcroft/Keyhole area. . . . .	pocket
Plate 7.	Possible selenium-rich Shingle series soils and sandstone outcrops of the Wasatch Formation, Campbell County, Wyoming, interpreted from Skylab photography. . . . .	pocket
Plate 8.	Geologic map of a part of central Wyoming showing actual mapping without extrapolation. . . . .	pocket
Plate 9.	Combined geologic interpretation of S-190A infrared bands for the Boysen test area . . . . .	pocket
Plate 10.	Geologic interpretation of the Skylab S-190A green band for the Boysen test area. . . . .	pocket
Plate 11.	Geologic interpretation of the Skylab S-190A red band for the Boysen test area. . . . .	pocket
Plate 12.	Geologic interpretation of the Skylab S-190A color photography for the Boysen area. . . . .	pocket



# LIST OF TABLES

	Page
Table 1. Summary of Skylab coverage provided in support of the "Multidisciplinary Study of Wyoming Test Sites." . . . . .	3
Table 2. High-altitude aerial photography provided in support of the "Multidisciplinary Study of Wyoming Test Sites." . . . . .	4
Table 3. Contributors to the University of Wyoming EREP program. . . . .	6
Table 4. Summary of eigen values and factor weights computed by Q-mode analysis of Hyattville area S-192 data. . . . .	129

## INTRODUCTION AND OBJECTIVES

Skylab sensor coverage was obtained over the Wyoming test site on each of the three manned Skylab missions. The S-190A cameras obtained useful coverage over almost 70 per cent of Wyoming (Fig. 1) and the high-resolution S-190B cameras obtained coverage for correspondingly smaller strips (limited by the 59-nautical-mile swath width of the S-190B cameras). Stereographic coverage was obtained from the S-190A and S-190B cameras on most of the successful data passes. S-191 and S-192 data were obtained only on a few selected passes (Table 1). These data were used by University of Wyoming investigators in an evaluation of the EREP sensors for a number of earth resources applications in several test areas. The three main objectives of this work were:

1. To evaluate the S-190, S-191 and S-192 sensors as tools for resource inventory and management.
2. To compare the Skylab data to the LANDSAT imagery and high-altitude aerial photography as applied to resource problems.
3. To determine essential parameters that limit or enhance the relative utility of the different sensors and sensor systems.

In all applications, emphasis was placed upon the simplest and least expensive of techniques so that the procedures defined might be more readily transferred to the user community.

## PERSONNEL

The EREP research program at the University of Wyoming was supported by personnel representing several University departments and a variety of interests. Although the emphasis of the investigation was

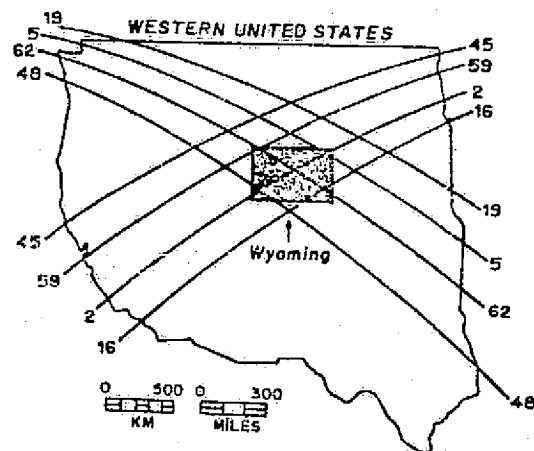
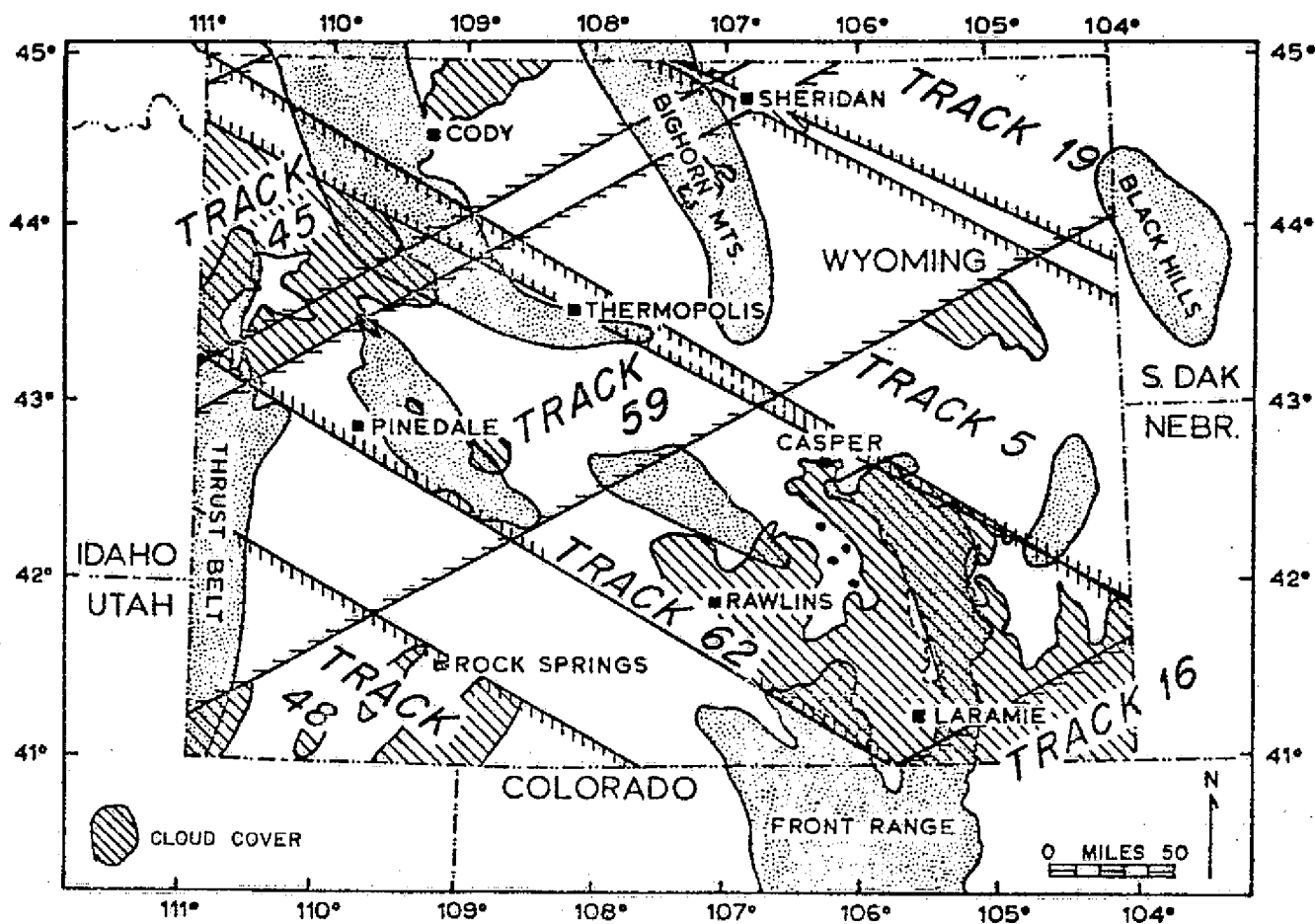


Figure 1. Index maps showing Skylab ground-track pattern (left) and S-190A coverage of Wyoming obtained during Skylab missions 2, 3, and 4 (cross-hatched areas denote cloud cover).

Table 1. Summary of Skylab coverage provided in support of the "Multidisciplinary Study of Wyoming Test Sites."

Mission	Mission Pass	PREP Pass	Date	Ground Track	S-190A	S-190B	S-191	S-192
2	6	6	6/9/73	19	X	X		X
2	8	8	6/11/73	48	X			X
2	10	10	6/13/73	5	X	X		X
3	2	13	8/4/73	48	X	X		
3	4	15	8/5/73	62	X	X	X	
3	20	31	9/10/73	16	X	X		
3	26	37	9/12/73	45	X	X		
3	28	39	9/13/73	59	X	X		X
3	32	43	9/15/73	16	X	X		
4	37	88	1/22/74	5	X	X		X
4	44	92	1/27/74	2			X	X

Table 2. High-altitude aerial photography provided in support of the "Multidisciplinary Study of Wyoming Test Sites." \*

Flight or Mission	Date	Estimated Line Miles	9" color	9" color IR	Multiband	Other
248	8/73	800				Thermal
310	5/75	890				

\* Specific areas of coverage from NASA Missions 248 and 310 are shown cross-hatched on the Index of available NASA photography of Wyoming (Fig. 2).

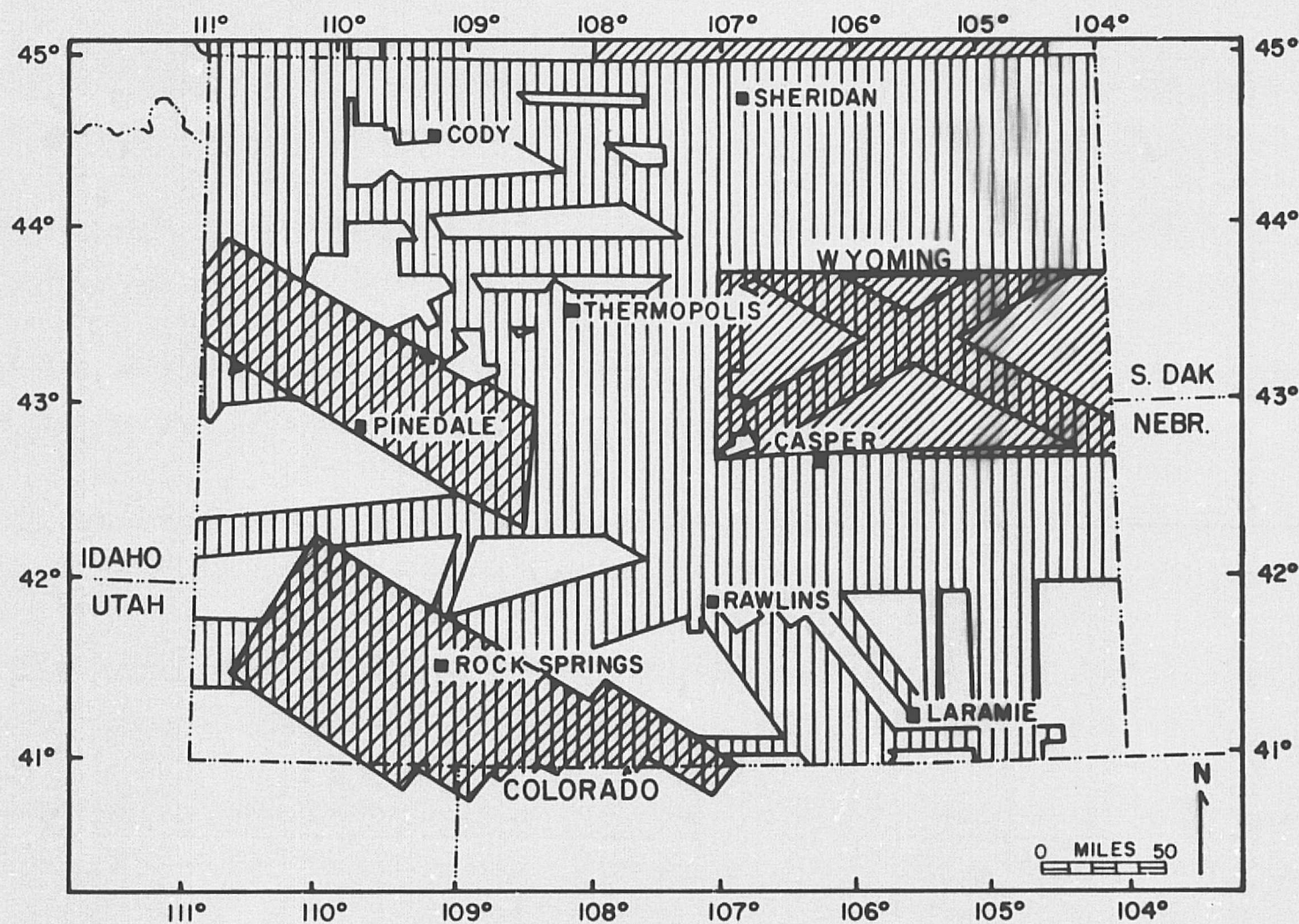


Figure 2. Index map showing high-altitude air photo coverage of Wyoming flown by NASA aircraft. Missions 248 and 210 were flown in support of the EREP investigation.



toward geologic applications, close cooperation between geologists, hydrologists, and plant scientists allowed maximum advantage in interpretation of the interdependence between rock, soil, water, and vegetation and also provided a greater capability for evaluation of the satellite data in multidisciplinary applications such as land-use. Those who contributed to this research are listed in Table 3.

Table 3  
CONTRIBUTORS TO THE UNIVERSITY OF WYOMING EREP PROGRAM

Name and Title	Contribution to EREP research
R. S. Houston, Principal Investigator	Administration, geologic mapping, and economic geology
R. W. Marrs, Co-Principal Investigator	Administration, remote-sensing, geology and land-use
L. E. Borgman Co-Investigator	Statistics, computer applications
R. B. Parker Co-Investigator	Linear features and tectonics
D. L. Blackstone Co-Investigator	Regional tectonics and structure
E. R. Decker Co-Investigator	Geothermal and computer processing
H. Fisser Co-Investigator	Range mapping and evaluation
B. Mears, Jr. Consultant	Geomorphology
P. Huntoon Consultant	Hydrology
R. C. Gordon Research Asst.	Range management and plant science
B. J. Tomes Research Asst.	Geology and hydrology

Name and Title	Contribution to EREP research
K. E. Kolm Research Asst.	Soils, geomorphology and geochemistry
N. Froman Research Asst.	Structure and economic geology
J. Earle Research Asst.	Geologic mapping and tectonics
B. Kaminsky Research Asst.	Computer-assisted mapping
J. Vietti Research Asst.	Geologic mapping
K. G. Downing Research Asst.	Regional tectonics
D. Worrall Research Asst.	S-192 comparative analysis
W. Lauer Photo Technician	Film processing and duplicating
K. Meister Technical/Clerical Asst.	Film librarian and clerical
K. McCarty Technical/Clerical Asst.	Film librarian and clerical
A. Zimmerman Draftsman	Drafting

#### DESCRIPTION OF THE TEST SITES

Wyoming is a semi-arid region of relatively high elevation and severe climate. Skies are exceptionally clear and the vegetation cover is sparse to moderate over much of the terrain. Yet, natural resources (particularly mineral resources) are abundant and the landscapes are incredibly diverse. This combination offers ideal conditions for testing and evaluation of remote-sensing systems for resource management.

Lithologic exposures vary from poor to excellent throughout Wyoming so that test sites for geologic mapping may be selected from any number of suitable areas. For example, the Medicine Bow test site, which was originally proposed as the prime test area, was largely cloud-covered during all EREP data takes; so the Bighorn/Owl Creek area was selected as an alternate geologic test site because it was successfully imaged on two EREP passes. Other sites were chosen for tests of other applications on the basis of coverage, special needs or interests, or on the basis of special occurrences or conditions.

The Green River Basin was chosen as a site in which to attempt mapping of the flat-lying, poorly consolidated, Tertiary formations common to Wyoming basins. Here the Tertiary sediments are present in a tremendous variety of landscapes and facies interrelationships. Some important facies changes are well documented and are expressed in surface outcrop. These units afforded an opportunity to test the Skylab photography in an attempt to delineate some very subtle geologic features.

The Madison Formation cropping out along the west flank of the Bighorn Mountains was selected as a test site in geohydrologic studies largely because of the recent interest in this aquifer as a potential source of water for development of energy and mineral resources in the Powder River Basin.

Interest in the coal, petroleum, and uranium of the Powder River Basin prompted attempts to map the baked-shale (used as road metal) outcrops associated with zones of burned-out coal and to employ the EREP data as a tool in a regional analysis of land-forms, land-use, and

vegetation. A more detailed land-use study was conducted for the Moorcroft/Keyhole area, which is one of the prime locations for residential and recreational development in this area (Marrs, 1975).

Range studies were conducted both in the Powder River Basin and in the Baggs area of south-central Wyoming, where the University of Wyoming maintains a controlled grazing site.

Wyoming and portions of adjacent states served as a test site in which the EREP and LANDSAT data were employed in tectonic analyses; although most of the linear elements used in these analyses were mapped in the mountain areas.

The Hyattville area, in north-central Wyoming, was chosen for comparative evaluations of the S-192 multispectral scanner data because it was one of the few areas of geologically diverse terrain for which S-192 data were available. These data were evaluated both through digital analyses and by direct measurements upon the S-192 imagery.

Attempts were also made to use the Skylab data as a tool for direct detection of anomalous haloes that might be associated with copper deposits of the Absaroka region and with uranium deposits in the Wind River and Powder River basins. These attempts were largely unsuccessful.

#### APPROACH

This study involves evaluations of each of the Skylab imaging sensors in earth resource applications. Those applications in which the surface expression of rocks, soils, and vegetation play a major role were approached via standard techniques of image interpretation and field mapping. In other applications, for which the surface expressions

provide only an indirect indicator of the significant parameters, image enhancement techniques were employed in the interpretation of the data and statistical procedures were used in drawing results from the data.

Image interpretations were made in a variety of ways using the standard photographic products provided by NASA and/or from photographic products enlarged or enhanced to allow for better interpretation. Photo-interpretive equipment used by investigators in this study includes the Kern PG-2 stereoplotter, the Bausch and Lomb zoom transfer scope, and the Richards MIM-3 interpretation table equipped with a Bausch and Lomb zoom stereoscope. Enlargement and reprocessing of the photographic data was accomplished through the custom color processing laboratory at NASA/JSC and via a similar color photo laboratory operated by the University of Wyoming since autumn, 1974. Image enhancement and data analysis capability was provided by the University computer center and the Department of Geology image analysis laboratory. This image analysis laboratory is equipped with a Joyce Loebel/Tech Ops isodensitracer, a Spectral Data PV/61 color additive viewer, and a Spatial Data 401/704 edge enhancer and image analyzer. Together, these facilities have allowed investigators a full range of image analysis capability to supplement the standard interpretative procedures.

Results of the image interpretation were checked against both published and unpublished information. Field investigations proved instrumental in checking many of the results.

## RESULTS OF INTERPRETATIONS OF SKYLAB DATA

Many of the significant results of this investigation have already been presented in final or preliminary form in "progress reports" or "special reports" submitted while the investigation was yet in progress. These results are summarized in this final report along with previously unreported results of the Skylab sensor evaluations. But, the results presented here represent only the "tip of the iceberg". Analysis of most of the Skylab data is yet to be completed, and the real "significant results" will only be realized as the data are applied to the daily problems of users. Even the conclusions drawn from these analyses represent something of a preliminary analysis. Continuing work will undoubtedly uncover new applications of the earth resources data and will produce better techniques with which to interpret and use the data.

### General Resource Applications

The field of resource applications to which the Skylab EREP data may be applied is extremely broad. Applications attempted by Wyoming investigators represent only a few of the possible and potential applications, but we feel that these studies represent a sample set (or a significant portion of a sample set) from which to determine the relative utility of the EREP sensors, their capabilities, and their critical limitations.

### Geology

The major emphasis of the Wyoming investigation was in the geologic applications of the satellite data. Attempts were made to employ the



EREP imagery in general outcrop and structure mapping programs, in geomorphic analyses, in tectonic studies, in mineral exploration and in several areas peripheral to geology, such as hydrology and soils. In all of these efforts the EREP data was used with some degree of success.

General Geologic Mapping. Geologic maps were compiled from S-190 photography in six different test areas. Outcrops within these areas represent lithologies ranging in age from Precambrian to Quaternary. This very large stratigraphic section includes igneous and metamorphic rocks (Precambrian) as well as a large number of marine and non-marine clastic formations. The major lithologies and their approximate time correlation are summarized in the stratigraphic nomenclature chart (Fig. 3).

Both the Green River and Powder River Basin test areas encompass broad expanses of poorly consolidated, sedimentary rocks of Tertiary age. These are interesting from a geologic standpoint because of major facies changes which reflect lateral variation in depositional environment and because of the cyclic repetition within a vertical section of the sedimentary units which records temporal changes in the sedimentary environment. The Tertiary sedimentary rocks are also of economic interest because they contain vast amounts of construction materials (sand and clinkers), trona, uranium, oil shale, some placer metals, and water.

In the Green River Basin the Tertiary sedimentary units are generally flat-lying and many of the lithologic distinctions are subtle. Vegetation is sparse and the surface geomorphology is moderately complex with some control exerted by both aeolian and fluvial processes.

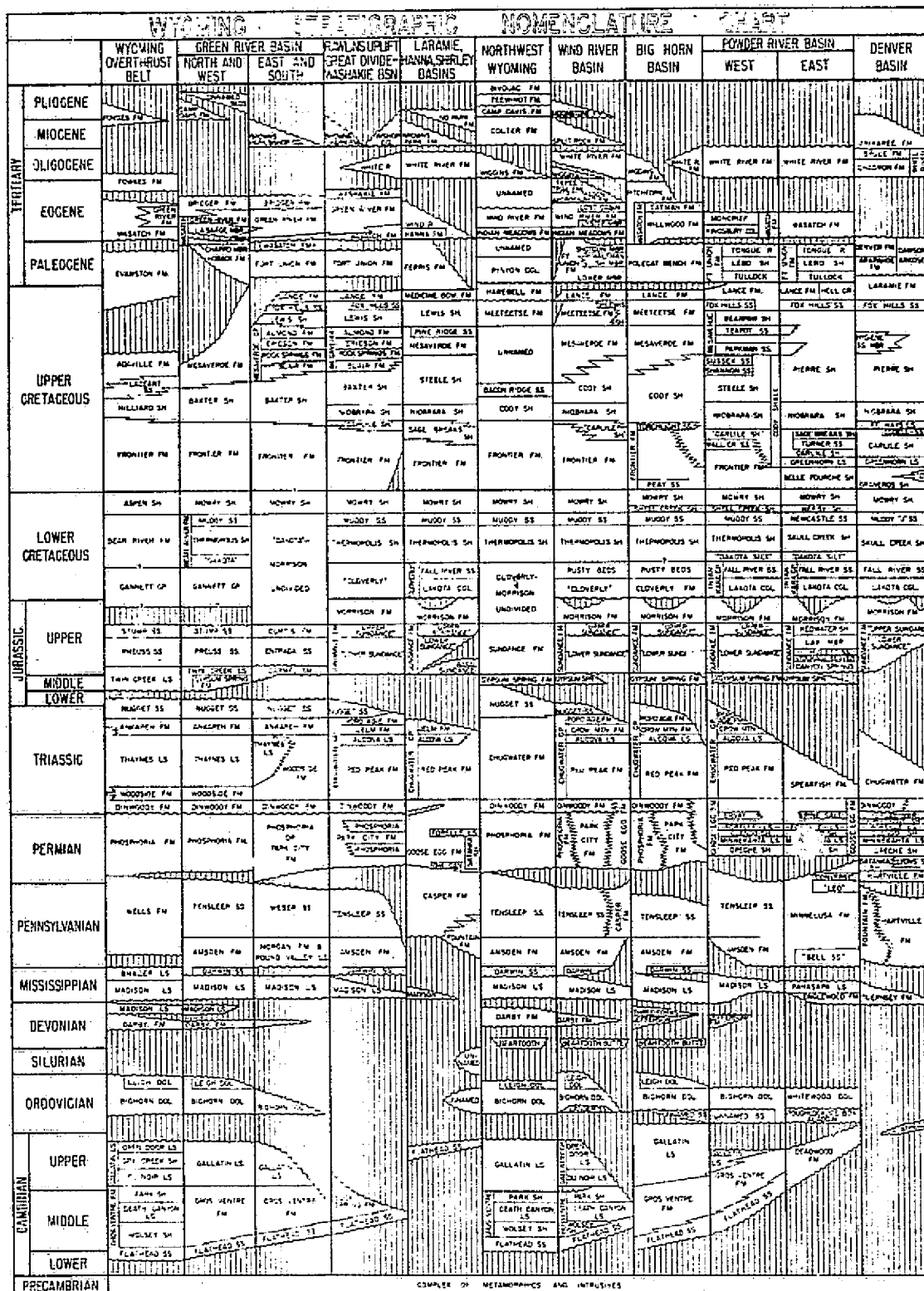


Figure 3. Wyoming stratigraphic nomenclature chart (from Wyoming Geological Association Guidebook, 1973).

ORIGINAL PAGE IS  
OF POOR QUALITY

S-190A multispectral photography (Fig. 4) was used in compiling a photogeologic interpretation of the northern Green River Basin. Stereoscopic coverage was only available from the S-190A cameras, so the S-190A photography was nearly as useful as the non-stereoscopic S-190B data on this data pass. The relatively sparse vegetative cover allowed good discrimination of many of the major formations and several sub-units within the formations (Fig. 5). However, several of the formational contacts normally used in field mapping could not be detected on the photography. Comparison between the photointerpretation and the regional geologic map of the area (Love and others, 1955) showed that the units chosen through photointerpretation parallel the formal geologic formations, but the contacts do not correspond precisely. They must, therefore, be considered "telegeologic" or "remote sensing" units.

The S-190A color photography was found most useful for mapping in this area because it contains the essential hue information that enables the interpreter to distinguish subtle changes in color which mark many of the contacts of the telegeologic units and some facies changes. The color infrared was also quite useful because it, too, recorded color differences; but the spatial resolution of color infrared photography was considerably poorer than that of the color photography.

The test area mapped in the Powder River Basin includes sedimentary units ranging in age from Cretaceous through Quaternary. The western two-thirds of the test area is covered by loosely consolidated sedimentary units of the Tertiary, Wasatch, and Fort Union Formations overlain by Quaternary alluvium flanking the major drainages. Cretaceous

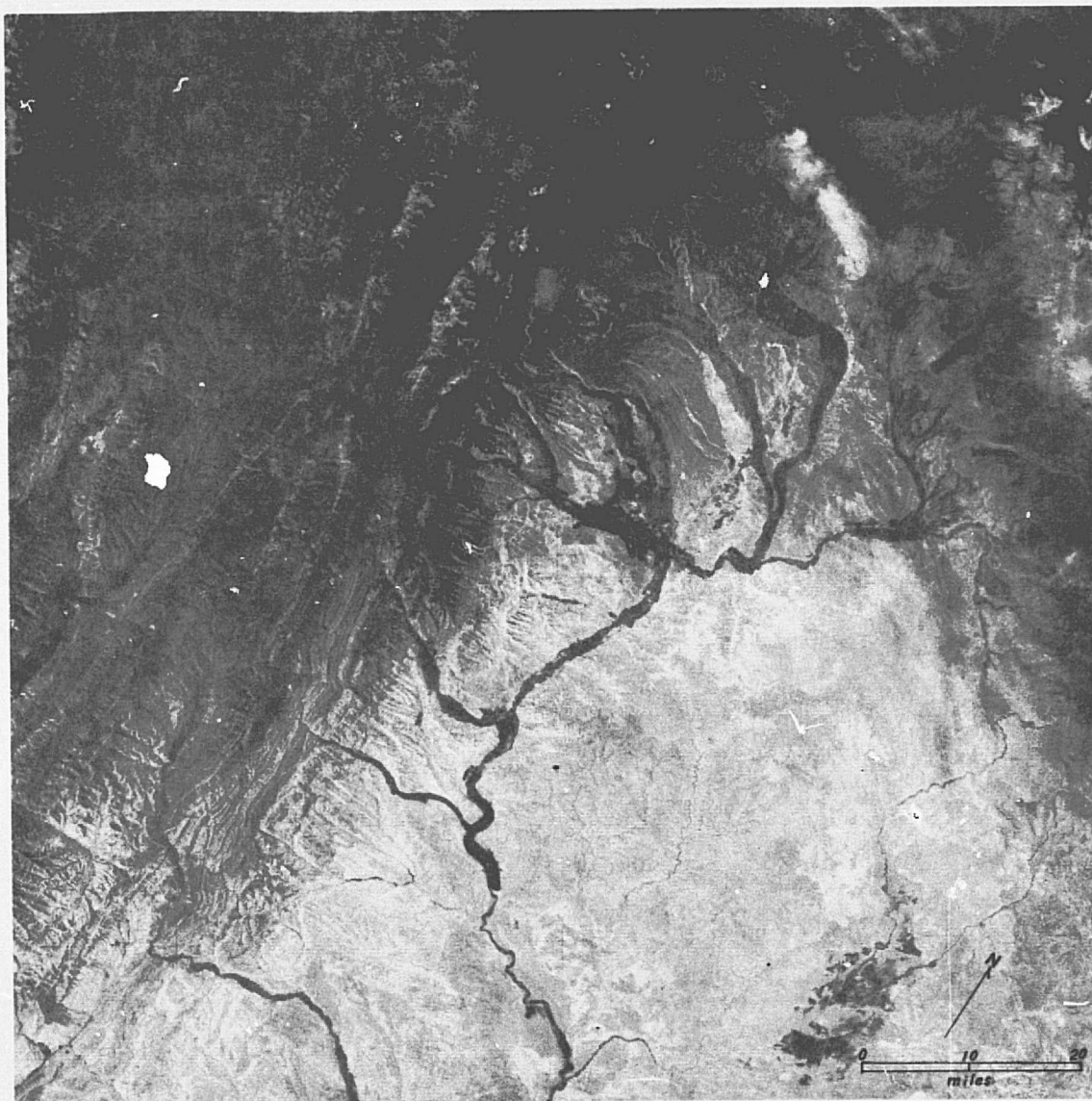


Figure 4. Skylab S-190A image (roll 41, frame 204, red band, track 59, pass 28, Sept. 13, 1973) of the Wyoming Thrust Belt, the Green River Basin, and the Wind River Mountains.

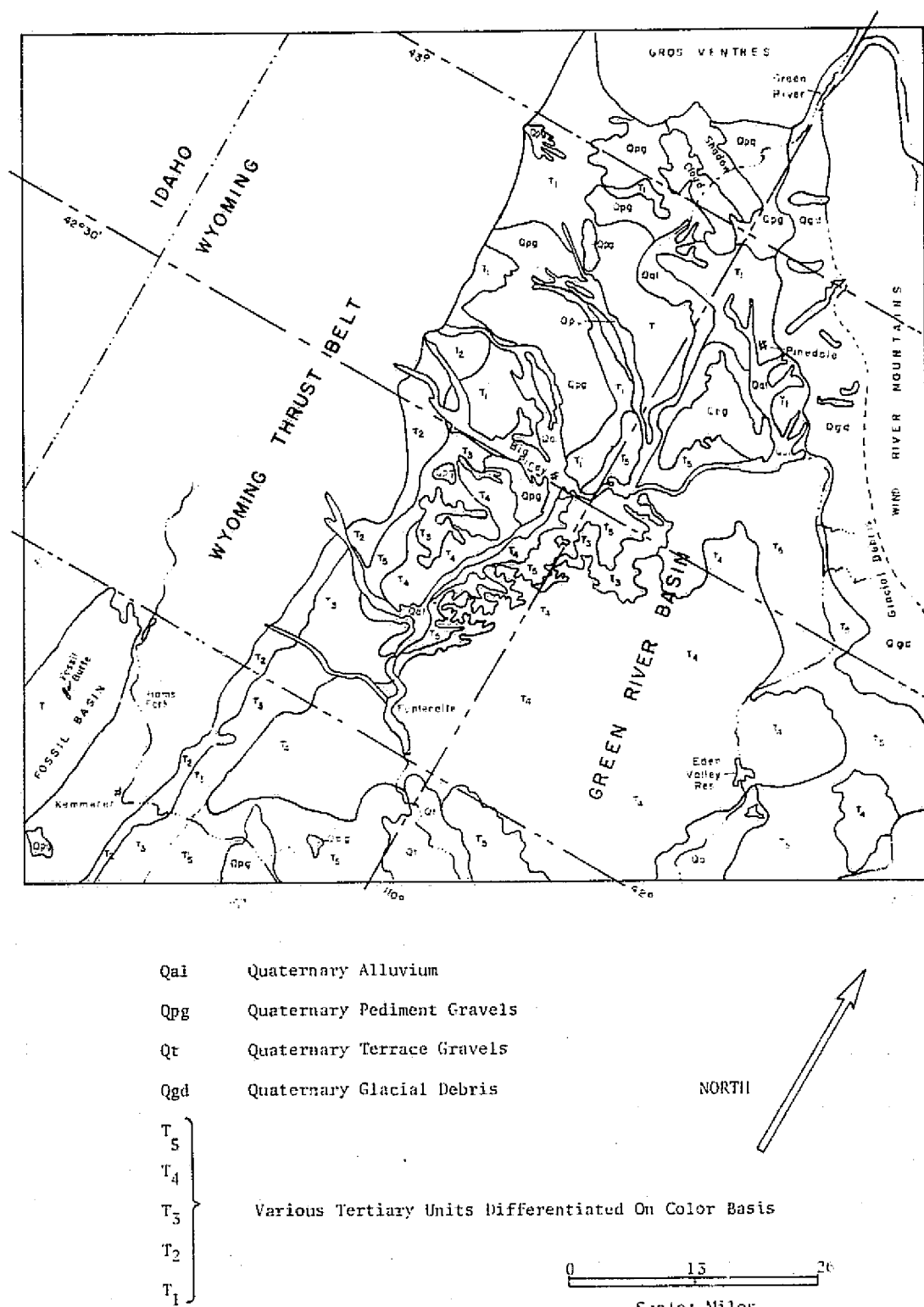


Figure 5. Geologic photointerpretation of the Green River Basin, Wyoming; interpreted from Skylab S-190A photograph 41-204 (Fig. 4).

sedimentary rocks crop out in the northeastern corner of the area where they lap onto the western flank of the Black Hills uplift.

An outcrop map (Fig. 6) interpreted from the S-190B color photography (Fig. 7) again, shows excellent correspondence with the regional geologic map (Love and others, 1955). In general, the contacts were easily located on the basis of contrasting geomorphic and tonal characteristics. Vegetation cover is heavier in the Powder River Basin than in the Green River Basin and caused some difficulty in defining the tonal contrasts that could be related to contrasts in rocks and soils.

Some formally recognized units were necessarily combined because they were not distinguishable on the Skylab photography. Others, such as the Fort Union Formation, were divided into several units that could be correlated with formational members and sub-members. The Lebo and Tullock members of the Fort Union Formation were not distinguishable, but the Tongue River Member was divided into a lower unit (characterized by badlands topography) and an upper unit (characterized by valley-and-mesa topography). This distinction was strikingly depicted in the stereo presentation of the S-190B photography. The subdivision of the Tongue River Member may not be geologically significant, but baked shale units appear to be concentrated in the lower unit.

Results from these initial efforts prompted attempts to employ the S-190 photograph in general geologic mapping of the structurally complex Greybull and Horn areas, which lie on the west and east flanks (respectively) of the Bighorn Mountains.

The study in the Horn area involved a detailed comparison of the LANDSAT imagery, the Skylab S-190B photography, and high-altitude aerial

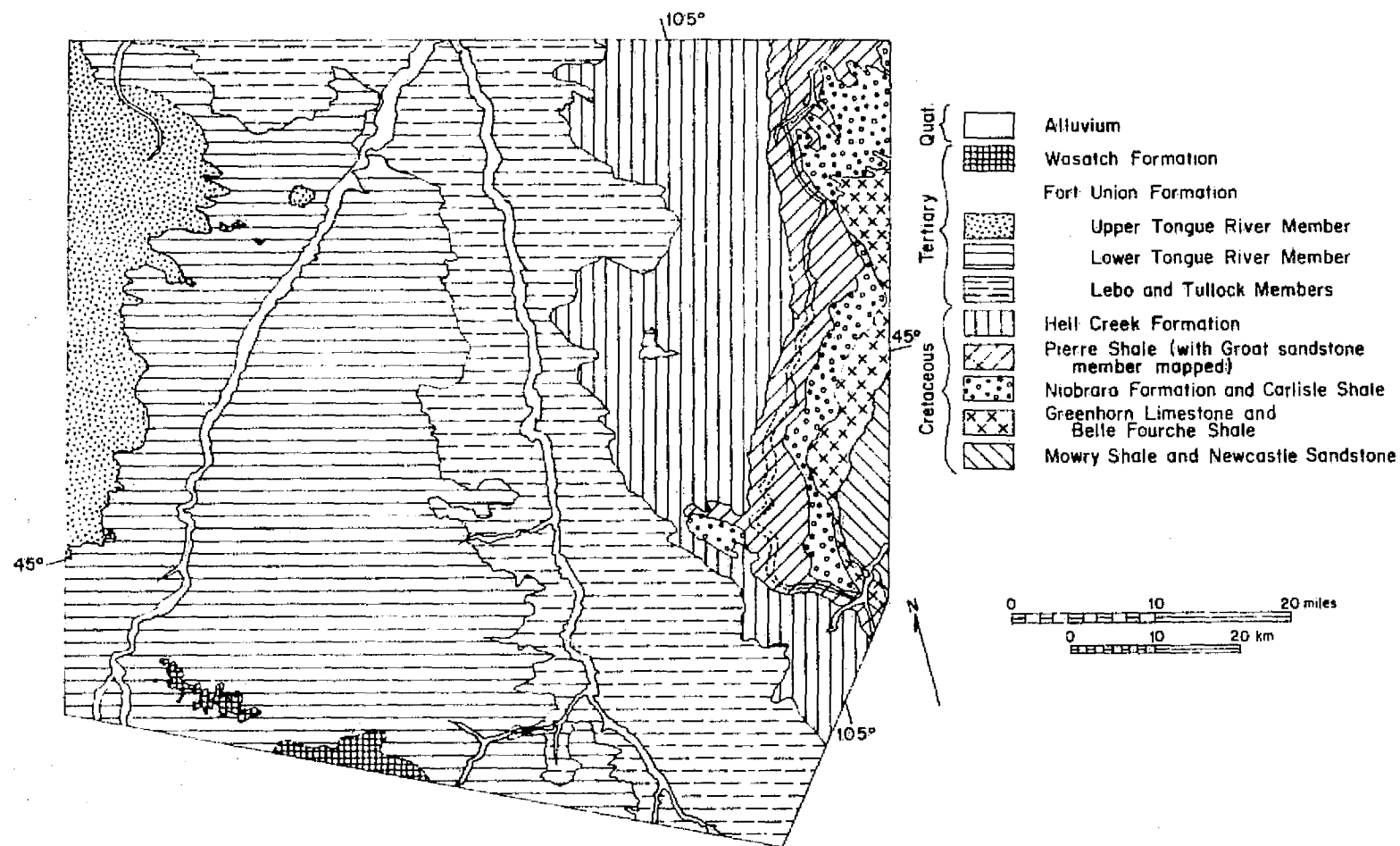


Figure 6. Outcrop map of the Black Hills/Powder River Basin area of northeast Wyoming (interpreted from Skylab, S-1908, color photograph 81-153).





Figure 7. Halftone reproduction of Skylab S-190B color photograph (roll 81, frame 153, track 19, pass 6, June 9, 1973). The area shown is a portion of the Powder River Basin lying immediately west of the Black Hills.

**ORIGINAL PAGE IS  
OF POOR QUALITY**



photography. The study was designed to estimate the value of improved resolution and the multi-level approach in geologic mapping. An excellent photogeologic map was constructed from the S-190B photography for this area in which rocks of Precambrian, Paleozoic, and Mesozoic age are intensely folded and faulted. The study is summarized in greater detail in a later section of this report and by Houston (1973b, p. 77-97).

In the Greybull test area sedimentary rocks of Cretaceous and Paleozoic age crop out in a series of tightly folded and faulted structures. A number of widely different lithologies are included in this stratigraphic section and many of these contrast sharply with adjacent units such that the interpreter has several distinct "marker" units with which to work. The resulting photogeologic map (Fig. 8a) was compared to an existing geologic map (Fig. 8b) at 1:125,000 scale. As in the previously discussed mapping attempts, the telegeologic units are somewhat different than the formal geologic units recognized in the area; but, the contacts were found to be mapped in greater detail on the S-190B photointerpretation and several structures were identified which did not appear on the published geologic map. It was concluded that the S-190B offers great potential for updating and improving existing geologic maps.

A fifth area in which the Skylab photography was applied to geologic mapping was a region of Precambrian igneous and metamorphic rocks in the Owl Creek Mountains in central Wyoming. In this area, a series of Precambrian greenstones have possible economic significance because they include some iron-rich metasedimentary beds. An attempt was made to segregate the greenstones from the surrounding igneous rocks by interpretation of the Skylab S-190B photography.

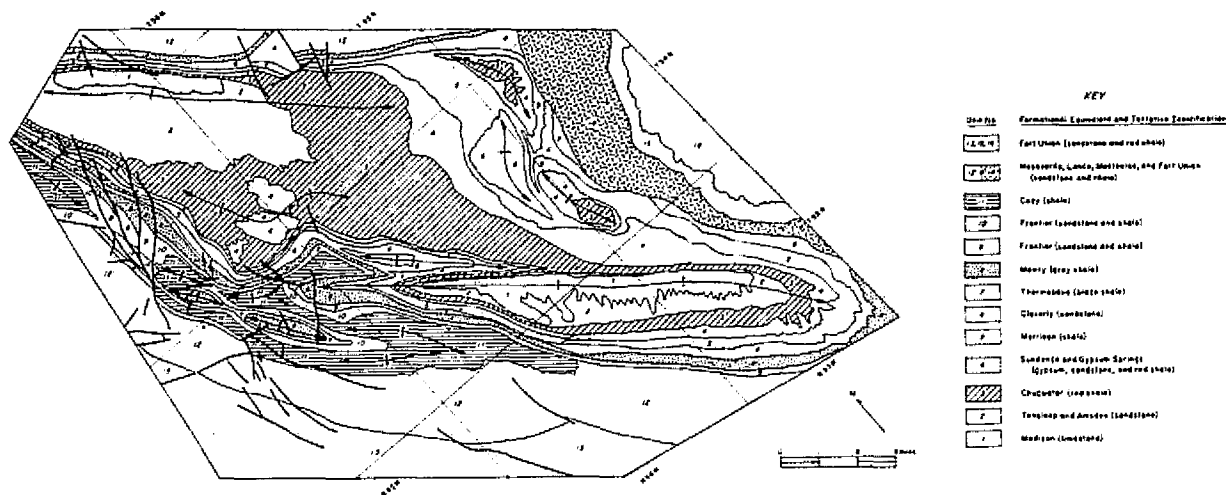


Figure 8a. Photogeologic map of the Sheep Mountain area near Greybull, Wyoming; interpreted from Skylab S-190A (roll 15, frame 227, track 5, pass 10, June 13, 1973).

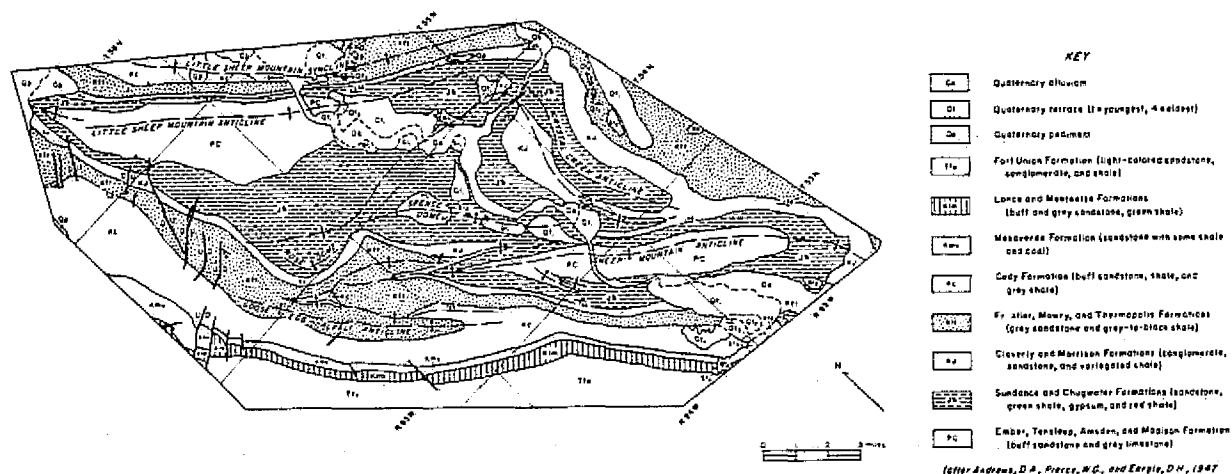


Figure 8b. 1:125,000-scale field geologic map of the Sheep Mountain area near Greybull, Wyoming (after Andrews and others, 1947).

Figure 9a is a geologic map showing the extent of the greenstone belt in the Owl Creek Mountains of Wyoming as known from published geologic maps. Figure 9b is a map of this greenstone belt as prepared from the Skylab photograph. Comparison of the geologic map (Fig. 9a) and the Skylab photogeologic map (Fig. 9b) shows that the known part of the belt was mapped with reasonable accuracy at 1:500,000 using the Skylab photograph. It was also possible to extend the belt to the east where no published maps were available. It is rarely possible for a photogeologist to be certain he is mapping in an unprejudicial manner when published maps are available and when the geologist has some familiarity with an area, as was the case for the western part of this greenstone belt. But, at the time the Skylab photogeologic map was prepared, there was no information on the eastern extension of the greenstone belt; so this can be considered unbiased photogeologic mapping. After mapping the belt, it was determined that H. Barnes of the United States Geological Survey had prepared a reconnaissance map of the eastern part of the greenstone belt. It was then possible to check the accuracy of the unbiased photogeologic mapping. Comparison of Barnes' map (Fig. 9c) and the Skylab map (Fig. 9b) shows that the "unknown" part of the belt was certainly mapped as accurately as the known.

The results of these five studies allowed the Wyoming research team to conclude that 1) the EREP S-190 photography is a valuable tool for general geologic mapping in sparsely-to-moderately vegetated areas where outcrops are relatively abundant, 2) direct photointerpretation techniques are usually effective in geologic mapping, 3) stereoscopic coverage greatly enhances the use of satellite photography for geologic mapping, 4) the S-190 photography is useful as a means of updating and improving some

WESTERN OWL CREEK GREENSTONE BELT  
FIELD GEOLOGIC MAP

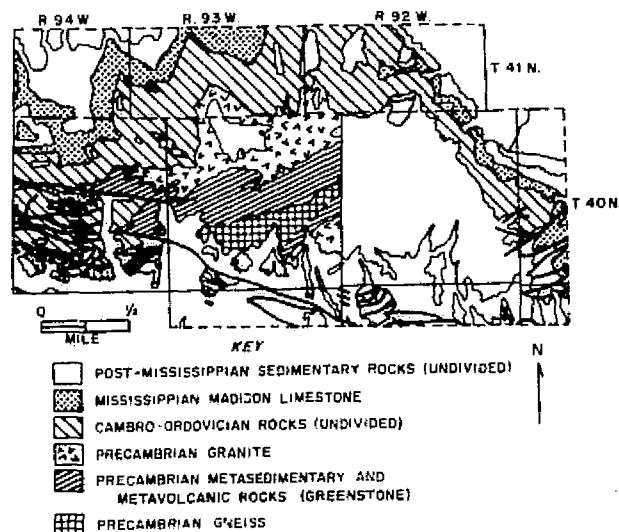


Fig. 9a. Geologic map of Precambrian units in the Owl Creek Mountains of Wyoming (Precambrian units after Duhling, 1969; other units after Love and others, 1955).

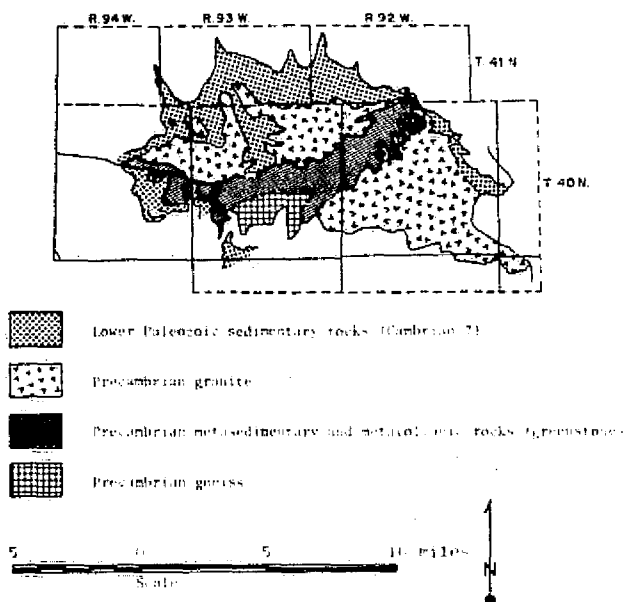


Fig. 9b. Photogeologic map of the Owl Creek greenstone belt as interpreted from Skylab S-190 photography (after Houston, 1974a).

EASTERN OWL CREEK GREENSTONE BELT  
FIELD GEOLOGIC MAP

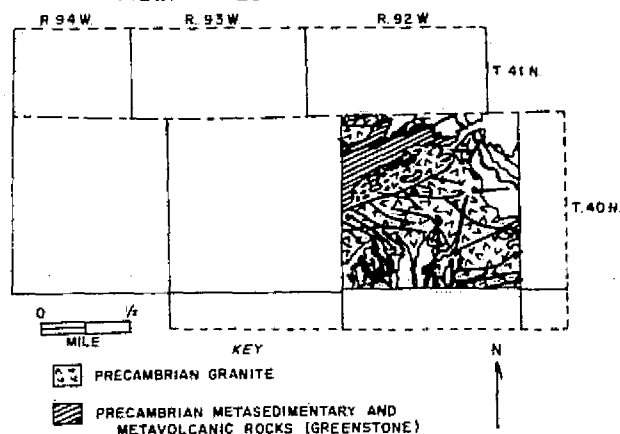


Fig. 9c. Reconnaissance geologic map of the eastern Owl Creek greenstone belt (after H. Barnes, USGS, personal communication, April, 1974).

existing geologic maps and 5) the photointerpretive techniques are applicable in widely different types of geologic terrain.

Tectonics. The broad image-swaths of the earth resources satellite systems give a regional overview ideal for tectonic analyses. Soon after the launch of the first ERTS (LANDSAT) in 1972, it was recognized that the satellite imagery offers a new perspective on the earth by which "linear features" or "photo linear elements" are strikingly displayed. Many of these linear elements can be related to discontinuities in the earth's crust and can be interpreted in terms of stress fields, zones of weakness, controls for mineralization, and regional tectonics. Subsequently, the LANDSAT data has been widely used as a means of identifying and mapping these linear elements. In northern and southern latitudes, the winter (snow-cover) LANDSAT imagery was found most effective for mapping of linear features enhanced by shadows. Shadow enhancement is a function both of the low elevation of the winter sun and the high albedo of the snow-covered earth which contrasts strongly with shadows. Many topographically expressed linear elements (those trending obliquely to the sun azimuth) are enhanced in these images.

The orbit of LANDSAT presents only one major disadvantage. The imaging cycle is repeated for successive image sets at almost the same time of day and with nearly the same viewing geometry. Therefore, the variation in elevation and azimuth of illumination is minimal (varying only with season) and the viewing aspect is constant. The resulting interpretations and analyses of linear elements are severely biased by this restricted imaging geometry.

Skylab offers a new and more variable geometry with which to view the earth. The Skylab orbit allowed image coverage to be acquired at almost any time of day; and hand-held photographs taken by the astronauts provide an oblique view that can be used in conjunction with the vertical views provided by the S-190 and S-192 sensors.

The advantage of the oblique view is illustrated by Figures 10 and 11 which show one of the hand-held, 70mm photographs taken by the Skylab astronauts and the interpretation of linear features made from this photograph. Many linear features which are not apparent on vertical views of this same area are enhanced on this oblique view. One very great disadvantage in using the oblique photography is the difficulty encountered in transferring the interpreted image data to a map. This difficulty can be overcome by using a rectified version of the oblique photo for the initial interpretation (Figs. 12 and 13).

In addition to Skylab's variable imaging geometry, the stereoscopic coverage of the S-190 system and the greater resolving power of the S-190 cameras (compared to LANDSAT) gives the Skylab system an even greater advantage in the study of photo linear features.

Several tests were designed to evaluate the Skylab S-190 data in the study of photo linear elements. Initially, an area in the Wind River Mountains, for which the major linear features had been mapped from LANDSAT imagery was also interpreted for major linear features using Skylab photography (Fig. 14). These two maps were then compared with respect to the dominant trends of the mapped linear features. In both the LANDSAT and Skylab interpretation a strong illumination angle bias is apparent

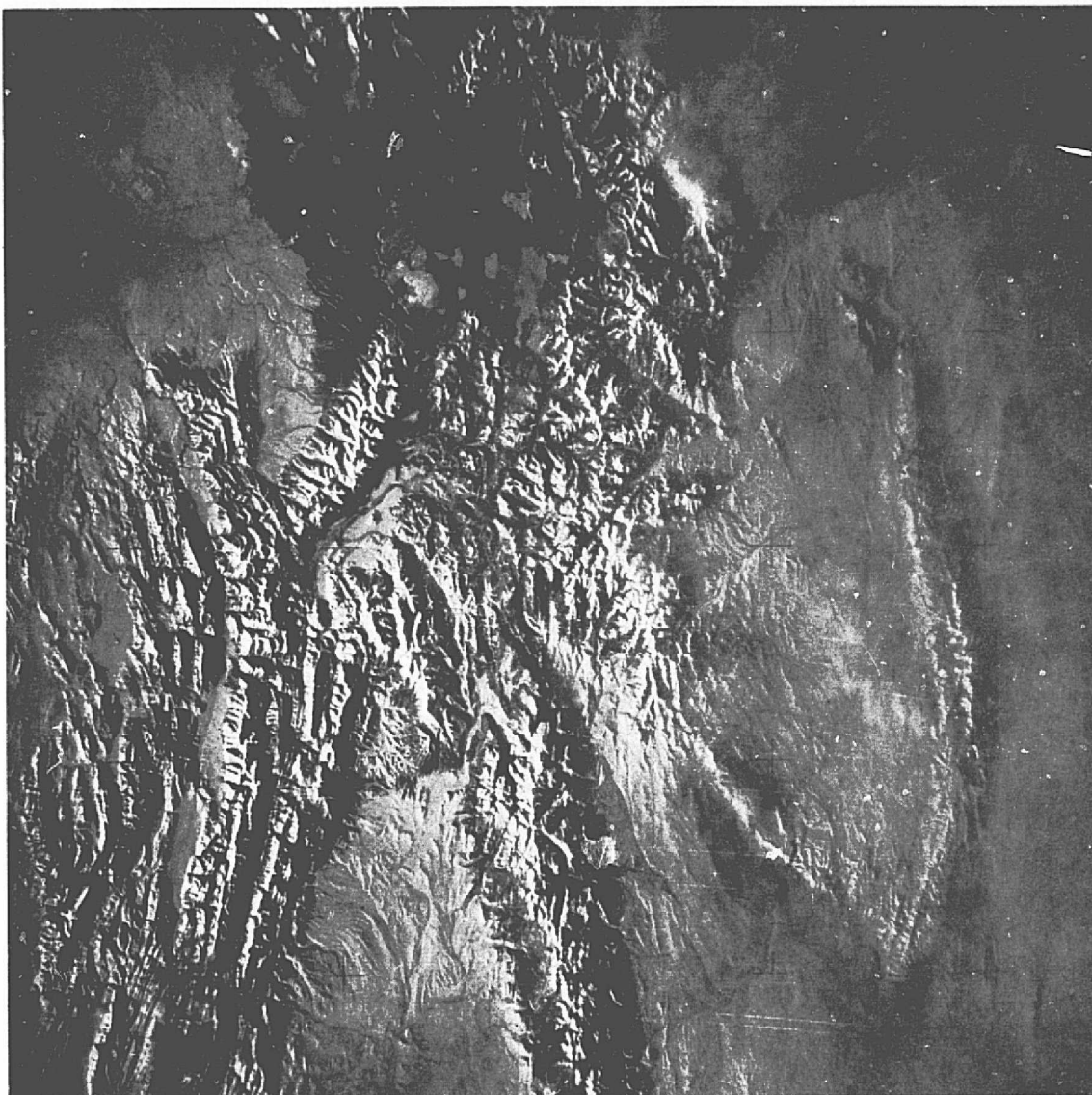


Fig. 10. Oblique photograph of snow-covered northwest Wyoming taken by Skylab astronauts on Skylab Mission 4.

ORIGINAL PAGE IS  
OF POOR QUALITY



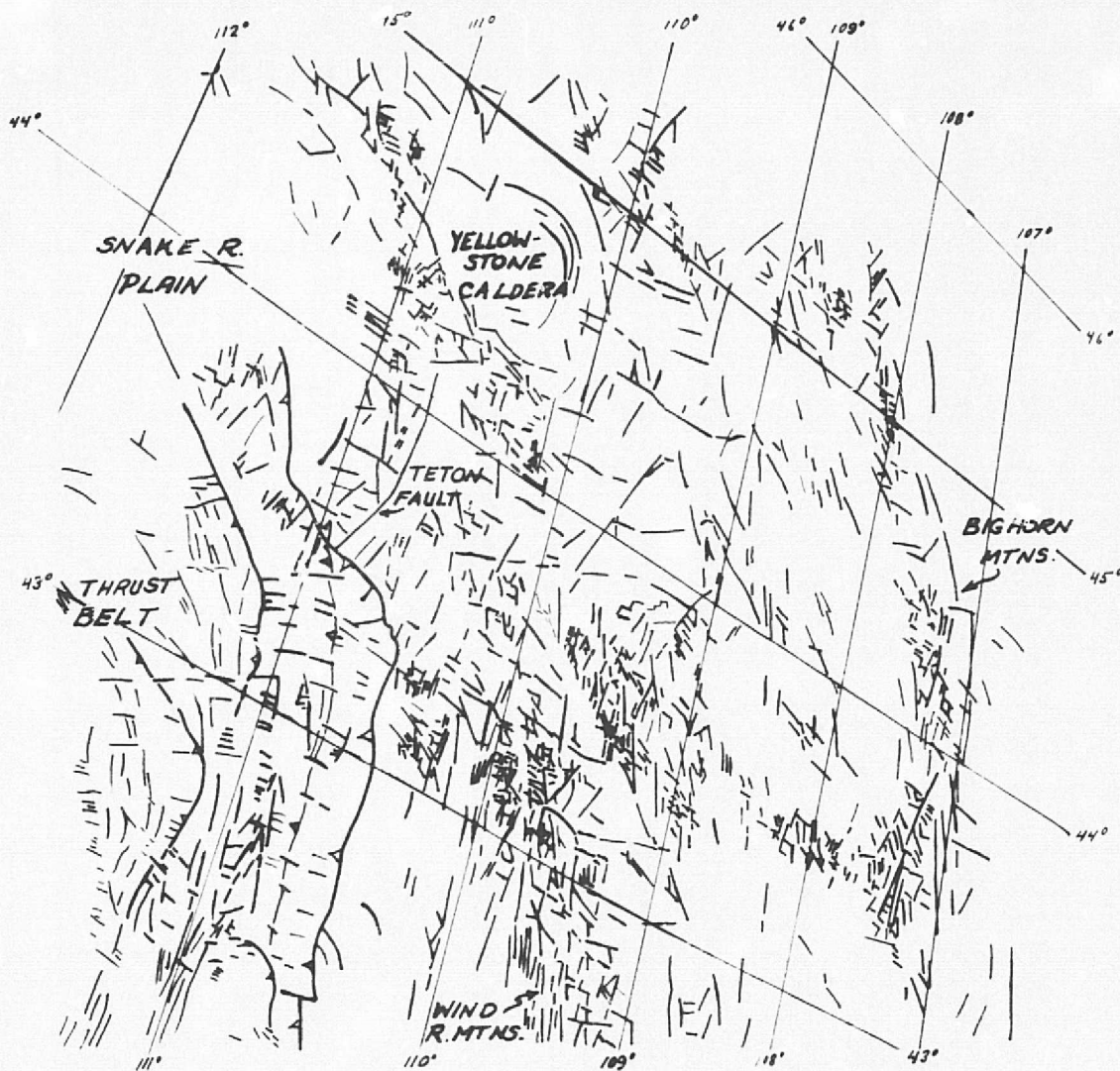


Fig. 11. Photo linear features interpreted from the Skylab 70mm oblique photo (see Fig. 10).



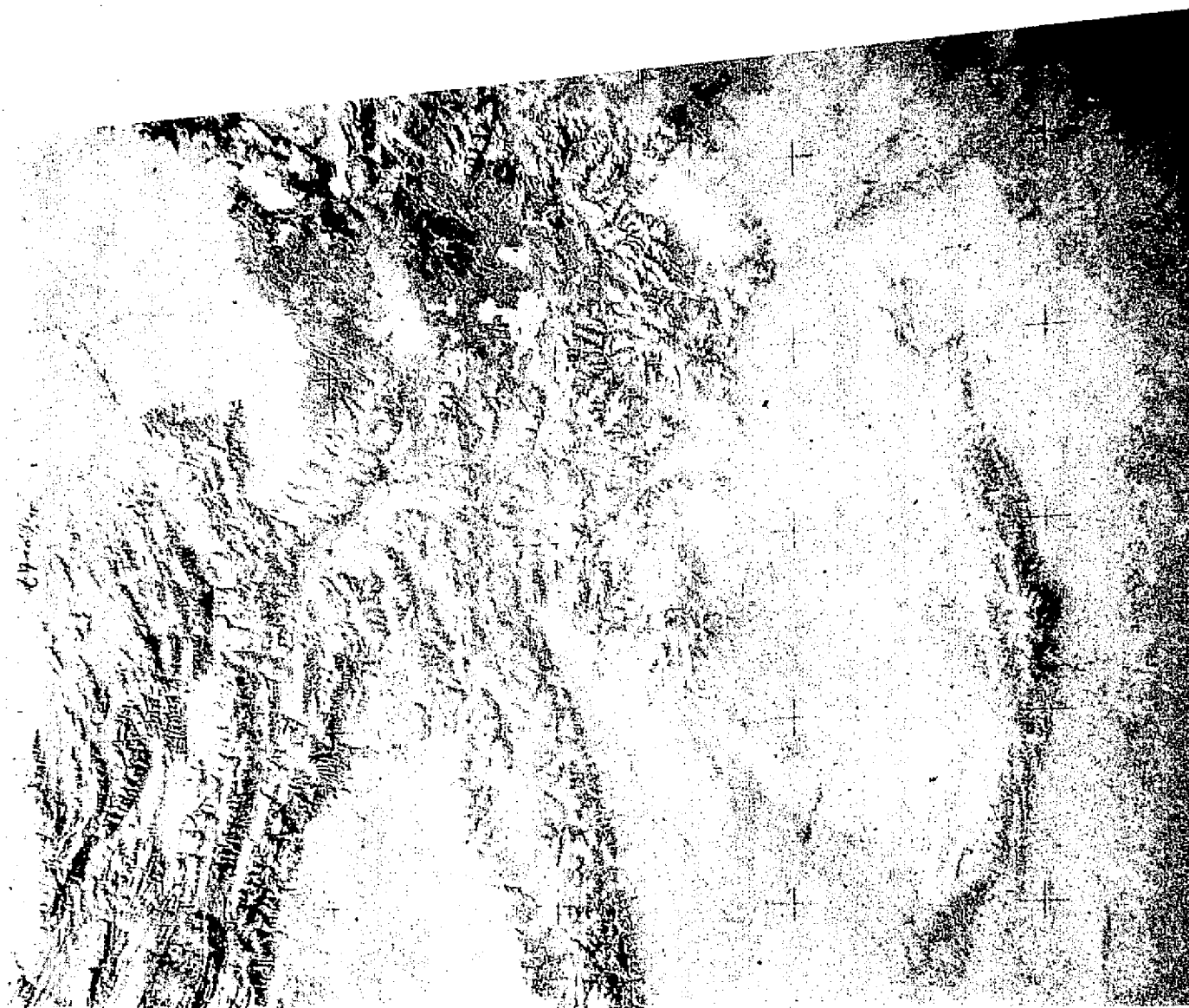


Fig. 12. Skylab hand-held oblique photo rectified to allow correlation with vertical photography and base maps.

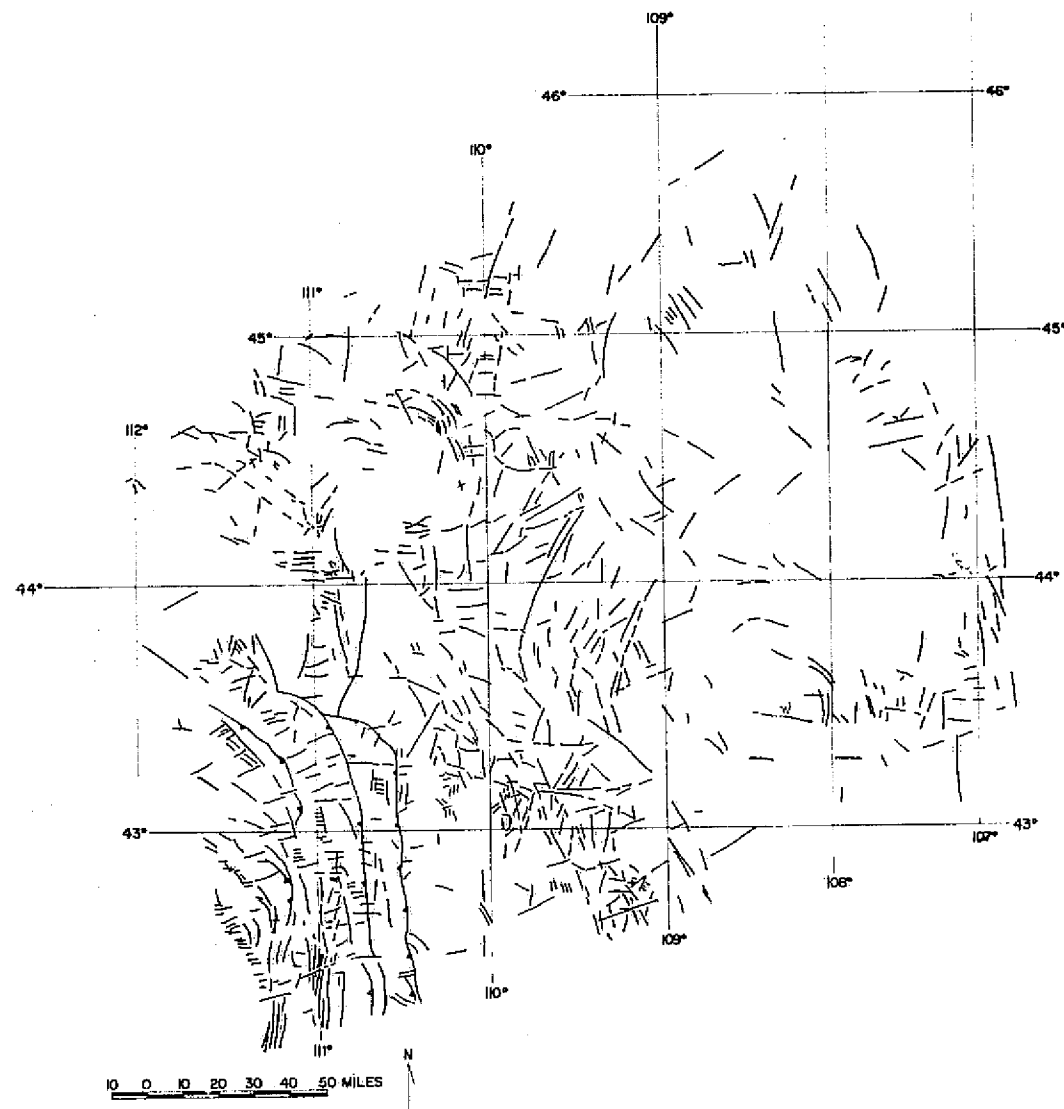


Figure 13. Linear features map prepared from rectified oblique photograph.

ERTS

SKYLAB

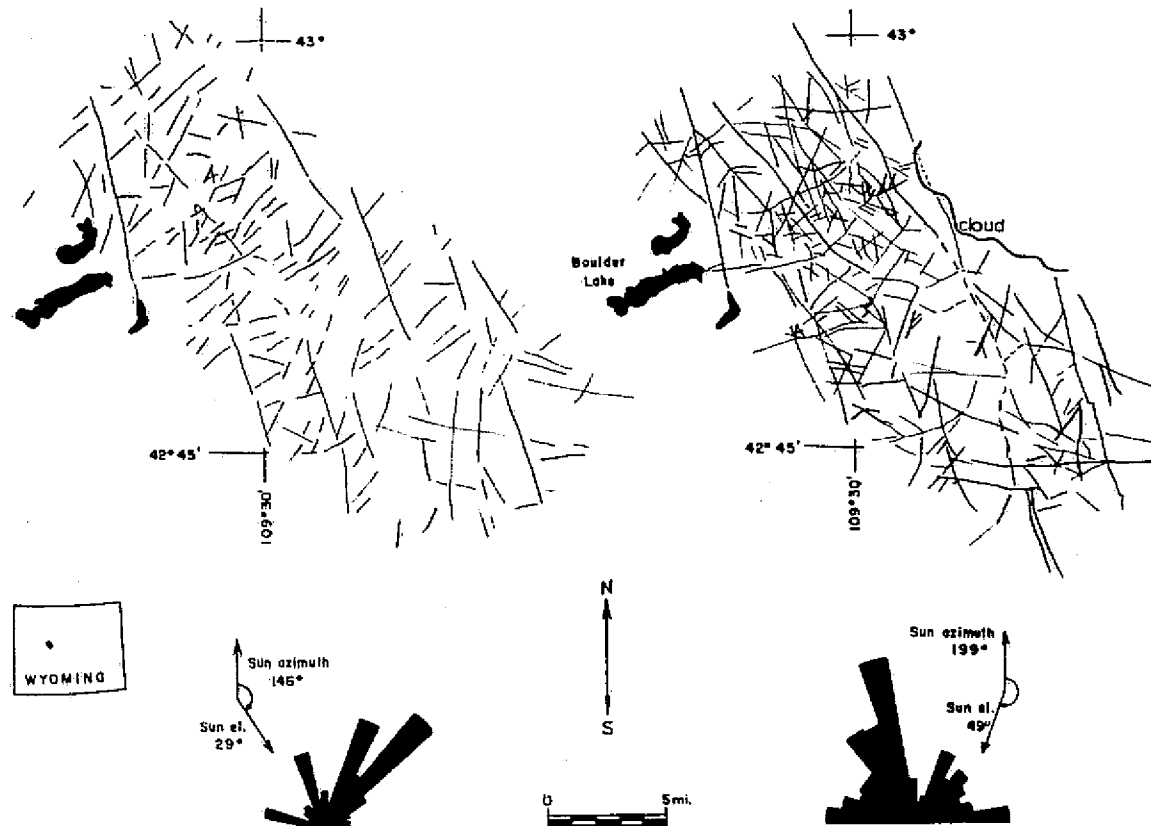
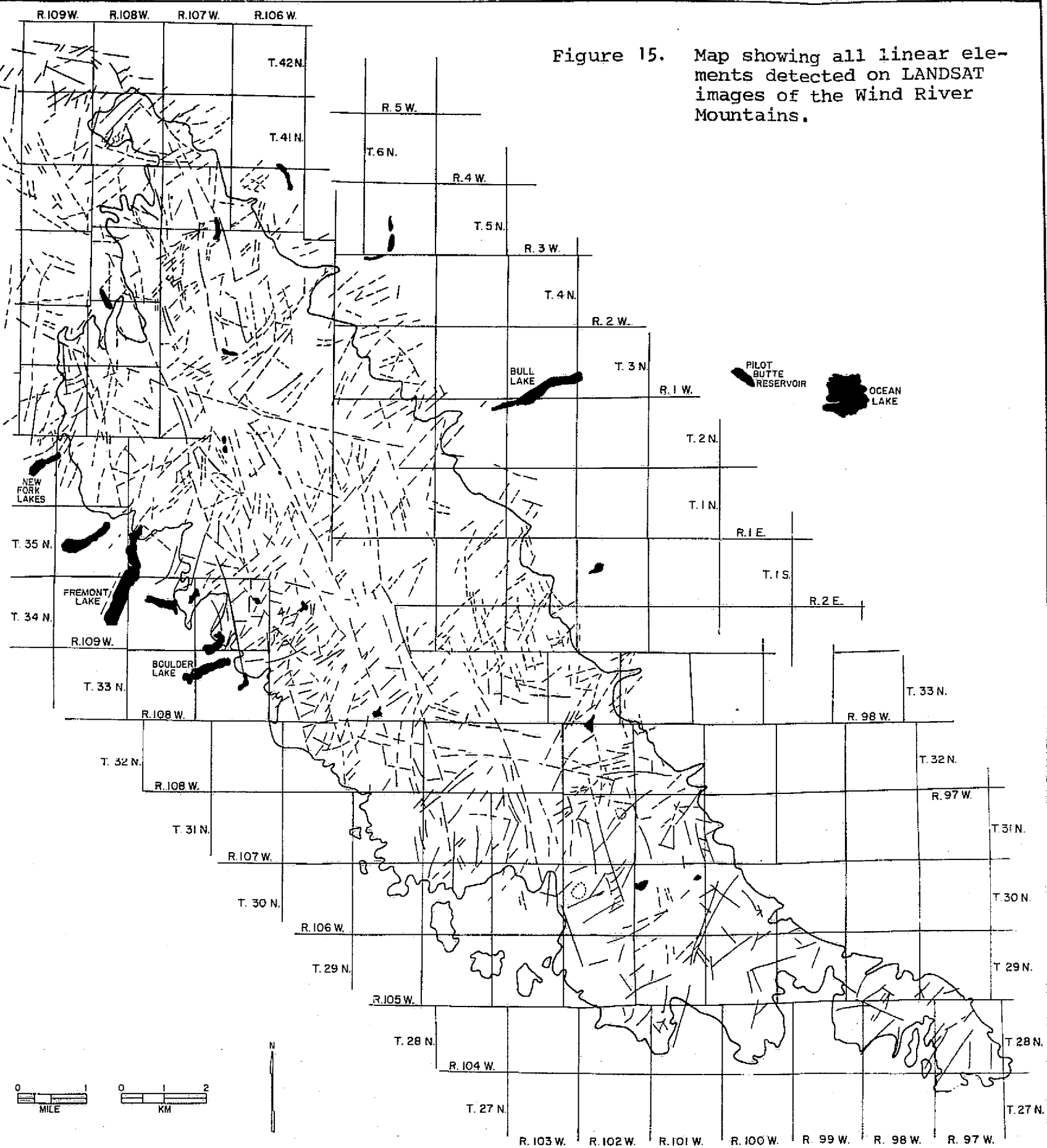


Fig. 14. Comparison of linear features mapped using LANDSAT MSS images and Skylab S-190B photographs of the Wind River Mountains test site.

in the trends. Linear features parallel or nearly parallel to the sun's azimuth are seldom detected and both interpretations are biased toward linear elements that trend approximately orthogonal to the sun's azimuth. A combined interpretation of the LANDSAT and Skylab images yields a better map than either of the two interpreted separately.

The next step in the EREP evaluation for tectonic studies was to compare the LANDSAT and Skylab linear features maps with regard to total information content. For this test, the Wind River Mountains test site was mapped both from LANDSAT (Fig. 15) and Skylab (Fig. 16), taking care to mark all visible photolinear elements. These two maps were then compared to give an estimate of the advantage of the greater resolving power of the S-190A photography. An absolute correlation between the two maps could not be made because of the bias introduced by the different sun elevations and azimuths and because of the partial cloud cover on the Skylab image. However, comparison of areas of common coverage between the two images shows that the better resolution of Skylab photography allows the interpreter to map more linear features from the Skylab photography than from the LANDSAT imagery.

The third test of the EREP data in tectonic applications was an attempt to define interrelationship between structural provinces using data or linear features derived from the S-190 photography. In this study, a strip of Skylab photography (Track 5, June 13, 1973) was interpreted for linear features in an area extending from the Beartooth Mountains of Montana, across the northern Bighorn Mountains and into the Powder River Basin of Wyoming (Fig. 17). The interpreted area was then divided into three zones (subdivided on the basis of structure and geomorphology) to be compared to one another.



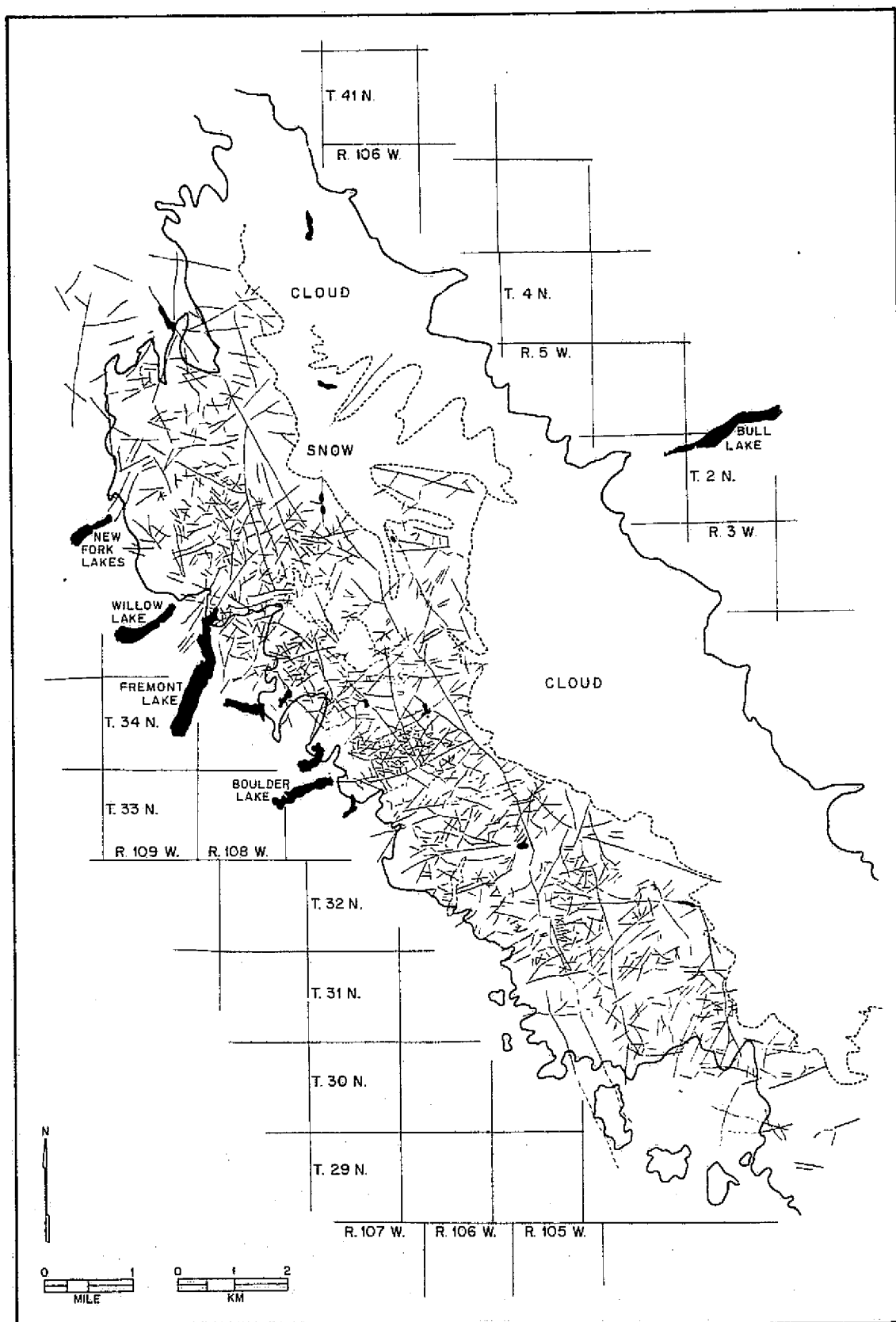
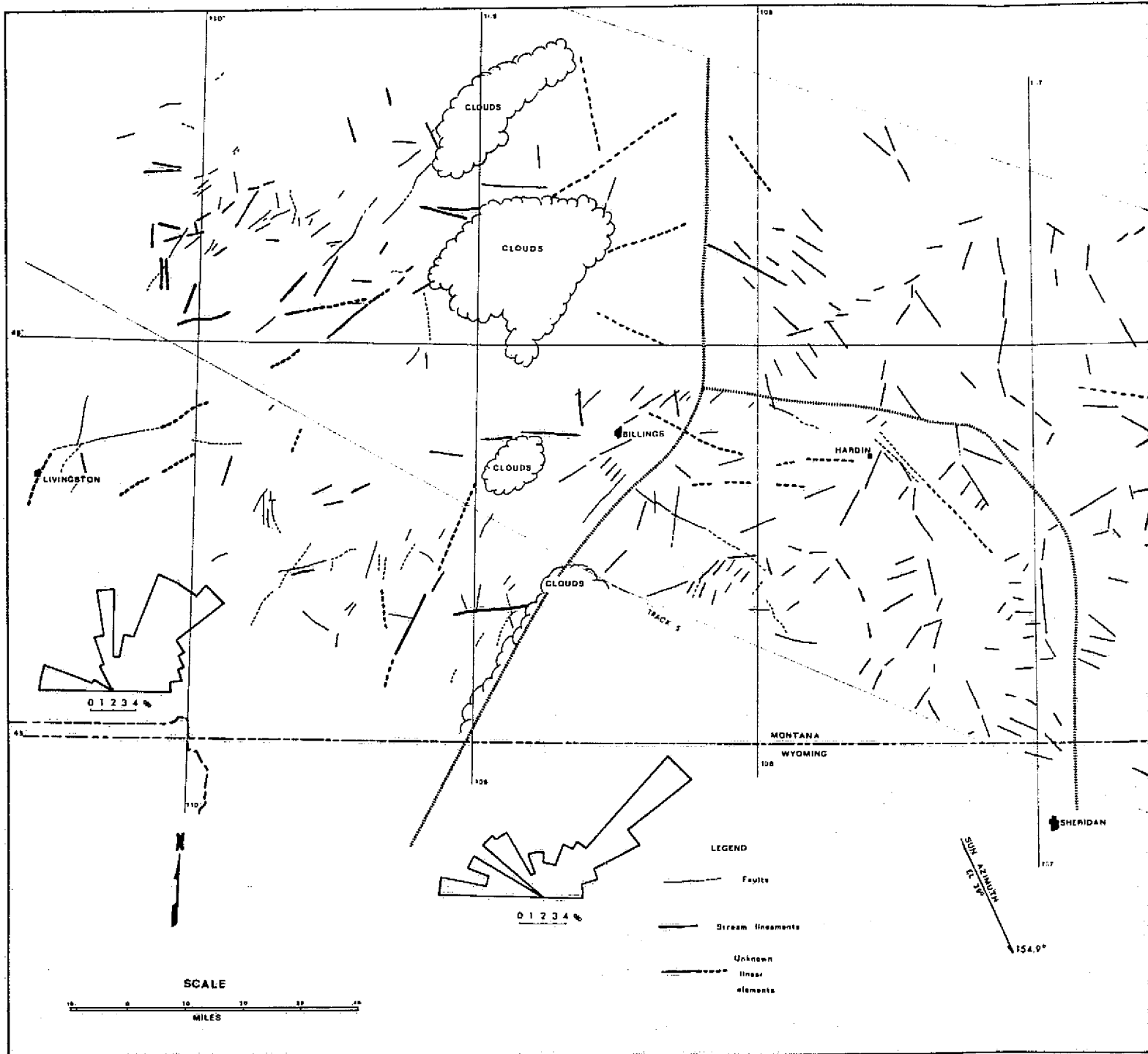


Figure 16. Map of all linear elements detected on Skylab S-190 photography of the Wind River Mountains test site.

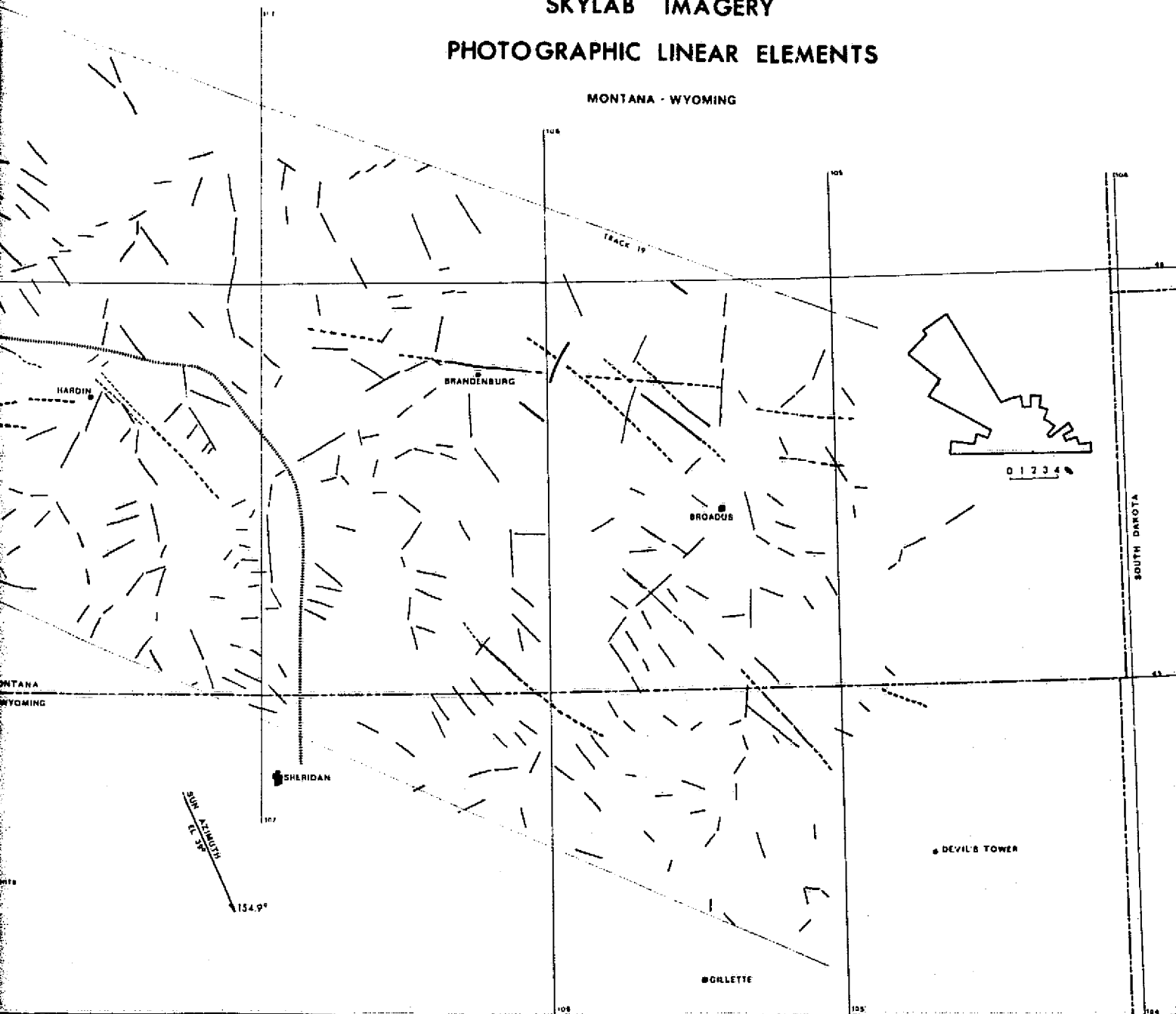


**Figure 17**

**SKYLAB IMAGERY**

**PHOTOGRAPHIC LINEAR ELEMENTS**

MONTANA - WYOMING



FOLDOUT FRAME 2



A rose diagram was constructed for each zone to summarize the trends of the linear elements. The two mountainous zones (Bighorn/Pryor Mountains and Beartooth/Crazy Mountains) have northeast and west-northwest trending sets of linear elements. A sun azimuth of  $155^{\circ}$  enhances the northeast-trending sets so that they appear dominant. The Beartooth/Crazy Mountain zone also exhibits a north-northwest-trending set of linear elements not apparent in the Bighorn/Pryor Mountains, and the Bighorn/Pryor Mountains zone shows a bimodal northwest trend (which must be very strong to overcome the negative bias introduced by sun azimuth). The only major trend seen in the Powder River Basin zone is an extremely strong northwest trend that correlates well with the northwest trend seen in the Bighorn Mountains.

These correlations can be interpreted in terms of structural interdependence through time. The strong northwest trend seen in the Bighorn/Pryor Mountains and in the Powder River Basin might be considered the "younger" trend because it effects the relatively young (Tertiary) sedimentary rocks of the Powder River Basin. The northeast- and west-northwest-trending sets might be considered an older set of features that might extend throughout the area and be masked in the Powder River Basin by the Tertiary cover. The absence of the strong northwest trend in the Beartooth/Crazy Mountains and the occurrence of the north-northwest trend might be interpreted in a number of ways. These trends could be an indication of a later development in the Beartooth/Crazy Mountains under a separate stress system, or of late rotation of the Beartooth/Crazy Mountains Block relative to the Bighorn/Pryor Mountains and Powder River

Basin. Each of these possibilities could have major implications with regard to the regional tectonic pattern and geologic history of the area. Further studies in adjacent areas and more detailed comparisons of the structural style in each of these areas should help define the true relationships.

The results of these applications tests were sufficiently encouraging so that a more comprehensive program was designed to attempt a re-evaluation of Wyoming tectonics using the earth resources satellite data. This program began with a compilation of a statewide map of linear features from LANDSAT winter imagery. This is to be supplemented by interpretations of all available Skylab coverage, which should help to remove illumination-angle bias. Analyses of these maps will be done with the same procedures used in the Beartooth-Powder River Basin test, but field checks and comparisons with published structural information will serve to improve the analysis of results.

Interpretation of both the LANDSAT and Skylab imagery has been completed for this project, and preliminary analyses have been made for the LANDSAT interpretations (Earle, 1975). The Skylab interpretations and published data are now being prepared for input into the statistical correlations. Completion of this project is presently scheduled for January, 1976.

Geomorphology and Landforms. Landforms are an integral part of the total geologic picture and the geomorphic processes that produce the landforms are controlled, in part, by the geology. Consequently, one cannot deal with the surface geology without using geomorphology as an interpretation guide. In constructing a geologic map, one looks to

differential weathering, drainage density, distinctive land-forms, and topography as clues to help in identification and mapping of lithologies and structures. In mapping photo linear elements one looks for linear discontinuities in the landforms as well as in the lithologies and topography. In all resource applications, the surface morphology is important.

Success in correctly identifying and mapping landforms is measured by the success achieved in all applications in which the surface morphology was used as a guide. Therefore, the EREP data were judged quite effective in geomorphologic applications; and, in fact, the S-190 photography is currently being used as an operational tool for compilation of land-form maps to be used in planning for mineral development in the Powder River Basin (U.S. Geological Survey, contract 14-08-0001-G-163).

The S-190 data has two particular attributes which are critical to its use as a land-form mapping base (i.e., good resolution and stereoscopic coverage). The resolution of the S-190A photography is just barely adequate for mapping land-forms at a scale of 1:100,000 and the stereo coverage allows direct interpretation from a magnified stereo model (with the 9-inch transparencies mounted on the Kern PG-2 stereoplotter). In some locations the S-190A data must be augmented by S-190B photography or aerial photography for accurate interpretation of the land-forms at 1:100,000 scale, but the advantage of regional perspective and ready correlation across broad areas more than offsets the detail limitations of the S-190A photography.

## Land Use and Environment

Mapping and monitoring of land-use has become increasingly important as attention is focused on the environment. Government agencies, in particular, are pressed by the need to obtain up-to-date land-use information quickly and efficiently. Satellite sensor systems provide the only reasonable hope for obtaining such data. The LANDSAT system, with its 18-day orbit cycle, has been very effective in land-use studies because the repetitive coverage allows the interpreter to view the surface in several seasons and better enables him to identify vegetation and use patterns by interpreting the seasonal or annual progression of change. This same repetitive coverage, when collected over a period of months or years, can be used to monitor land-use change.

In land-use applications, the EREP data does not offer the repetitive coverage; so the LANDSAT system has a decided advantage. However, the EREP sensors do offer the advantage of greater resolution. The importance of having higher resolution is best appreciated by comparing land-use interpretations made from LANDSAT and EREP imagery (Pls. 1 and 2) to a field-checked land-use map (Pl. 3). The EREP S-190B photography definitely yields a better interpretation than the LANDSAT data when mapping at a scale of 1:62,500 (Marrs, 1975). Comparison of the images enlarged to the map scale (Pls. 4, 5, and 6) shows that the lack of detail in the LANDSAT interpretation is strictly a function of resolution and contrast. The LANDSAT data does provide sufficient detail for mapping at scales of 1:125,000 or smaller, but, in many areas, land-use maps must be of a larger scale to be useful as a planning base. In the Moorcroft/Keyhole area, even the Skylab S-190B interpretation is marginal for mapping some land-use classes; but, for most classes, the detail available

from the Skylab data compares favorably with that interpreted from the aerial photography.

An optimum satellite system for land-use applications would combine the advantages of LANDSAT coverage with resolution equivalent to that of the S-190B camera; but, until such a system is available, a combined interpretation of the Skylab and LANDSAT data may provide the best alternative. A land-use interpretation, such as that of Plate 2, could first be made from the Skylab (or aerial) photography. This would then provide a base with accurate delineation of the land-use boundaries. Identification of vegetation and other time-variable phenomena could then be improved through interpretation of LANDSAT repetitive coverage. The LANDSAT data would also serve to monitor change in the area except in situations where changes effect the configuration of the land-use boundaries.

The values of a higher resolution system in monitoring change was demonstrated in an effort to map the Wyodak coal mine near Gillette, Wyoming (Marrs, 1974a). An attempt was first made to map the mine area from the LANDSAT imagery; but the attempt was unsuccessful due to the limited resolving power of the LANDSAT scanner. Even a very careful density slice of the area produced only a rough outline of the two large pits. The Skylab S-190B data was applied to this problem with somewhat greater success. Many of the activities within the mine area are readily identified on an enlargement of the S-190B photograph (Fig. 18a). Density slicing of this photograph helps to establish boundaries around the different areas of activity (Fig. 18b).



Figure 18a. Enlargement of Skylab S-190B image showing the Wyodak coal mine near Gillette, Wyoming (roll 88, frame 020, color photograph, track 59, pass 28, Sept. 13, 1973).

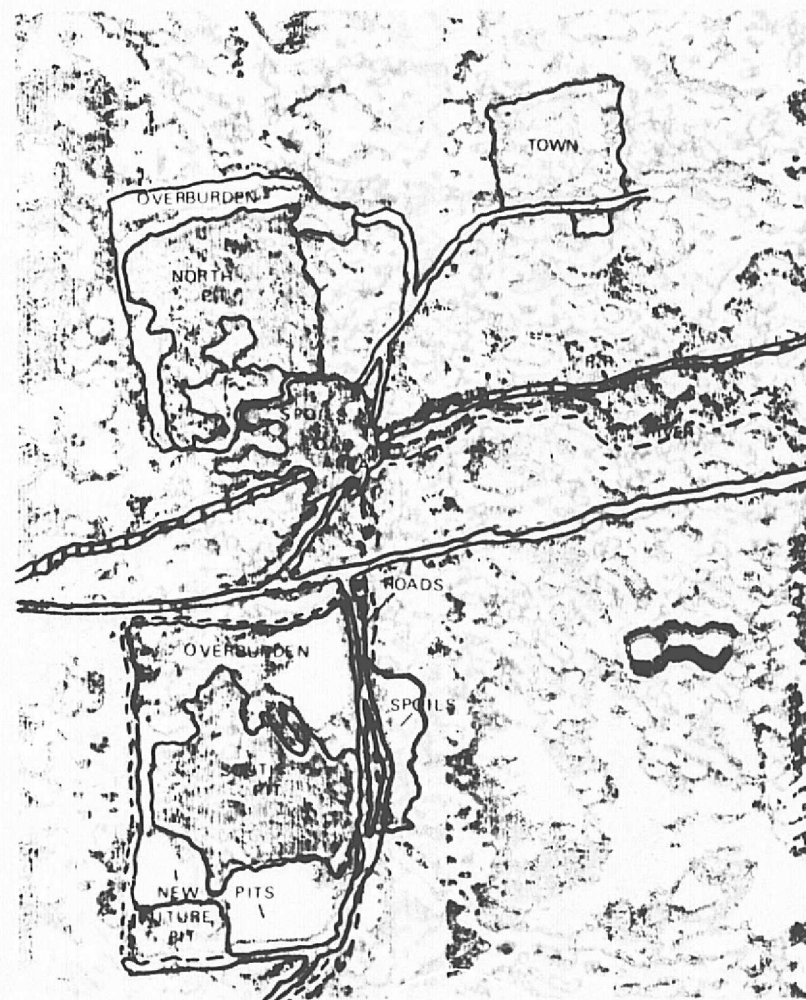


Figure 18b. Interpreted isodensity contour map compiled from an isodensitracing of the S-190B photograph (after Marrs, 1974a).

Similar techniques were employed in another land-use related study in which the Skylab S-190B photography was used to map sandy, selenium-rich soils in an area to be strip-mined for coal (Kolm, 1975a and 1975b). A reference site was first defined near the AMAX Belle Ayre mine in Campbell County, Wyoming (Fig. 19). The Skylab S-190B photography of this site (Fig. 20) was then interpreted (with the aid of density contouring) to produce a map of the sandy soils (Fig. 21). This map was then compared to a field checked interpretation of the same area compiled from 1:124,000 scale aerial photography (Fig. 22). The two maps were found to compare favorably, so the Skylab interpretation was expanded to yield a map of all similar soils in Campbell County (Pl. 7). This map was intended to serve as a guide for controlling redistribution of the selenium in the soils to be disturbed by coal mining operations (the strippable coal reserves extend the full length of Campbell County).

Soil samples were gathered in the AMAX Belle Ayre reference site in an effort to determine the nature and geochemical relationships among the various soils. The conclusions of the geochemical analyses were surprising. All of the Wasatch-derived soils were found to contain soluble selenium compounds concentrated in the "A" horizons. Originally only the Shingle series soils (sandy) were thought to contain high concentrations of selenium because indicator plants (*Astragalus bisulcatus*) are concentrated on the Shingle series soils. Factors other than selenium concentration control the growth of the indicator species in this area, but the presence of the indicators is a serious concern because they

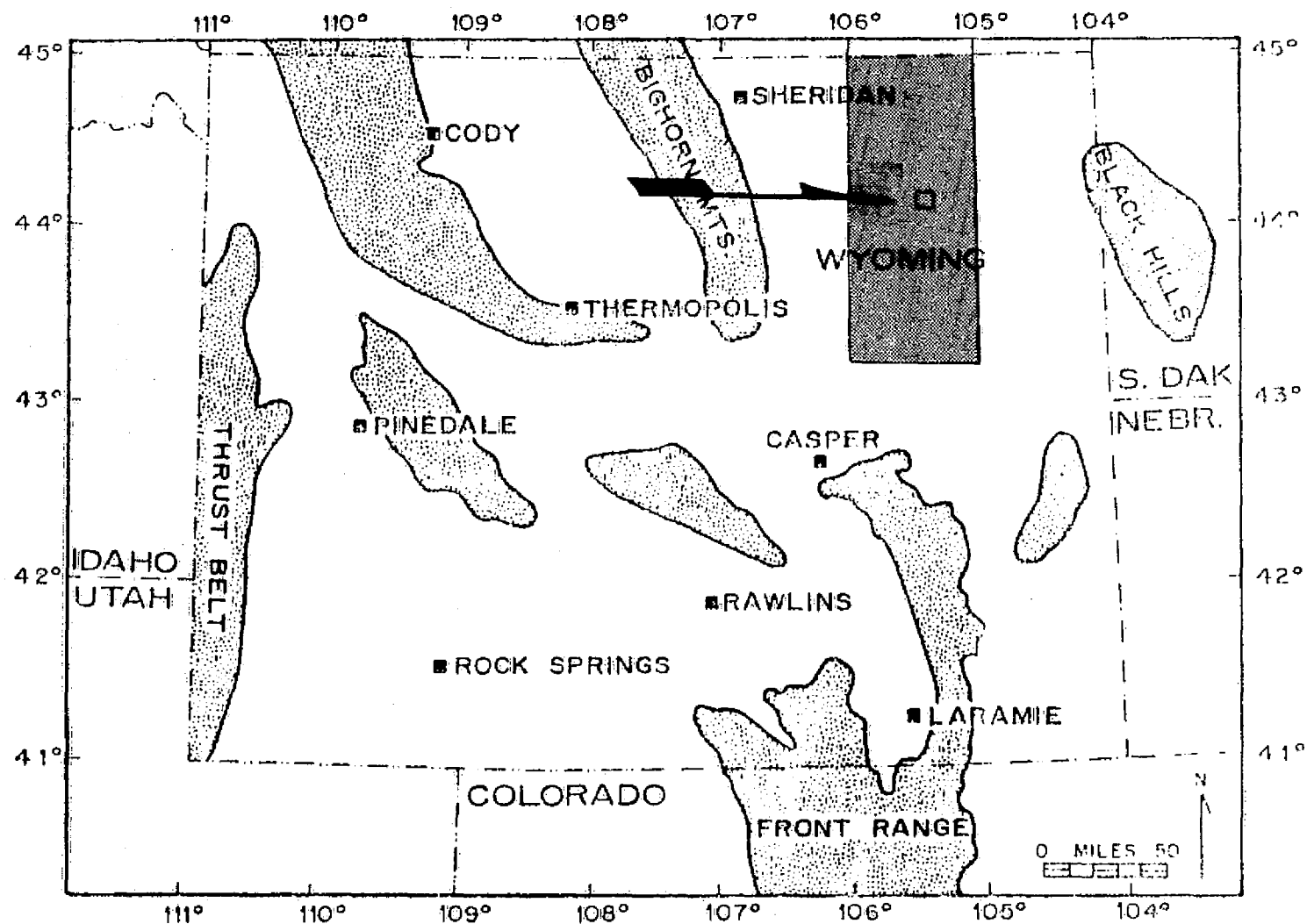


Fig. 19. Index map of Wyoming showing the location of the reference site (arrow) and the area mapped from Skylab photography (shaded area, after Kolm, 1975a).



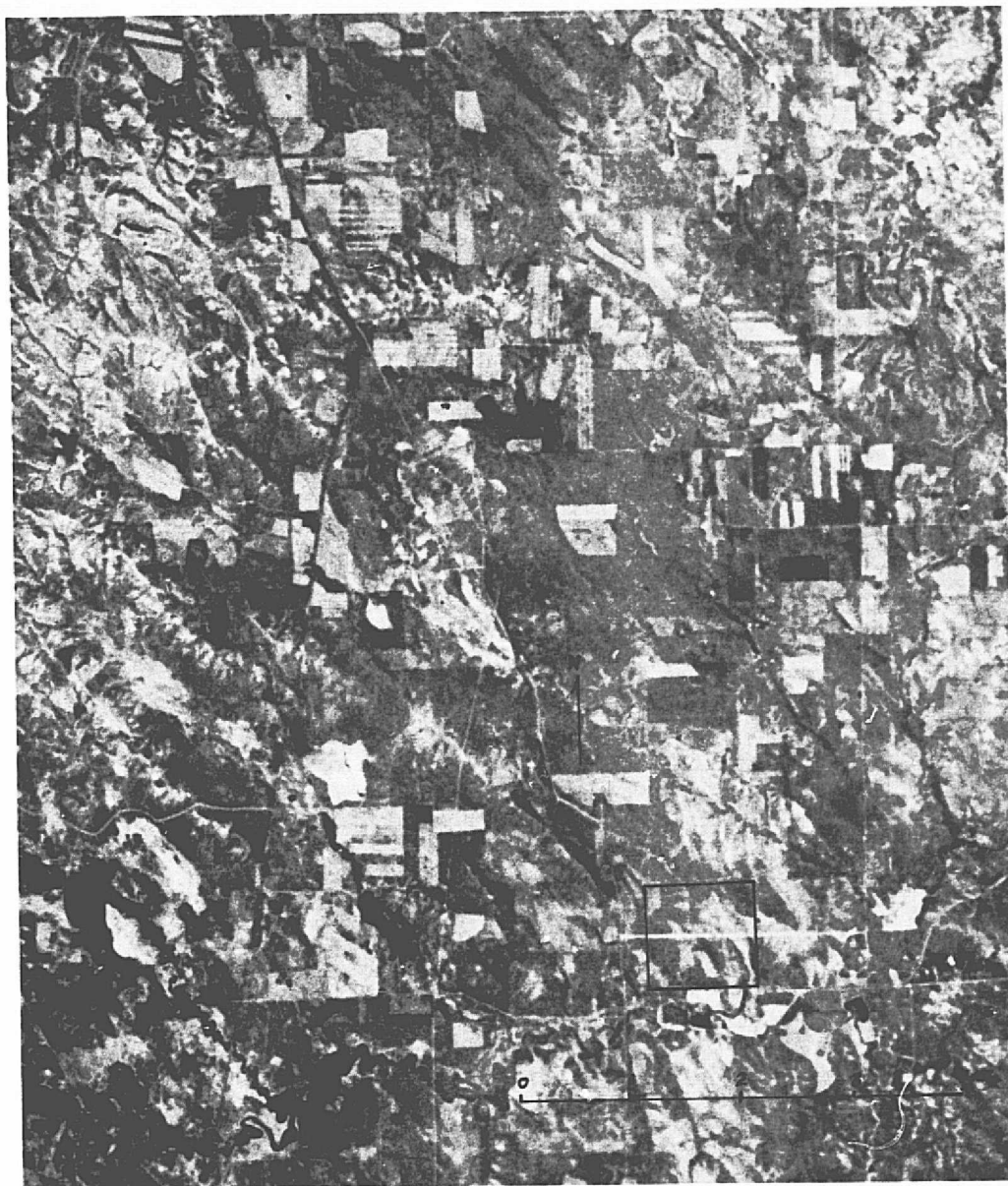


Fig. 20. Enlarged S-190B photograph (roll 88, frame 20, color, track 59, pass 28, Sept. 13, 1973) used for the reference site interpretation. The reference area lies within the square.

ORIGINAL PAGE IS  
OF POOR QUALITY

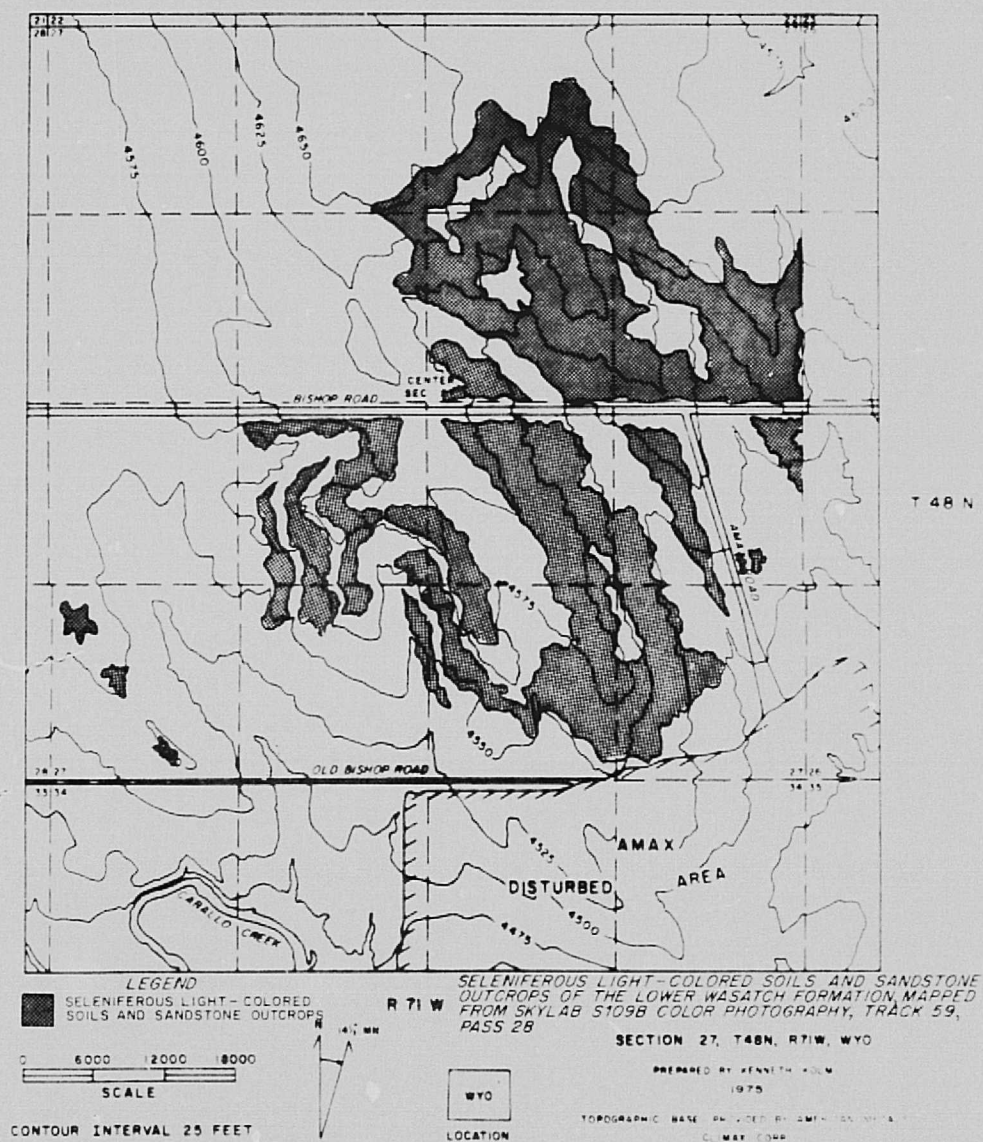
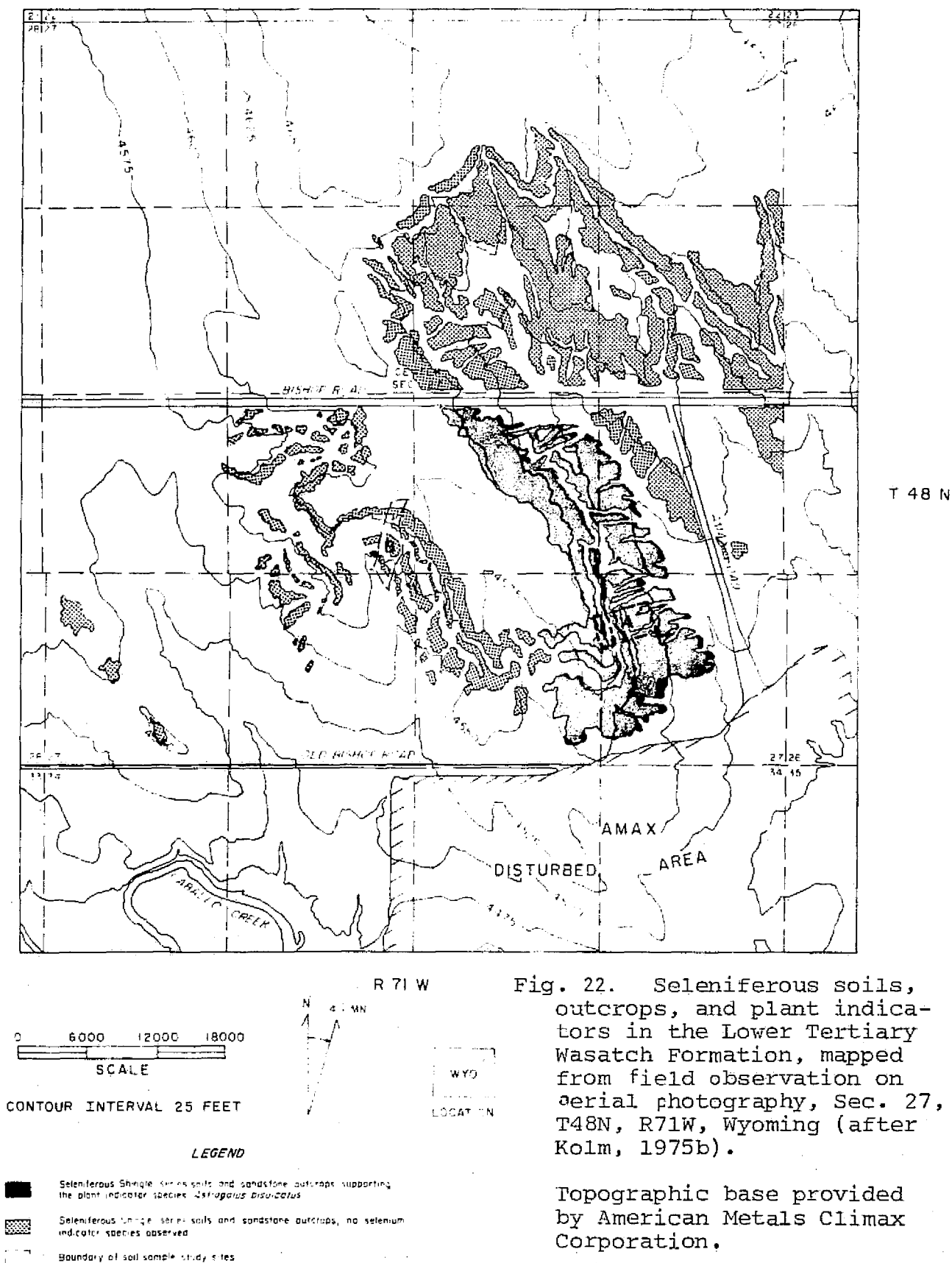


Figure 21. Seleniferous soils mapped from Skylab S-190B photography of the Amax, Belle Ayre reference site (after Kolm, 1975a).



convert the mineralogic forms of selenium to more soluble forms and concentrate these more soluble selenium compounds in the upper few inches of soil. Here they may be leached into ground water or taken up by other tolerant plant species and introduced into the food chain through grazing herbivores (cattle, sheep, etc.).

The Skylab-produced map of the sandy (Shingle series) soils serves as a guide to locating present or potential sites of selenium indicator/converter infestations. These sites can then be treated with special care to minimize the danger of contamination of ground water or the food chain with the toxic selenium compounds.

#### Hydrology

The hydrologic application of the Skylab EREP data is severely restricted by lack of repetitive coverage and poor quality of the S-192 thermal data. One of the original objectives of the Wyoming EREP investigation was to attempt to use the thermal channel of the S-192 scanner to map upwelling hot or cold waters and areas of shallow ground water. However, only a very limited amount of S-192 imagery was obtained for Wyoming, and the thermal channel of that data was ruined by severe low-frequency noise. Consequently, the only hydrologic analyses attempted for the Wyoming site employed the photographic data as an indirect tool for studying groundwater via structural analyses. This was accomplished with some success in the area of Medicine Lodge Creek (Tomes, 1975).

Medicine Lodge Creek lies along the west flank of the Bighorn Mountains in north-central Wyoming (Fig. 23). The Lower Paleozoic rocks that



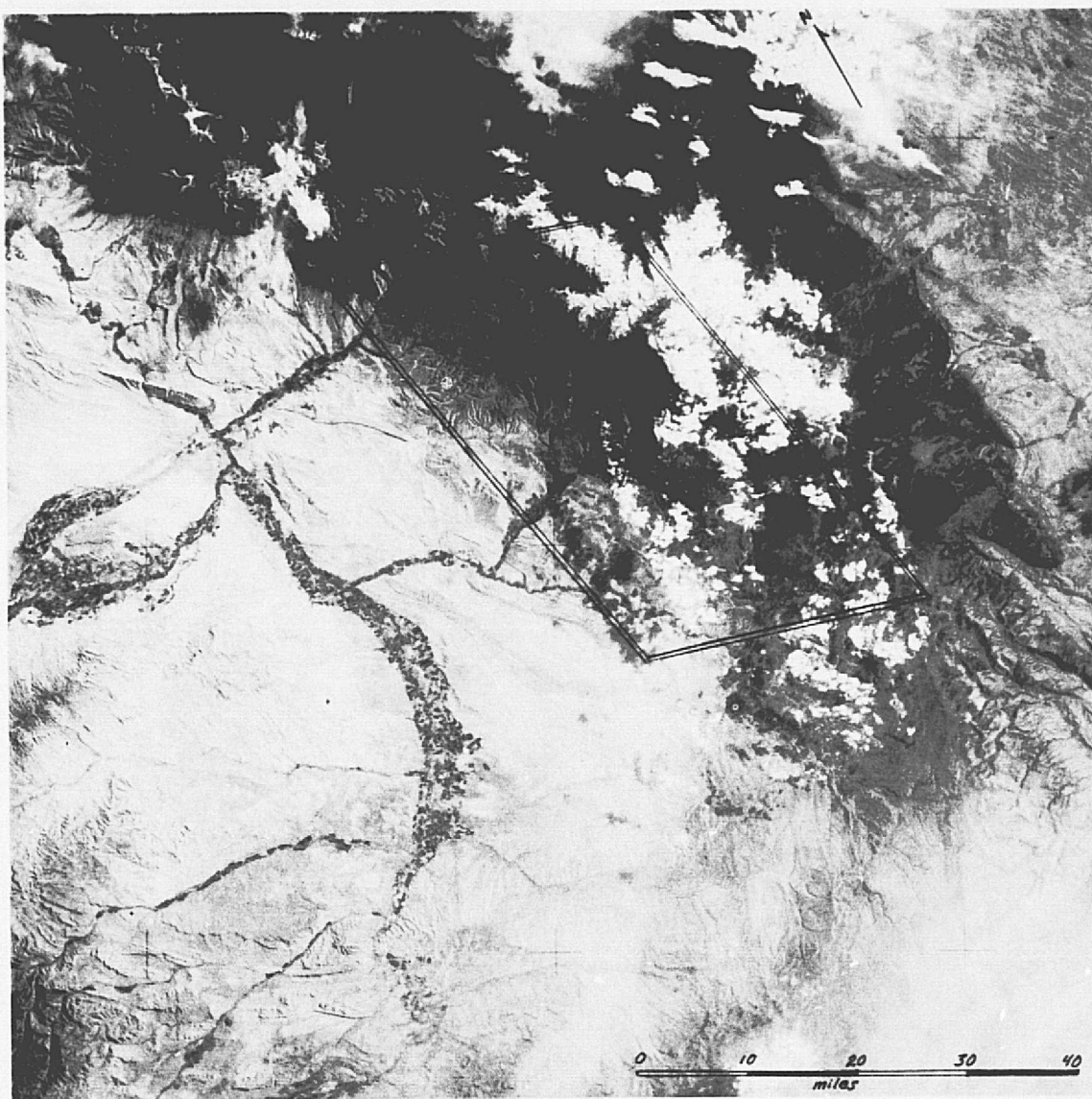


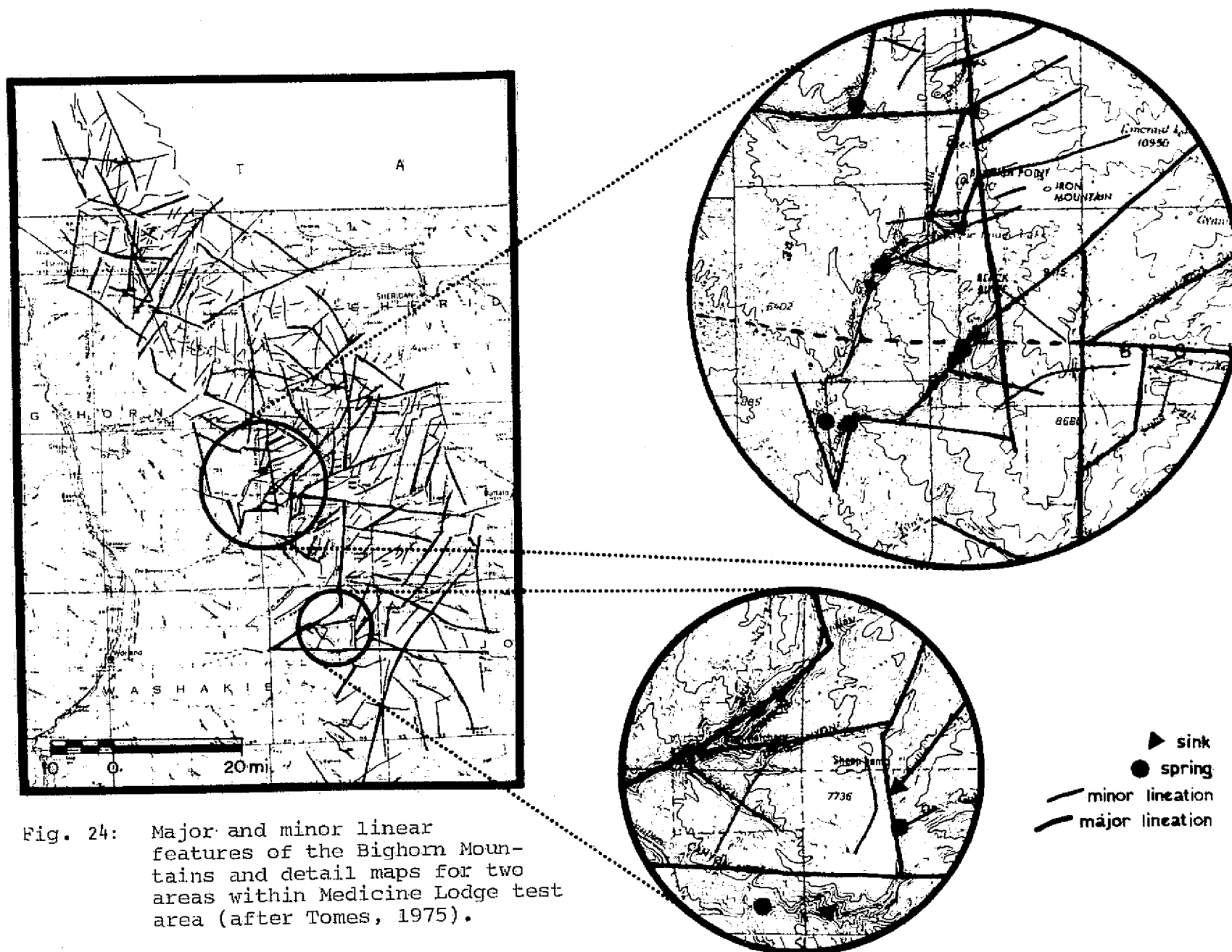
Figure 23. Skylab S-190A photograph (roll 18, frame 211, red band, track 5, pass 10, frame 228, June 13, 1973) showing the Medicine Lodge study area along the west flank of the Bighorn Mountain (after Tomes, 1975).

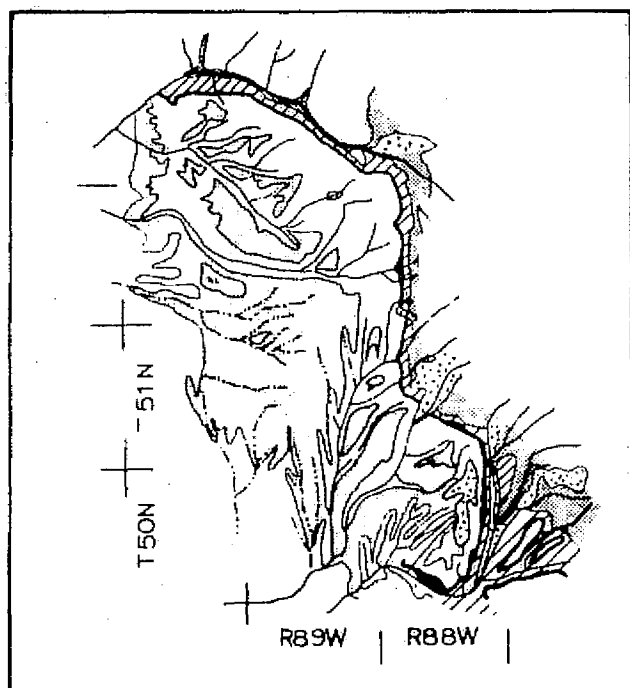
crop out in this area include the Bighorn dolomite and the Madison limestone, which are generally considered the major aquifers carrying water from the mountains into the Bighorn Basin. The geology of the area is poorly understood and little data is available regarding structure or groundwater.

Runoff flows from the Precambrian core of the Bighorn Mountains across the outcrop of the Paleozoic formations and into the Bighorn Basin. The Paleozoic aquifer is relatively impermeable unless fractured, but the water normally carried in surface streams often sinks as it flows across the Bighorn dolomite, the first Paleozoic carbonate rock encountered in the downstream direction. Further downstream (but up section) a portion of the water reappears in springs. Field studies indicate that these sinks and springs (and the flow of ground water) are fracture controlled. Therefore, the LANDSAT and EREP imagery were used to map linear features that might correlate with the major fractures in the area (Fig. 24) and to refine the geologic maps for the area (Fig. 25). The linear features within the Medicine Lodge study area were then checked in the field and compared to field maps. A direct correlation was found between the linear features and the faults. Many of the faults that control ground water flow in the area are visible on the Skylab photography. The sinks and springs found in the area commonly correspond to intersections of the mapped faults.



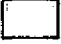

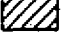

#### Crops and Range

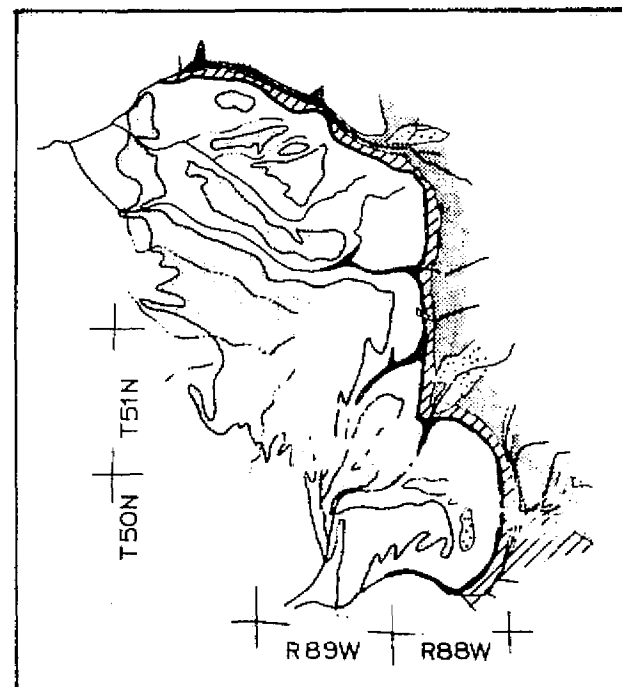
A heavily farmed area near Riverton, Wyoming was chosen as a test site for mapping crops from the Skylab photography (Fig. 26). Investigators from the University of Wyoming, Plant Science Department first





25a

-  Tertiary sediments
-  Pennsylvanian Tensleep sandstone
-  Mississippian Madison limestone
-  Ordovician Bighorn dolomite
-  Cambrian formations undivided
-  Precambrian rocks



25b

Fig. 25a. Geologic map compiled by Darton (1906).

Fig. 25b. Darton's geologic map updated and geographically corrected using Skylab photography (after Tones, 1975).





Figure 26. Portion of Skylab S-190B photograph showing the Riverton agricultural area (roll 33, frame 169, track 62, pass 4, August 5, 1973).

ORIGINAL PAGE IS  
OF POOR QUALITY

subdivided the test area into "use" categories (range, water, farmland, etc.) and then attempted to identify the crops within the area of farmland by direct photointerpretations. The interpreter was familiar with most crops grown in Wyoming, but unfamiliar with the Riverton test area. The resulting crop map (Figs. 27a, 28b) were compared to a high-altitude color-infrared aerial photograph and checked against available field observations. This evaluation demonstrated that the individual field boundaries were accurately mapped and most of the crops (>75%) were correctly identified.

The FREP S-190 photography was used in a detailed mapping program which evaluated LANDSAT, Skylab, and aerial photography for rangeland mapping. The test site was a six by twenty-five-mile area near Baggs, Wyoming where the University of Wyoming maintains surveillance on a four-pasture rest/rotation unit (Fig. 29). Range vegetation maps were compiled at a scale of 1:24,000 (Figs. 30, 31, and 32) from LANDSAT, Skylab (S-190A and S-190B) and aerial photography. The aerial photo interpretation was field checked and amended as necessary. Sample transects were set up and resampled in conjunction with each LANDSAT overpass. The resulting data allowed accurate definition of the range community in each map unit and clippings provided biomass estimates for correlation with changing scene reflectance through the grazing season (Gordon, 1974).

#### Mineral Exploration and Economic Geology

Three attempts were made to locate construction materials or metallic minerals by direct interpretation of the Skylab photography. In each case, the interpreter tried to identify and delineate a "color anomaly" associated with the economic material. These efforts produced questionable success.

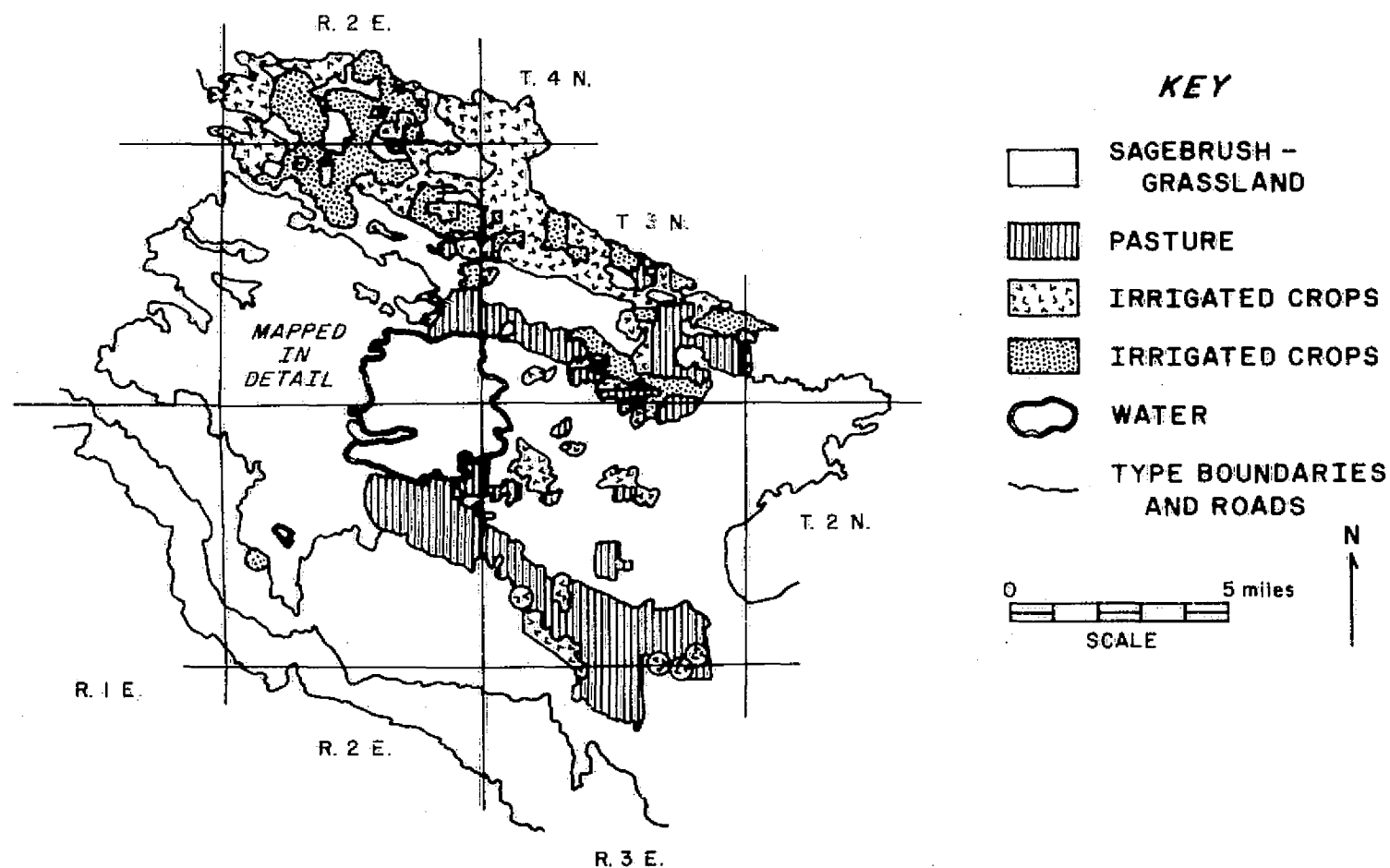


Figure 27a. Generalized crop and agricultural use map of the Riverton area interpreted from Skylab S-190B photography (Fig. 26).

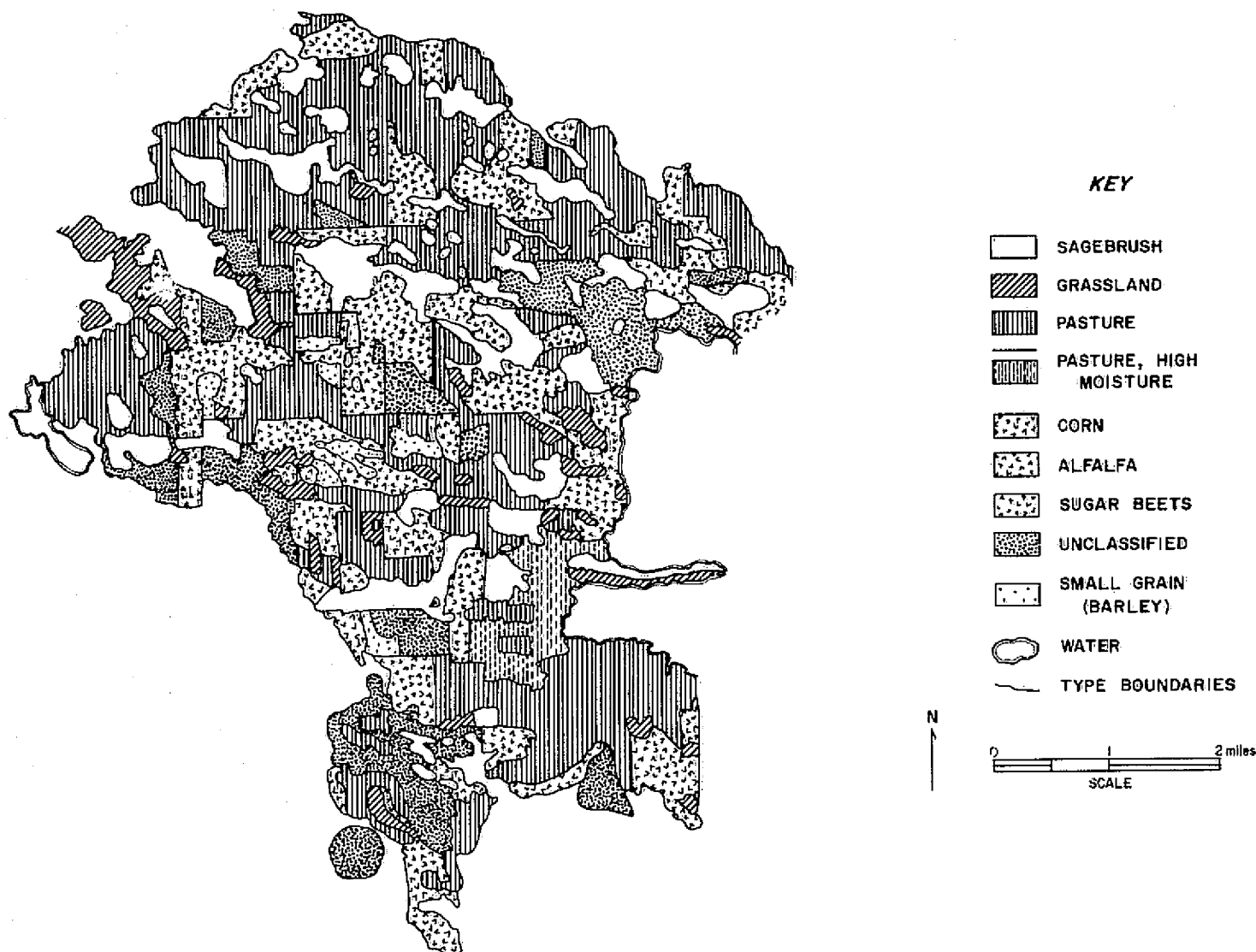


Figure 28b. Detailed crop map for a portion of the Riverton agricultural area. Interpreted from Skylab S-190B photography (Fig. 26).

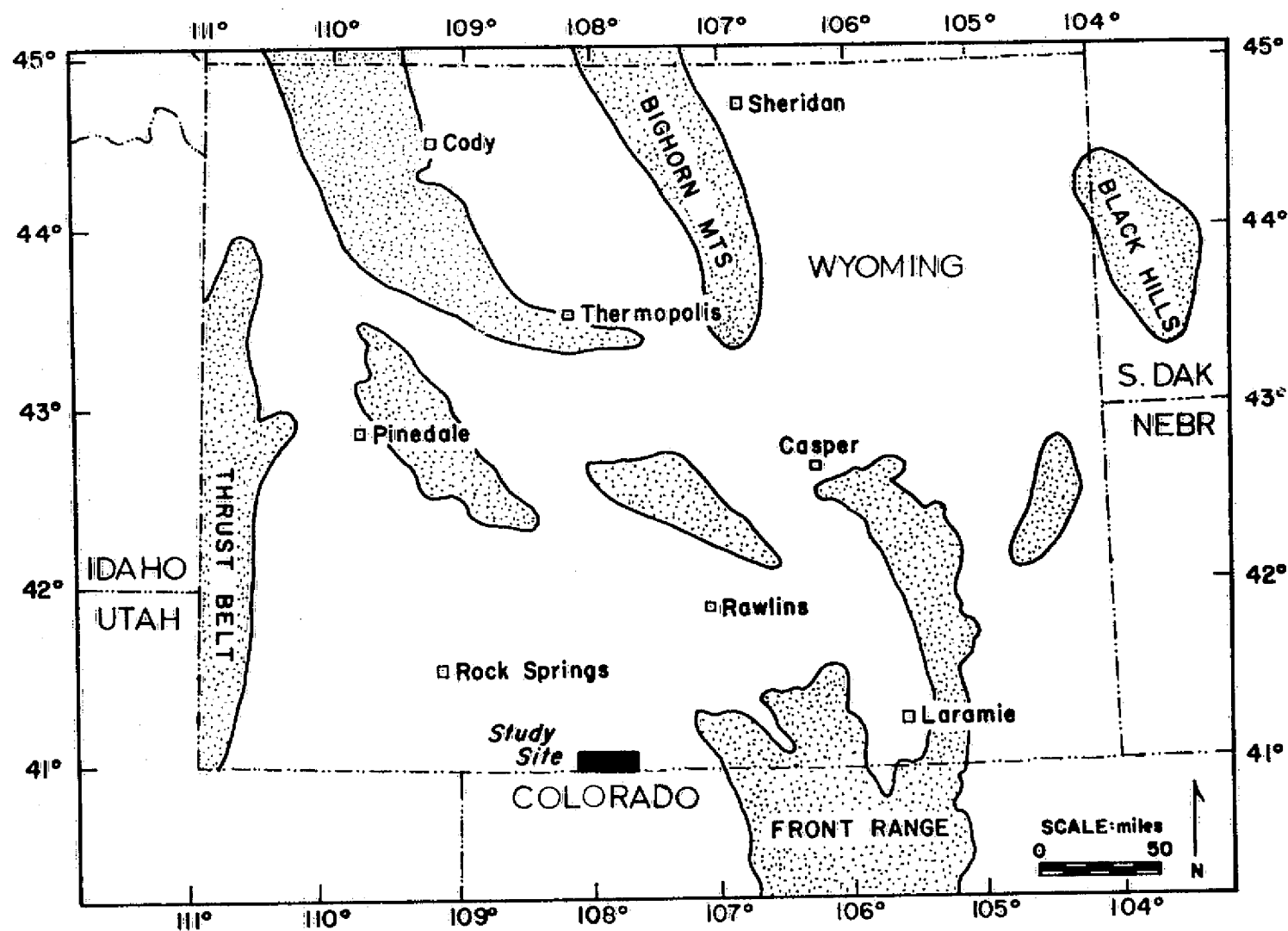
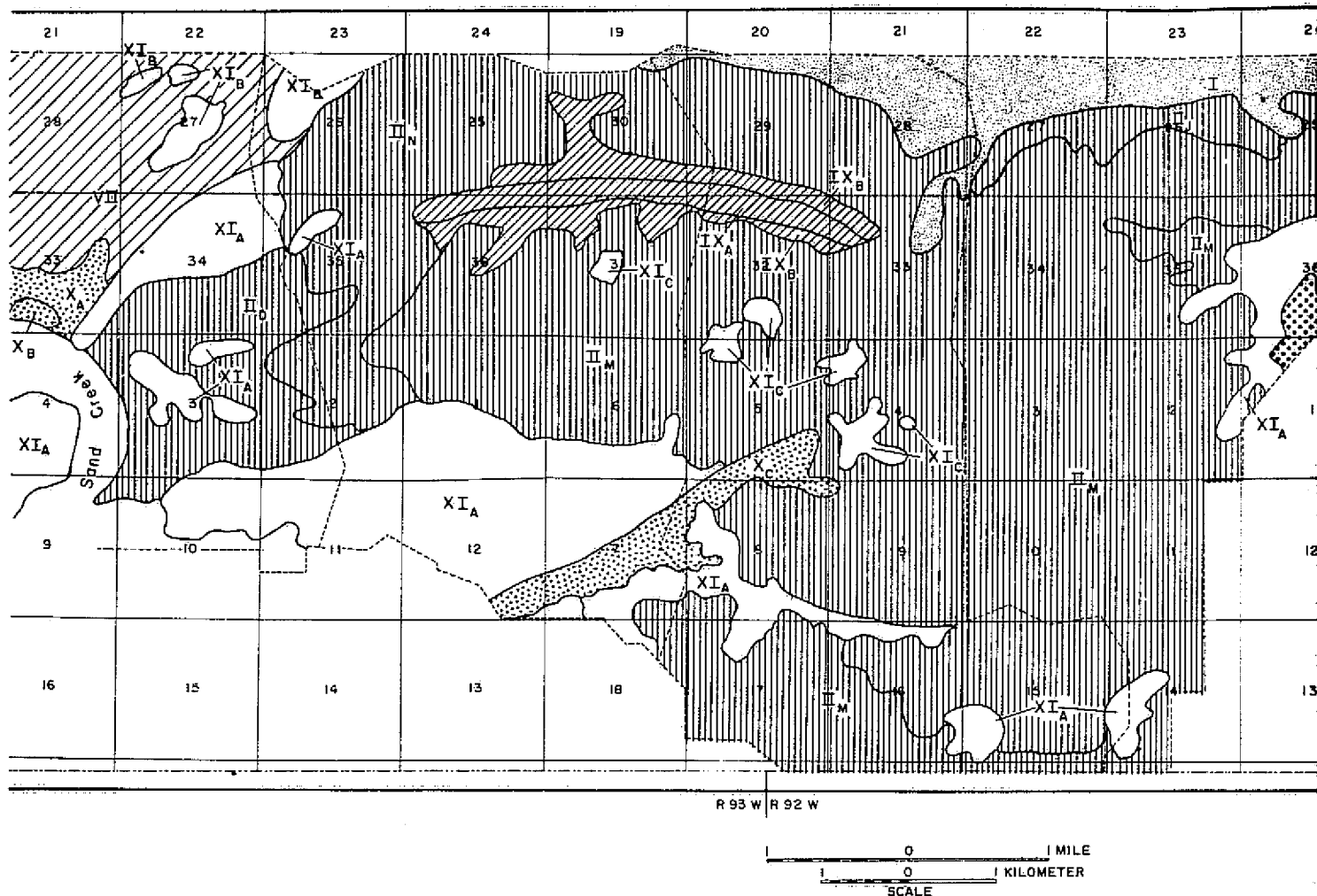


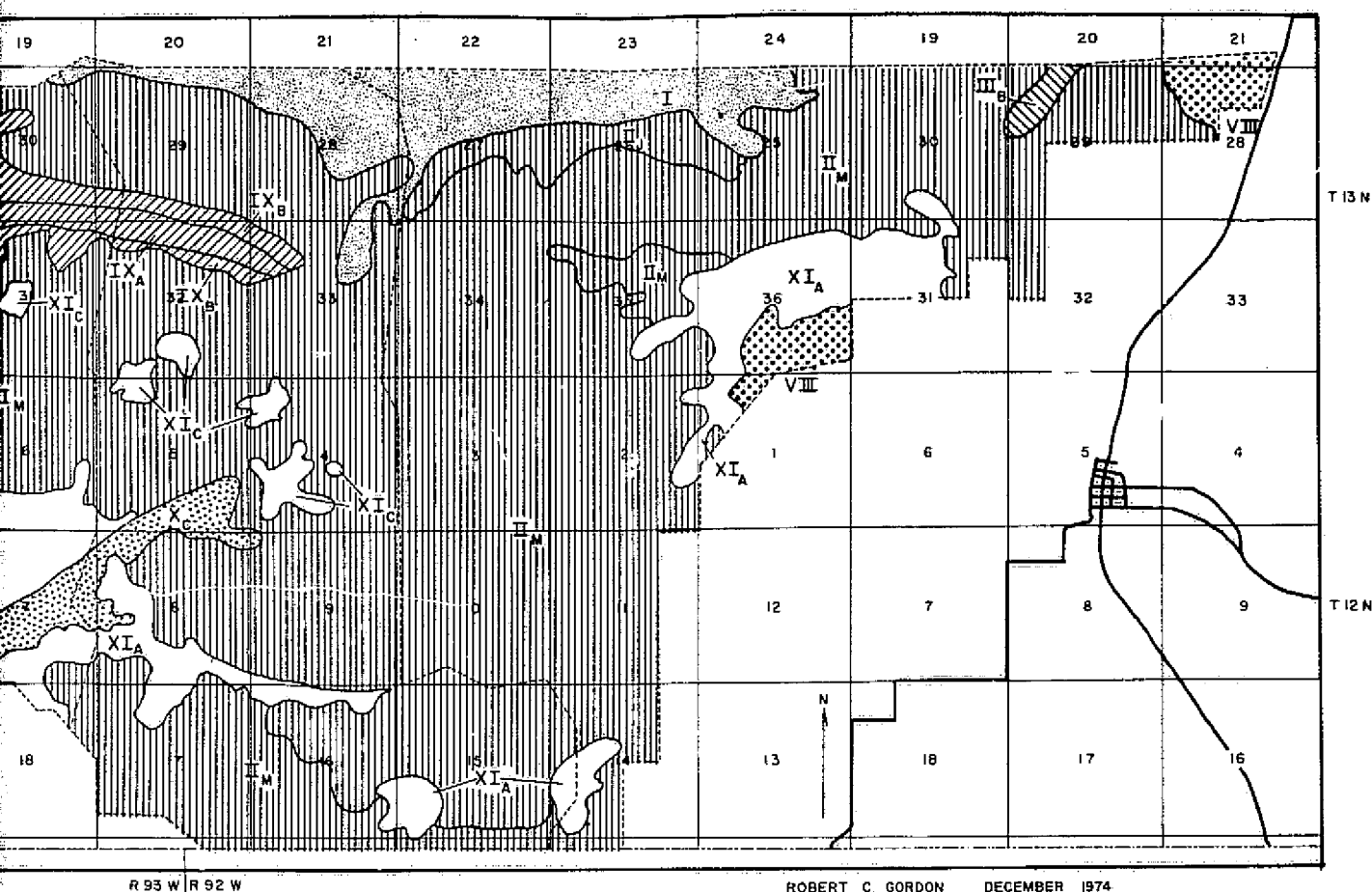
Figure 29, Location of Baggs study site. (after Gordon, 1973, p. 3)



# RANGE VEGETATION TYPES

■ Type 0	<i>Agropyron cristatum</i> : Crested wheatgrass	▨ Type VI
▤ Type I	<i>Agropyron smithii</i> -- <i>Artemisia tridentata</i> : Western wheatgrass and basin big sagebrush	▧ Type VII
▥ Type II	<i>Artemisia tridentata</i> -- <i>Agropyron smithii</i> : Basin big sagebrush and western wheatgrass	▩ Type VIII
▦ Type III	<i>Artemisia tridentata</i> -- <i>Agropyron spicatum</i> : Basin big sagebrush and bluebunch wheatgrass	▪ Type IX
▧ Type IV	<i>Artemisia tridentata</i> -- <i>Atriplex</i> species: Basin big sagebrush and saltbush	▫ Type X
▨ Type V	<i>Artemisia tridentata</i> -- <i>Carex eleocharis</i> : Basin big sagebrush and needleleaf sedge	▬ Type XI

Figure 30a. Range vegetation map developed from LANDSAT-1 imagery of the Baggs test site.



0 1 MILE  
0 1 KILOMETER  
SCALE

## RANGE VEGETATION TYPES

0 <u>Agropyron cristatum</u> : Crested wheatgrass	III Type VI	<u>Artemisia tridentata</u> -- <u>Gutierrezia sarothrae</u> --
C <u>Agropyron smithii</u> -- <u>Artemisia tridentata</u> : Western wheatgrass and basin big sagebrush	IV Type VII	<u>Agropyron smithii</u> : Basin big sagebrush, broom snakeweed, and western wheatgrass
I <u>Artemisia tridentata</u> -- <u>Agropyron smithii</u> : Basin big sagebrush and western wheatgrass	V Type VIII	<u>Artemisia tridentata</u> -- <u>Stipa comata</u> : Basin big sagebrush and needleandthread
II <u>Artemisia tridentata</u> -- <u>Agropyron spicatum</u> : Basin big sagebrush and bluebunch wheatgrass	VI Type IX	<u>Artemisia tridentata</u> : Basin big sagebrush
III <u>Artemisia tridentata</u> -- <u>Atriplex</u> species: Basin big sagebrush and saltbush	VII Type X	<u>Juniperus osteosperma</u> : Utah juniper
IV <u>Artemisia tridentata</u> -- <u>Carex eleocharis</u> : Basin big sagebrush and needleleaf sedge	VIII Type XI	<u>Sarcobatus vermiculatus</u> -- <u>Artemisia tridentata</u> : Black greasewood and basin big sagebrush
	IX	Bare ground

FOLDOUT FRAME 3



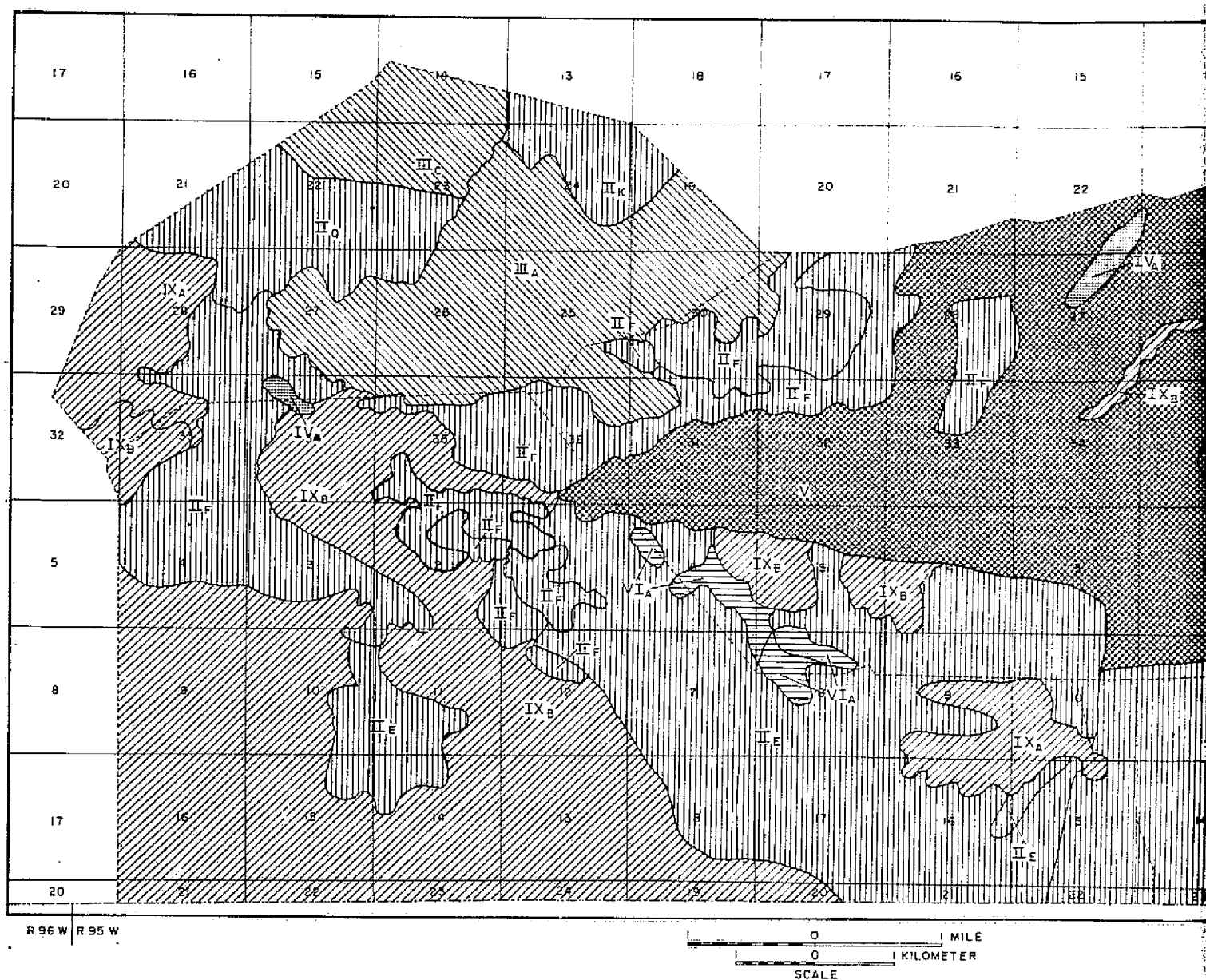


Figure 30b. Range vegetation map developed from LANDSAT-1 imagery of the Baggs test site.

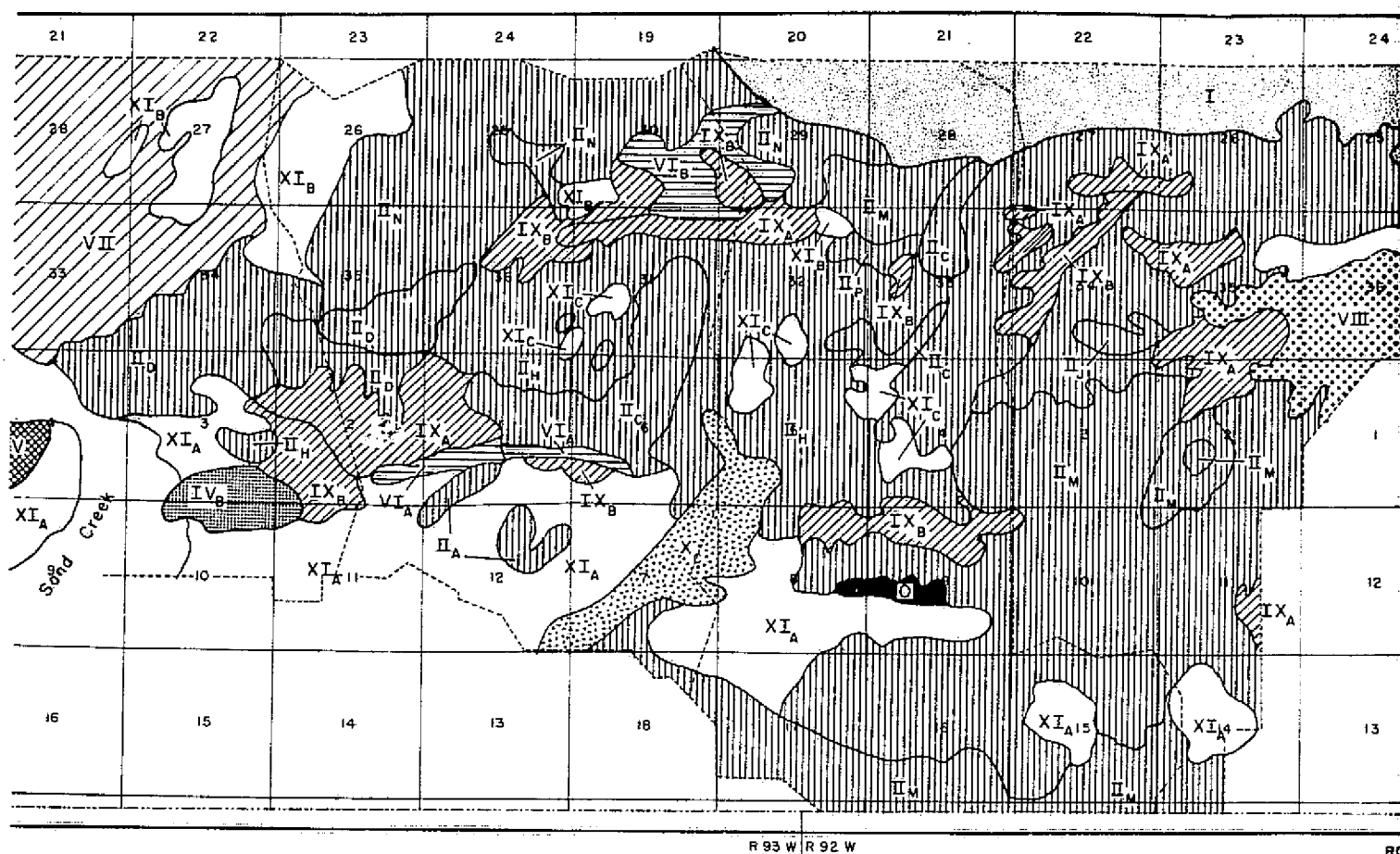
Type O	<i>Agropyron cristatum</i> : Crested wheatgrass
Type I	<i>Agropyron smithii</i> -- <i>Artemisia tridentata</i> : Western wheatgrass and basin big sagebrush
Type II	<i>Artemisia tridentata</i> -- <i>Agropyron smithii</i> : Basin big sagebrush and western wheatgrass
Type III	<i>Artemisia tridentata</i> -- <i>Agropyron spicatum</i> : Basin big sagebrush and bluebunch wheatgrass
Type IV	<i>Artemisia tridentata</i> -- <i>Atriplex</i> species: Basin big sagebrush and saltbush
Type V	<i>Artemisia tridentata</i> -- <i>Carex eleocharis</i> : Basin big sagebrush and needleleaf sedge

# RANGE VEGETATION

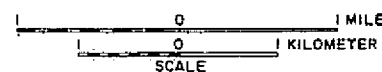
Type
Type
Type
Type
Type
Type







R 93 W R 92 W

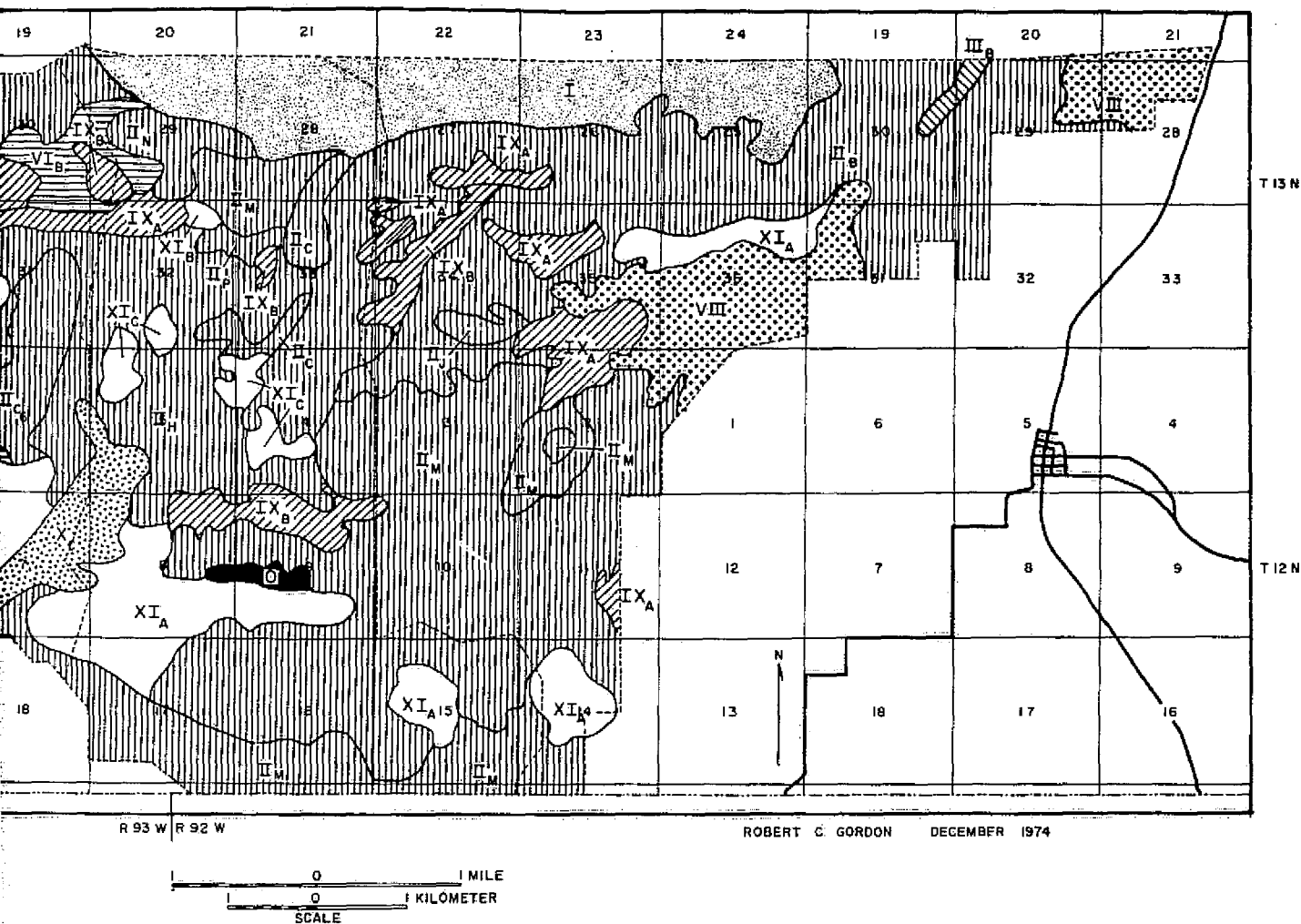


# RANGE VEGETATION TYPES

- Type O *Agropyron cristatum*:  
Crested wheatgrass
- ▤ Type I *Agropyron smithii* -- *Artemisia tridentata*:  
Western wheatgrass and basin big sagebrush
- ▥ Type II *Artemisia tridentata* -- *Agropyron smithii*:  
Basin big sagebrush and western wheatgrass
- ▧ Type III *Artemisia tridentata* -- *Agropyron spicatum*:  
Basin big sagebrush and bluebunch wheatgrass
- ▨ Type IV *Artemisia tridentata* -- *Atriplex* species:  
Basin big sagebrush and saltbush
- ▩ Type V *Artemisia tridentata* -- *Carex eleocharis*:  
Basin big sagebrush and needleleaf sedge

- Type VI *Agropyron*
- Type VII *Artemisia*
- ▬ Type VIII *Artemisia*
- ▭ Type IX *Juniperus*
- ▮ Type X *Sarcobatus*
- ▯ Type XI *Baccharis*

Figure 31a. Range vegetation map interpreted from Skylab photographs of the Baggs test site.



## RANGE VEGETATION TYPES

Agropyron cristatum:  
Crested wheatgrass

Agropyron smithii -- Artemisia tridentata:  
Western wheatgrass and basin big sagebrush

Artemisia tridentata -- Agropyron smithii:  
Basin big sagebrush and western wheatgrass

Artemisia tridentata -- Agropyron spicatum:  
Basin big sagebrush and bluebunch wheatgrass

Artemisia tridentata -- Atriplex species:  
Basin big sagebrush and saltbush

Artemisia tridentata -- Carex eleocharis:  
Basin big sagebrush and needleleaf sedge

▨ Type VI Artemisia tridentata -- Gutierrezia sarothrae --  
Agropyron smithii: Basin big sagebrush, broom  
snakeweed, and western wheatgrass

▧ Type VII Artemisia tridentata -- Stipa comata:  
Basin big sagebrush and needleandthread

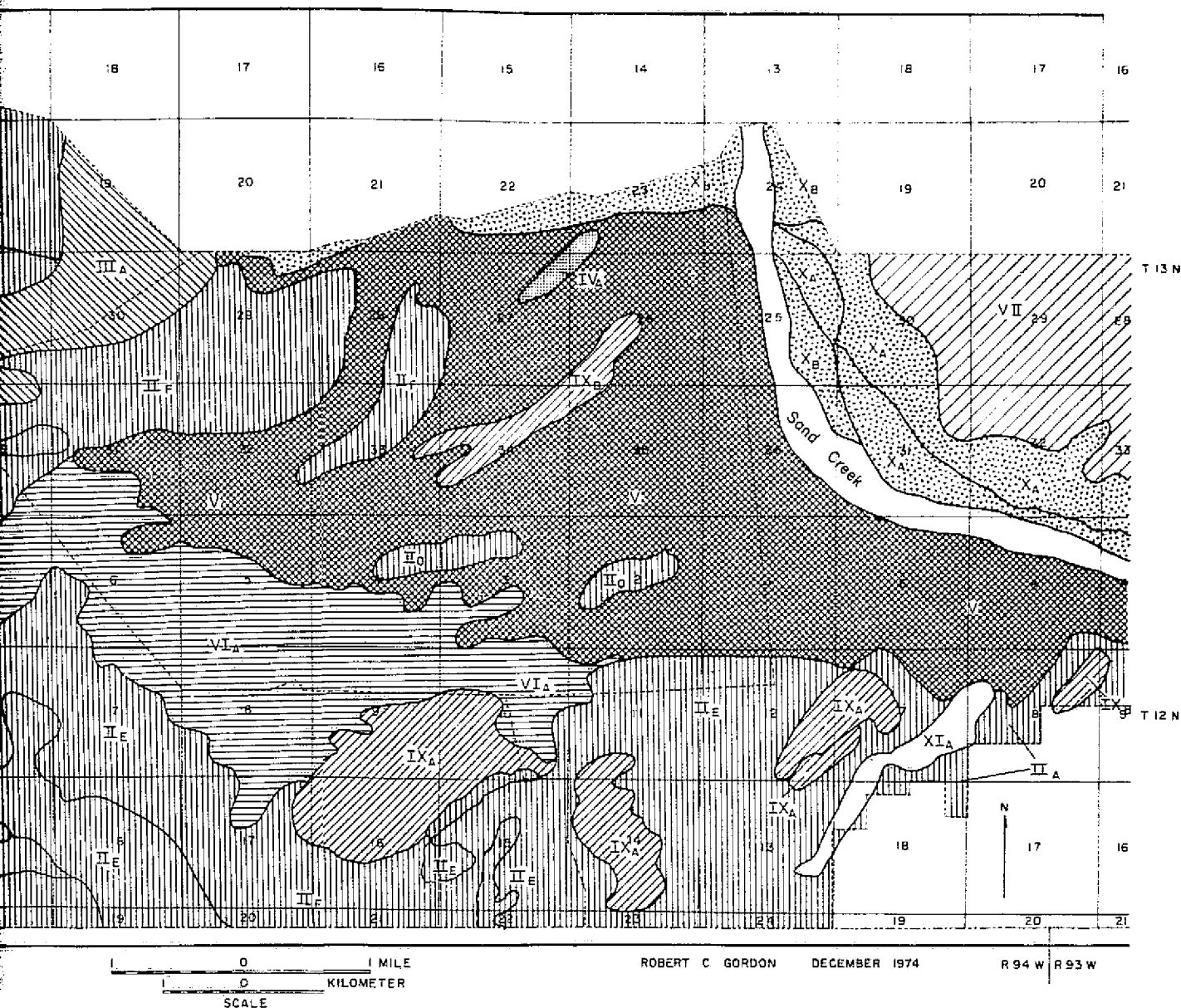
▩ Type VIII Artemisia tridentata:  
Basin big sagebrush

▨ Type IX Juniperus osteosperma:  
Utah juniper

▩ Type X Sarcobatus vermiculatus -- Artemisia tridentata:  
Black greasewood and basin big sagebrush

□ Type XI Bare ground





## RANGE VEGETATION TYPES

- |          |  |           |  |
|----------|--|-----------|--|
| Type 0   | <i>Agropyron cristatum</i> :<br>Crested wheatgrass   | Type VI   | <i>Artemisia tridentata</i> -- <i>Gutierrezia sarothrae</i> --<br><i>Agropyron smithii</i> : Basin big sagebrush, broom<br>snakeweed, and western wheatgrass |
| Type I   | <i>Agropyron smithii</i> -- <i>Artemisia tridentata</i> :<br>Western wheatgrass and basin big sagebrush    | Type VII  | <i>Artemisia tridentata</i> -- <i>Stipa comata</i> :<br>Basin big sagebrush and needleandthread  |
| Type II  | <i>Artemisia tridentata</i> -- <i>Agropyron smithii</i> :<br>Basin big sagebrush and western wheatgrass    | Type VIII | <i>Artemisia tridentata</i> :<br>Basin big sagebrush   |
| Type III | <i>Artemisia tridentata</i> -- <i>Agropyron spicatum</i> :<br>Basin big sagebrush and bluebunch wheatgrass | Type IX   | <i>Juniperus osteosperma</i> :<br>Utah juniper   |
| Type IV  | <i>Artemisia tridentata</i> -- <i>Atriplex</i> species:<br>Basin big sagebrush and saltbush                | Type X    | <i>Sarcobatus vermiculatus</i> -- <i>Artemisia tridentata</i> :<br>Black greasewood and basin big sagebrush  |
| Type V   | <i>Artemisia tridentata</i> -- <i>Carex eleocharis</i> :<br>Basin big sagebrush and needleleaf sedge       | Type XI   | Bare ground  |

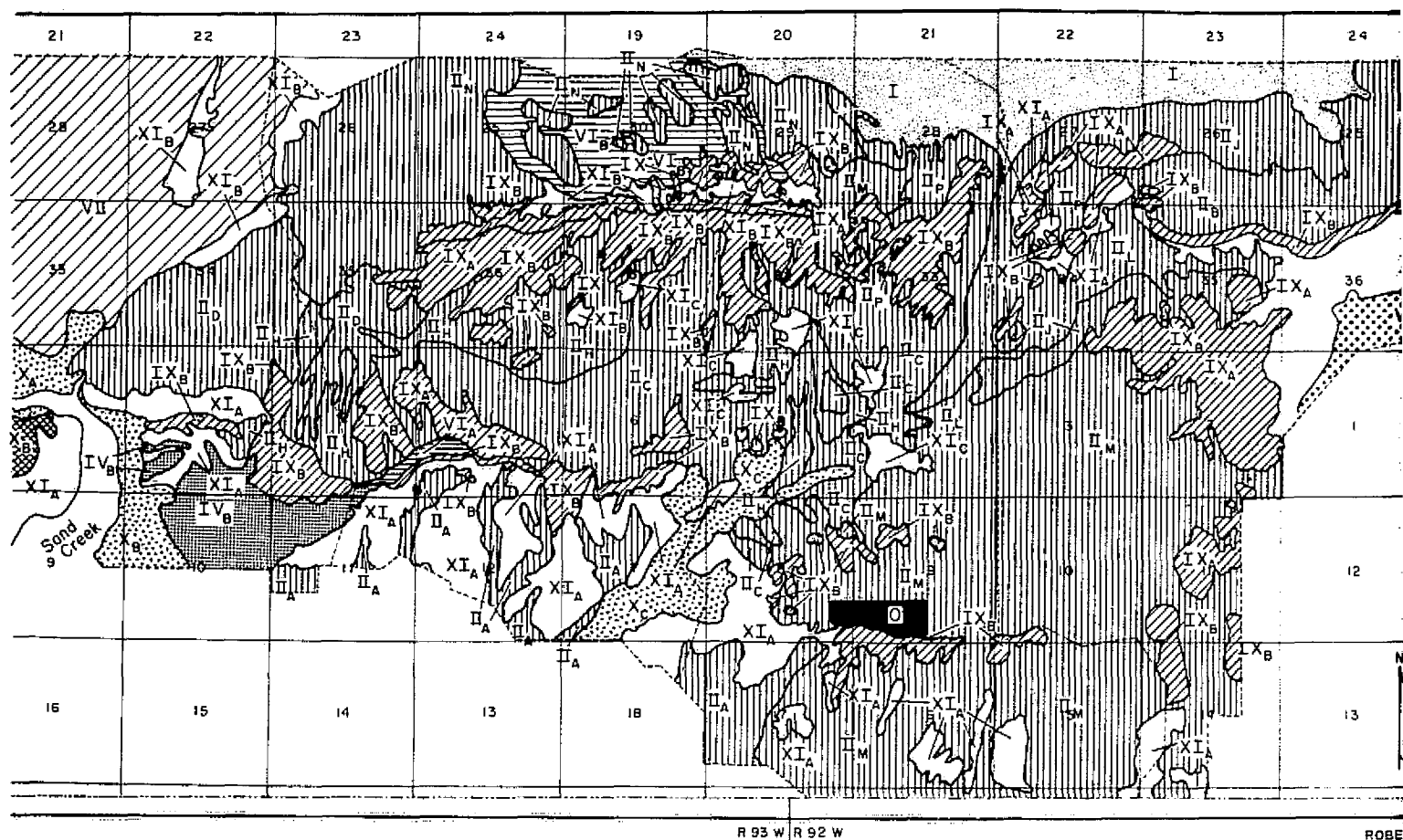


Figure 32a. Range vegetation map of the Baggs test area compiled from low-level aerial photography supplemented with ground reconnaissance.

R 93 W R 92 W

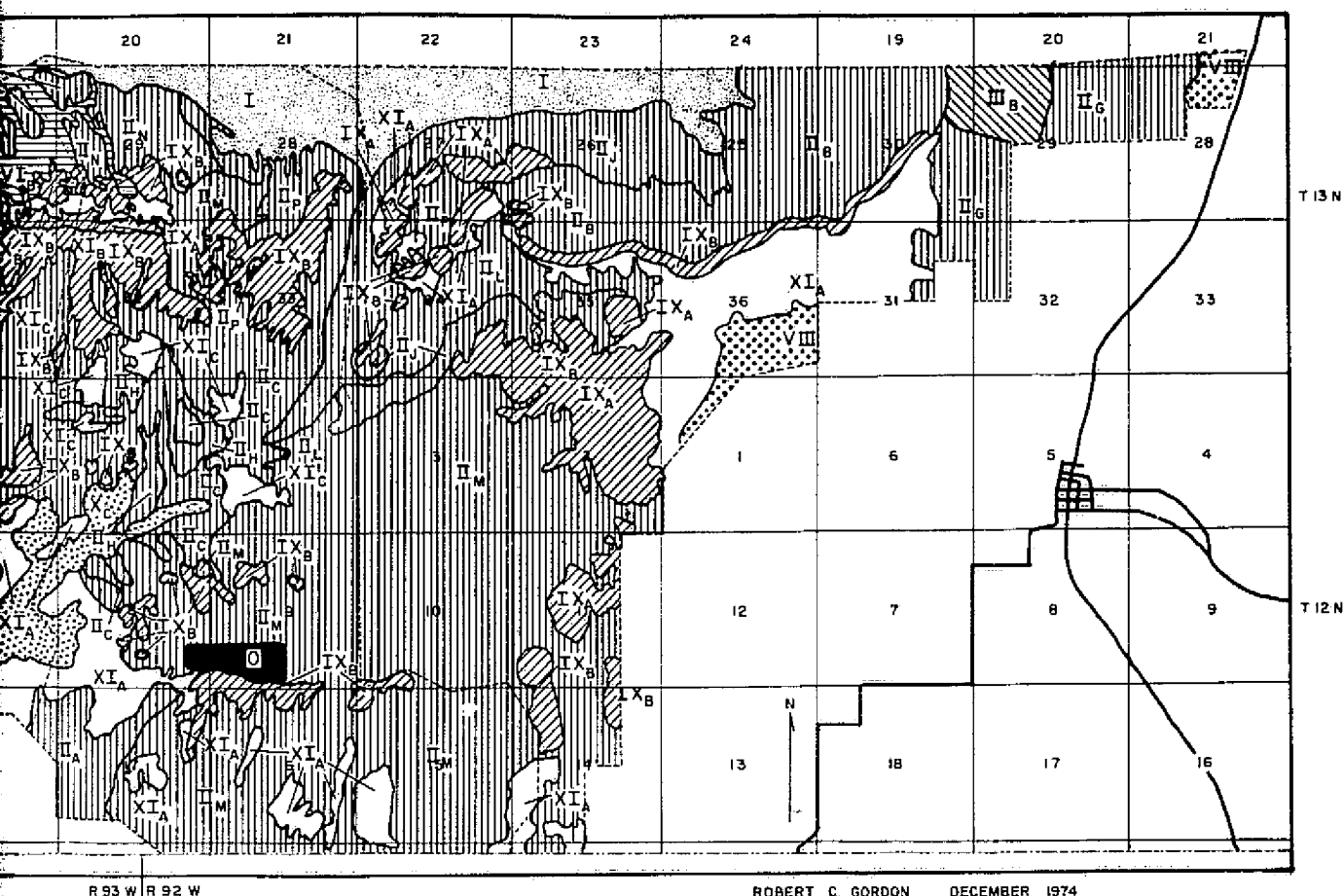
ROBE

0 1 MILE  
0 1 KILOMETER  
SCALE

# RANGE VEGETATION TYPES

- Type O *Agropyron cristatum*:  
Crested wheatgrass
- ▤ Type I *Agropyron smithii* -- *Artemisia tridentata*:  
Western wheatgrass and basin big sagebrush
- ▥ Type II *Artemisia tridentata* -- *Agropyron smithii*:  
Basin big sagebrush and western wheatgrass
- ▦ Type III *Artemisia tridentata* -- *Agropyron spicatum*:  
Basin big sagebrush and bluebunch wheatgrass
- ▧ Type IV *Artemisia tridentata* -- *Atriplex* species:  
Basin big sagebrush and saltbush
- ▨ Type V *Artemisia tridentata* -- *Carex eleocharis*:  
Basin big sagebrush and needleleaf sedge

- ▩ Type VI *Artemisia tridentata* -- *Agropyron spicatum*:  
Basin big sagebrush and bluebunch wheatgrass
- Type VII *Artemisia tridentata* -- *Agropyron smithii*:  
Basin big sagebrush and western wheatgrass
- Type VIII *Artemisia tridentata* -- *Agropyron smithii*:  
Basin big sagebrush and western wheatgrass
- ▬ Type IX *Artemisia tridentata* -- *Agropyron spicatum*:  
Basin big sagebrush and bluebunch wheatgrass
- ▭ Type X *Artemisia tridentata* -- *Agropyron smithii*:  
Basin big sagebrush and western wheatgrass
- ▮ Type XI *Artemisia tridentata* -- *Agropyron smithii*:  
Basin big sagebrush and western wheatgrass



the  
from  
phy

## RANGE VEGETATION TYPES

Agropyron cristatum:  
Crested wheatgrass

Agropyron smithii -- Artemisia tridentata:  
Western wheatgrass and basin big sagebrush

Artemisia tridentata -- Agropyron smithii:  
Basin big sagebrush and western wheatgrass

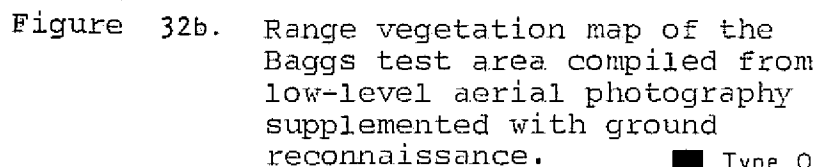
Artemisia tridentata -- Agropyron spicatum:  
Basin big sagebrush and bluebunch wheatgrass

Artemisia tridentata -- Atriplex species:  
Basin big sagebrush and saltbush

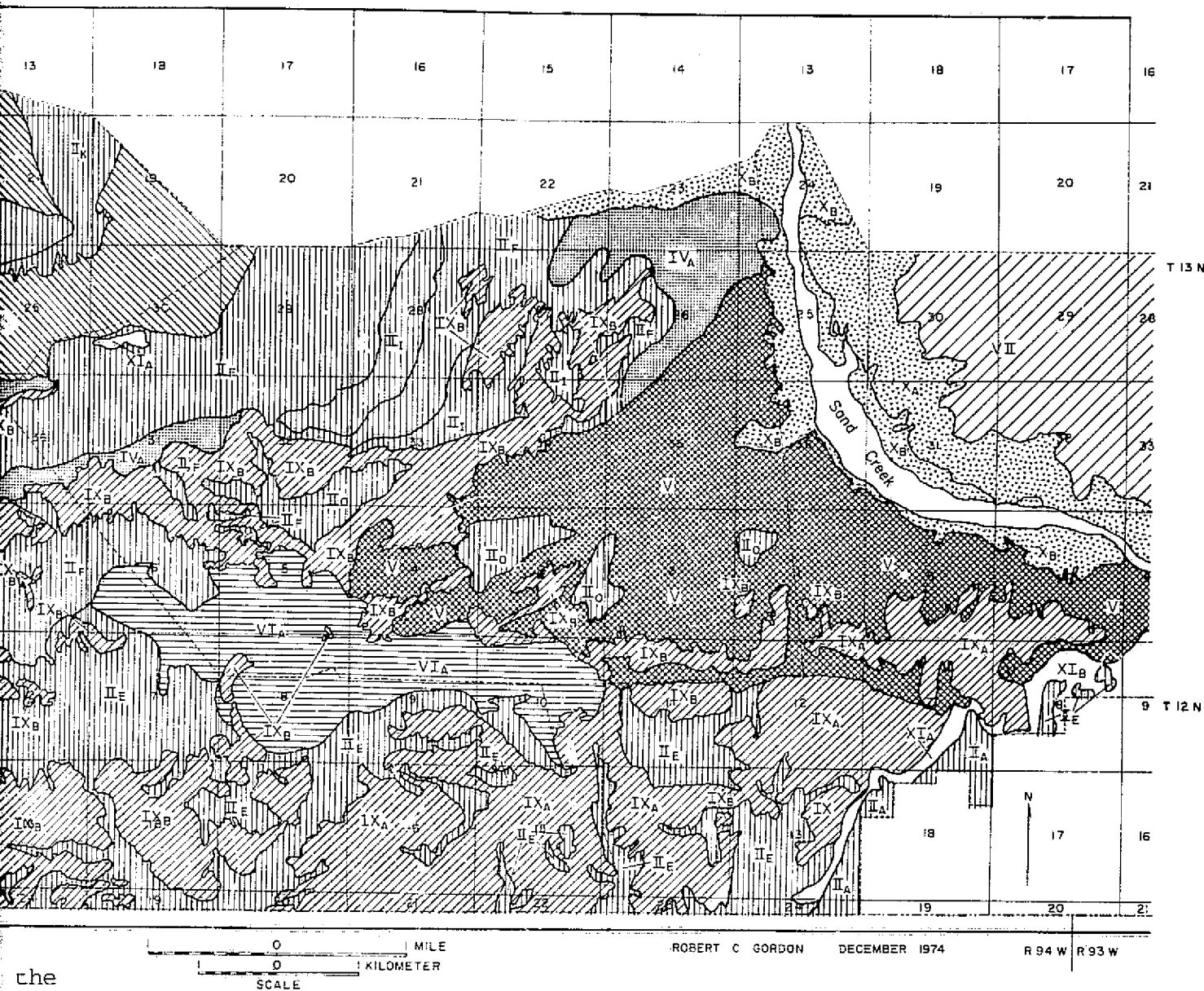
Artemisia tridentata -- Carex eleocharis:  
Basin big sagebrush and needleleaf sedge

- |  |           |  |
|--|-----------|--|
|  | Type VI   | <u>Artemisia tridentata</u> -- <u>Gutierrezia sarothrae</u> --<br><u>Agropyron smithii</u> : Basin big sagebrush, broom<br>snakeweed, and western wheatgrass |
|  | Type VII  | <u>Artemisia tridentata</u> -- <u>Stipa comata</u> :<br>Basin big sagebrush and needleandthread  |
|  | Type VIII | <u>Artemisia tridentata</u> :<br>Basin big sagebrush   |
|  | Type IX   | <u>Juniperus osteosperma</u> :<br>Utah juniper   |
|  | Type X    | <u>Sarcobatus vermiculatus</u> -- <u>Artemisia tridentata</u> :<br>Black greasewood and basin big sagebrush  |
|  | Type XI   | Bare ground  |



61





the  
d from  
raphy  
a

### RANGE VEGETATION TYPES

Type O	<i>Agropyron cristatum</i> : Crested wheatgrass	Type VI	<i>Artemisia tridentata</i> -- <i>Gutierrezia sarothrae</i> -- <i>Agropyron smithii</i> : Basin big sagebrush, broom snakeweed, and western wheatgrass
Type I	<i>Agropyron smithii</i> -- <i>Artemisia tridentata</i> : Western wheatgrass and basin big sagebrush	Type VII	<i>Artemisia tridentata</i> -- <i>Stipa comata</i> : Basin big sagebrush and needleandthread
Type II	<i>Artemisia tridentata</i> -- <i>Agropyron smithii</i> : Basin big sagebrush and western wheatgrass	Type VIII	<i>Artemisia tridentata</i> : Basin big sagebrush
Type III	<i>Artemisia tridentata</i> -- <i>Agropyron spicatum</i> : Basin big sagebrush and bluebunch wheatgrass	Type IX	<i>Juniperus osteosperma</i> : Utah juniper
Type IV	<i>Artemisia tridentata</i> -- <i>Atriplex</i> species: Basin big sagebrush and saltbush	Type X	<i>Sarcobatus vermiculatus</i> -- <i>Artemisia tridentata</i> : Black greasewood and basin big sagebrush
Type V	<i>Artemisia tridentata</i> -- <i>Carex eleocharis</i> : Basin big sagebrush and needleleaf sedge	Type XI	Bare ground

FOLDOUT FRAME 2

Construction Materials. Coal outcrops are relatively difficult to map from photography because the coal seams are relatively thin and are easily eroded. Consequently, the coal outcrops commonly lie along a valley bottom or on a low ridge-slope covered by soil or resistant sandstone ledges. In other areas the coal beds have been ignited (by lightning or other causes) at the outcrop and have "burned out" for some distance into the outcrop. Shale layers overlying these burning coal beds are baked and partially oxidized to produce "clinker" beds. The clinkers, then, mark the upper boundary of a former coal outcrop and they are also useful as a road-base material. The oxidized shale layers are red in color and resistant to erosion so that they often form a distinctive dissected topography with numerous small erosional remnants (buttes and ridges) capped by the baked shale layers.

The baked shale outcrops are recognizable both by their distinctive red color and their geomorphic pattern. In the northwestern Powder River Basin, where the baked shales are associated with coal seams of the Fort Union Formation, the Skylab, S-190B photography was successfully used to map the large baked shale outcrops (Fig. 33).

Mineralization and Alteration. Two separate attempts were made to locate possible mineralized areas by direct photointerpretation. Copper mineralization in the Absaroka volcanic province is known to be associated with the color anomalies that reflect intense alteration of the volcanic rocks. Efforts to locate and define these color anomalies on color and/or color infrared EREP photography were largely unsuccessful (Marrs, 1974a p. 27). Several interpreters were asked to locate strong color anomalies visible on the EREP color infrared photograph of the Absarokas region (Fig.

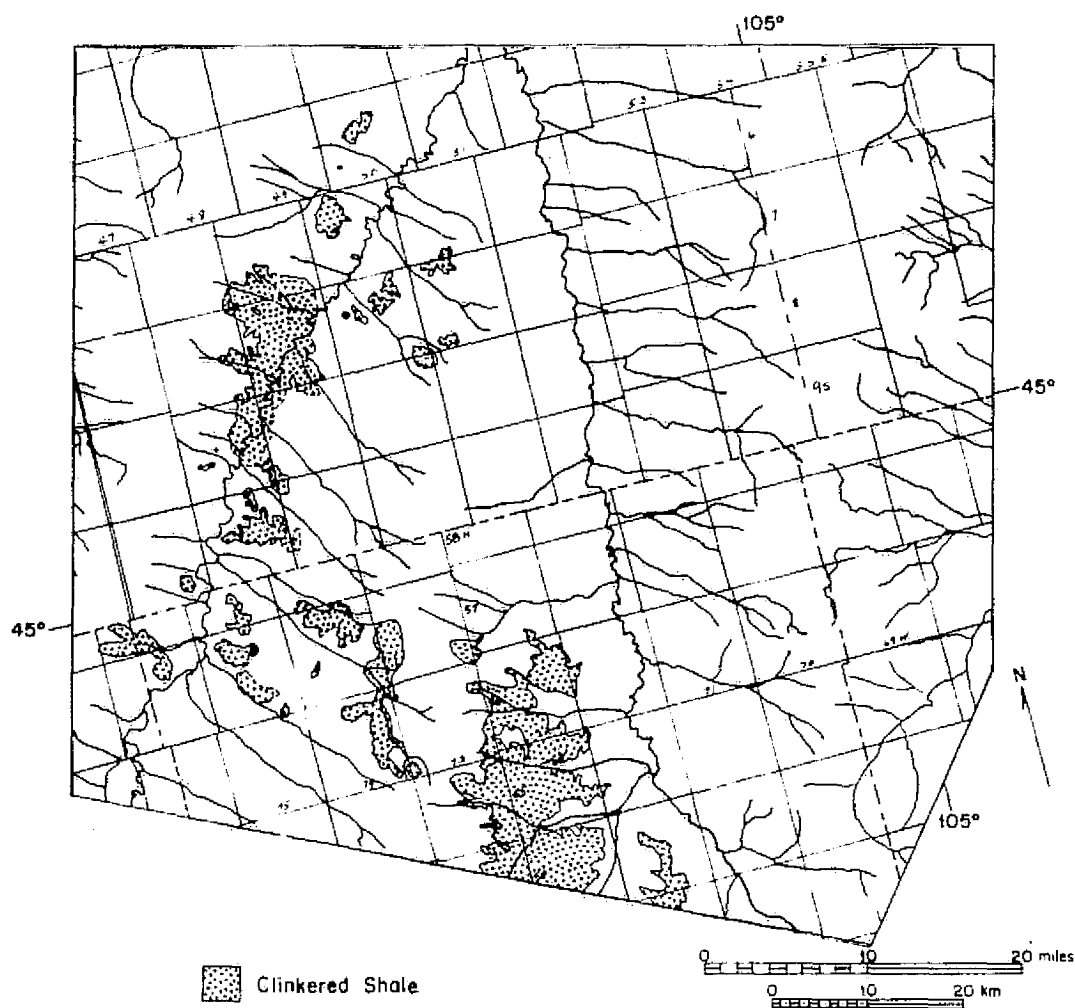


Figure 33. Map of baked shale outcrops in Powder River Basin of northeast Wyoming interpreted from Skylab, S-190B, color photography (see Fig. 7).

34). Each interpreter located several anomalies, but the located areas were strikingly different. Figure 35 is a typical comparison of the results obtained by two interpreters. Interpreter 1 defined sixteen "possible" zones of alteration. Interpreter 2 located twelve. Only four of the alteration zones were located by both interpreters.

A similar attempt to map altered areas associated with uranium mineralization in the Powder River Basin met with similar results. Alteration maps from LANDSAT and EREP image interpretations (Figs. 36 and 37) were compared to a map of the known area of alteration (Fig. 38). All were in agreement on the general area of alteration, but the boundaries of the areas mapped showed little correspondence. The effort was judged "unsuccessful" because the areas of greatest interest, the alteration fronts, could not be reliably located. Nevertheless, it was concluded that the EREP interpretations have some utility because some of the mapped areas include areas of known alteration and mineralization. Therefore, the interpretations may be useful as a tool for isolating areas of interest to be studied further by more definitive methods. It may also be possible to process the images in some way to enhance the color anomalies so that they can be mapped. So far, enhancement procedures have failed to produce the necessary contrast.

#### Comparative Studies

A major part of the evaluation of the Skylab EREP packages were the comparisons made between the different sensors and bands and between Skylab, LANDSAT, and aerial photography. Comparisons were made between the different satellite systems in a number of applications, several of which are discussed in previous sections. A geologic mapping program in the

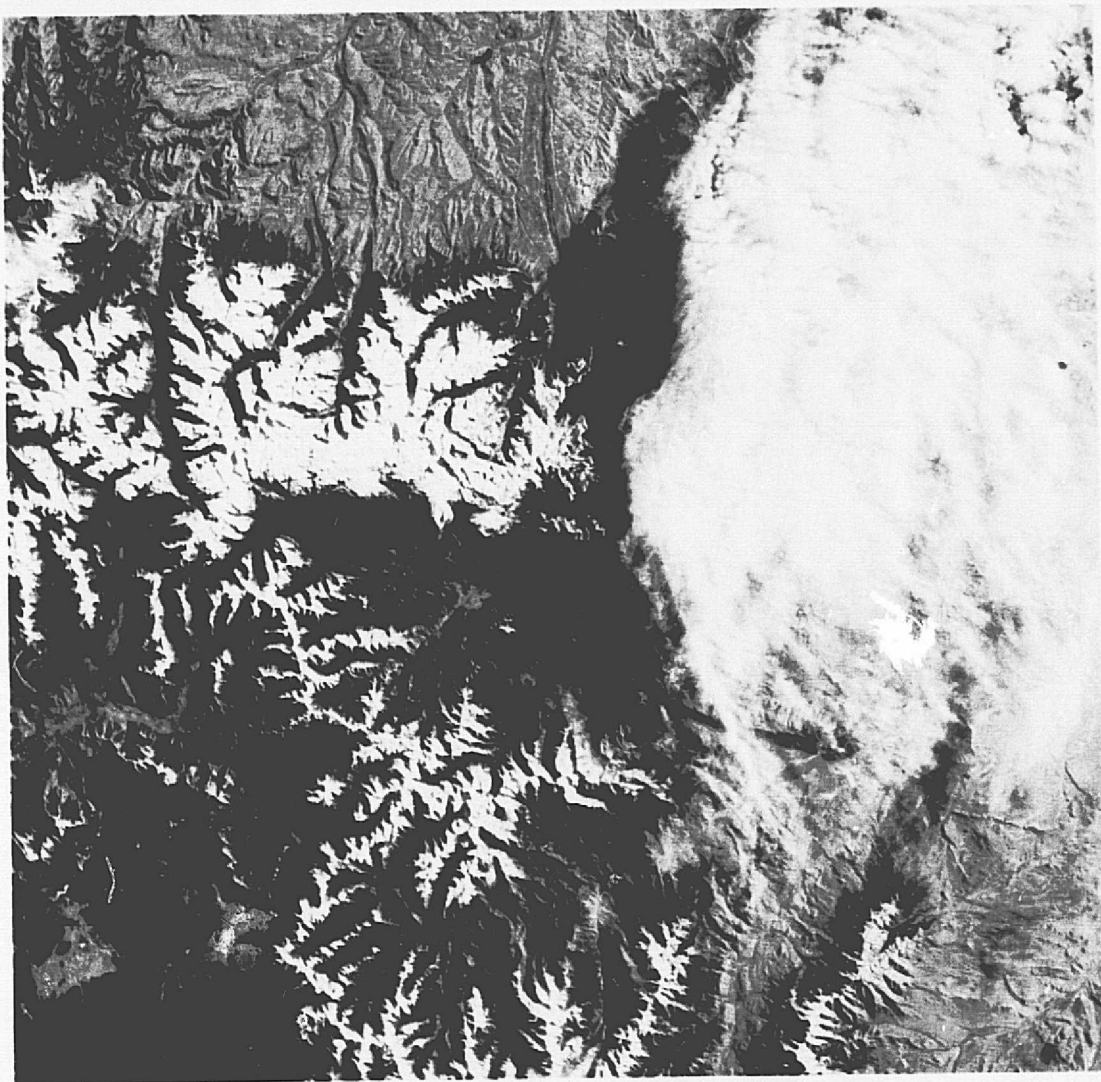


Figure 34. Skylab S-190A photograph of the Absaroka Range and Beartooth Mountains, Wyoming and Montana (roll 15, frame 225, color infrared, track 5, pass 10).

ORIGINAL PAGE IS  
OF POOR QUALITY

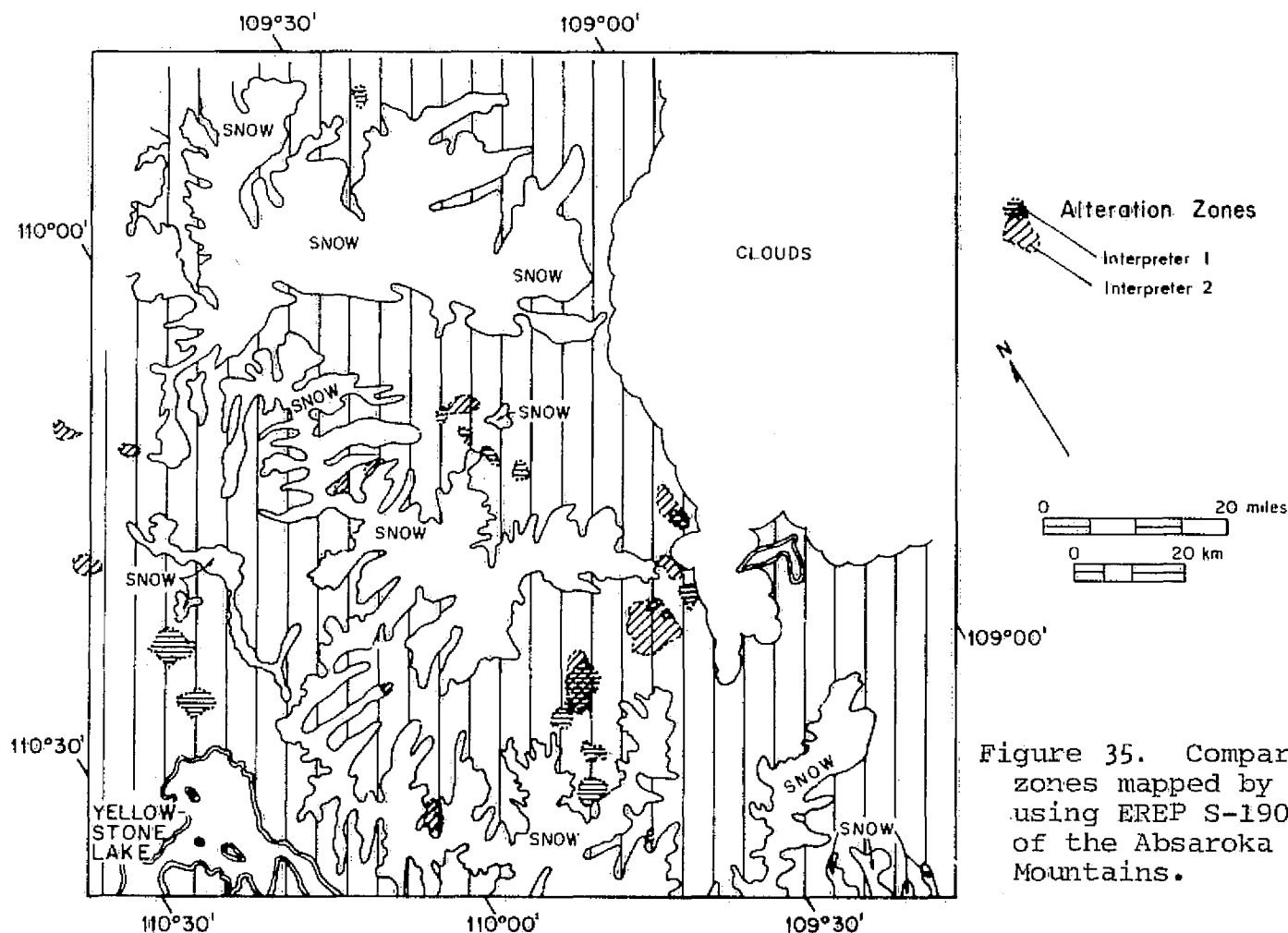


Figure 35. Comparison of alteration zones mapped by two interpreters using EREP S-190A image 15-225 of the Absaroka and Beartooth Mountains.

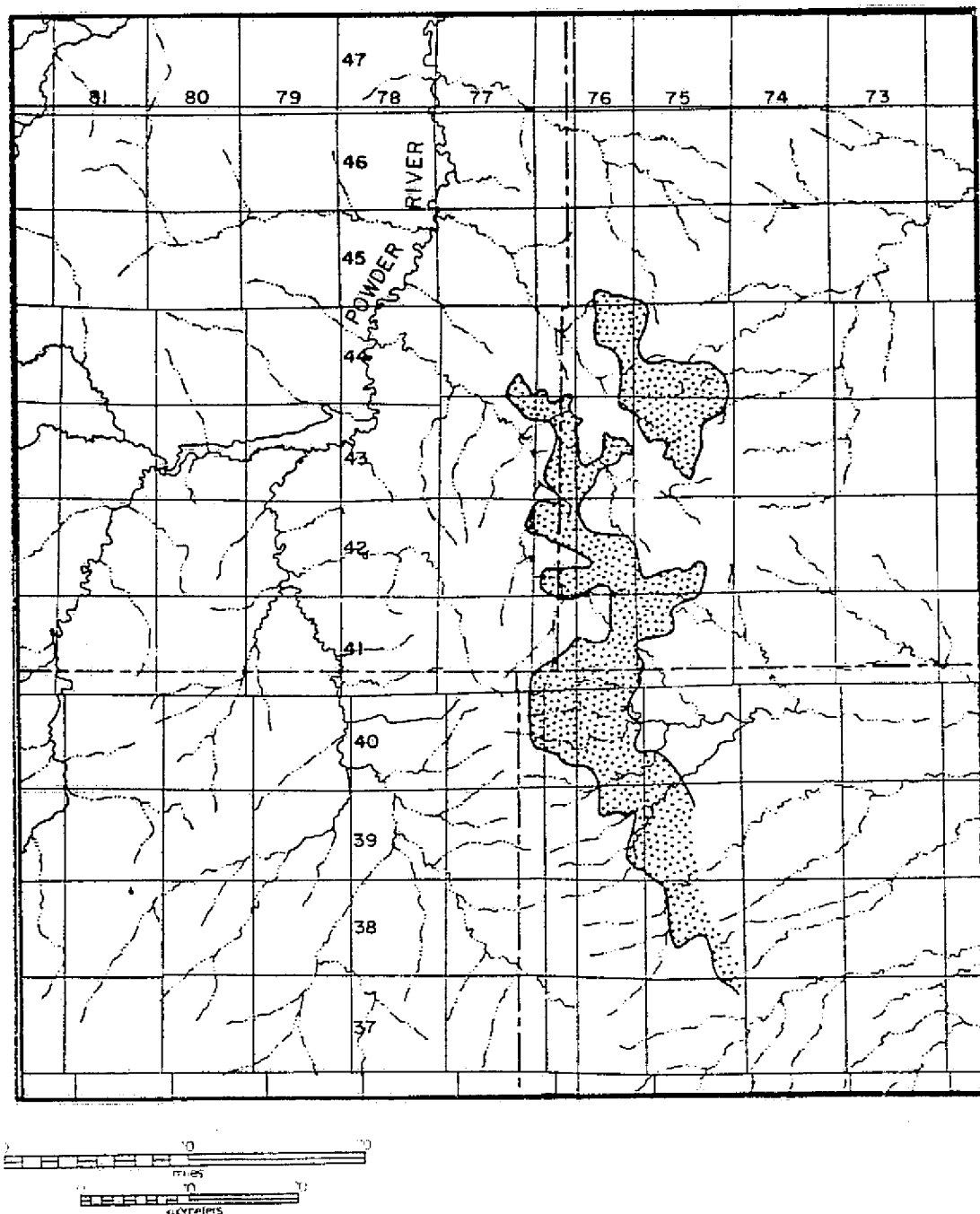


Fig. 36. Alteration map interpreted from LANDSAT color composite image 1047-17182 (after Marrs, 1974b, p. 13).

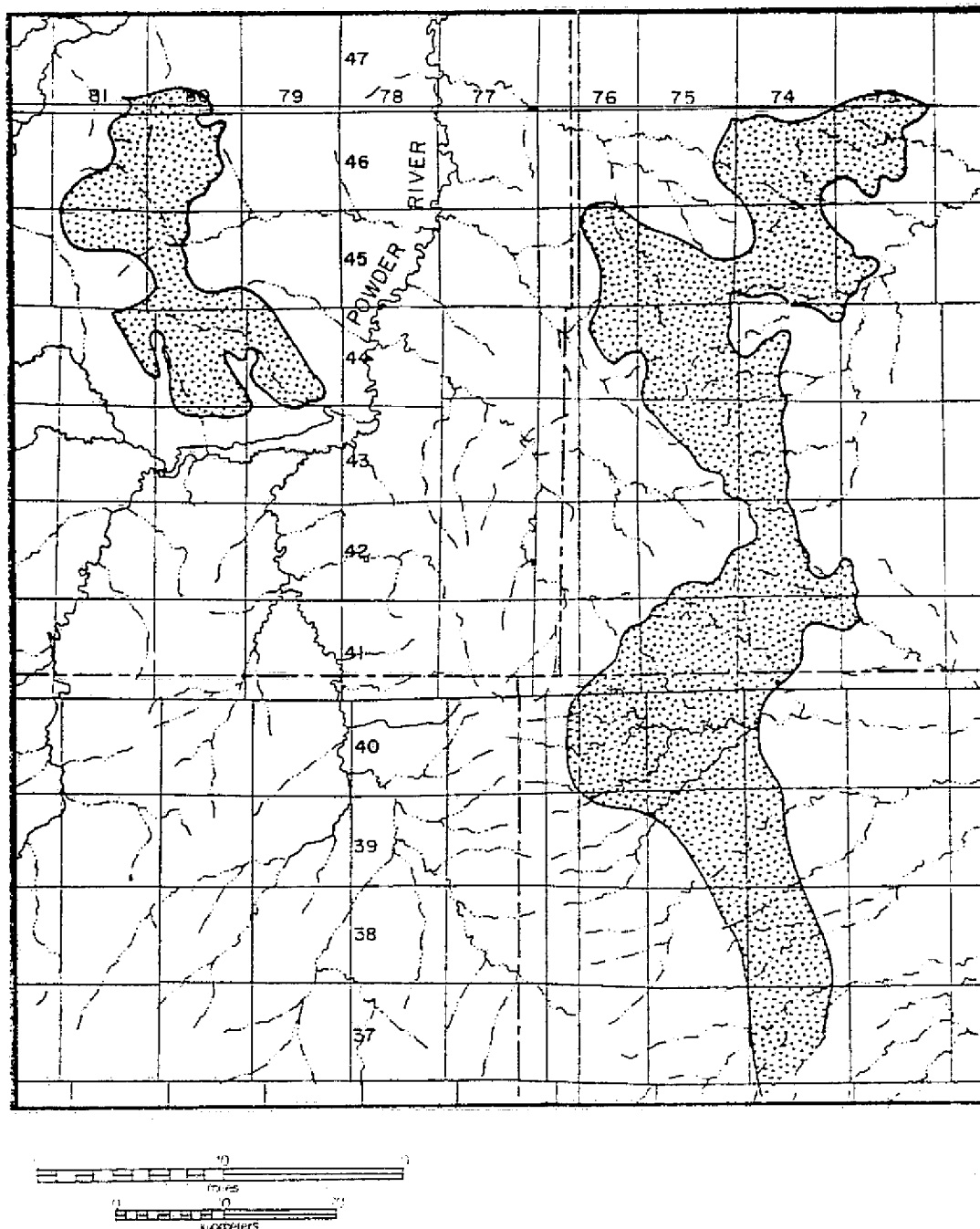


Fig. 37. Area of alteration mapped from Skylab S-190A color image (roll 16, frame 231, track 5, June 13, 1973) (after Marrs, 1974b, p. 14).



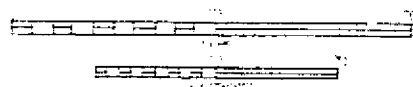
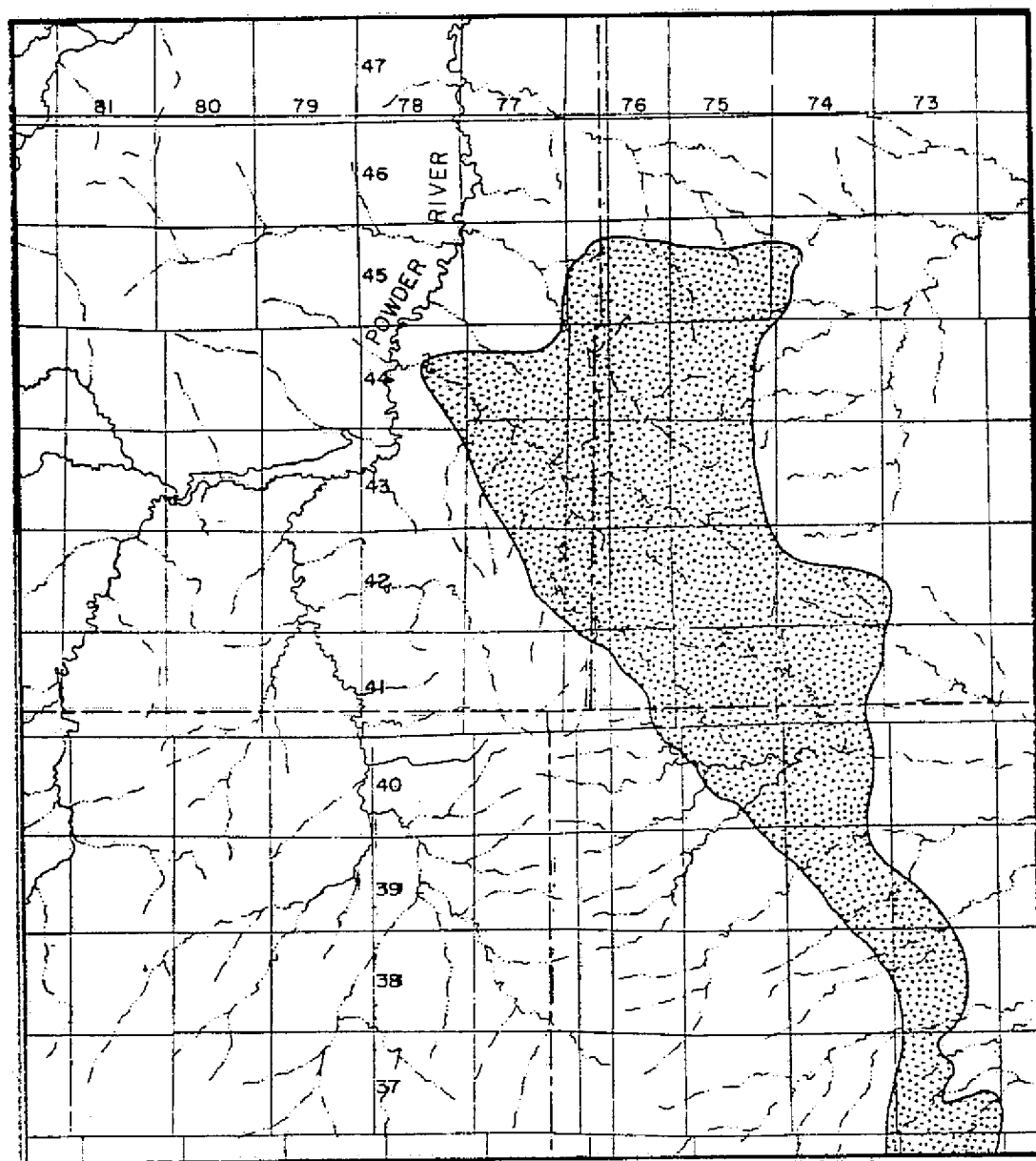


Fig. 38. Map showing extent of known uranium alteration in the southern Powder River Basin (after Sharp and Gibbons, 1964, plate 3).

Boysen area (Fig. 39) was used as a comparative test of the S-190A bands; and an area near Hyattville, on the eastern edge of the Bighorn Basin (Fig. 39), was used as a test area for evaluation of the S-192 scanner data. Each type of comparison contributes to the overall evaluation of earth resources satellite systems and brings us closer to a determination of the optimum specifications for the sensors and the platform.

#### Comparisons in the Boysen Test Area

Description of the Test Area. The Boysen Reservoir area of north-central Wyoming was chosen as a test site for comparison of the S-190A multispectral photography. Rocks varying in age from Precambrian to Quaternary crop out in the area and are complexly folded and faulted. The general geology of the area is well known and has been recently summarized by Keefer and others (1970, Pl. 12). The Boysen test area comprises a series of uplifted blocks that are thrust to the south and southwest over the northern margin of the Wind River Basin. The main fault is the east-striking South Owl Creek Mountain's fault that crops out at the north end of the Boysen Reservoir (Pl. 11, T. 40 N., R. 94 W.). This thrust fault marks the southern limit of the broad, east-striking, anticlinal uplift of the Owl Creek Mountains. The Owl Creek uplift has a broad, gently dipping, north flank and a narrow, steeply dipping-to-overtured, south flank. It is cut, nearly at right angles, by the Wind River Canyon, where rocks ranging in age from Precambrian to Cretaceous are exposed. The canyon cuts the north flank of the uplift over a distance of approximately 15 miles, from an area near Boysen Dam to the town of Thermopolis. The steeply dipping, south flank of the uplift is

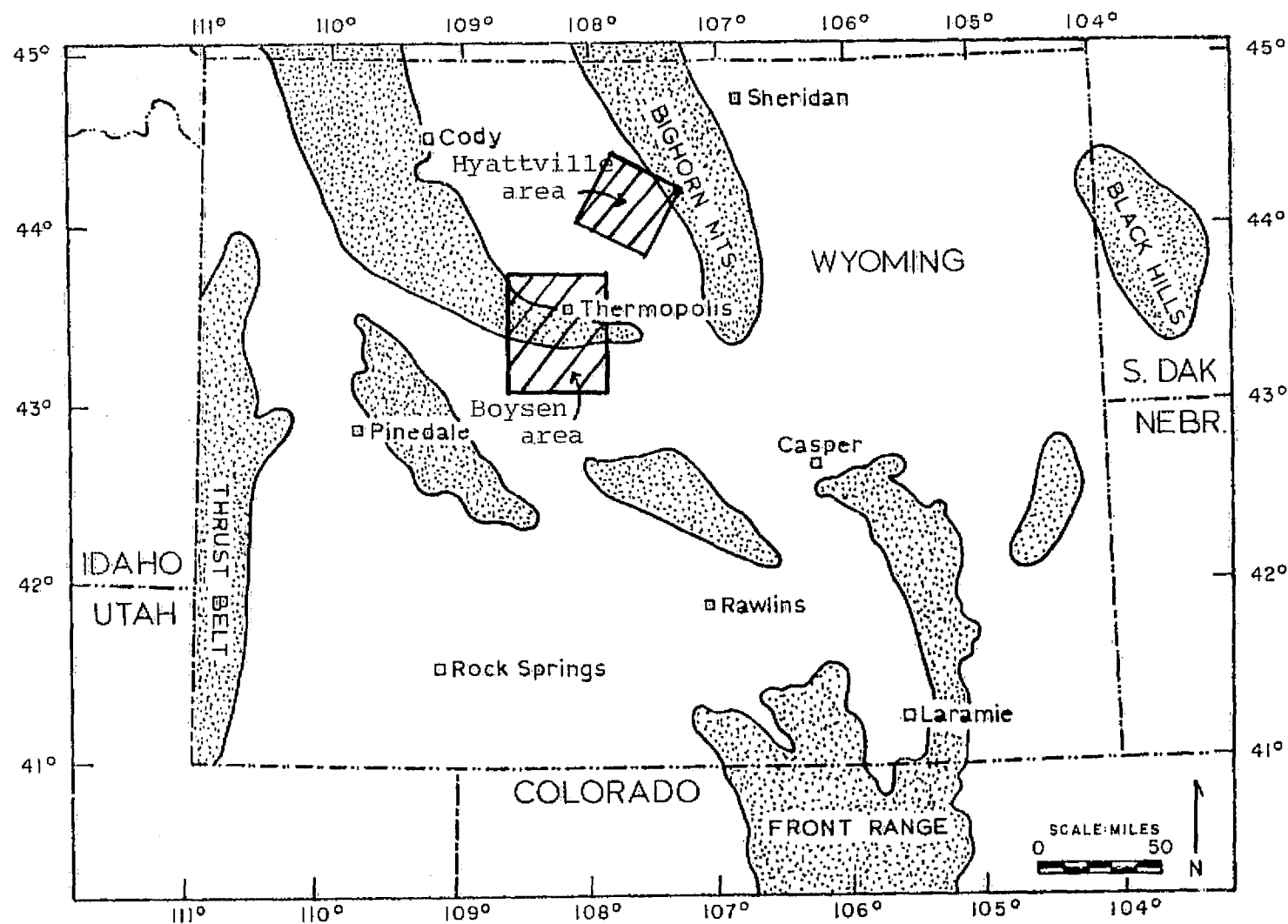


Fig. 33. Index map showing the locations of the Boysen test area and the Hyattville test area.

complexly faulted into a series of grabens, horsts, and rotated blocks. One major fault, the Boysen Fault, exposes the Precambrian core of the uplift north of Boysen Dam (Pl. 11, T. 40 N., R. 93-95 W.).

West of the main uplift, fault blocks are oriented northwest and are typically asymmetric with steep limbs and faults on the southwest. The most prominent block of this series is faulted on both northeast and southwest margins and is probably wedge-shaped in northeast cross-section.

North of the main uplift the same northwest orientation is exhibited by folds that are asymmetric, with faulted and overturned limbs to the southwest.

This complicated structure is well-exposed in much of the area so it is ideal for use in evaluation of Skylab imagery for geologic mapping of semi-arid lands. The main South Owl Creek Mountains Fault system is not as well exposed as other structural features because it is covered by on-lapping rocks of late Tertiary age and extensive Quaternary deposits that are most abundant on the steep, south flank of the uplift. Geomorphic features, such as pediments, are exceptionally well-developed on the south flank of the Owl Creek Mountains, and the abundant vegetation on these surfaces also tends to obscure structure.

Geologic Mapping Using S-190A Photography. All S-190A film products were interpreted for the area. Limited mapping was achieved with every band, but the two best map products were interpreted from the color and red-band film transparencies. This quality difference is clearly related to two factors; spatial resolution and, in the case of color, the use of diagnostic color for mapping certain rock types. Color infrared photography is often best for geologic mapping (Houston, 1973b) by the Skylab

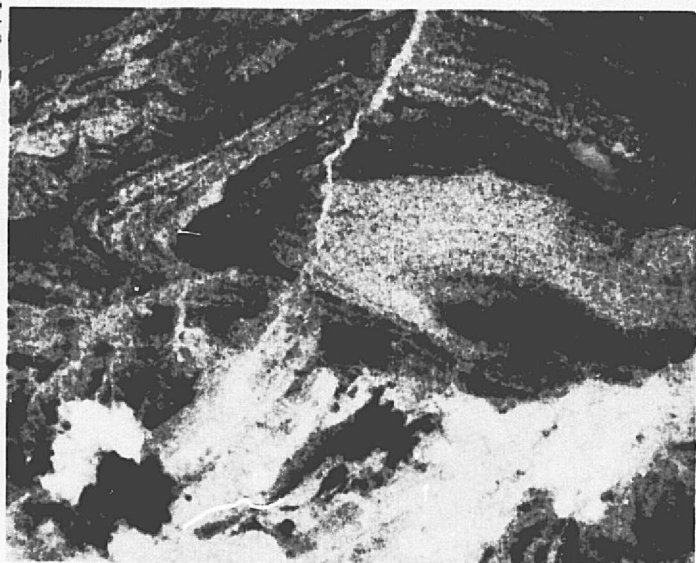
color infrared product does not have spatial resolution comparable to that of the Skylab S-190A color.

Figure 40 illustrates the variation in spatial resolution of the various S-190 film products. Plate 9 is a compilation of all geologic information that could be obtained from stereoscopic interpretation of the two infrared bands (.7-.8  $\mu$ m and .8-.19  $\mu$ m). Major faults and some major folds were detected, but the two bands proved to be extremely poor for general geologic mapping.

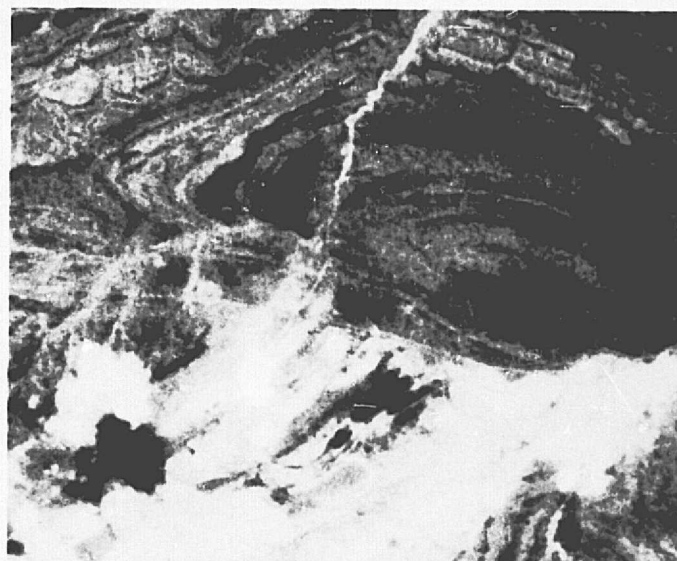
The infrared film is useful for some purposes despite its poor spatial resolution. For example, zones peripheral to Boysen Reservoir, thought to be marked by increased soil moisture, can be seen as a dark zone on the infrared transparencies, and areas of exceptionally vigorous vegetation can be mapped because of their bright tone on the infrared photography. Thus, despite its very limited resolution, the infrared film may be useful in crop studies. The vigorous crops shown in these September images are probably alfalfa and sugar beets. Localities numbered on Plate 9 are areas of specific interest discussed further in Appendix A.

Interpretation of the green band (0.5-0.6  $\mu$ ) transparencies were used to make a very generalized regional tectonic map (Pl. 10). Contacts between geologic units showing contrast in the green were traced and basic structural patterns outlined.

Contrast between some rock types is good in the green band. For example, red beds show very dark tones on green-band photographs and contrast strongly with light-colored sandstones and limestones. This results from the exceptionally low reflectance of the red shale and sandstone in the



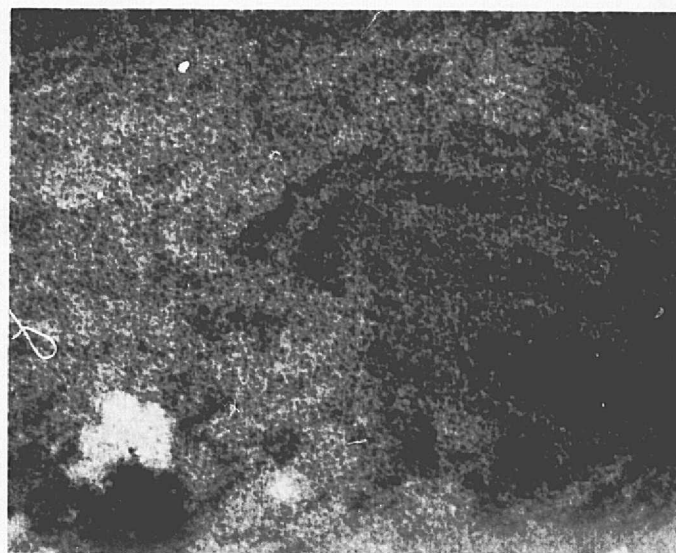
S-190A GREEN (500-600 nm)



S-190A RED (600-700 nm)



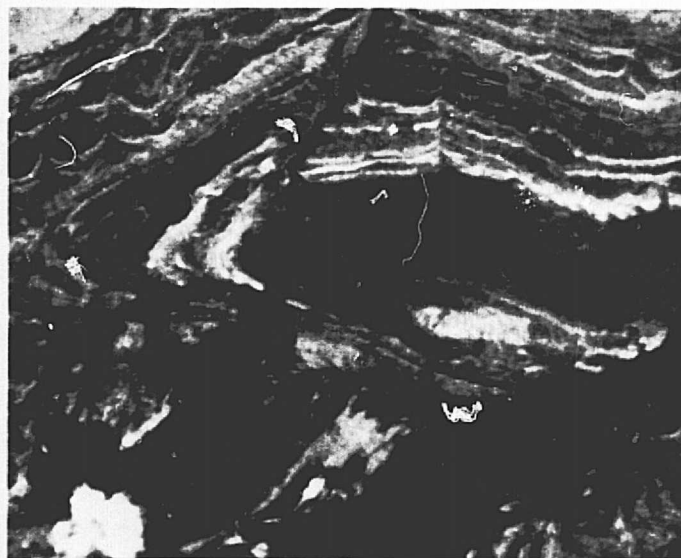
S-190A IR1 (700-800nm)



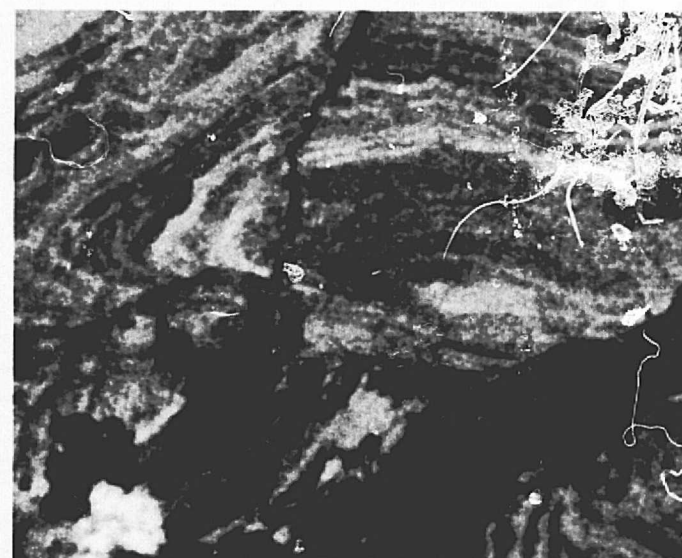
S-190A IR2 (800-900 nm)



S-190A IR1 (700-800 nm)

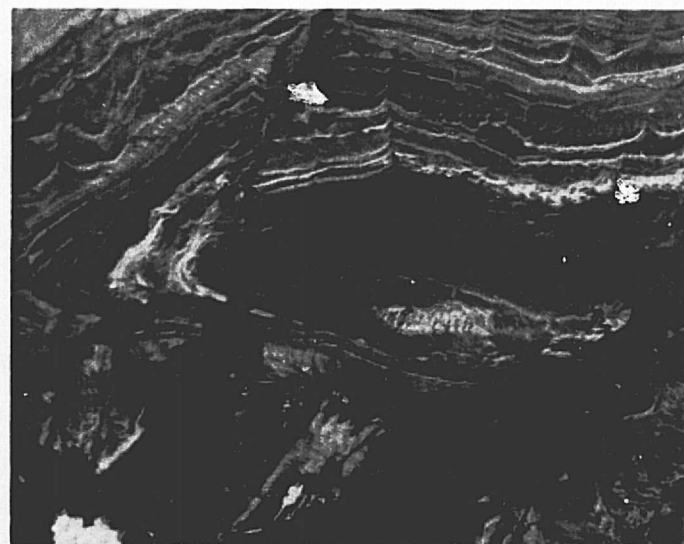


S-190A IR2 (800-900 nm)



S-190A COLOR (400-700 nm)

S-190A COLOR INFRARED (500-880 nm)



S-190B COLOR (400-700 nm)

Figure 40. Comparison of S-190A bands and S-190B photograph for a small part of the Boysen area. Resolution differences are readily apparent in these enlargements.

C-2  
FOLDOUT FRAME 2

green spectral region. Other rock types, such as black shales, will also produce very dark tones on green band photographs, so this tonal feature is not unique to red beds, but it can be helpful in rock identification when the interpreter is familiar with the geologic section.

The green band photograph is somewhat hazy, due in part to atmospheric scattering of green light. Vegetated areas do not show sharp contacts with non-vegetated areas or areas of sparse vegetation. Where a modest vegetative cover is preserved, much of the area is hazy and dark in appearance on the green band, and very few of the rock characteristics can be recognized.

The overall characteristics of the green band photography suggest that it is a poor choice for geologic mapping, and, if color or color infrared film products are available for use in identifying red beds, there is no reason to choose the green band for geologic study. Numbered localities on Plate 10 are discussed in Appendix A.

Red band (.6-.7  $\mu$ m) photographs are particularly useful for mapping certain deposits of Quaternary age and for preparation of regional tectonic maps (Pl. 11). They are not as useful as the color and color infrared photography because individual rock types usually cannot be recognized and traced over large areas. Contrast between units is not noticeably better than for the green band, but spatial resolution seems better (largely because of better haze penetration). The improved resolution (compared with green band photographs) makes possible recognition of smaller units and a better determination of direction and degree of dip of rock units in the stereo mode.



A comparison of Plate 8 and Plate 11 shows that the red-band interpretation is a useful regional tectonic map of this area and that all major faults and folds have been identified. The red band is also useful in mapping alluvium and pediment gravels (compare Pls. 10 and 11), although Quaternary contacts cannot be as readily located in the southern part of the area as they are in the north. The distribution of pediment gravels shown on the red-band map (Pl. 11) is significantly broader than that shown on the geologic map (Pl. 8). Pediment surfaces are gently dipping, planar features that are developed primarily on sedimentary rock units along the margins of major uplifts. These surfaces may extend many miles into basin areas, and are normally cut indiscriminantly across sedimentary rock units of different erosional susceptibility (Fig. 41). The origin of these surfaces is not fully understood, but they may be developed during interglacial periods by aggrading streams or rivers. The surfaces are commonly covered by thin gravel deposits, and geologic maps typically show only these gravel deposits as the pediment surface. The gravel deposits may not cover the entire pediment surface; thus, the geologic map shows the distribution of the pediment gravel, but not necessarily extent of the pediment surface.

The pediment surfaces have a heavier vegetative cover than other areas, and are covered with grass rather than sage/grass mixtures. The red-band map of these features is largely a vegetation map in which vegetation approximately coincides with the distribution of pediments. Where there is adequate relief (approximately 200') the Skylab image can also be used to



Figure 41. Oblique aerial scene showing a typical pediment surface.

gain a stereo-view of these surfaces. The red-band map probably will give the geomorphologist a good estimate of the maximum extent of pediment surfaces in an area such as this, but it is not an accurate map of pediment gravels.

The red-band map of alluvium in the southern part of the area shows a relationship opposite to that discussed above. The geologic map indicates a much greater extent of alluvium than the red-band map. In mapping alluvium with Skylab red-band photographs, the assumption must be made that the alluvium coincides approximately with the vegetated valley floor of streams and rivers. Vegetation shows with a distinctive dark tone in this band because of the strong absorption by chlorophyll, so the vigorous vegetation in these alluvial-filled valleys is readily mapped. The difference between the red-band interpretation and true extent of alluvium in this southern area may be the result of floods that have spread alluvium well beyond the current stream channels. Some of the alluvium mapped by field geologists may also include Pleistocene terrace gravels and colluvium. The red-band map shows the probable extent of recent alluvium in stream and river valleys, but does not include material of the earlier valleys and floodplains.

In contrast to the problems encountered in the southern part of this area, the alluvium is well mapped in the northern area.

Another feature of the red-band photograph, relative to color and color infrared, is that faults and linear features are not as readily detected on the red-band photographs. All major faults known in this area were mapped with red-band photographs, but minor faults and linear features were more difficult to detect. This may result from higher resolution in the color photograph and the ability of infrared to better

detect moist fault zones or vegetation along fault systems. Numbered locations on Plate 11 indicate features discussed in Appendix A.

Skylab S-190A color infrared photography shows a distinctly poorer resolution than the S-190A color photography. The graininess of the infrared color film is such that maps prepared from it are poorer than those prepared with red-band photographs. The only advantage of the color infrared photography is that red beds can be recognized by their characteristic yellow color. Since red bands can also be detected on color photography the color infrared has no advantage over color film. However, if no color photography were available, color infrared and red band photography might be a good alternative mapping combination.

The spatial resolution for Skylab S-190A color infrared photography is superior to that of LANDSAT imagery, but these image products are close enough in overall characteristics for meaningful comparison. It was anticipated that Skylab infrared photography would be superior to LANDSAT images because it would have somewhat superior resolution and stereo-coverage. The Skylab color infrared photography did show slightly improved resolution and the advantage of stereo-viewing, but marker units were not as easily recognized as they were with the LANDSAT color-composite images. Red beds show on Skylab infrared positive transparencies as distinct greenish-yellow units much as they show on LANDSAT infrared images, but with the Skylab photography only the deep red Permo-Triassic red beds can be recognized (Fig. 42). Red beds that are present in the Wind River Formation (of Tertiary age) can be identified only on LANDSAT infrared images. In the field the Tertiary red beds are normally more of a rose color and are

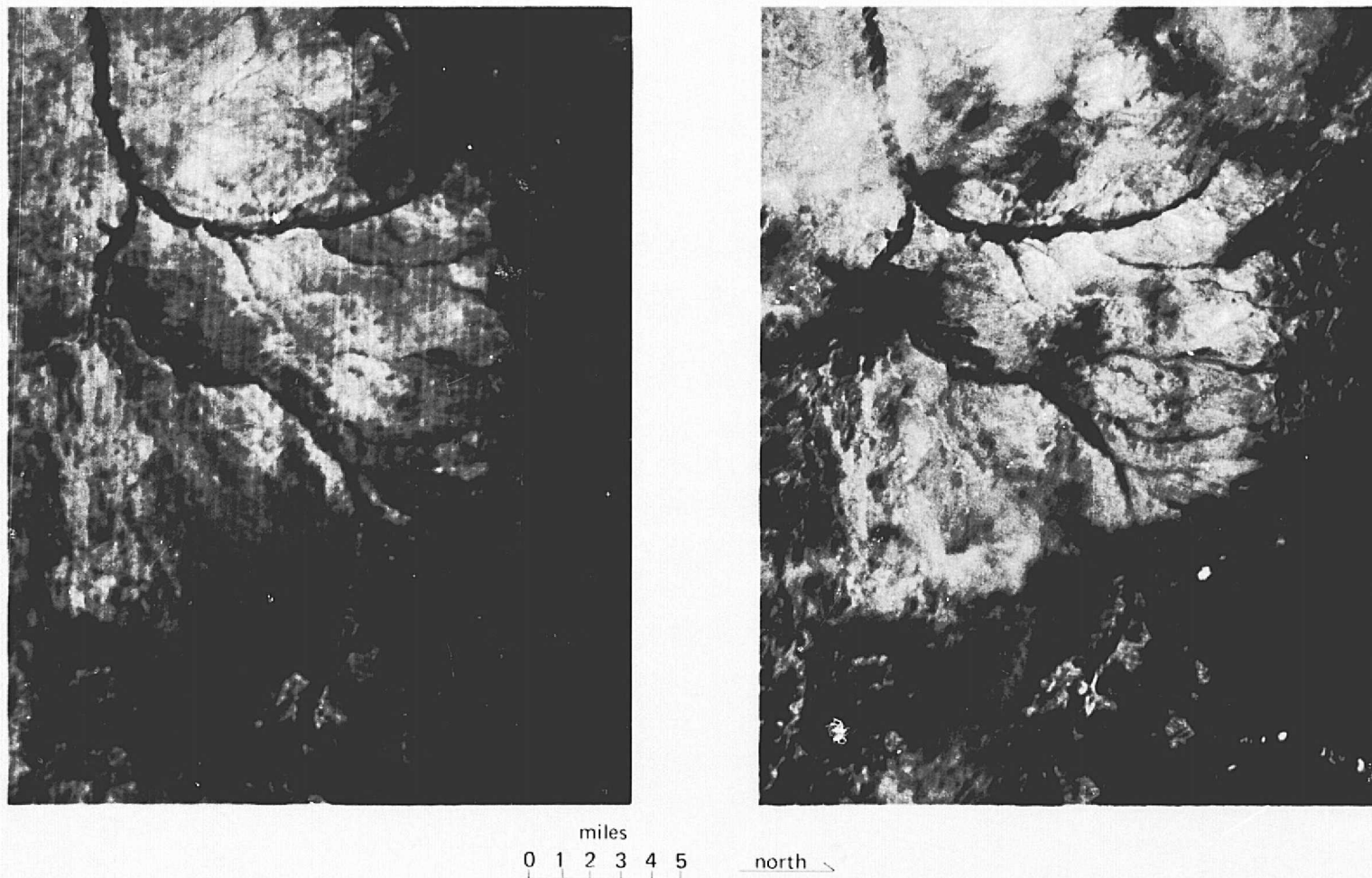


Figure 42. Comparison of LANDSAT color composite imagery (left) and Skylab S-190A color infrared photography (right) showing the marked difference in presentation of Tertiary red beds on the LANDSAT and Skylab imagery. The red beds are distinctly yellow on the ERTS color composite but appear blue-white on the Skylab photo. LANDSAT color composite image 1013-17291; Skylab S-190A photograph, roll 37, frame 208, track 59, pass 28, Sept. 1973.

variegated as compared with the deep solid reds of the Permo-Triassic units (Fig. 43), but both can be recognized by a distinct yellow color on LANDSAT images. The Tertiary red beds are somewhat paler in color on LANDSAT images than are the Permo-Triassic red beds, but, in most cases, it is difficult to be certain from a LANDSAT image which of the red bed sequences is present. Thus, by using the LANDSAT infrared images and Skylab infrared color photographs in combination, it is actually possible to distinguish between Tertiary and Permo-Triassic red beds.

The distinct dark tone (typically deep blue in color) that characterizes the black shales of the Thermopolis Shale and Mowry Formation on LANDSAT images is also apparent on Skylab infrared photographs, but the Skylab color infrared photograph does not show as strong an enhancement as the LANDSAT image (Fig. 44). The reason for the enhancement of these units in LANDSAT infrared color composite image may be a function of two factors; vegetation enhancement and contrast. The vegetation enhancement is a negative effect because these shales support very little vegetation as compared with many of the lithologic units in the Wyoming section. Thus, they appear distinct as compared with other units that are more heavily vegetated and appear bright (or red) in the infrared.

Figure 45 shows that the Thermopolis Shale has extremely low reflectance throughout the visible and near infrared spectrum, and the difference between the reflectance of Thermopolis shale and other units increases with wavelength. The greater difference in reflectance in the near infrared should produce a natural "contrast stretch" in the near infrared band, but color infrared film is not as sensitive to infrared radiation as



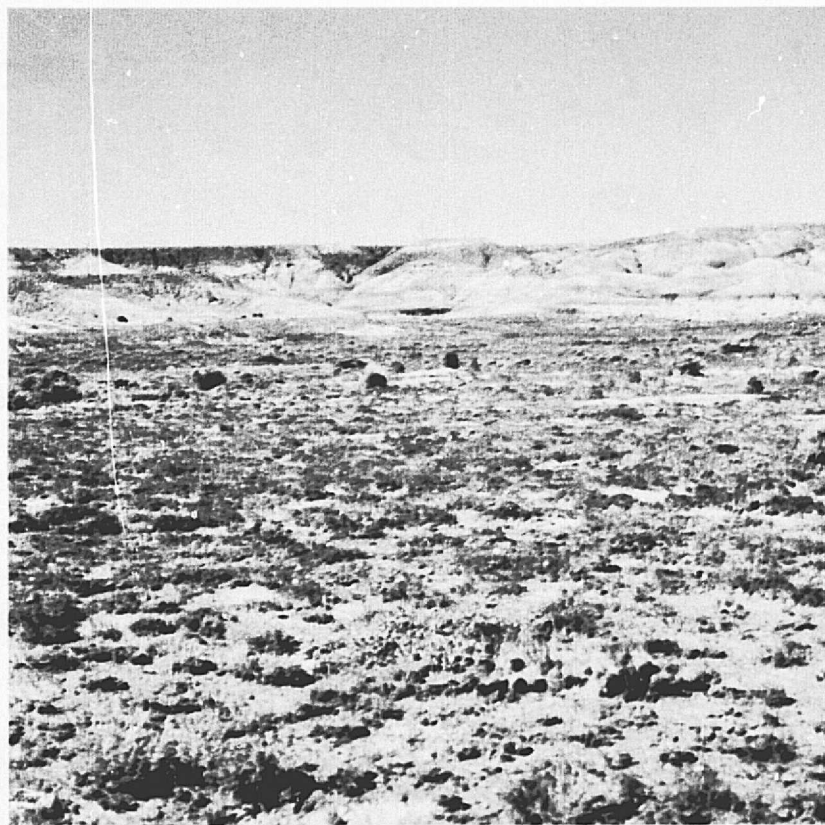


Figure 43. Field scenes comparing the relatively pale Tertiary red beds (left) to the bright orange-red Permo-Triassic red beds (right).

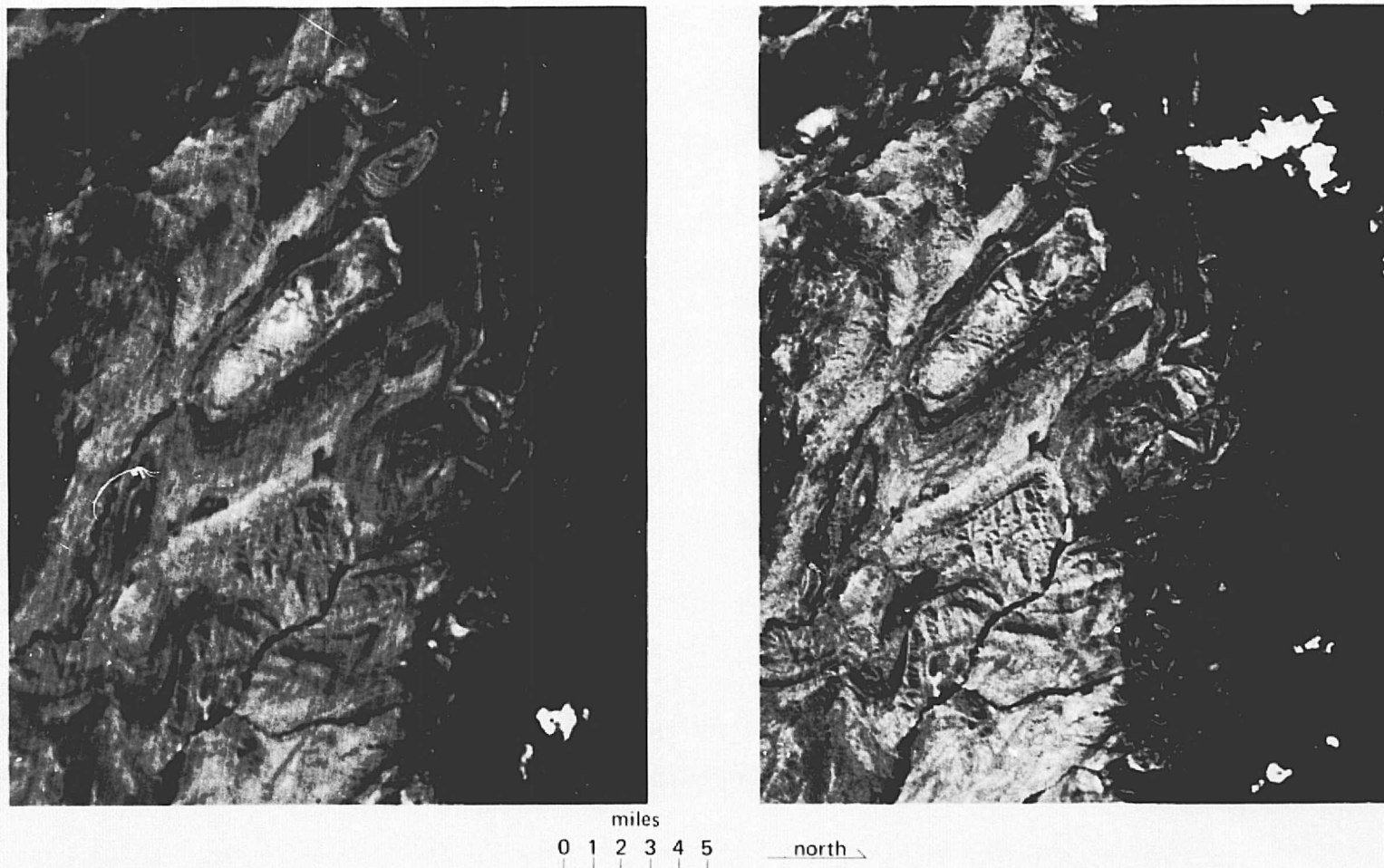


Figure 44. Comparison of LANDSAT color composite imagery (left), and Skylab color infrared photography (right), of an area in which the Thermopolis and Mowry shales are used as a geologic marker unit. Areas that are yellow on both the LANDSAT and Skylab images correspond to outcrops of Triassic red beds. LANDSAT color composite image 1013-17294; Skylab S-190A photograph, roll 21, frame 211, track 62, pass 4, August 1973.



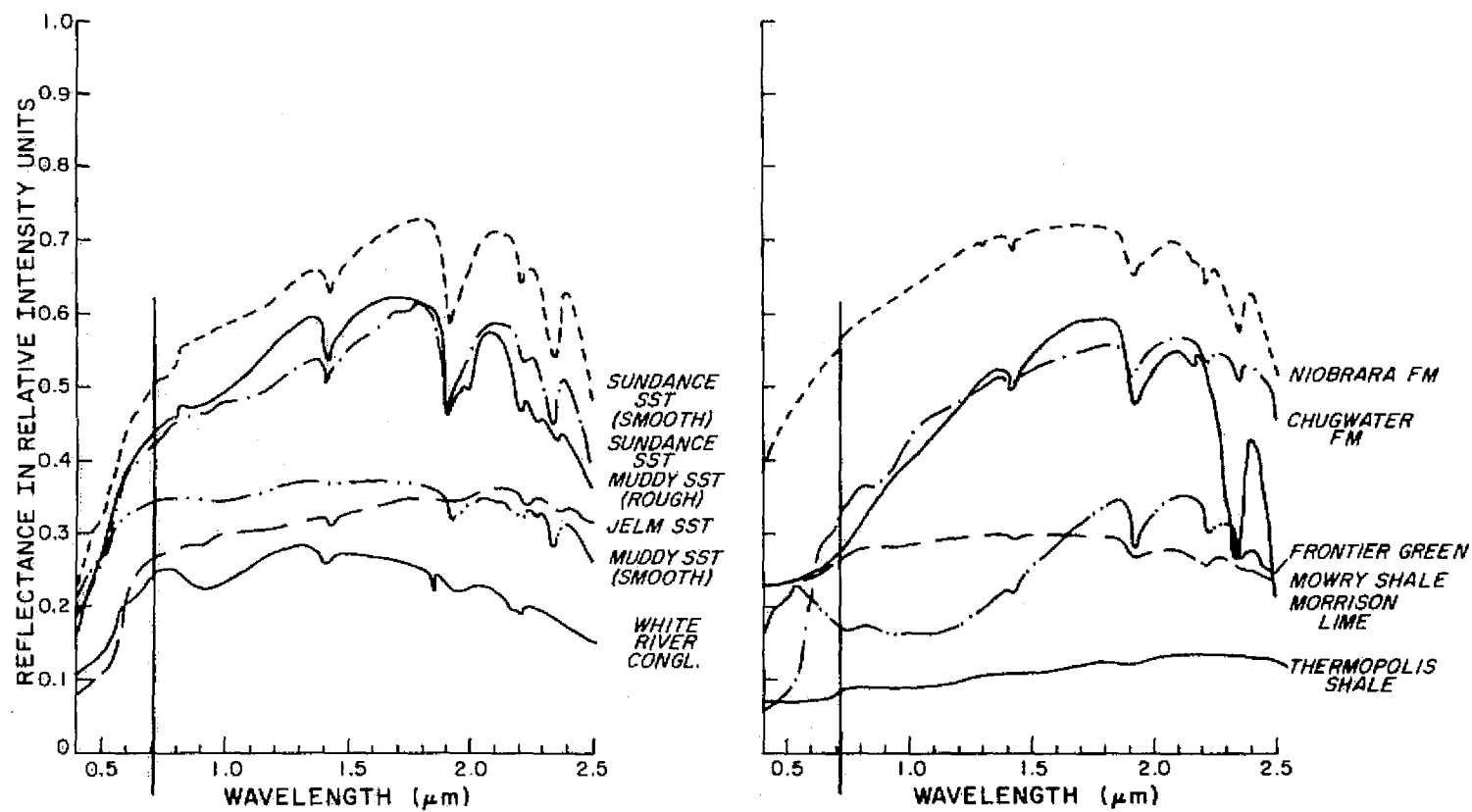


Figure 45. Spectral reflectance curves for some Wyoming rocks (After Short and Lowman, 1973).

it is to green- and red-band radiation (Fig. 46), so the difference is nullified.

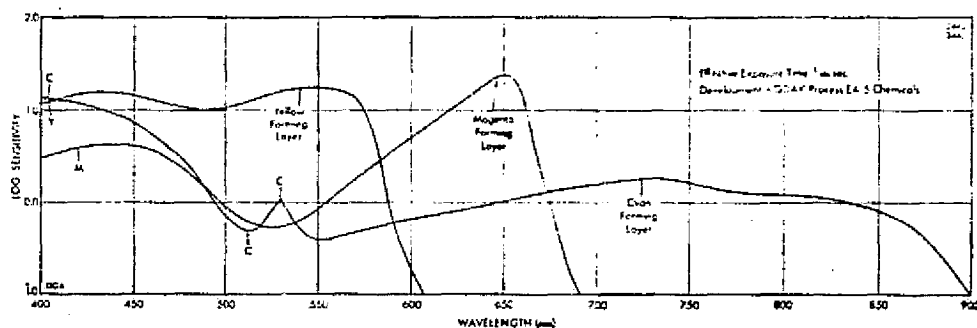
These same factors may explain the enhanced contrast between the Thermopolis shale and other units observed on the LANDSAT composite image. First, the LANDSAT infrared bands extend further into the infrared spectrum (1.1  $\mu\text{m}$ ) than does the infrared band of Skylab S-190A (.88  $\mu\text{m}$ ). Thus a greater proportion of the recorded energy comes from the "contrast stretched" infrared portion of the spectrum. Also, the LANDSAT scanner is not limited by film sensitivity as is the Skylab photography, and the actual infrared scene brightness values may not be subdued relative to the red and green bands as was the case for the color infrared film.

Skylab color photography is the best of the S-190A products for geologic mapping. All major geologic structures can be recognized, key units such as red beds can be traced over large distances, attitudes of bedding and the trace of faults can be delineated. An evaluation of the Skylab geologic map can be made by comparing Figure 40 and Plate 8.

Specific geologic features noted on the Skylab color film positive are shown by number on Plate 12. At locality one, Permo-Triassic red beds are accurately placed, although the lower contact is not in the same location as on the geologic map, because non-red beds of the Triassic Dinwoody Formation are not included in the remote sensing unit. Alluvium is accurately mapped at this locality. It was omitted on the regional geologic compilation (Pl. 8), but it does show on more detailed geologic maps (Phillips, 1958). Pediment gravel is well mapped at this locality; but, to the east, more pediment gravel is shown than was mapped by field geologists. The extent of pediment gravel is only partially field checked but it is the researcher's opinion that (1) the field geologist shows too little

2443/3443

### Spectral Sensitivity Curve



### Spectral Dye Density Curves

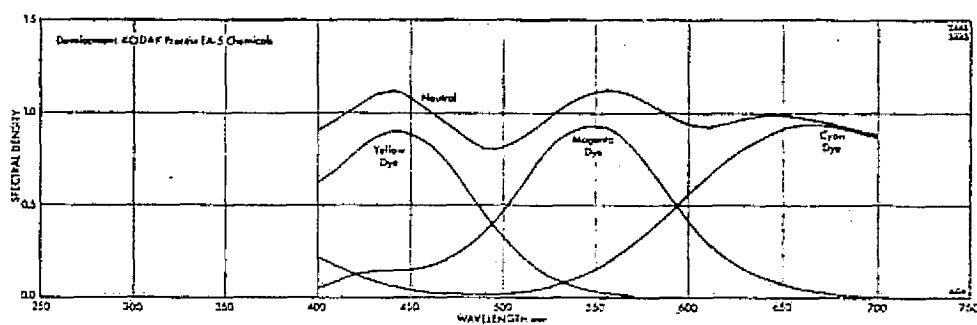


Figure 46. Spectral sensitivity and dye density for Kodak color infrared film (type 2443).

pediment gravel because he ignores scattered thin veneers of gravel, (2) the photo interpretation shows too much gravel because small, patchy units are lumped into one large unit and small formation outcrops cannot be seen, and (3) the photo interpretation is a map of a surface with characteristic vegetation that may or may not have a uniform ground cover.

At locality two, the remote sensing units mapped by the photogeologists are the dark shales of the Cretaceous Mowry and Thermopolis Formation that are so distinctive on LANDSAT color composite images and fairly well displayed on Skylab color infrared photographs. These units are not strongly expressed on the color photography, but are distinctive enough to be mapped.

Locality three is the approximate contact between the Mesaverde Formation and Cody Shale. This contact is marked by a distinctive tone and textural change and is accurately mapped on that basis. The reason for this distinctive tone of the Cody Shale is discussed below.

At locality four, the unit mapped is an iron-stained, concretionary siltstone within the Fort Union Formation. The unit is darker in color than surrounding rocks. It is an example of a remote sensing unit within a formation.

At locality five, the line mapped is a contact between the Fort Union Formation and Quaternary alluvium. The alluvium was not distinguished on the Skylab color photograph because it was not marked by characteristic vegetative cover. As noted in the discussion of red-band photography, it was only possible to map floodplain alluvium by the presence of vegetative indicators.

The general quality of mapping alluvium and pediment gravel in the area of locality six was much like that of the red-band photograph except somewhat less accurate when compared with geologic maps of the area. For example, if a comparison is made of the pediment shown at locality seven in red band (Pl. 11), color, (Pl. 12) and the regional map (Pl. 8), the red band is closer to the geologic map. In fact, it proves more accurate than the regional geologic map compilation when compared to available maps at 1:24,000.

At locality eight, a small patch of red beds were recognized using the Skylab S-190A color photography. Geologic relationships are extremely complicated in this area (Pl. 8), but the Skylab interpretation was surprisingly accurate. At locality eight "A", red beds, with a red-orange color much like that of the Permo-Triassic, are present. They were interpreted to be Tertiary red beds. In the field, they were seen to be as red as the Permo-Triassic red beds which is an unusual color for the Wyoming Eocene red beds. Their interpretation as Tertiary is simply a best guess since no significant difference in color or texture was noted in the field between these particular Tertiary red beds and those of Permo-Triassic age.

A comparison of Plate 12 and Plate 8 shows that major faults and folds can be distinguished on the Skylab color photograph at locality nine. Certainly, all faults were not recognized, but the major east-striking and northeast-striking systems were noted. Despite failure to distinguish some of the major lithologic units, the asymmetric anticline on the hanging wall of the South Owl Creek Mountains thrust was mapped.

Locality ten marks a part of the contact between a limestone-dolomite unit, consisting of the Bighorn Dolomite of Ordovician age at the base and the Madison Limestone of Mississippian age at the top. These lithologies are marked by high reflectance relative to underlying shales, limestones, and sandstones of Cambrian age. The contact is a good marker on most Skylab images.

The Tensleep Sandstone is also a unit of high reflectance, but, locality eleven shows that the base of this unit was accurately mapped due to a difference in vegetation cover between the Tensleep and underlying units.

Locality twelve is the contact between the Tensleep Sandstone and overlying Park City Formation. This contact is difficult to locate on the S-190A color photography because the contrast in reflectivity between the dolomitic limestones of the Lower Park City and sandstones of the Upper Tensleep Sandstone is not strong. In other areas (to the west) the Phosphoria Formation takes the stratigraphic position of the Park City Formation. The Phosphoria Formation characteristically has very little vegetation as compared with the underlying Tensleep Sandstone.

A series of linear features noted on the Skylab image at locality thirteen proved to be an area of minor faulting, again illustrating the value of space images for fault mapping.

At locality fifteen, four contacts are mapped. The contact between the Park City Formation and Dinwoody Formation is accurately mapped because gypsiferous units of the Dinwoody Formation have very high reflectance as compared with underlying beds of the Park City Formation. It is also

possible to pick both the lower and upper contacts of the major Triassic-Jurassic red-bed sequence. This sequence extends from the base of the Dinwoody Formation to the top of the Gypsum Spring Formation and includes Red Peak Formation, Crow Mountain Sandstone, and Popo Agie Formation, in addition to the units previously noted. The units contain red siltstones, sandstones, and mudstones; and, in the Thermopolis area, only the Dinwoody Formation could be distinguished from other red bed sequences. The Skylab map also shows a contact of Quaternary alluvium that is fairly accurate, but extensive deposits of terrace alluvium present in this area are not distinguishable on the photograph.

One of the most interesting features of Skylab mapping is the distinct tonal character shown by some shale units. The Cody Shale, of Cretaceous age, appears as a very light-bluish-gray unit on Skylab color photographs. The Cody Shale can be accurately mapped over much of its outcrop area by use of this distinctive tone. In some areas, where the Cody Shale is present, its bluish tone is distinctly darker so that identification is uncertain. In these areas the Cody Shale supports a relatively thick stand of grass and sagebrush. This is a good example of bedrock influencing vegetation, or an illustration of the fact that we must often map a rock-vegetation unit. Compared to the units that it contacts, the Cody Shale has a sparse vegetative cover. The typical vegetation is sage in bunches with little or no grass in association (Fig. 47). At localities marked sixteen the distinctive tone of the Cody Shale does not show on the Skylab color photograph although the Cody does crop out in this area. The tone of the unit is distinctly darker due to the more extensive vegetative cover. A thin soil has developed on the Cody Shale in these areas.

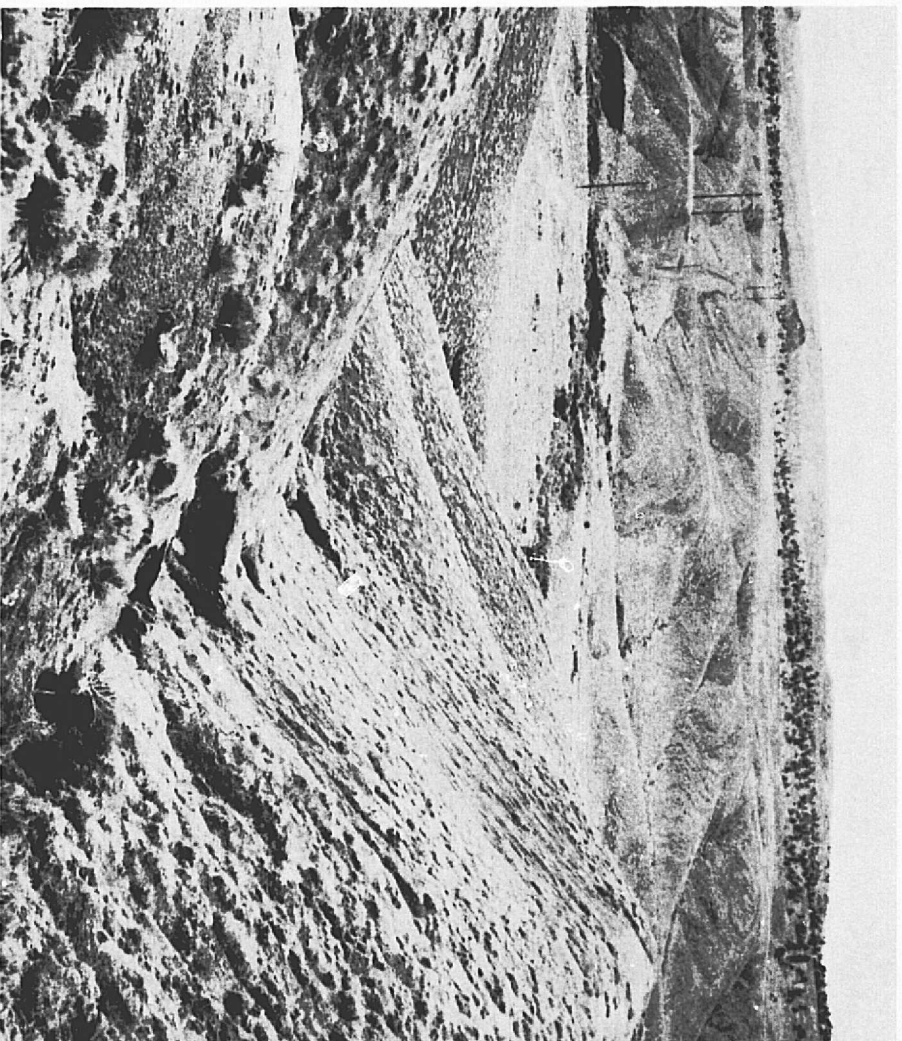


Figure 47. Field scene showing the peculiar distribution of sagebrush on outcrops of the Cody Shale.



The soil is derived from slope-wash from sandstones of the Mesaverde Formation and Frontier Formation exposed at higher levels. The soil supports grass as well as sagebrush; hence, the change in tone seen on the photograph.

At localities seventeen and eighteen, study of the Skylab stereo-images indicates that all beds dip toward the northeast. This proved to be a problem in interpretation of the structural geology, because the Mesaverde Formation, that overlies the Cody Shale, should lie in the axis of a syncline with southwest-dipping beds on the northeast and northeast dipping beds on the southwest (Fig. 48). This area has not been mapped in detail, but unpublished mapping by geologists of the United States Geological Survey suggests that the Mesaverde Formation is exposed in a syncline. This area was, therefore, checked in the field and it was determined that the sandstones of the Mesaverde Formation do, indeed, dip to the southwest on the northeast limb of the syncline. However, the dip reversal was so abrupt that it could not be detected on the Skylab photograph. Furthermore, beds of the Frontier Formation, that also should dip southwest, proved to be overturned by an unmapped thrust fault present on the west limb of the anticline. This illustrates both the problem with the resolution of Skylab S-190A photographs and the advantage of the space photography in drawing attention to areas where geologic mapping must be updated.

Locality nineteen is an area where pediment surfaces are well-developed but show no distinctive vegetation patterns and cannot be recognized on the Skylab photographs.

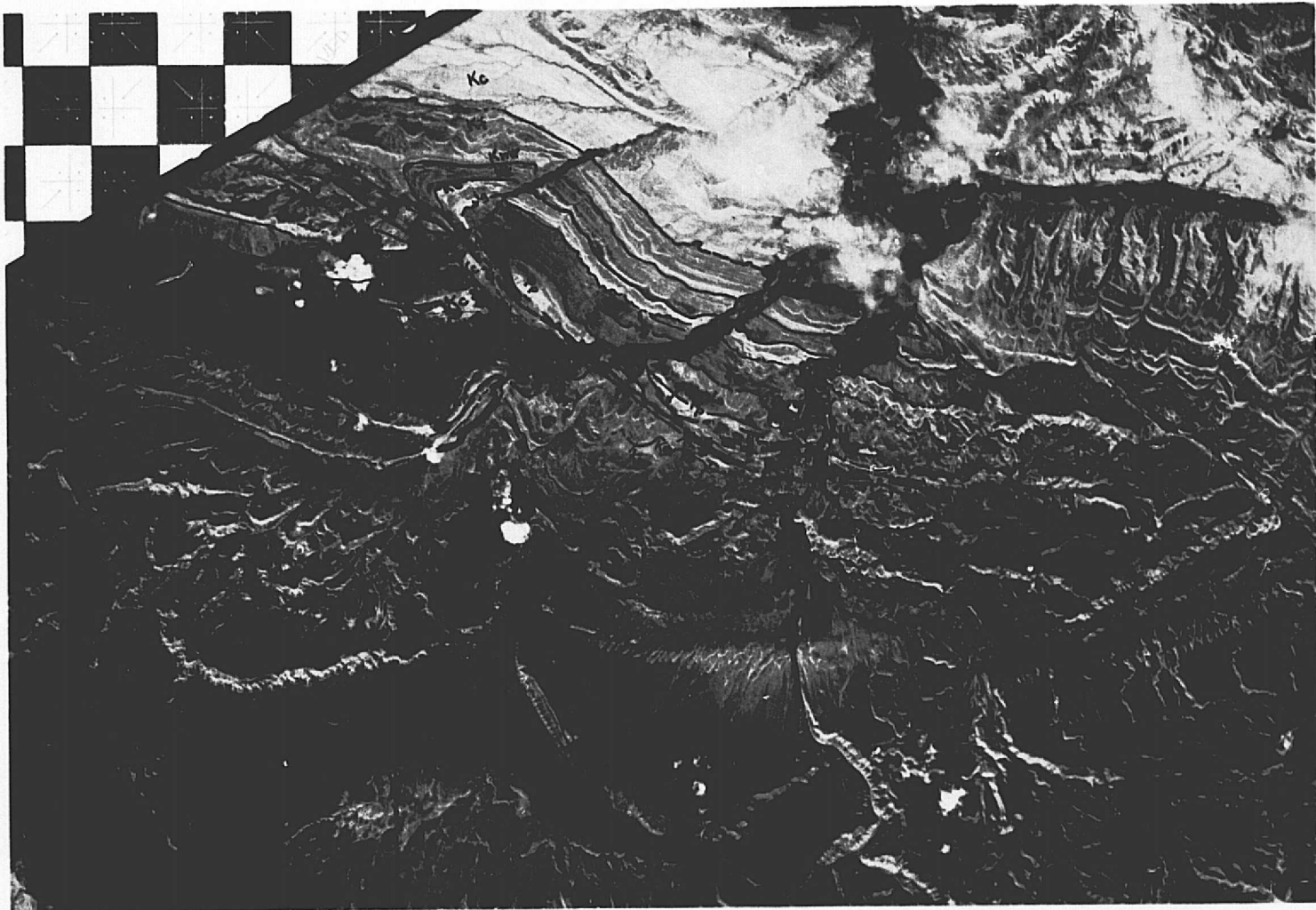


Figure 48. A detailed geologic interpretation of an area near Thermopolis, Wyoming (from Skylab S-190B, track 59, roll 88, frame 18, September 13, 1973).

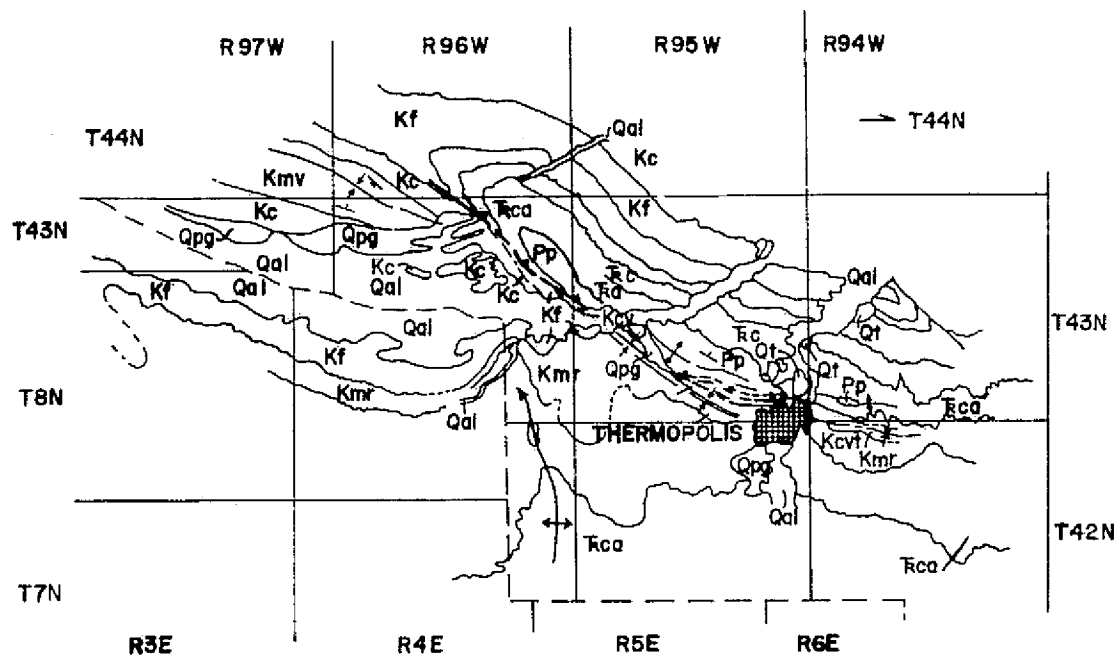
Locality twenty shows a linear feature that proved to be a sharp fold rather than a fault. This problem is a common one and is simply another example of a partial, but not critical, misinterpretation that is the result of a resolution limitation.

It was not possible to compare the Skylab S-190B photograph with S-190A because S-190B camera did not obtain stereo-coverage of this area. Some limited mapping was done on enlarged Skylab S-190B color photographs. An overlay was made from the Skylab S-190B interpretation. It compares to the geologic map with surprising accuracy.

As a further check on the mapping potential of Skylab S-190B photographs, a photograph of the Thermopolis area was enlarged to approximately 1:250,000 scale and used as a map base in the field. Figure 49 is a geologic map of a small area near Thermopolis, Wyoming made using this technique. The map is superior to available reconnaissance geologic maps of this area (compare Fig. 49 with Pl. 8 ) and was completed in approximately one and one-half days. Reconnaissance mapping is certainly one of the most useful features of the imagery. The Skylab base should be used in conjunction with a good topographic base at the same scale, and stereo-coverage should be used where possible.

#### Comparisons of Skylab, LANDSAT, and Aircraft Data for General Geologic Mapping in the Horn Area

A comparison of Skylab S-190B photography, LANDSAT multispectral scanner imagery, and high-altitude aerial photography was made to determine the importance of image resolution in geologic mapping from space imagery (Houston, 1973b). The test site was the Horn area or the east



Reconnaissance geologic map of Thermopolis, Wyoming area prepared with Skylab S-190B color photograph

Pp=Park City Formation  
Tca=Chugwater Formation and Alcova Limestone  
Kvt=Cloverly Formation and Thermopolis Shale  
Kmr=Mowry Shale  
Kf=Frontier Formation  
Kc=Cody Shale  
Kmv=Mesaverde Formation

SCALE  
5 4 3 2 1 0 5 10 MILES

Figure 49. Reconnaissance geologic map of a small area near Thermopolis, Wyoming. The enlarged S-190B photograph (Fig. 48) was used as a mapping base.

flank of the Bighorn Mountains (Fig. 50), where folded and faulted rocks of Paleozoic and Mesozoic age are partially exposed through a cover of Tertiary and Quaternary sediments.

Initially, a geologic interpretation was made from the LANDSAT data for a large area corresponding to the 1:250,000-scale Arinto map (latitude 43 to 44 degrees north, longitude 106 to 108 degrees west; see Houston, 1973b, p. 85). This map was compared to the Wyoming Geologic Map (Love and others, 1955) and was found accurate throughout most of the interpreted region. However, the structurally complex Horn area was not adequately mapped from the LANDSAT imagery.

A second interpretation of the Horn area was then compiled from the Skylab S-190 photography (Fig. 51). This interpretation shows that the Skylab S-190B photography offers significantly more geologic detail than does the LANDSAT image (Fig. 52). Much of the area not adequately mapped from LANDSAT was accurately mapped from the Skylab photo interpretation. However, even the high-resolution stereo photography from the S-190B camera was not sufficiently detailed to map the very complex structure near the south end of the "Horn". Consequently, the South Horn area was selected for more detailed examination via 1:120,000 scale color infrared aerial photography.

The resulting photogeologic interpretation (Fig. 53) yields detail comparable to 1:125,000-scale geologic maps (Hose, 1955; Richardson, 1950; Fig. 54). In a few areas the accuracy of the photogeologic interpretation is better than that of the detailed maps; but, in other areas (particularly those where vegetation is dense) the interpretation lacks the detail of the field maps.

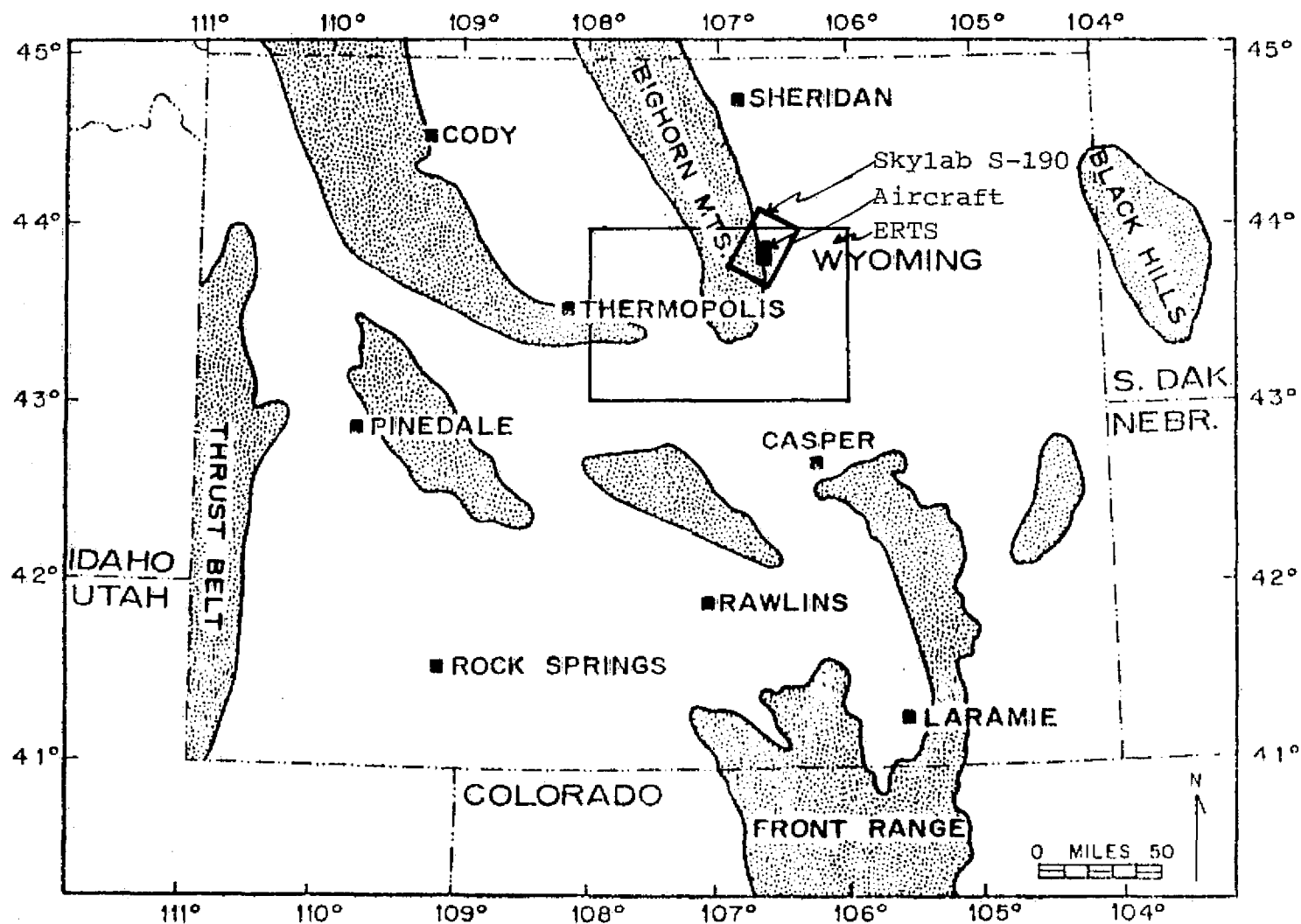


Figure 50. Index map showing the location of the three areas mapped from Skylab, ERTS (LANDSAT), and aerial photography.



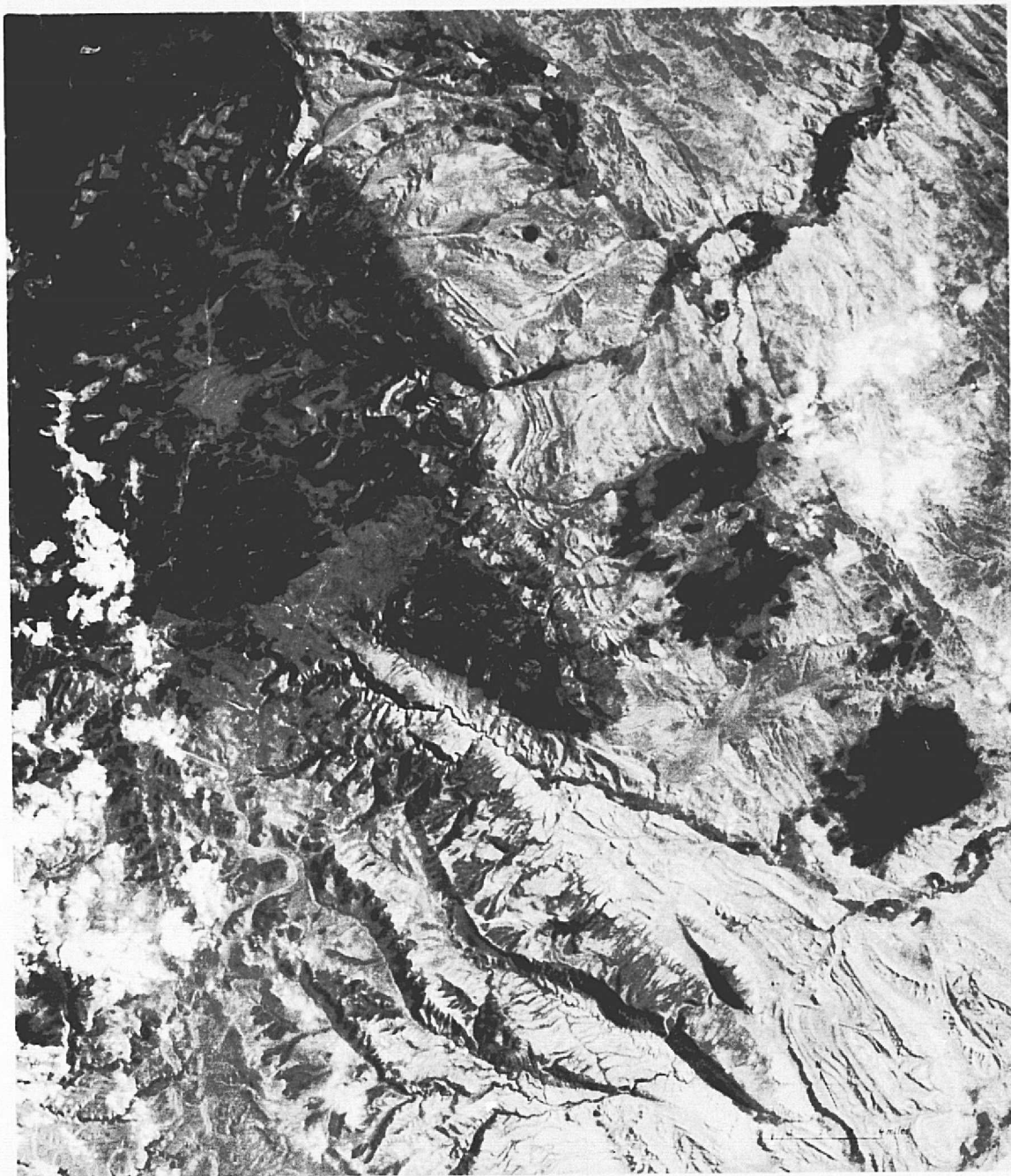


Figure 51. Skylab 190B photograph of the Horn area (roll, 82, frame 146, track 5, pass 10, June 13, 1973).

ORIGINAL PAGE IS  
OF POOR QUALITY

PHOTOGEOLOGIC MAP UNITS  
AND APPROXIMATE GEOLOGIC  
MAP UNIT EQUIVALENTS

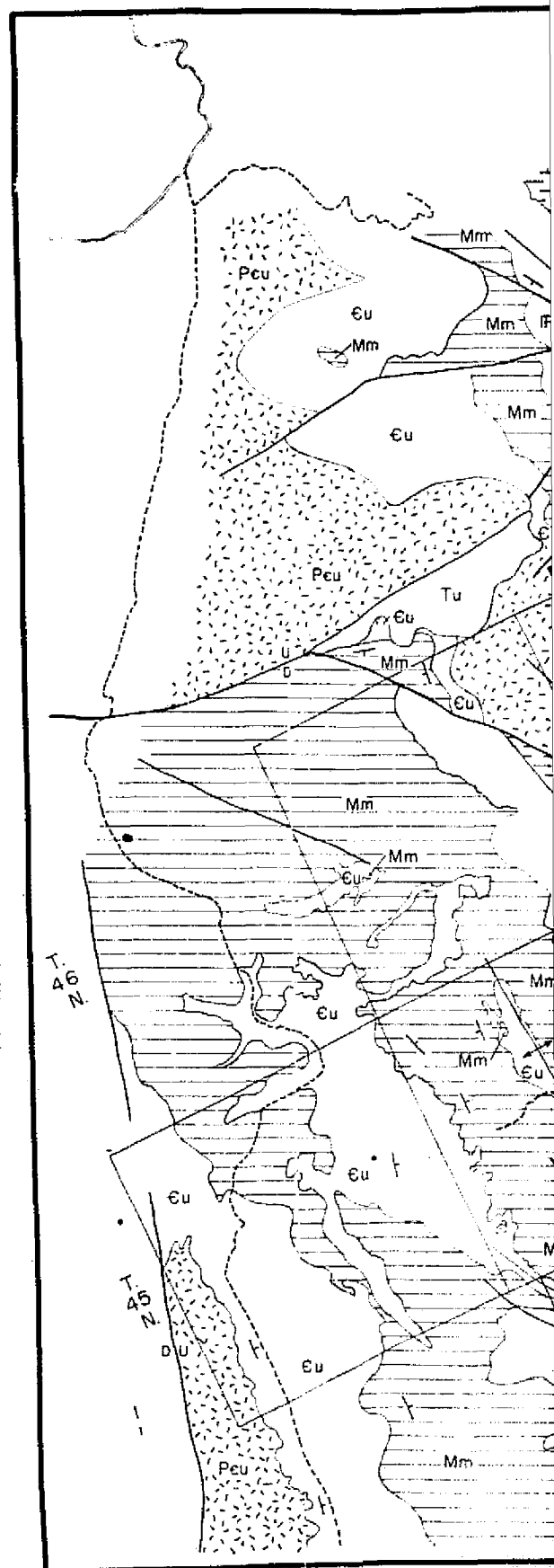
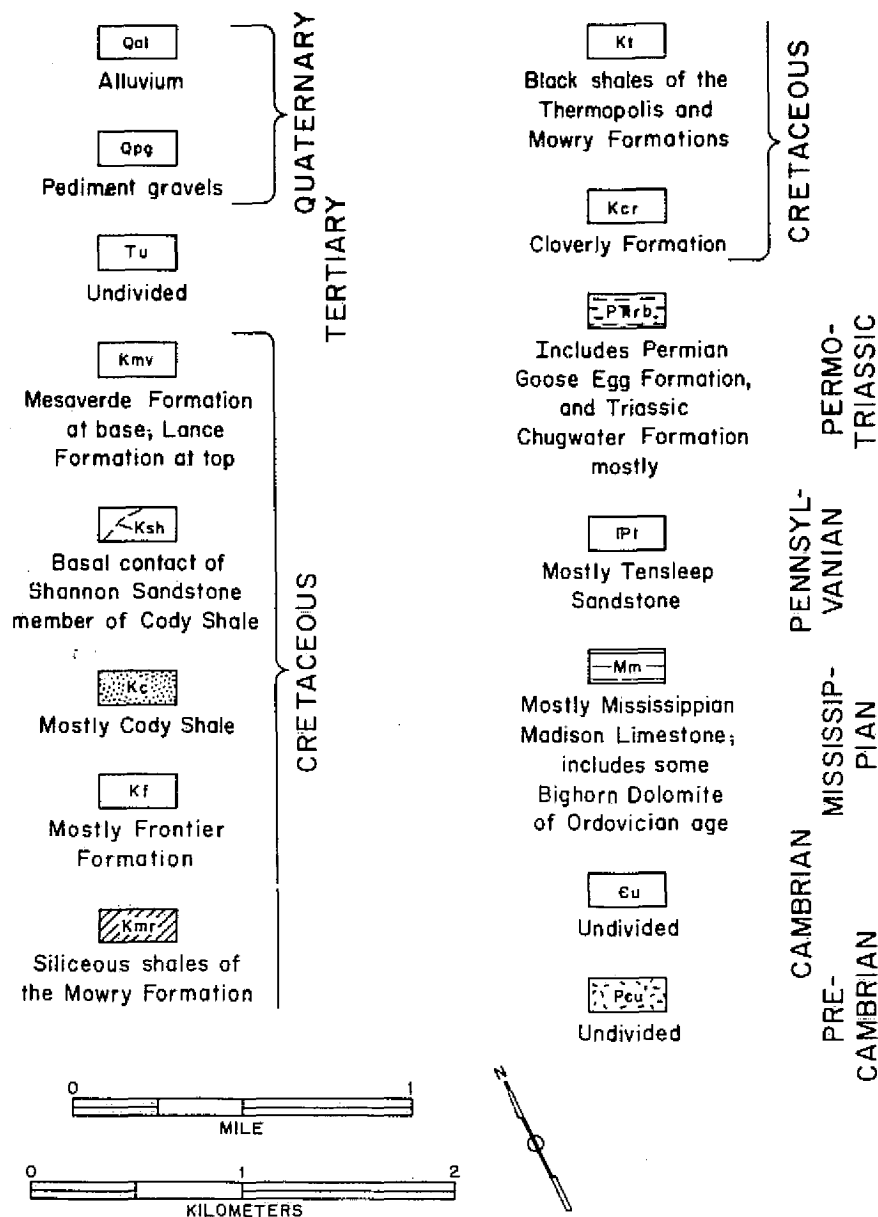
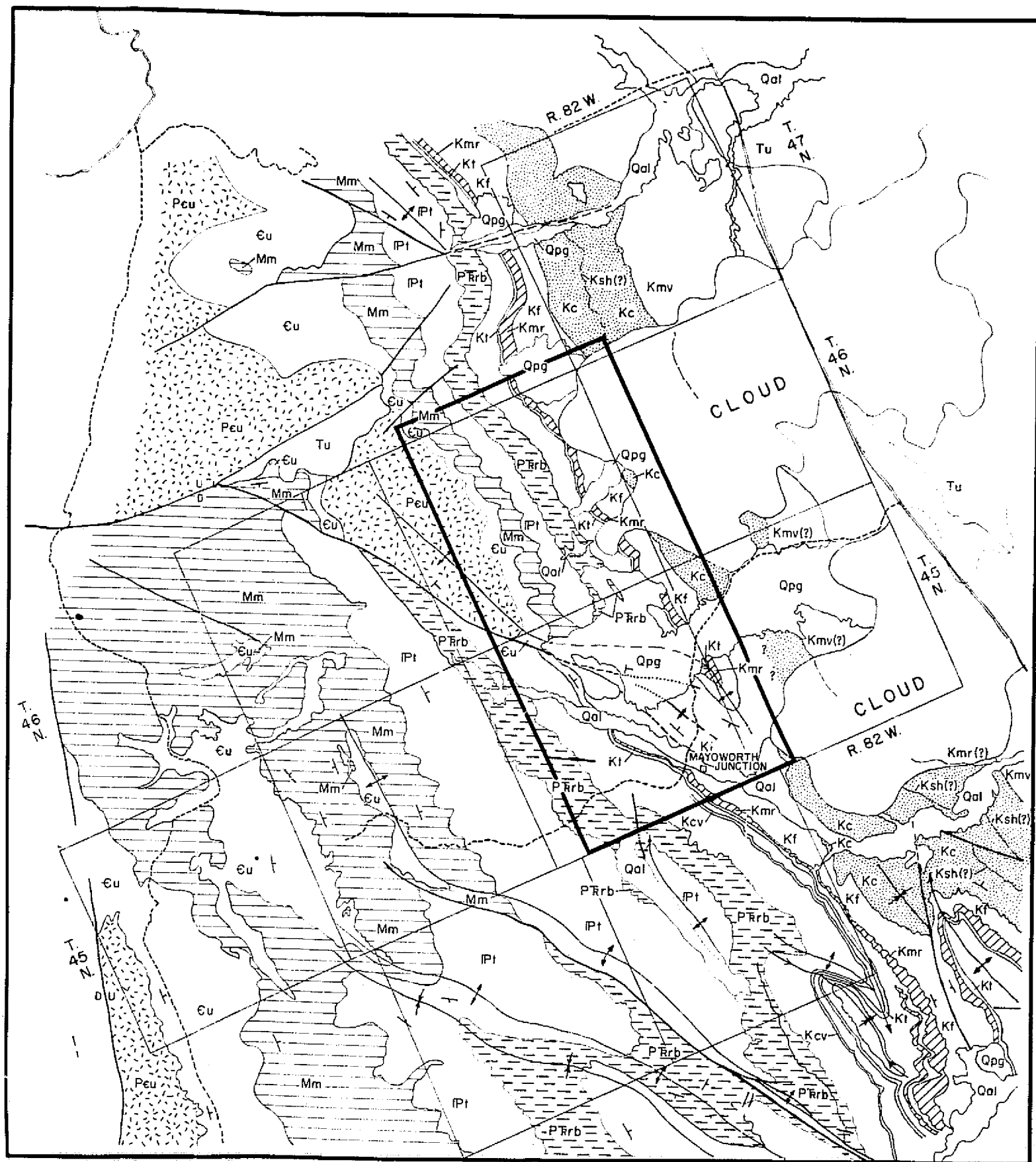


Figure 52. Reconnaissance geologic map of the Horn area from Skylab S-190B and Skylab S-190A photography.





PHOTOGEOLOGIC MAP UNITS  
AND APPROXIMATE GEOLOGIC  
MAP UNIT EQUIVALENTS

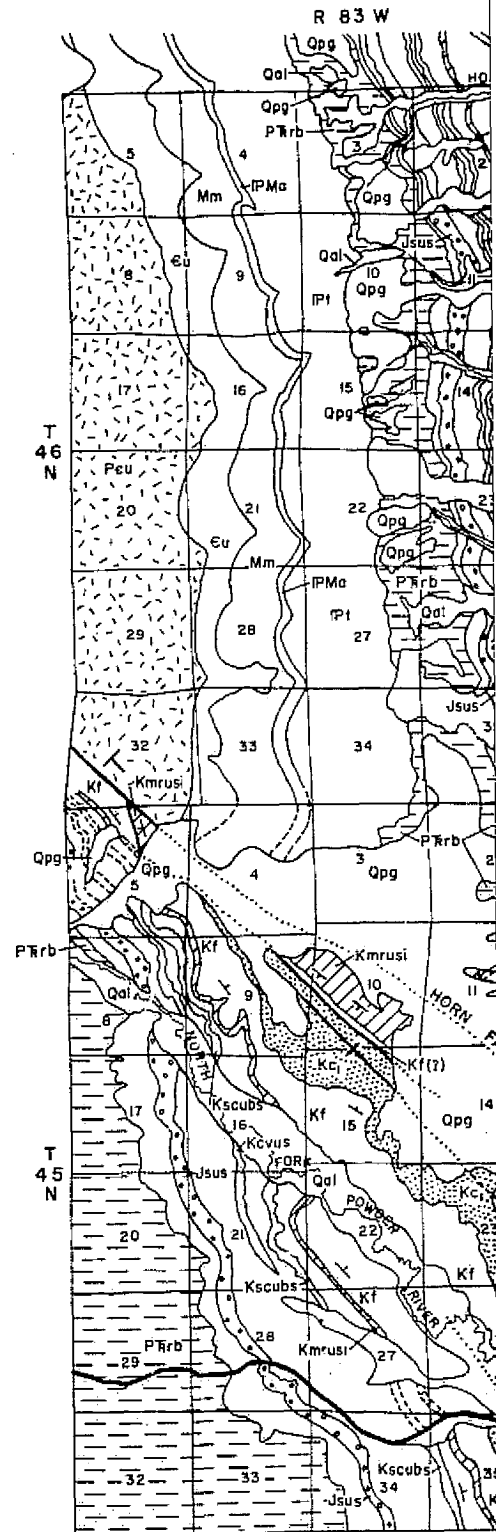
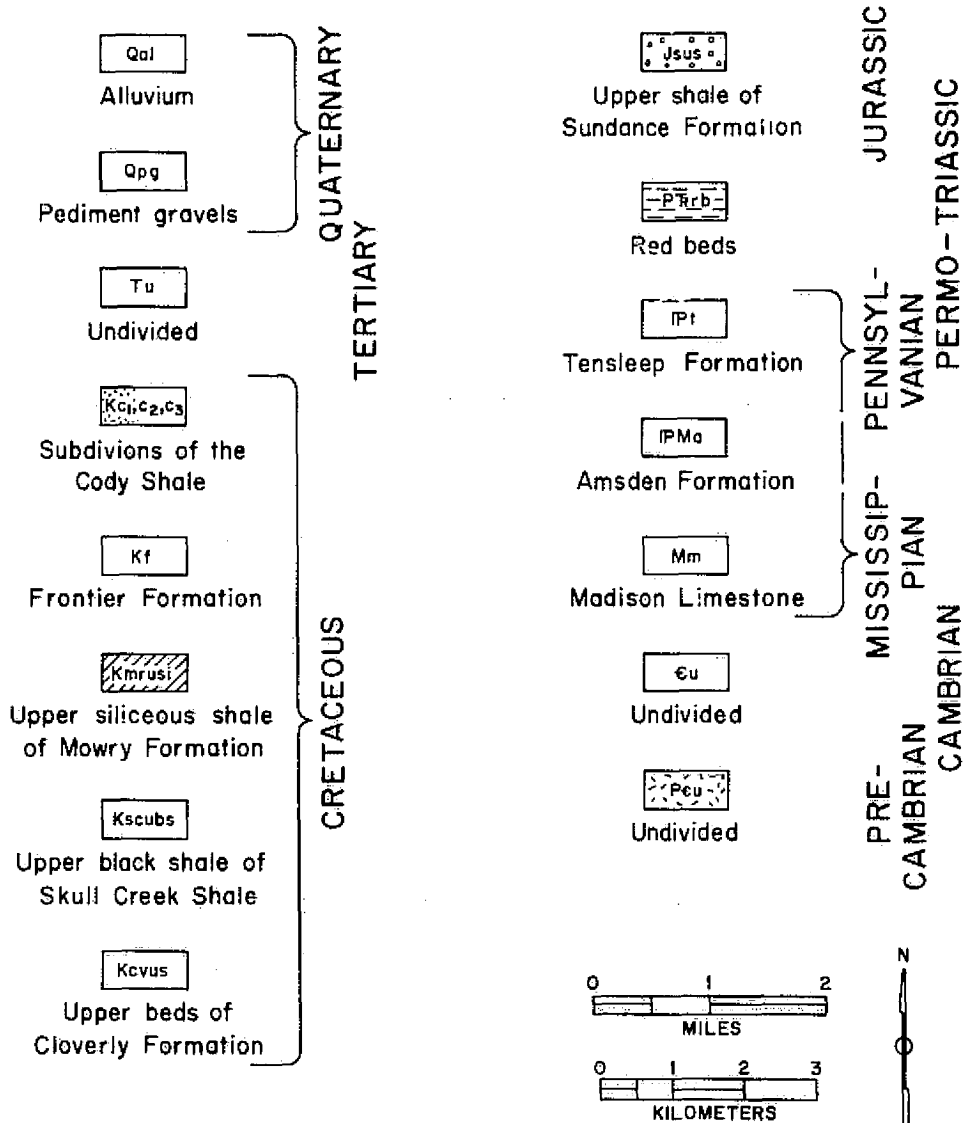
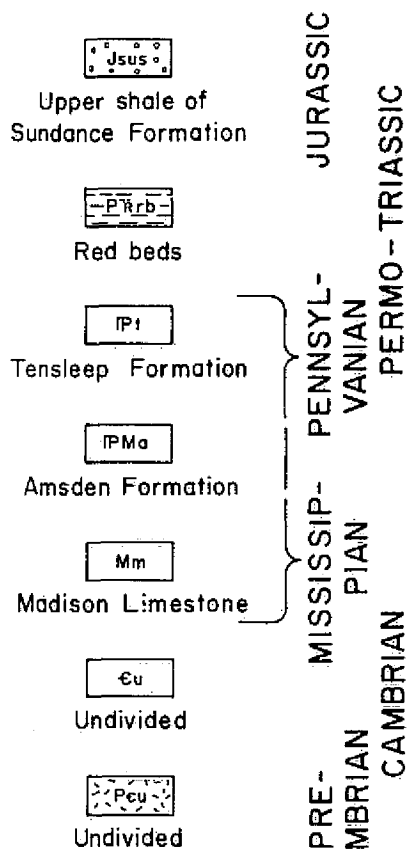
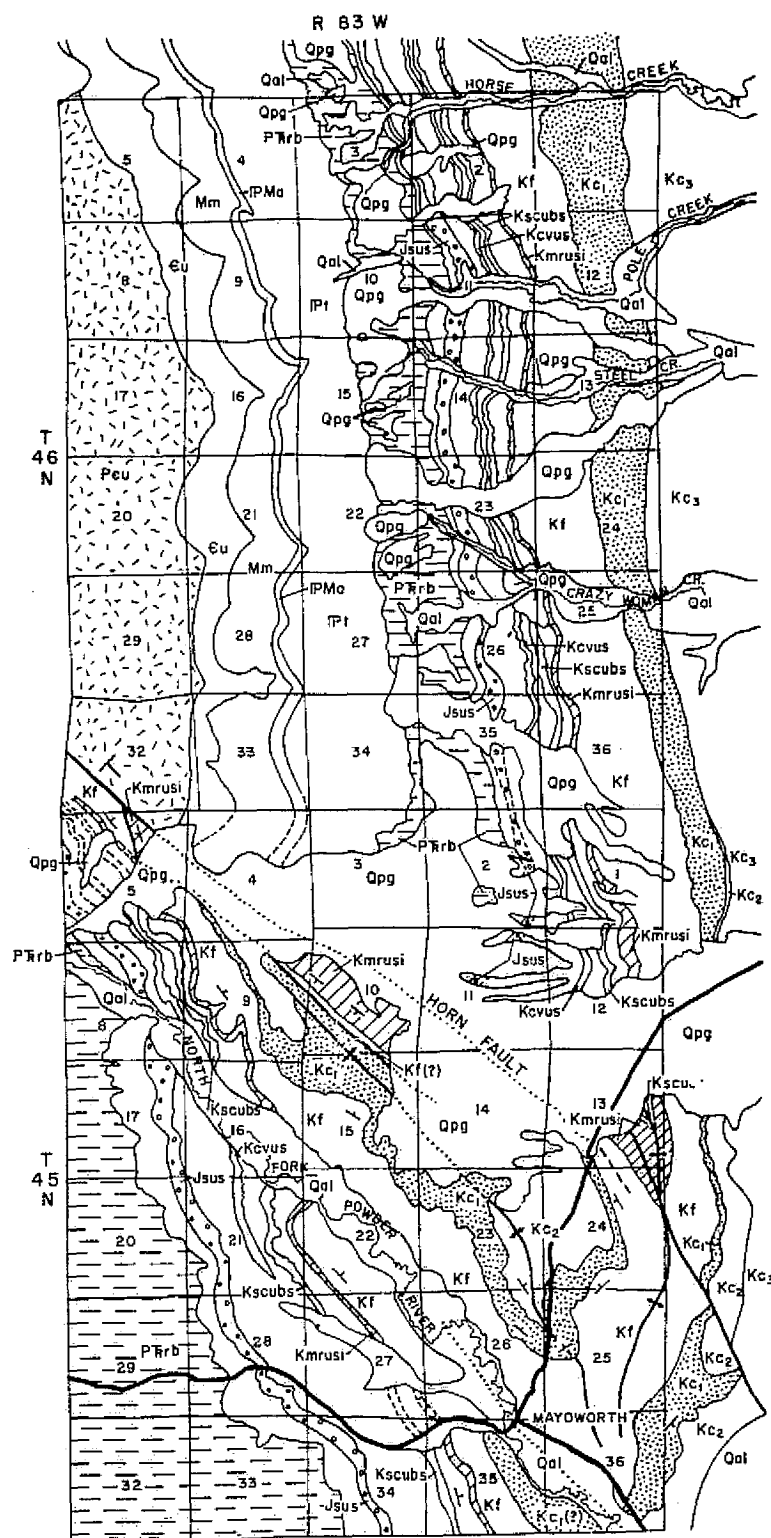


Figure 53. Photogeologic map of the Horn area prepared from color infrared aerial photography (NASA Mission 72-138, Sept. 10, 1972).

# MAP UNITS GEOLOGIC VALENTS



map of the Horn area pre-  
or infrared aerial photo-  
mission 72-138, Sept. 10.



# GEOLOGIC MAP UNITS

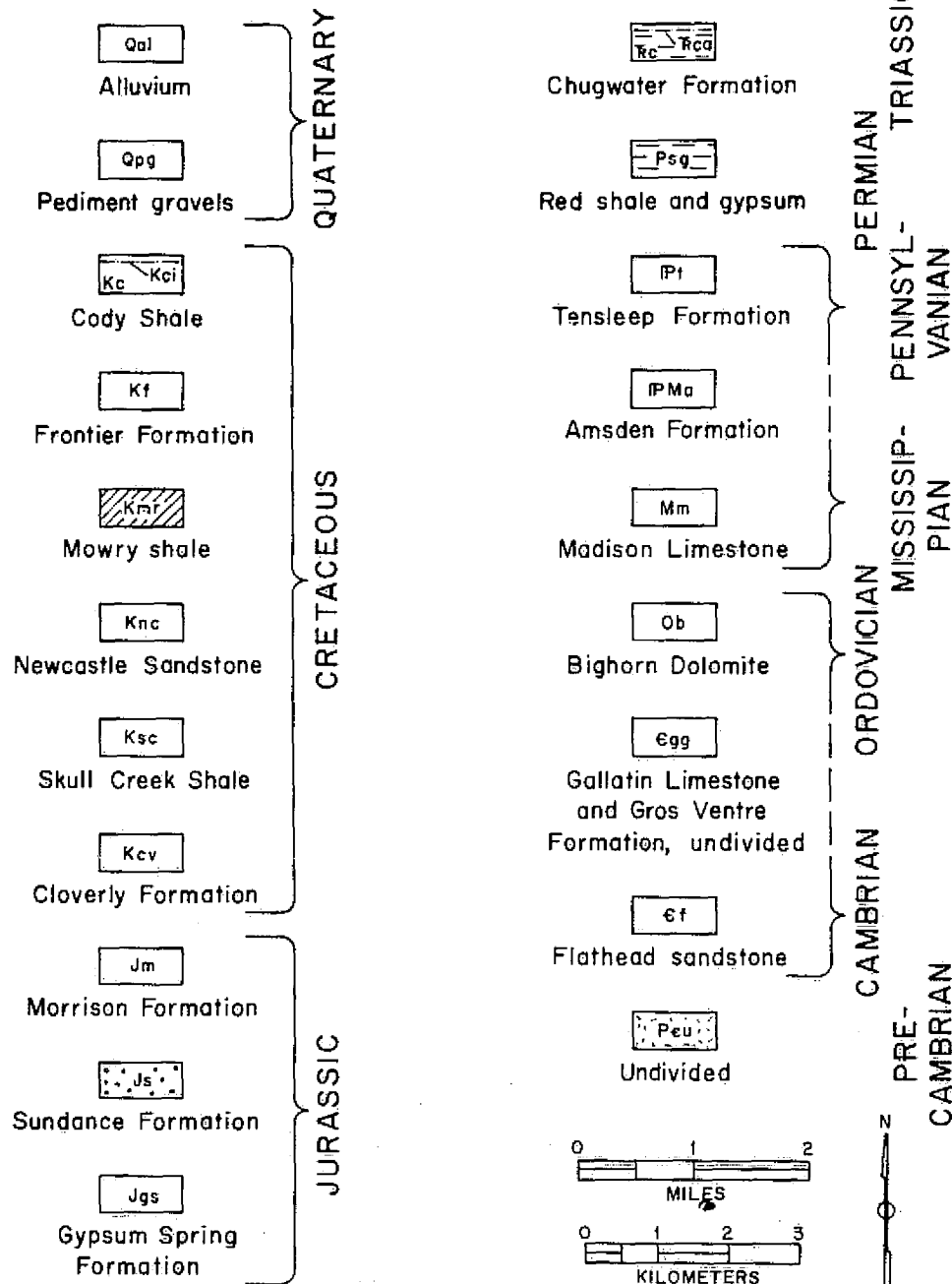
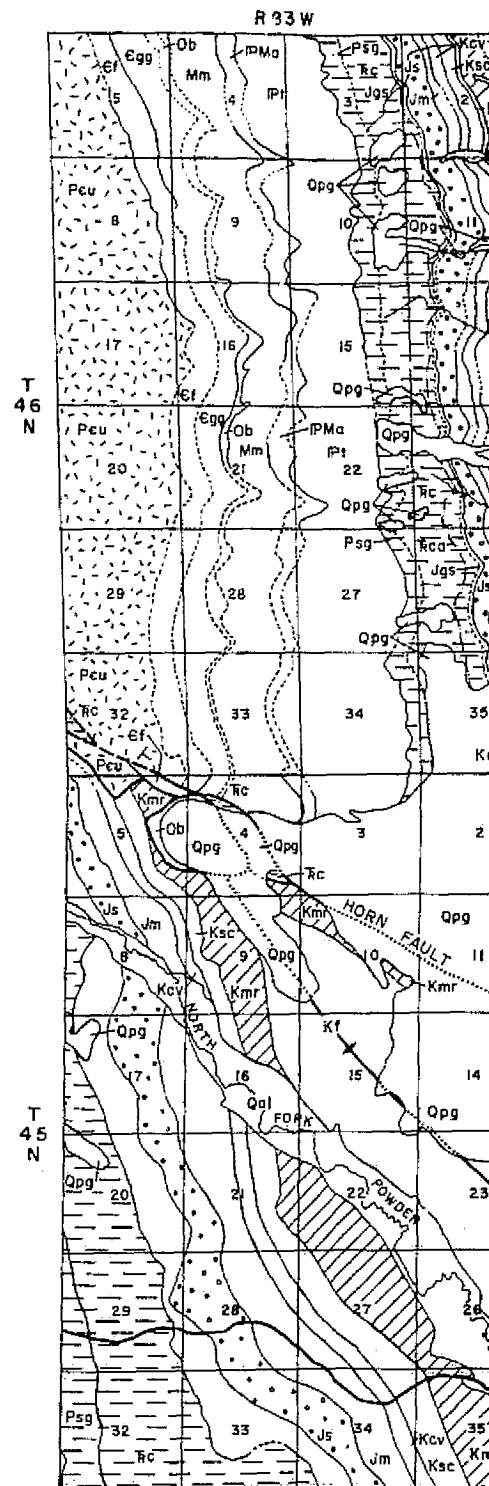
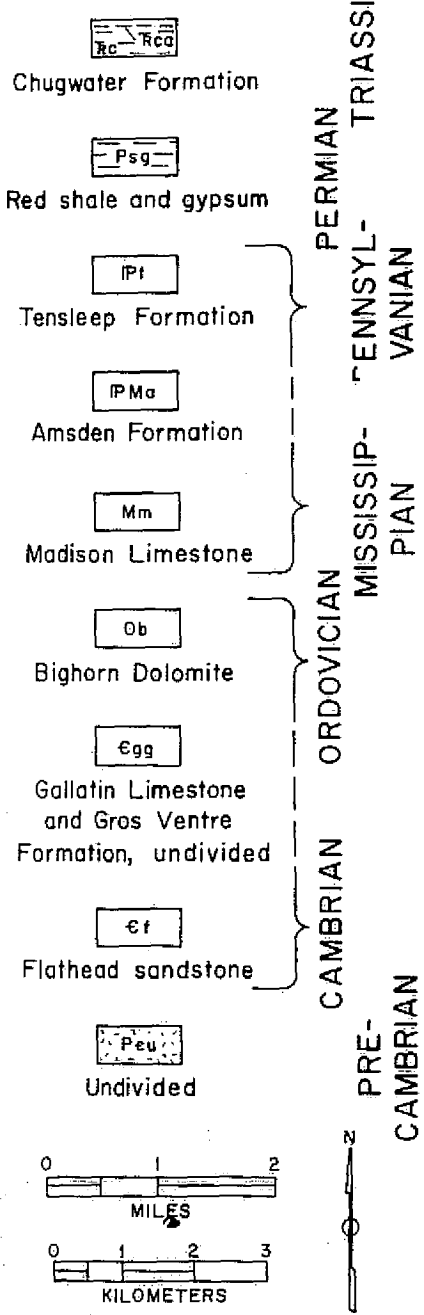


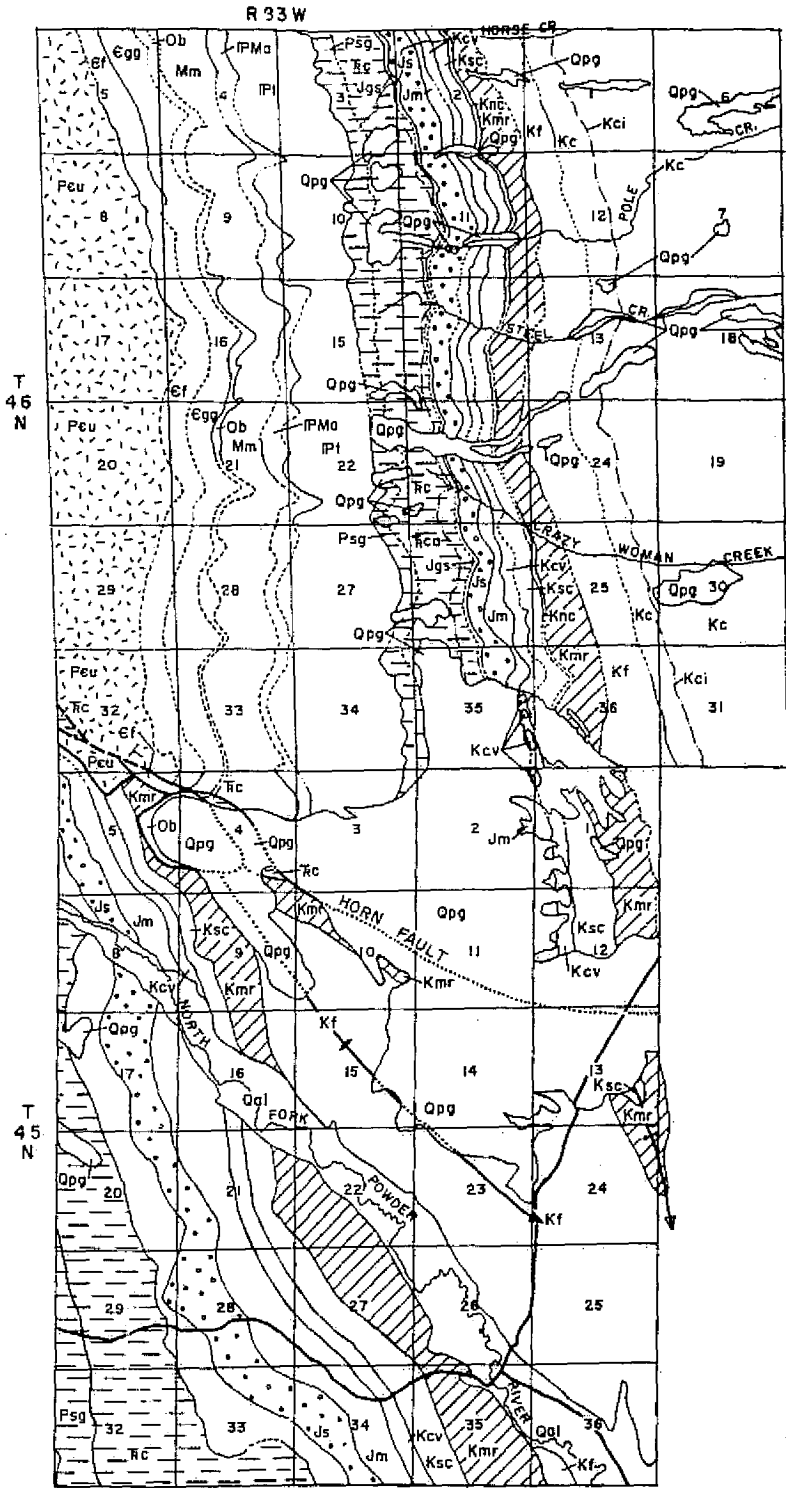
Figure 54. Field geologic map of the Horn area (after Hose, 1955 and Richardson, 1950).



UNITS



Map of the Horn area (after Chardson, 1950).



--	--	--	--	--	--	--	--	--	--

The results of this study suggest that the quality (accuracy) of a photogeologic interpretation hinges upon three main factors: 1) the image resolution and interpretability, 2) the geologic complexity, and 3) the amount of vegetative cover. Consequently, a new level of utility is achieved with each successively higher resolution imaging system.

However, in situations where image detail is adequate from the satellite sensor systems, an acceptable reconnaissance map is easily constructed from the satellite data; and the greatest mapping efficiency achieved by using the satellite imagery for the initial photogeologic compilation and the more detailed information, provided by aerial photography, supplements this interpretation in geologically complex or covered areas.

Stereoscopic presentation and rock color information are also important image qualities affecting the image interpretability. These qualities are advantageous in almost all types of geologic terrain.

#### Evaluation of the Skylab S-192 Imagery of the Hyattville Area

Skylab S-192 images were compared and evaluated for an area on the west flank of the Bighorn Mountains near Hyattville, Wyoming (Fig. 39). The major geologic structures in this area are a series of northwest-striking folds developed in Mesozoic and Early Tertiary sedimentary rocks. The eastern part of the Hyattville area is a series of westward-dipping hogbacks found in the Paleozoic sedimentary rocks.

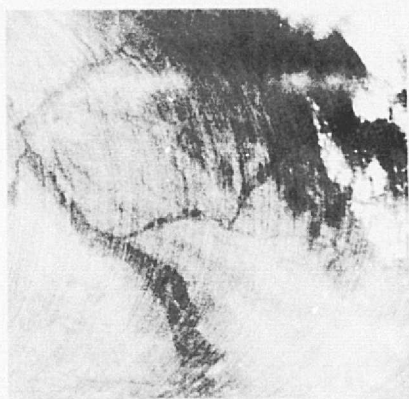
Evaluations and comparisons of the S-192 images were done both qualitatively (by visual inspection) and quantitatively (by densitometry).

Twelve of the thirteen S-192 bands (all except band 6) were available in image format for the Hyattville area.

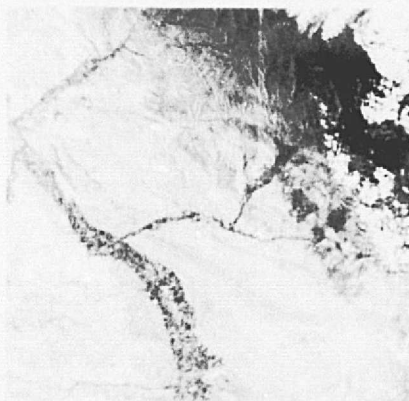
#### Qualitative Evaluation

Visual inspection of the S-192 images (Fig. 55) reveals band-to-band characteristics similar to those of S-190A photography; but the contrast between rock units is clearly greater in the infrared bands. The blue band (0.41-0.46) is the poorest of the twelve bands due to scattering of the blue light (haze) and noise in the system. The blue band is of very little value in mapping. The blue/green (0.46-0.51) is a relatively low-contrast image as predicted from the rock spectra (Fig. 45), but it does show red beds as distinctively dark. Carbonate rocks (Niobrara Formation) are the only rocks that are particularly bright in the blue spectral region. Band three (green, 0.52-0.56) is also a low-contrast band, as predicted from the spectral reflectance curves, but contrast is somewhat higher than in the blue bands. Red beds are very dark in this part of the spectrum (Fig. 45, Chugwater Formation). The green band is not well-suited to geologic mapping. Band four (green-red 0.56-0.61) is not very useful for geologic mapping because contrast between rock units is not strong in this spectral region, but the green-red band shows effects related to absorption by chlorophyll in plants. Contrasts in biomass are enhanced and structural features marked by rock units that have low or high biomass are enhanced. The green-red band appears to be most suitable for structural studies. Several small closed anticlines were noted on this band that were more difficult to detect on other images. Band five (red, 0.62-0.67) is a low-contrast image that is not suitable for geologic mapping in this area. Band six (red, 0.68-0.77) was not available for

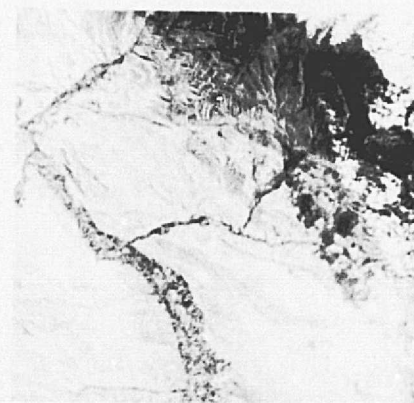




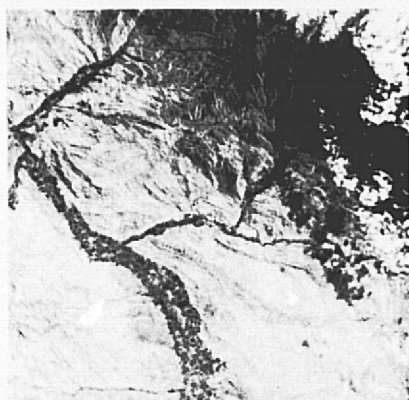
SDO 22 (0.41 - 0.46  $\mu\text{m}$ )



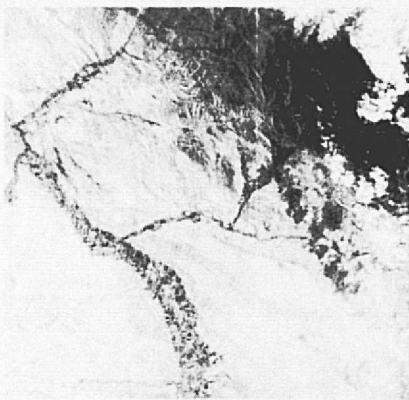
SDO 18 (0.46 - 0.51  $\mu\text{m}$ )



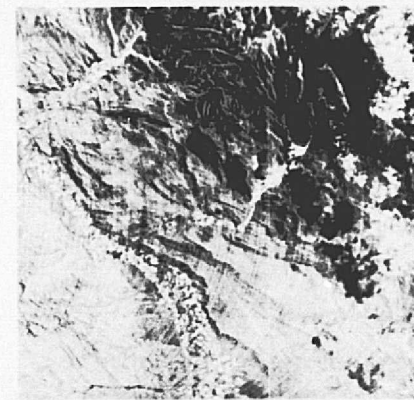
SDO 1 (0.52 - 0.56  $\mu\text{m}$ )



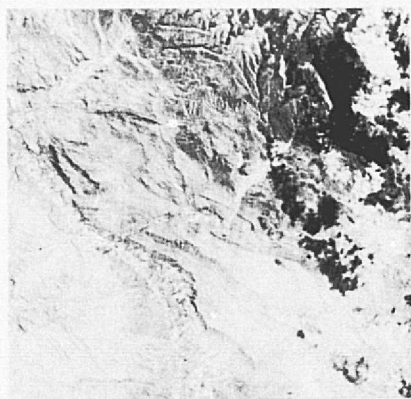
SDO 3 (0.56 - 0.61  $\mu\text{m}$ )



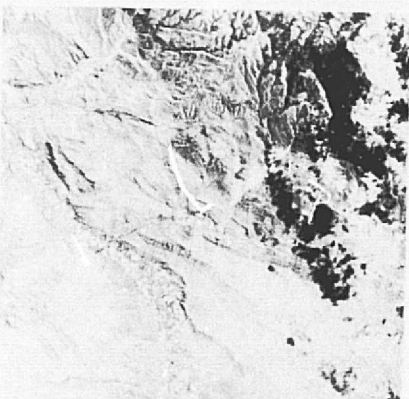
SDO 5 (0.62 - 0.67  $\mu\text{m}$ )



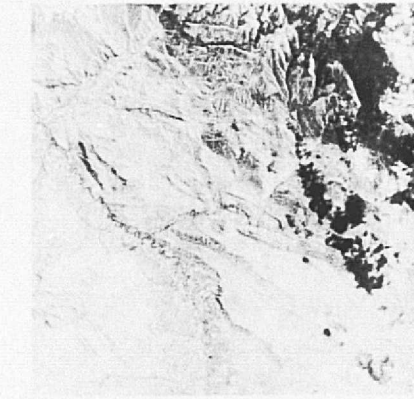
SDO 9 (0.78 - 0.88  $\mu\text{m}$ )



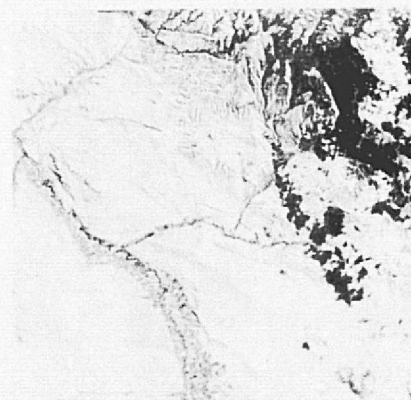
SDO 19 (0.98 - 1.03  $\mu\text{m}$ )



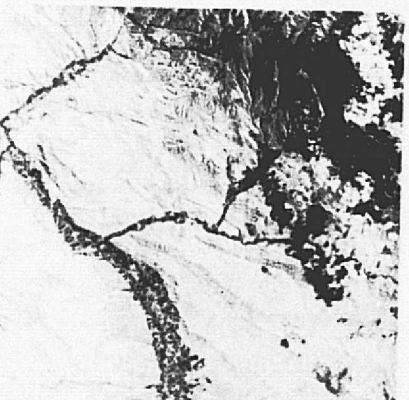
SDO 20 (1.03 - 1.09  $\mu\text{m}$ )



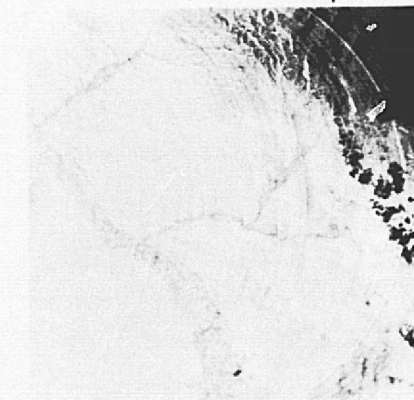
SDO 17 (1.20 - 1.30  $\mu\text{m}$ )



SDO 11 (1.55 - 1.75  $\mu\text{m}$ )



SDO 13 (2.10 - 2.35  $\mu\text{m}$ )



SDO 21 (10.2 - 12.5  $\mu\text{m}$ )

Figure 55. Skylab S-192 images of the Hyattville area. Note that the infrared bands show greater contrast than the visible bands.



evaluation, but would be expected to show particularly good information for mapping vegetation or rock-vegetation units. Band seven (0.78-0.88) was expected to be useful in detecting rocks rich in ferric iron due to the ferric ion absorption band in the 0.86-um range. The best test for this is the sedimentary red beds that contain ferric iron in moderate amounts. Inspection of these units on the imagery shows that absorption in this range is masked by the general increase in reflectance in the infrared. Visually, the red beds seem slightly darker in band 7 as compared with band 8, suggesting a slight change in reflectance. This effect might be useful in mapping ferric iron-rich rocks such as hematite iron formation; but the relatively small (<3%) concentration of ferric iron in red beds does not control the reflectance in this spectral region. Band 7 shows good contrast between most sedimentary rock units. This may be a characteristic of many of the near infrared bands where spectral response curves for a typical group of Wyoming sedimentary rocks (Fig. 45) and spectral response curves of other common rocks (Fig. 56) show greater differences in percent reflectance for the infrared region than for visible range.

Band eight (0.98-1.08 um) shows good contrast between most rock units. Band 8 records reflectance in a spectral region containing a ferrous iron absorption band that should be quite helpful in studying iron rich rocks such as pyroxenite, gabbros, or peridotites with abundant pyroxenes. Most sedimentary rocks are not characterized by high ferrous iron so this absorption band may not be particularly useful in the study of sedimentary rocks. A green sandstone of the Frontier Formation

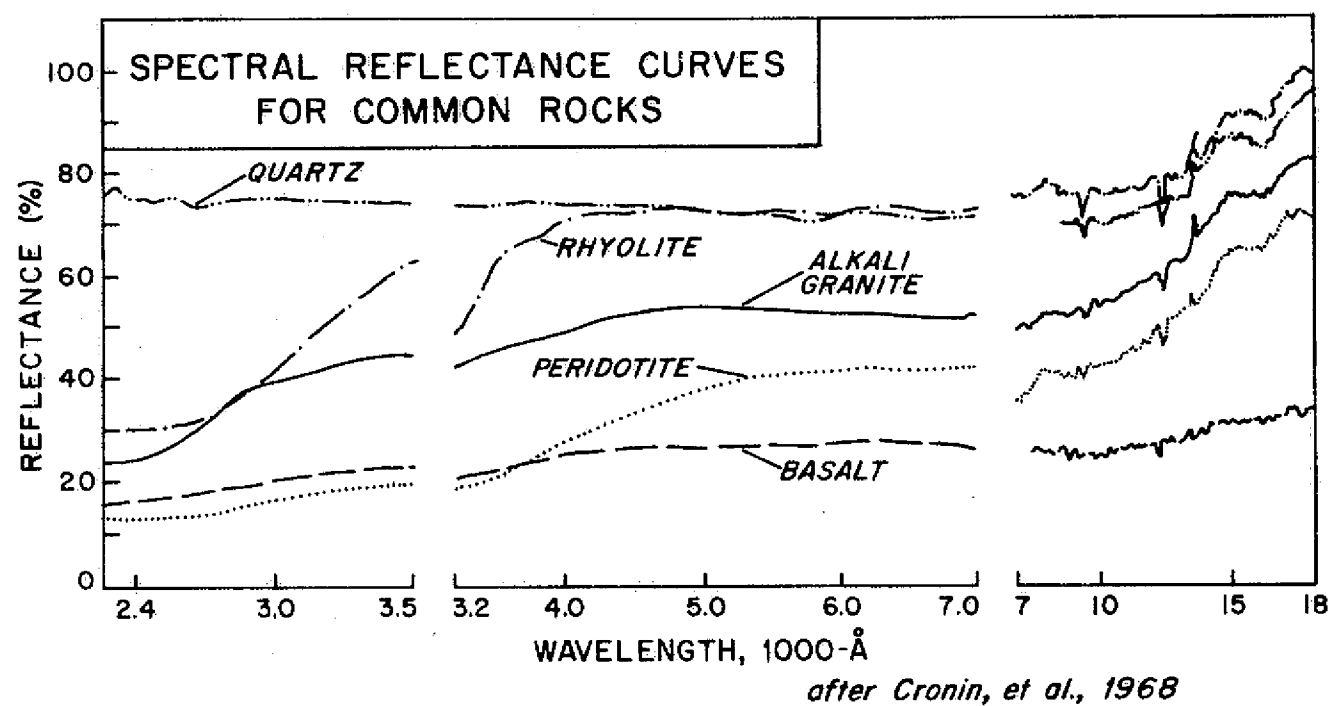


Figure 56. Spectral reflectance curves for some common rocks.

(Fig. 45) seems to show a spectral response suggestive of the presence of ferrous iron, but none of the sedimentary units in the test area are known to be rich in ferrous-iron, and none are enhanced in band eight.

Band nine (1.09-1.19  $\mu\text{m}$ ) shows excellent contrast between rock units and is useful for geologic mapping, but none of the common sedimentary rocks seem to have distinctive spectra in this range.

Band ten (1.20-1.30  $\mu\text{m}$ ) is quite similar to band nine in all respects.

Band eleven (1.55-1.75  $\mu\text{m}$ ) is in the spectral range where vigorous vegetation does not have high reflectance. Sedimentary rocks have good contrast but not as strong a contrast as in the 0.8-1.20  $\mu\text{m}$  range. Basically, the band 11 image is uniformly lighter in color for all rock units, a condition which may be due to the uniformly higher reflectance for almost all rocks in this spectral region.

Band twelve (2.10-2.35  $\mu\text{m}$ ) shows about the same characteristics as band eleven except that contrast is less and the image has an overall brightness greater than band eleven. Band 12 spans the 2.2  $\mu\text{m}$  region where altered rocks should show a reflectance low related to absorption by clay minerals. None of the rock units in the Hyattville area are particularly distinct on this band.

Band thirteen (the thermal infrared band) is uniformly bright and low contrast. The only features then that can be recognized are slopes of contrasting low and high emittance on hogbacks and in canyons. Low frequency noise is particularly bad on band 13.

Conclusions drawn from the qualitative evaluations of the S-192 imagery suggest only that the near infrared bands show higher contrast between rock units than visible and thermal infrared bands. No definitive conclusions were drawn as to what bands or band combinations would be most useful for geologic mapping.

#### Quantitative Image Evaluations

A quantitative analysis of the S-192 imagery was undertaken in an attempt to define the "best" bands and to construct color composites of those best bands for visual enhancement of lithologic contacts. The Hyattville area was chosen as the test site. In the quantitative analysis, film opacities were measured for fifteen geologic units along traverses intersecting twelve lithologic contacts. Differences of opacity were then used as contrast values for comparison of the different S-192 bands. The possibility for photographic enhancement of lithologic units depends upon the assumption that a rock unit will reflect in a unique spectral pattern which is different than that of neighboring units. The spectral pattern is recorded digitally by the S-192 system and reconstructed as separate images representing each of twelve different spectral bands. Any enhancement technique should maximize the difference in spectral patterns exhibited by neighboring units. There are two ways of doing this: 1) by computer manipulation of the digital data, and 2) by optical, or photographic manipulation of the imagery provided by NASA. A subsequent study has examined the relative contrasts directly from the digital data. The petrology of each rock unit is not the only factor controlling the

spectral reflectance pattern exhibited by the outcrop area of a rock unit. Other controlling factors are: 1) degree of weathering, 2) vegetation cover, 3) sun angle and azimuth, 4) viewing geometry, 5) slope angle, 6) temperature, 7) water saturation, 8) atmospheric conditions and the optical depth of the atmospheric column, 9) shadowing, and 10) the attitude of the outcropping beds (Houston and others, 1975, p. 104). Any analysis of multispectral images must consider these complications and should be accompanied by a field check of critical relations.

Visual enhancements are normally presented as color contrasts. Variations in color are dependent upon three psychological factors: hue, saturation of hue, and brightness. In making an additive color composite, these factors can be predicted by estimating the amount of each primary color present for a given unit in the three bands of the color composite (Wenderoth and others, 1974, Ch. 3). Thus, by taking any combination of bands of an S-192 image, a color composite can be formed whose colors can be predicted by measurement of the opacities on each band and careful control of the compositing process (Lauer and others, 1975).

Before constructing color composites, it is necessary to select appropriate bands to be used as components of the color composite. This was accomplished by determining the total geologic contrast exhibited by each spectral band and then selecting three of the higher-contrast S-192 bands representing broadly different spectral regions.

Relative opacity values were measured for fifteen lithologic units on each S-192 band. The opacity values were measured using a Spatial Data Systems video densitometer (Fig. 57). Figure 58 presents the data

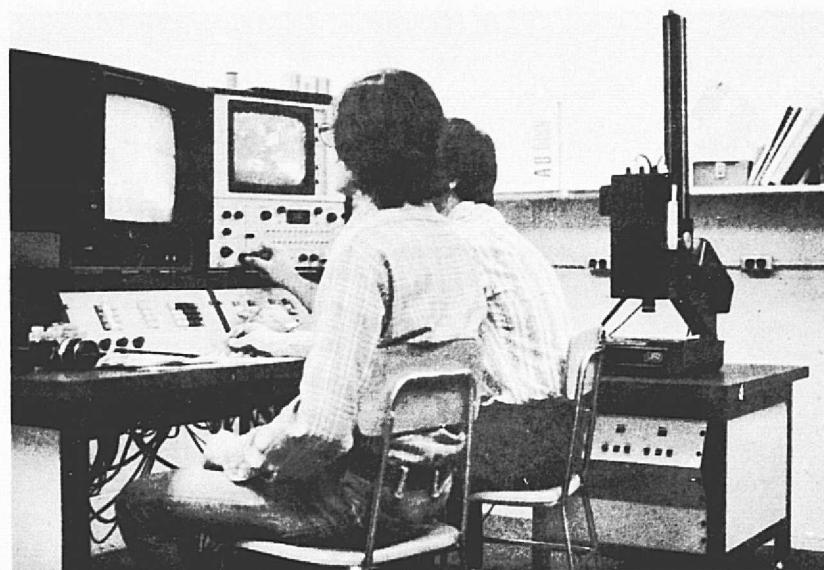


Figure 57. Photograph of the Spatial Data video analysis system used in making density measurements from the Skylab S-192 imagery.

ORIGINAL PAGE IS  
OF POOR QUALITY

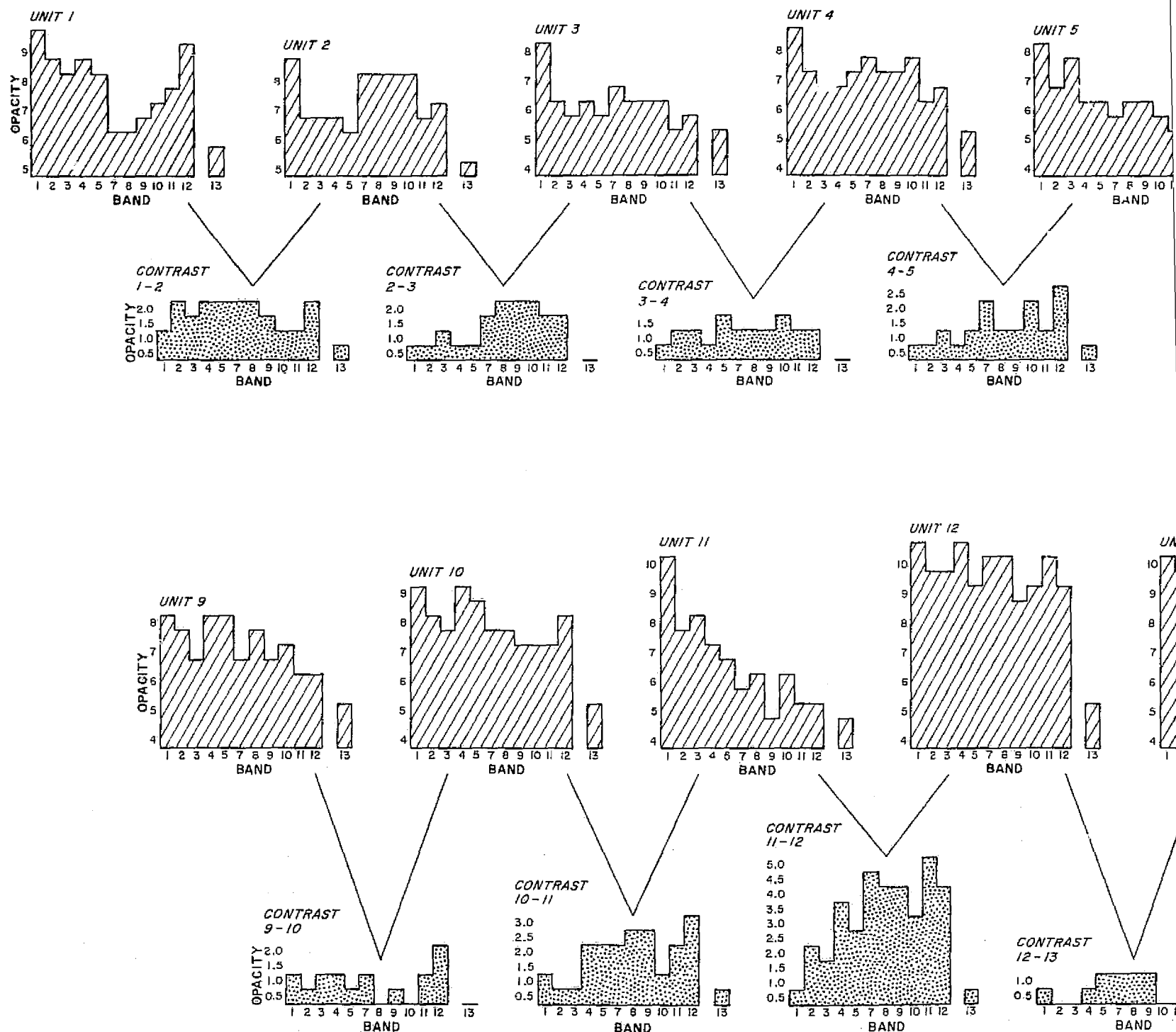
transmittance (the inverse of opacity) versus the band (wavelength) measured. The density contrasts between units are also plotted as histograms. Some units show clear patterns of changing density with wavelength (unit 11, for example); for other units, no strong spectral pattern is apparent.

The contrast values between units are consistently greater in the infrared range. Figure 59 shows summations of all contrast values for all fifteen units plotted by wavelength/band. The near infrared bands can clearly be seen to display the greatest total amount of contrast. The reason for this is not altogether clear, but the low frequency noise in some of the visible-range bands and in the thermal infrared band is at least partly to blame for their low contrast rating. The trend toward higher reflectance of rocks in the infrared spectral region (Fig. 56) may also be a contributing factor.

The densities for the various units are plotted for each band in Figure 60. Using these, one may predict the hue of a color produced by combining three of these in a standard additive color composite -- as shown in Wenderoth and others (1974). For example, if bands 1, 3, and 5 were displayed in primary colors blue, green, and red, respectively, the hue for unit 5 would be composed of:

Unit 5 = 8 blue + 7.5 green + 6 red (assuming saturation and brightness values are the same for each color) or 37.2% blue, 34.9% green, and 27.9% red.

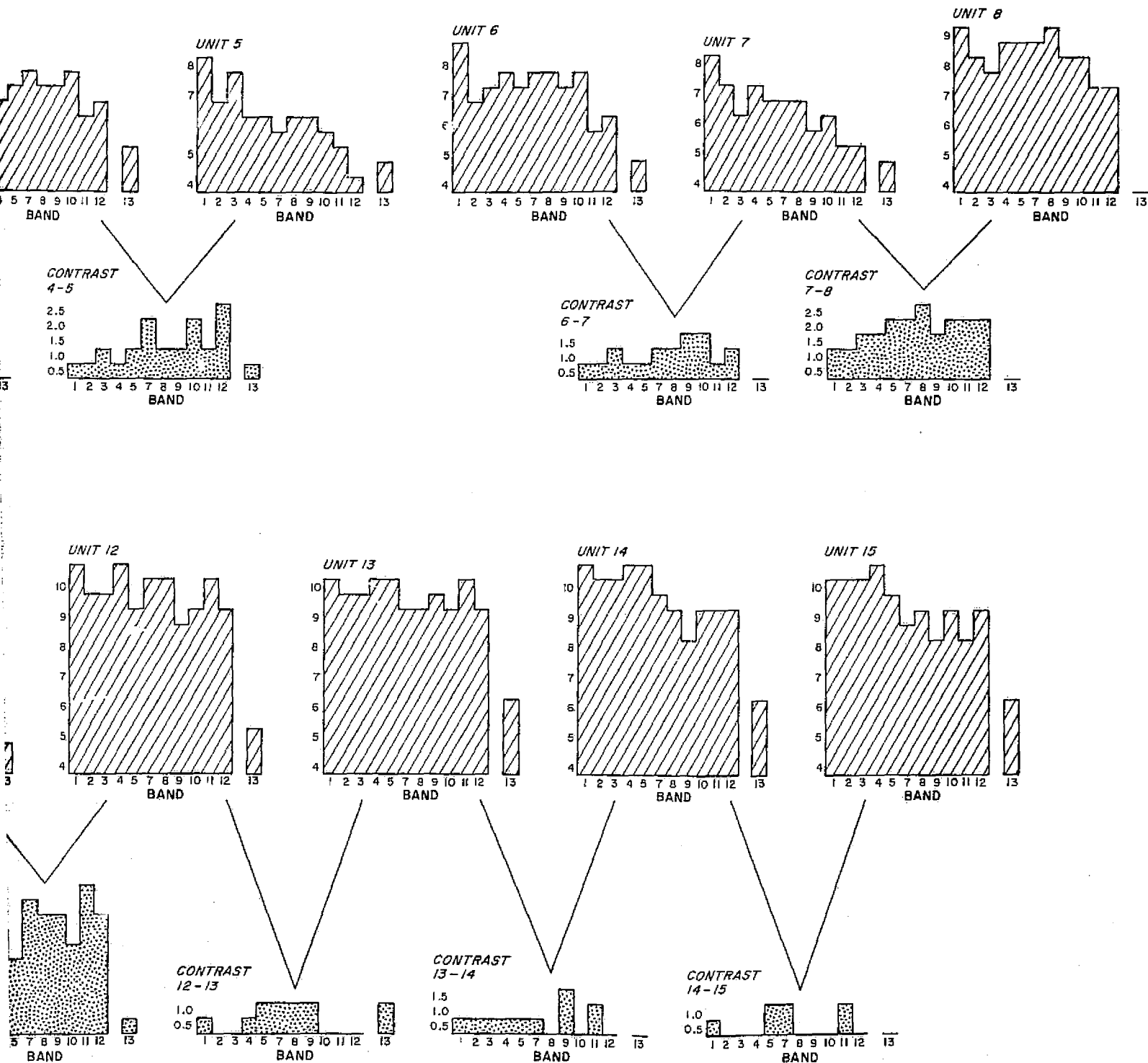
Using this procedure, the various bands were compared to identify band combinations where the density proportions for a rock unit differ greatly from the proportions for an adjacent unit. This contrast should



FOLDOUT FRAME

Figure 58. Histograms showing relative opacity and contrast for fifteen lithologic units cropping out

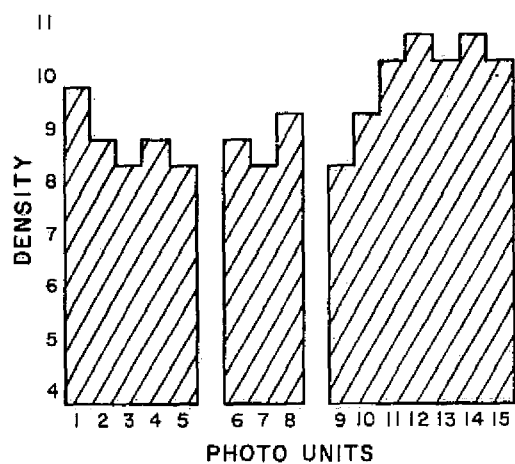




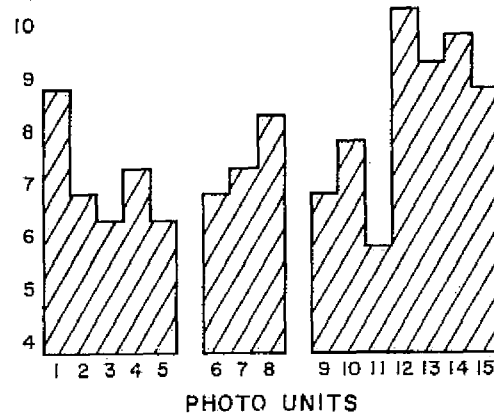
s showing relative opacity and contrast values of each S-192 image for  
ithologic units cropping out in the Hyattville test area.

**FOLDOUT FRAME 2**

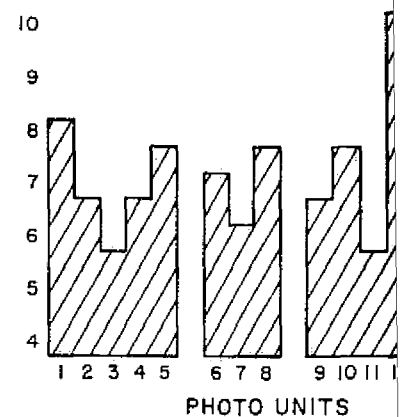
**BAND 1**



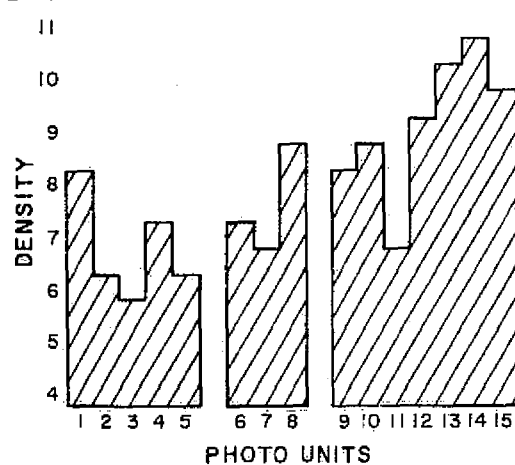
**BAND 2**



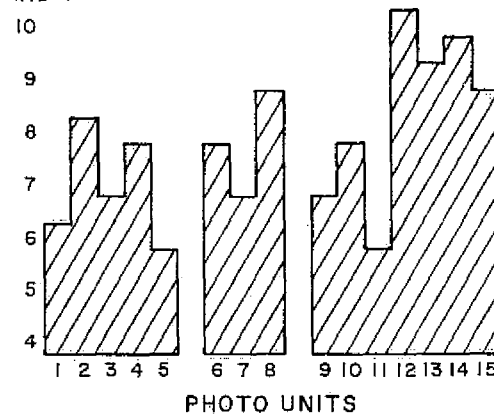
**BAND 3**



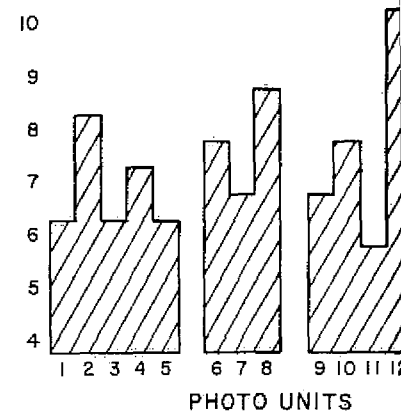
**BAND 5**



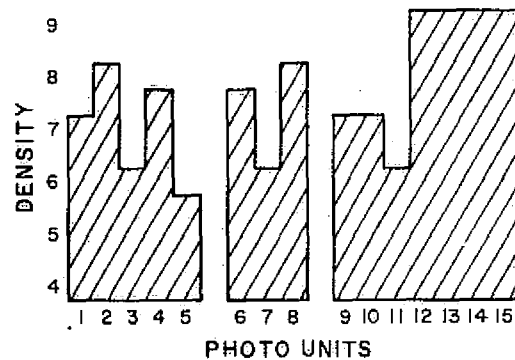
**BAND 7**



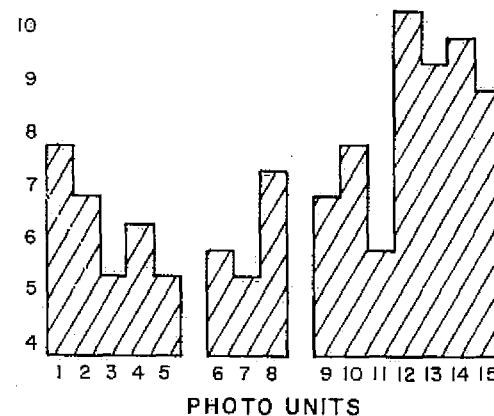
**BAND 8**



**BAND 10**



**BAND 11**



**BAND 12**

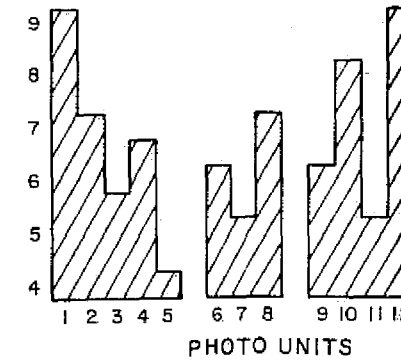
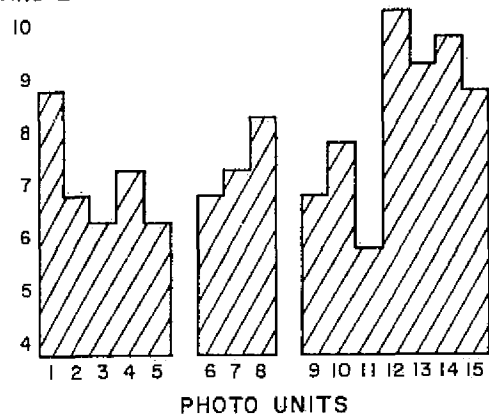


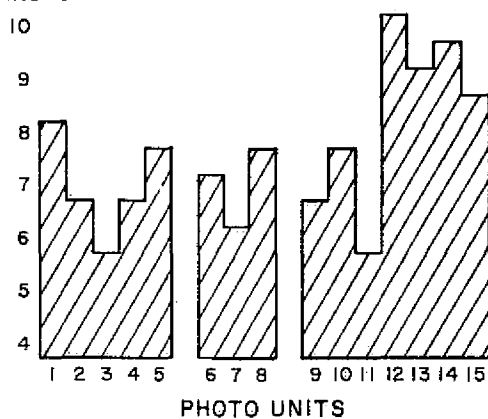
Figure 59. Summary histograms comparing total band-to-band contrast for lithologic units.

FOLDOUT FRAME /

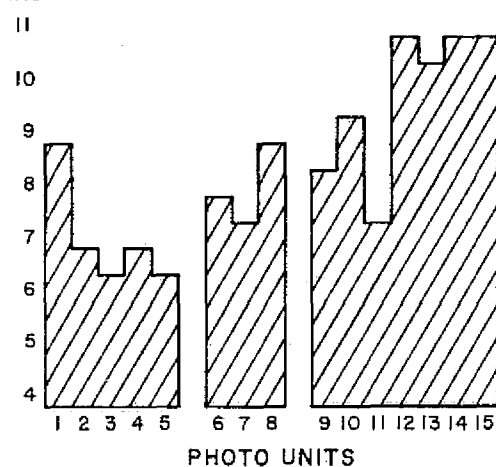
**BAND 2**



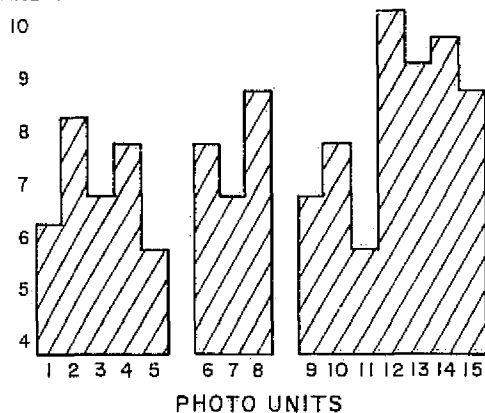
**BAND 3**



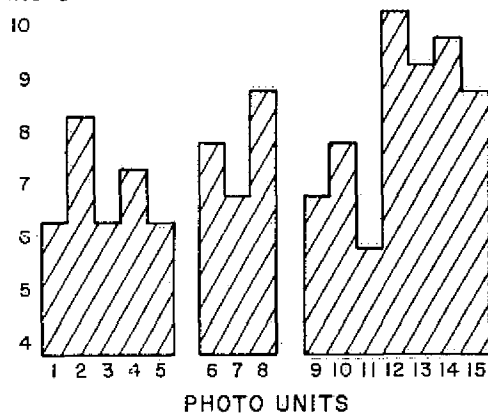
**BAND 4**



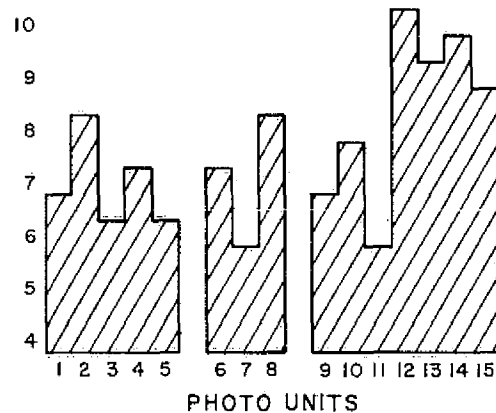
**BAND 7**



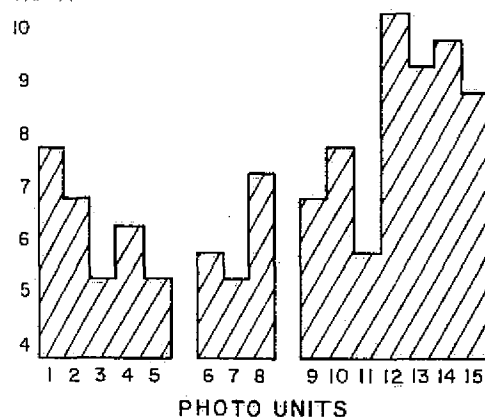
**BAND 8**



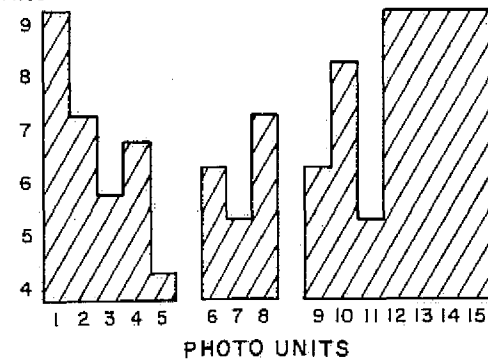
**BAND 9**



**BAND 11**



**BAND 12**



**BAND 13**

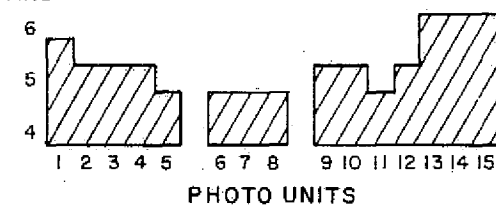


Figure 59. Summary histograms comparing total band-to-band contrast for all fifteen lithologic units.

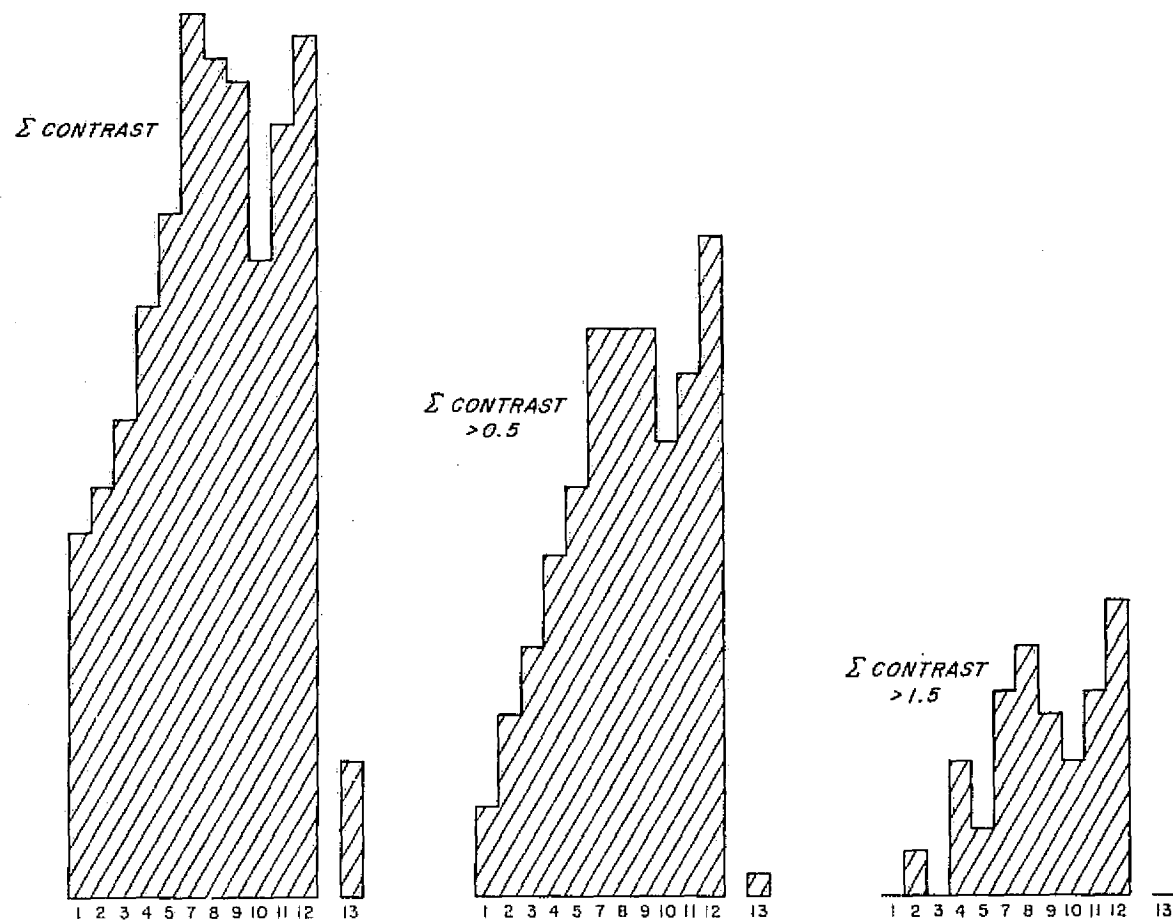


Figure 60. Histograms summarizing image opacities measured for each unit on each of the twelve available S-192 bands.

produce a difference in hue in a color composite. This procedure was attempted (Fig. 61) but the results were poor. The resulting diazo composites produced little (if any) enhancement of the lithologic contacts. Closer examination showed that none of the diazo duplicates recorded the full range of grey levels present on the original transparency imagery, and contrasts were generally reduced. This loss of contrast reduces the information content of each diazo duplicate such that the advantage gained in the color rendition was largely counterbalanced by the loss of contrast.

The value of densitometric measurements, such as those mentioned above, is that they provide relatively quick ways of comparing different multispectral bands, and also provide checks on enhancement techniques. Clearly the diazo composite method is not an optimum compositing technique. Alternate ways of constructing color composites (digital, optical, or video) are available and should serve to produce color enhancement, particularly if the raw data can be "contrast stretched" prior to compositing. The densitometric measurements are useful for predicting possibilities for enhancement of a given contrast by color compositing.

The densitometric analyses of the S-192 imagery confirm the results of the qualitative comparisons of the S-192 multispectral images. The near infrared images do have higher contrast than the visible and thermal infrared bands. The densitometric measurements also allow selection of "best" bands to be used either separately or in combination. For the Hyattville area bands 7, 8, and 12 yield the highest total contrast values (Fig. 59) but bands 9 and 11 are also relatively high contrast. All of

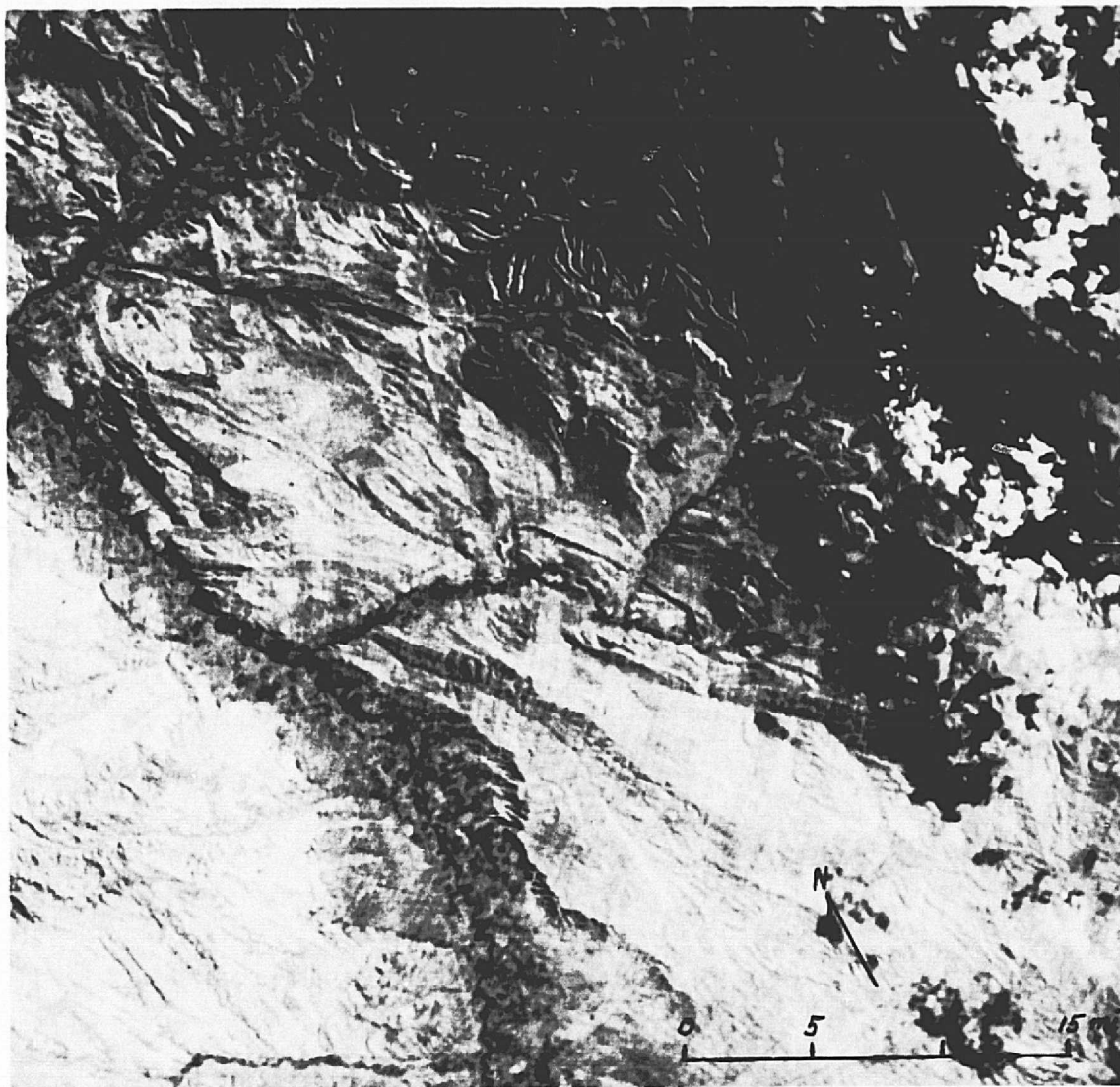


Figure 61. Diazo color composite from Skylab S-192 imagery of the Hyattville area. Contrast measurements indicate that the three bands used in this composite provide the best contrast between lithologic units. (Band 12=green, Band 9=red, Band 5=blue.

ORIGINAL PAGE IS  
OF POOR QUALITY

these "best" bands lie in the near infrared region. Three (bands 9, 11, 12) represent data in the spectral region beyond the LANDSAT bands and the photographic spectral range. Consequently, we may conclude that much of the best data for lithologic mapping is not recorded by LANDSAT or by any photographic technique.

This conclusion is left somewhat in doubt, however because the Skylab S-192 scanner data and the images used in this analysis have not been calibrated to a precise base level. Apparent differences in contrast may be the result of variations in the sensor sensitivity or of variations in film processing.

Contrast values recorded on computer maps printed from the S-192 digital data were correlated with the image contrast values to determine whether or not film processing errors are significant. Results of these comparisons are discussed in the following sections.

#### Digital Evaluations of S-192 Data

The digital computer analysis may be divided into four phases. The first phase consisted of developing and confirming computer programs to read the NASA tapes and dependably retrieve reflectance data from selected geographic areas. The second phase involved the production of computer alphanumeric maps with the on-line printer for each of the thirteen reflectance bands. These were verified by comparison with the photographic coverage of the same region. In the third phase, pair-wise clustering was studied from two-dimensional frequency histograms of sites sampled from the test region. Histograms for each of the seventy-eight pairs possible from the thirteen reflectance bands were visually inspected and

alphanumeric maps were prepared for the several pairs showing the greatest apparent clustering tendencies. The fourth phase consisted of applying R-mode and Q-mode factor analysis to the reflectance vectors in the test region and preparing alphanumeric maps of the weights on each factor.

Tape Read Problems. The decoding of the NASA tapes to obtain reliable data on the selected test region took much longer than was anticipated.

The data were furnished on two 7-track 800 bit/inch computer compatible magnetic tapes. The pre-processing (by Johnson Space Center) consisted of scan line straightening, GMT to scan line correlation and latitude and longitude to field of view labeling. Along with the tape 13 positive transparencies corresponding to each of the 13 scanner channels of the tape data were furnished. Also received was one data format control book (TR543).

Much of the data given in the Data Format Control Book does not specifically describe the computer tape, and much of the basic descriptive information that was supposed to be included on the tape was missing. Some of the ancillary data which was present also proved incorrect.

Approximately 40% of the information data block was missing. Only a small portion of this was pertinent to this geological mapping project. However, the missing data did cause some suspicion concerning the accuracy of the reflectance data. Of the data not included, which was of importance in mapping, was the scanner calibration information. Also missing



were the start and stop locations (bytes) of test calibration data points. No indication was given on the tape or in the data format book concerning the presence or lack of calibration, or scaling gain or bias factors. This scanner calibration, which by all indications in the format book had to be present but was not present.

This lack of information led to uncertainty concerning 1) the actual starting location of the data sets, 2) the location of this information within the reflectance data, and 3) how many bytes of test data were present. The importance of knowing the starting locations of the data set can be appreciated when one realizes that calibration data is visually indistinguishable from true reflectance values.

Also, when combining different reflectance sets, information concerning the range and scale of values is helpful. The problem of scale becomes obvious when one compares the reflectance values from the one data set which was repeated on the tape. Both normal- and half-resolution values were furnished for the thermal infrared band (10.2 - 12.5  $\mu$ ). Upon inspection of this band, it becomes obvious that one of the data sets is comprised of values consistently 30% greater than the values for the other corresponding data set. No indication of differing calibration or scaling was provided. Clearly, one of the two bands was not a true representation of scene brightness.

One other difficulty was the problem of precise registration of the or more data sets (pixel to pixel) for interpretation or manipulation. The registration was complicated by the original tape formatting. The 13 distinct bands were grouped together by scan line. Each group includes a short ancillary information data set. In addition to the two differing resolution types (one comprising twice the number of points as the other

set), there are three different starting locations for reflectance values within each scan line set.

Digital enhancement involves alignment of corresponding data from different energy levels (light frequencies) so that one can emphasize different data, or data trends which aid in distinguishing features of (geologic) importance. To compare different data sets, exact alignment of corresponding ground locations represented by the data must be made for different bands. Registration proved to be difficult due to the different resolutions and the noncorresponding starting locations.

Alphanumeric Maps. Alphanumeric density level maps were prepared for each reflectance band and were compared with the image representation of the band provided by NASA. These density maps generalized the reflectance data into 26 discrete brightness levels so that observed patterns could be directly correlated with the image patterns. However, they provided no substantial improvement in interpretability of the S-192 data. The density level maps did allow a roughly quantitative check of brightness contrasts across known geologic contacts. Therefore, they served as a check for the image contrast determinations made via image densitometry. The digital maps confirmed the contrast relationships measured from the S-192 imagery.

Pair-wise Visual Clustering. Let  $R_{ip}$  and  $R_{jp}$  denote the reflectances in the  $i$ -th and  $j$ -th bands respectively for the  $p$ -th pixel (or site). The interval  $(\min_p R_{ip}, \max_p R_{ip})$  was divided into a reasonable number of sub-intervals. Similar sub-intervals were laid out for  $R_{jp}$ . Finally, the

reflectance values for each pixel were classified according to the pair of sub-intervals within which they fell (i.e. which cell). The number of frequency of pixels in each cell were tabulated to produce a two-dimensional histogram. If many pixels had reflectance values in the same range for  $R_{ip}$  and  $R_{jp}$ , the histogram would show high frequency for the corresponding sub-intervals.

An alphanumeric map was prepared on the cell frequencies to locate any clustering present for every possible choice of pairs of reflectance bands. The clustering observed was quite disappointing. Generally, the frequencies "smeared out" in an elongated cloud of relatively high values with "knobs" of slightly higher frequencies here and there.

On the chance that these "knobs" of high frequency were not just random fluctuations, the two-dimensional frequency space for several of the more "bumpy" frequency maps were visually partitioned into regions surrounding each "bump" or cluster. An alphanumeric symbol was assigned to each "bump" and the pixels or sites having reflectances falling within the region around the "bump" were printed on a geographic or aerial map with that symbol.

For example, if there were a substantial fraction of the area of the region covered by water, there would be a high frequency of reflectance values in the range of reflectances characteristic of water. This would show up as a cluster of high frequency in the histogram alphanumeric map. The letter assigned to this cluster would then print out on the geographic map indicating reflectances characteristic of water relative to the two reflectance bands involved in the histograms.

The technique fails if the region does not have sharp reflectance differences between the significant ground features. Then the frequencies do not show distinct clumps or clusters, but rather a gradual gradation from one ground feature signature to another.

The pair-wise visual clustering classification and consequent geographic map produced disappointing results in the Big Horn Basin test area. Apparently, the regional colors grade from one to another in a very gradual way with little of the dramatic contrast needed for useful clustering.

Factor analysis and factor weight maps: Let the vector of reflectances at a given pixel or site be designated by  $\underline{R}_p$ . That is,

$$\underline{R}_p = (R_{1p}, R_{2p}, R_{3p} \dots R_{13p})$$

where  $R_{ip}$  is the numerical value for the  $i$ -th reflectance band at the  $p$ -th pixel. Factor analysis is a group of procedures which attempt to determine factor vectors,  $\underline{F}_1, \underline{F}_2 \dots \underline{F}_k$  such that

$$\underline{R}_p = W_{1p}\underline{F}_1 + W_{2p}\underline{F}_2 + \dots + W_{kp}\underline{F}_k$$

and  $K$  is as small a number as possible. In the above representation,  $W_{ip}$  is a number, depending on the pixel,  $p$ , which is called the weight for factor  $\underline{F}_i$  at that pixel. The factor vectors are independent of the pixel index, and in the present case have 13 components:

$$\underline{F}_i = (F_{i1}, F_{i2}, F_{i3} \dots F_{i13})$$

Factor analysis methods are not procedures for producing a unique answer from a given data set, but may be better characterized as a "hunting license" permitting a search for significant representations of the data in terms of linear combinations of various factor vector sets.

The significance of factor analysis for computer mapping of multi-component, remote sensor data lies in the possibility that various factor vectors or assemblages of reflectance values may characterize particular ground features (e.g. rock formations) which are present simultaneously with other types of ground features (e.g. vegetation patterns). An alphanumeric geographic map of  $W_{ip}$  versus pixel position, where  $F_i$  is the vector factor representing the rock type, would then effectively strip away the vegetation factor and emphasize that aspect of the reflectance vector which carries information on the geology.

Two basic factor analysis approaches were studied relative to the Big Horn Basin test area. These are the R-mode and Q-mode techniques. Each will be discussed, in turn. Briefly, the results were that the R-mode analysis did not appear to lead to useful results, while the Q-mode methods showed much promise. In fact, a computer program was developed, (later found to be a variation on a method proposed by Klovan and Imbrie (1971)), which allowed Q-mode analysis to be applied to the very large sets of S-192 data. In most previously published geological studies involving Q-mode, (Klovan, 1975), the method was restricted by computer capability to a hundred or fewer locations. By contrast, in the present study, Q-mode factor analysis was done on 108,000 locations through the new computer algorithm.

R-Mode Factor Studies. Let D be a matrix with n rows and N columns, where n denotes the number of variables (reflectance bands in current study) and N designates the number of locations (pixels or sites within the text region). The (i,j) element of D, designated by  $D_{ij}$ , is the reflectance,  $R_{ip}$ , for the i-th band at the pixel or site corresponding to the j-th location.

In R-mode analysis, the mean and standard deviation for the i-th row of D are computed from the formulas:

$$\bar{D}_i = \frac{1}{N} \sum_{j=1}^N D_{ij}$$

$$\sigma_i = \left[ \left( \frac{1}{N-1} \right) \sum_{j=1}^N (D_{ij} - \bar{D}_i)^2 \right]^{1/2}$$

The data matrix is then converted to a new normed data matrix,  $Z_R$ , with elements,  $Z_{R,ij}$ , where

$$Z_{R,ij} = (D_{ij} - \bar{D}_i) / \sigma_i$$

The matrix of correlation coefficients, R, relating the variables is given by

$$R = \frac{1}{N} Z_R' Z_R$$

where the prime stands for the matrix transpose. The symbol, R, is the source of the terminology, R-mode, designating this procedure because R provides the basic starting point for determining the factor vectors  $F_i$ .

The justification for the procedure is given in Appendix A. In brief, however, a sequence of constants,  $\lambda_i$ , called eigenvalues, are determined from the equation

$$\text{Determinant } (R - \lambda_i I) = 0$$

There will be  $n$  of these:  $\lambda_1, \lambda_2, \dots, \lambda_n$ . Each defines a factor  $\underline{F}_i$ , which is called the eigenvector of  $R$  corresponding to  $\lambda_i$ , and is computed from the equation

$$R\underline{F}_i = \lambda_i \underline{F}_i$$

If the eigenvalues are numerically different from one another, the resulting factor vectors will be perpendicular to one another and each may be adjusted to unit length.

If the eigenvalues are then ranked in order of decreasing size and the factor vectors are correspondingly ranked, the first  $k$  factors will "explain"

$$\frac{1}{N} \sum_{i=1}^k i,$$

a fraction of the total variance in  $R$ .

For the Big Horn Basin test area, R-mode analysis on three randomly selected sites produced 8 factor vectors which explained 95% of the total variance. This is really very little reduction from the 13 components in the original data sets. Hence the method was deemed to be unsuccessful for this case.

The method was similarly tried on other sets of randomly selected sites and, in each case, the numbers led to the same conclusion. Hence the method was abandoned in favor of the more promising Q-mode methods.

Q-Mode Factor Studies. The development of Q-mode factor analysis is similar to that for R-mode with several significant differences. Let  $D$  be the  $n \times N$  data matrix of reflectance values as defined earlier. However, this time it will be normed differently. The columns of  $D$  will be normed to unit length by the formulas

$$L_j = \left( \sum_{i=1}^n D_{ij}^2 \right)^{1/2}$$

and

$$Z_{Q,ij} = D_{ij}/L_j$$

Each column of  $Z_Q$  represents the reflectances at that location after "brightness" or "faintness" has been adjusted so that all are at the same general intensity (i.e., unit length).

After this norming, how should the similarity or dissimilarity of the reflectances at two sites be measured? One appealing measure is the cosine of the angle between the two vectors. This cosine is defined by the scalar product

$$\cos_{km} = \frac{\sum_{i=1}^n Z_{Q,ik} Z_{Q,im}}{L_k L_m}$$

If the two normed reflectance vectors are identical, the cosine will be unity. If they are perpendicular to each other, in the vector sense, the cosine will be zero. In a natural way, the cosine measures similarity between sites. This is contrasted with the correlation coefficients in  $R$  which measured degree of relationships between reflectance bands as averaged over the region.



An  $N \times N$  cosine matrix providing the cosines between all sites is obtained by the equation

$$C = Z_Q^T Z_Q$$

The standard procedure for determining factor vectors from  $C$  is based on the eigenvectors and eigenvalues of  $C$ . The procedure is as follows:

$$\text{Let } \lambda_1, \lambda_2, \lambda_3, \dots, \lambda_N$$

be the ordered eigenvalues of  $C$  determined from

$$\text{determinant } (C - \lambda_j I) = 0$$

and  $V_1, V_2, \dots, V_N$  be the corresponding eigenvectors derived from the formula

$$CV_j = \lambda_j V_j$$

The eigenvalues for  $j > n$  will be zero in this case because the rank of the matrix  $C$  is, at most,  $n$ . The vector factors,  $F_j$ , may be computed from

$$F_j = Z_Q V_j \sqrt{\lambda_j}$$

The first  $R$  factor vectors will "explain"

$$\frac{1}{N} = \sum_{j=1}^k \lambda_j$$

fraction of the length of the vectors in  $C$ .

Q-mode analysis is intuitively very appealing in geological studies, and has, in fact, been used quite effectively in a variety of earth science applications. The main difficulty has always been, however, that the matrix,  $C$ , had to be kept small enough for computation of the eigenvectors. That is, if 200 locations or sites were involved,  $C$  is a  $200 \times 200$  matrix

and computer storage for a direct approach to the eigenvectors of  $C$  begins to be a problem. Certainly the 108,000 locations in the Big Horn Basin test area threaten the computer with impossible "indigestion."

One method for overcoming this problem was reported in an earlier NASA report (Houston, Marrs, and Borgman, 1975). The method determined factors by Q-mode analysis of sets of locations of tractable size and then combined them to obtain acceptable overall factors. The sequential Q-mode procedures were applied to 777 sampled sites and produced quite acceptable factor sets with one very dominant factor explaining over 98% of the total length of the vectors in  $Z_Q$  and two or three additional vectors explaining the majority of the rest of the total length.

This appeared promising enough to deserve further effort. While re-examining the whole problem of Q-mode analysis on very large data sets, a computer algorithm was discovered which makes such computations quite simple. This method was later found to be a variation of a technique outlined by Klován and Imbrie (1971). At any rate, as a consequence of the new computer program, a Q-mode factor analysis was run on the 108,000 pixels in the test area. The eigenvalues and factors produced are listed in Table 4.

Table 4. Summary of eigenvalues and factors computed through Q-mode analysis of Hyattville area S-192 data.

j = 1 $\lambda_j = .98844$		2 .00517	3 .00203	4 .00148	
Factors:	1st	2nd	3rd	4th	Band
1					
1	.10240	.18692	-.23624	-.09554	Green-Yellow (.56-.61 $\mu$ m)
2	.11507	.28924	-.45414	-.19125	Orange-Red (.62-.67 $\mu$ m)
3	.12920	.28356	.23215	-.01564	IR (.78-.88 $\mu$ m)
4	.13420	.35157	-.22595	.11777	IR (1.55-1.75 $\mu$ m)
5	.12151	.28651	-.34220	.11615	IR (2.10-2.35 $\mu$ m)
6	.51754	-.23440	-.19352	.73040	Thermal IR (10.2-12.5 $\mu$ m)
7	.16102	.40116	.32231	.11809	IR (1.20-1.30 $\mu$ m)
8	.15241	.31609	.36925	.00438	IR (.98-1.03 $\mu$ m)
9	.62774	-.37827	.27163	-.26939	Thermal IR (10.2-12.5 $\mu$ m)
10	.32864	.06362	-.25477	-.36177	Violet-Blue (.46-.51 $\mu$ m)
11	.16681	.35972	.31071	.06647	IR (1.09-1.19 $\mu$ m)
12	.26852	-.05455	-.05456	-.41396	Violet (.41-.46 $\mu$ m)

The agreement of this overall analysis with the sequential analysis of the 777 pixel set was quite close. The sequential analysis took about 40 minutes computer time. The new algorithm required only about 30 seconds once the data had been read into the computer. The interpretation of the factor table and its consequences in mapping is as follows:

The first factor may be interpreted as representing the dominant "color" of the region. Its overwhelming dominance of the other factors shows why the straightforward attempts at cluster mapping failed. The region is almost entirely uniform and presents no strong contrasts.

The second and subsequent factors represent orthogonal deviations or "anomalies" from the regional reflectance. Considering each of them individually, strips away the regional color and mathematically looks only at various aspects of the pattern producing features.

The second factor vector is high in near infrared, (1.09-1.75  $\mu\text{m}$ ) and low in thermal (10.2-12.5  $\mu\text{m}$ ) bands. It emphasizes certain of the vegetation and dark heat-poor areas. A factor weight map for this factor is given in Figure 62. High weights (dark-toned regions) indicate high IR - low  $\theta\text{IR}$ . The black shale streak trending diagonally across the top of the map shows up quite dramatically. It is a dark toned area (low IR - lower  $\theta\text{IR}$ ). The river bottom and certain of the vegetation patterns are depicted by light colored patterns (low IR- high  $\theta\text{IR}$ ).

The third factor is low in orange-red (.62-.67  $\mu\text{m}$ ) and one of the IR bands (2.10-3.35  $\mu\text{m}$ ) while it is high in two other IR bands (.98-1.03  $\mu\text{m}$  and 1.20-1.30  $\mu\text{m}$ ). The factor weight alphanumeric map for this factor is shown in Figure 63. Certain different vegetation patterns seem to be enhanced by this map as represented by the positive weights. The red shale beds in the lower part of the map appear to be showing up well. Also certain of the drainage features are enhanced, particularly in the lower left corner of the area.

The fourth factor is high in thermal (10.2-12.5  $\mu\text{m}$ ) and low in violet and violet-blue (.41-.51  $\mu\text{m}$ ). This factor may be reaching down into the background noise since scan-line arcs show up strongly on the alphanumeric map. The particular combination of bands in the fourth factor vector seem

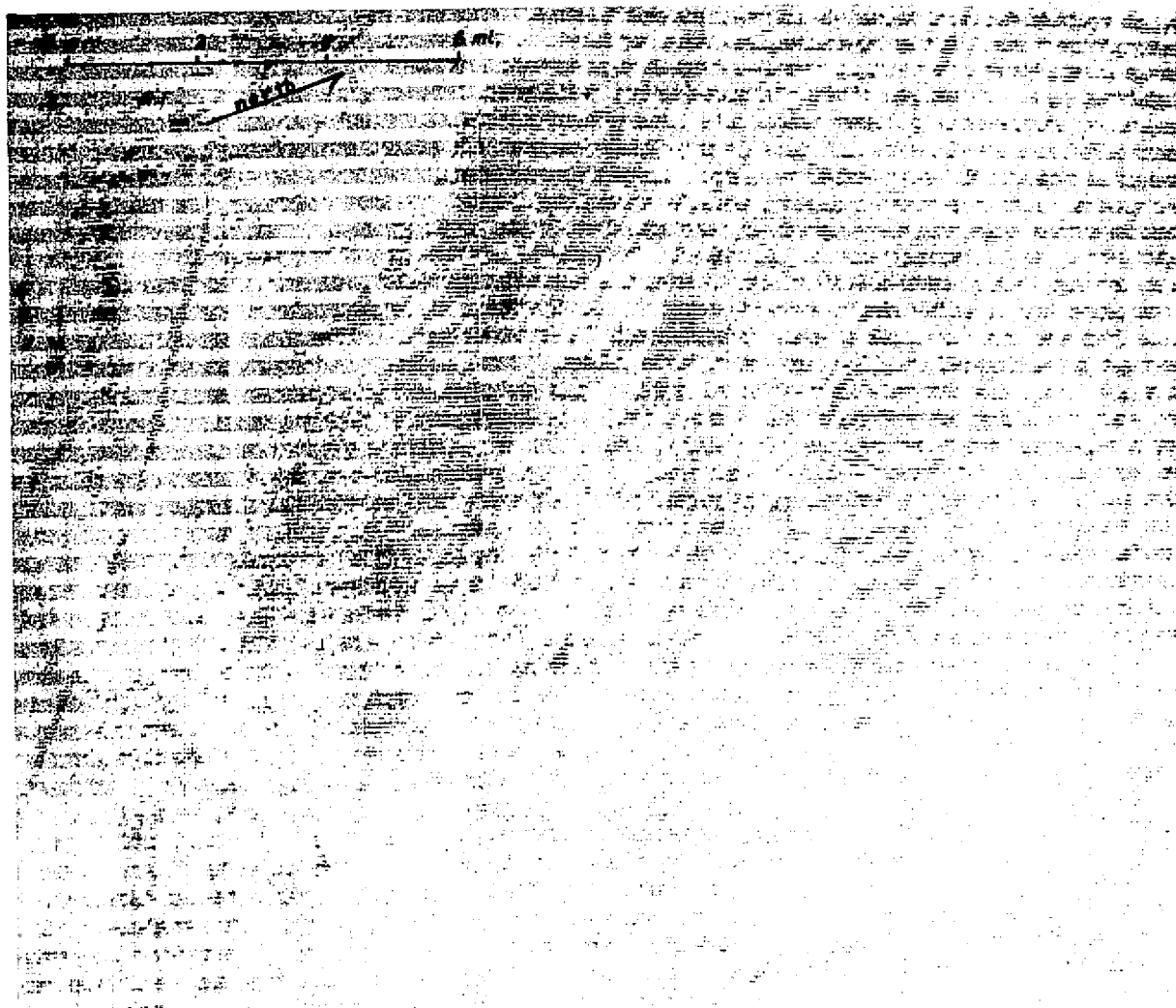


Figure 62. Alphanumeric pattern map at the Hyattville test area. Values plotted were computed via Q-mode pattern recognition. All points are scaled according to their component (weight) relative to Factor 2.

ORIGINAL PAGE IS  
OF POOR QUALITY

132

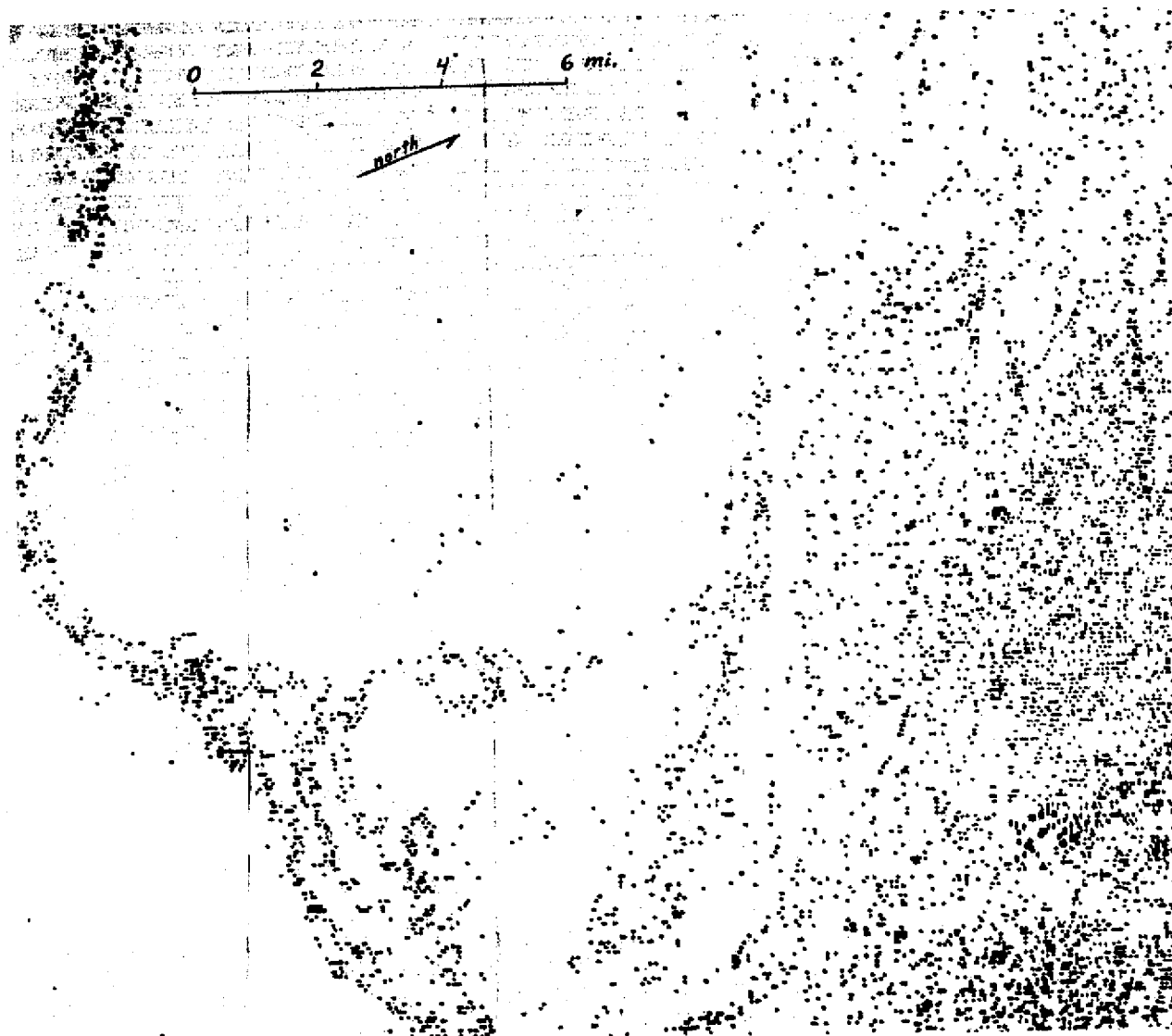


Figure 63. Alphanumeric pattern map of the Hyattville test area. Values plotted were computed via Q-mode pattern recognition. All points are scaled according to their component relative to Factor 3.

to "erase" the strong pattern of vegetation along Paint Rock and Alkali Creeks. Whether the map resulting from the fourth factor is significant or not is not clear at this time. Therefore a map of the fourth factor is not included in the report.

Preliminary evaluation of the alphanumeric maps (Figs. 62 and 63) produced with the weights (for factors 2 and 3) from the Q-mode factor analysis of the digital S-192 data demonstrated general utility for discrimination of ground patterns. Maps for Q-mode factor sets two and three proved useful in differentiating classes of vegetation, geology, and drainage features. Factor set four did not produce any apparent distinction between ground patterns.

Figure 64, an S-190A color photograph of the Hyattville area and eastern Big Horn Basin was compared directly to the factor maps. The photo shows the Mesozoic Chugwater Formation which is readily visible as a reddish band across the photo. Also evident in the photo are the various bluish shades which represent vegetation (grass, sagebrush, trees). Gullies and ridges are apparent. The distinctive dark areas with strong geometric patterns are areas of irrigated fields along tributaries to the Bighorn River. Hyattville is located near the center of the map area (Fig. 65).

The computer map derived from the twelve Skylab S-192 bands using factor 3 weights (Fig. 63) shows dark areas corresponding to areas of heavy vegetative cover and/or red shale outcrops. Light toned areas correspond to all classes that have been suppressed. The No Wood River valley runs along the bottom edge of the map, and branches northward into Paint Rock Creek and Alkali Creek. Irrigated land along each of these creeks is represented by the pattern of dark dots on the image. These computer maps

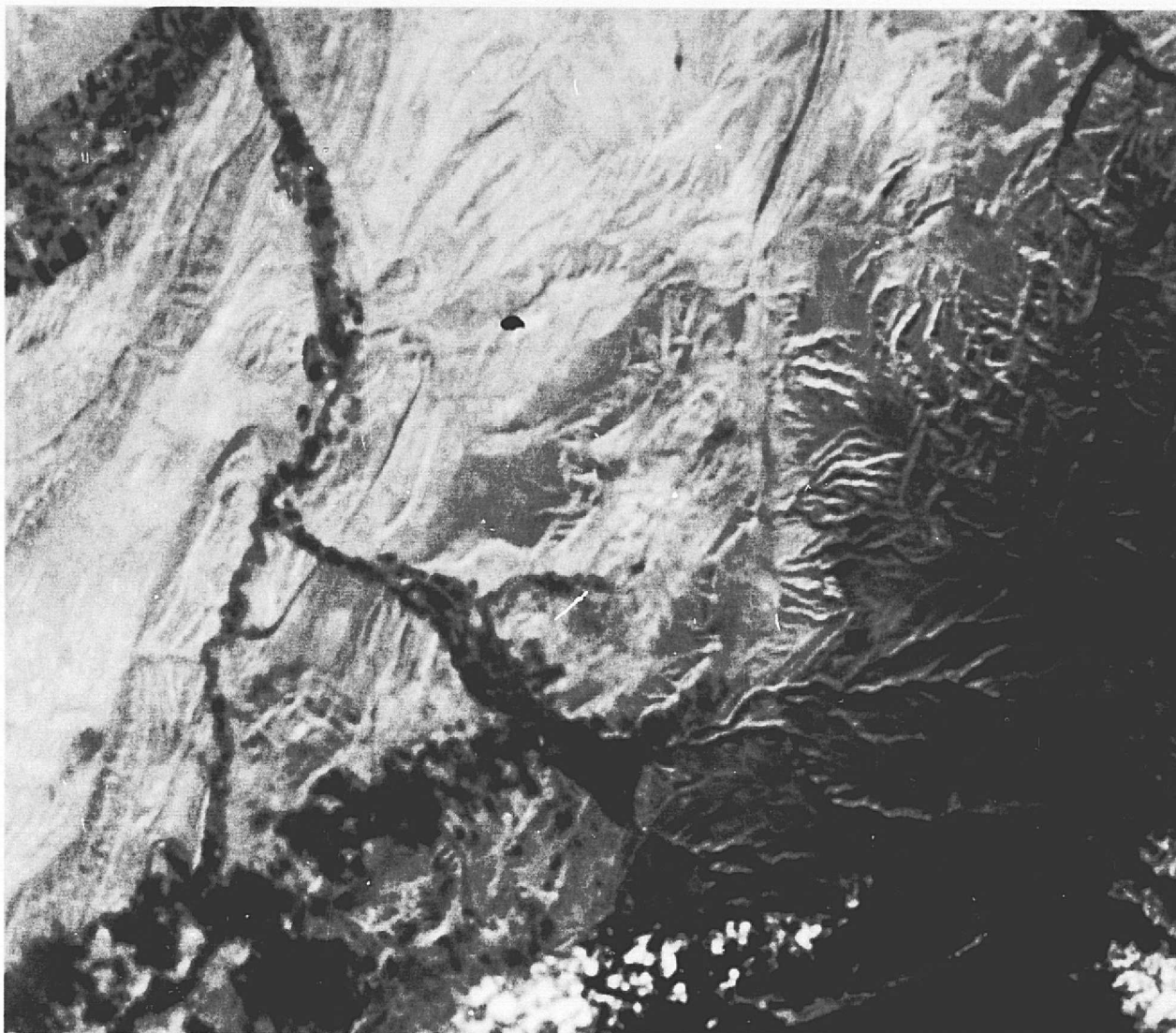


Figure 64. S-190A color photograph of the Hyattville test area. (track 5, pass 10, roll 16, frame 228, June 13, 1973).

ORIGINAL PAGE IS  
OF POOR QUALITY



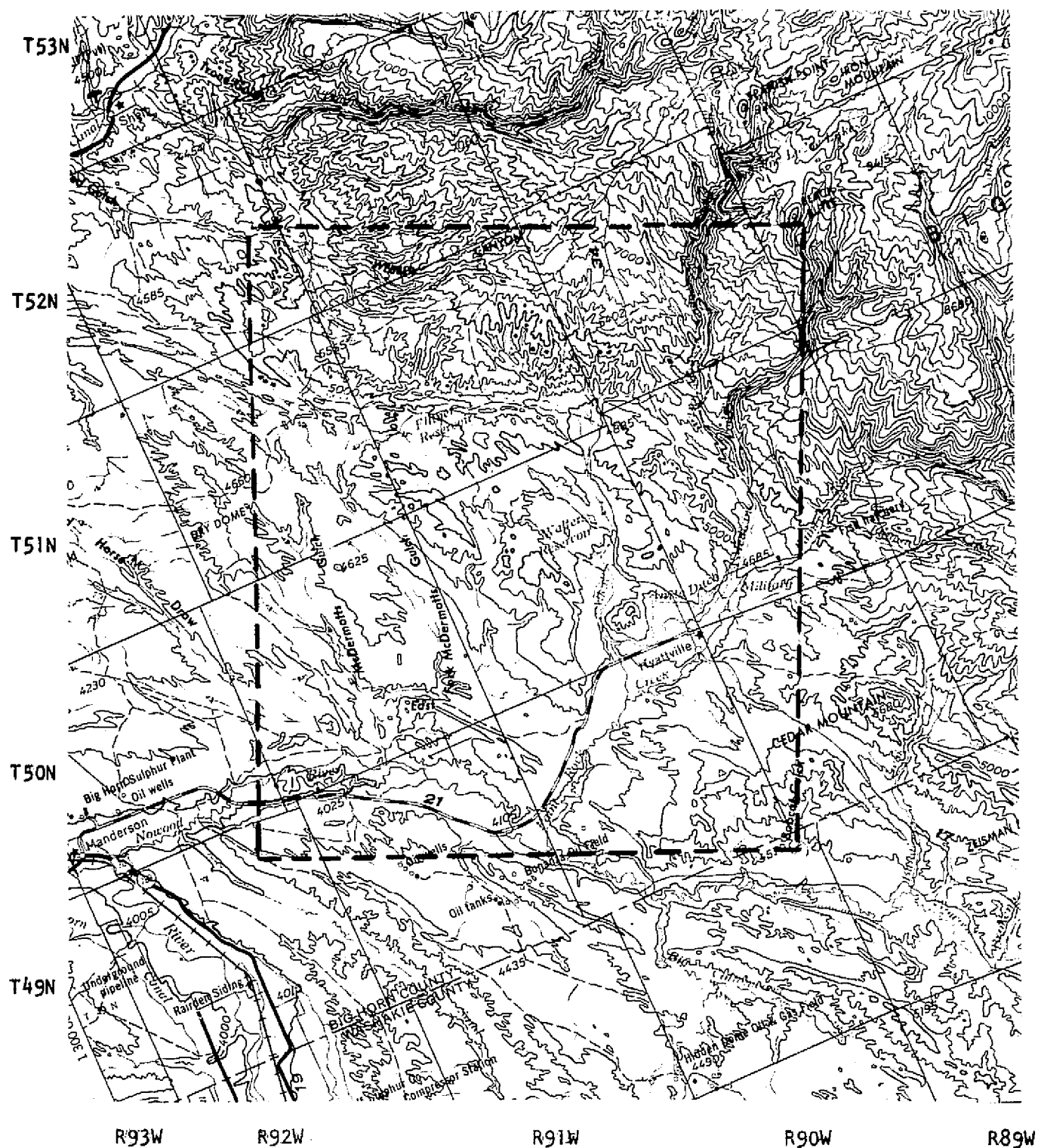


Figure 65. Topographic map of the Hyattville test area (A.M.S., 1:250,000-scale, Sheridan two-degree sheet). Map area corresponds to region covered by color photograph (Fig. 64). Area outlined corresponds to region of figures 62 and 63 analyzed by computer.

were correlated with the imagery and geologic maps using a Bausch and Lomb ZT-4 transfer scope.

The correlations showed that the pattern of points corresponds to areas of densest vegetation on the image. Sparsely vegetated zones (ridges and gullies) in this more mountainous region lie within the white areas not identified by the computer as regions of heavy vegetation. The line of points running horizontally across the bottom of the map corresponds very well to the red shale outcrops. It follows the trend of the rocks and widens out where the iron rich soil has washed over the basin.

The ability to discriminate outcrops of red (iron enriched) rocks is valuable in geologic mapping and in prospecting for uranium roll fronts (or their corresponding oxidized alteration zones).

The factor 2 alphanumeric map of the Hyattville area was designed to suppress both zones of heavy vegetation and zones of no vegetation. Only the regions of light vegetative cover were assigned symbols. The heavily vegetated river valleys are blank areas. The distinctive thin line cutting across the top of the map corresponds to the black Mowry/Thermopolis shale. The shale outcrop is apparent in the photograph as it cuts across Paint Rock Creek near its intersection with No Wood River.

Figure 62' does not emphasize the red beds. Its major application may be in vegetative discrimination, which can be accomplished with more efficiently than with the factor 3 map.

Additional Comments on Q-Mode Analysis. The Q-mode procedures appear highly promising, particularly in light of the speed with which the factors can now be determined from all the pixels in a region selected for alphanumeric mapping. The new computer algorithm makes possible a number of very intriguing lines of investigation.

It should be mentioned that considerable further enhancement may be achieved by rotations or oblique transformations on the space defined by factors 2, 3, and , perhaps, 4. This has not been investigated. Also the physical appearance and contrast in the alphanumeric maps depends critically on what ranges of weight values are assigned the blank character and the other symbols available. For example, the red-bed area in the factor 3 map might be enhanced by assigning blanks to all other ranges except those appearing in the red-bed area, and then subdividing the range of values in the red-bed area into finer subdivisions with various symbols assigned to each subdivision. This should produce a display of fine structure in that area.

Another interesting possibility is the introduction of the Q-mode factor vectors, as determined by the computer, into the video display system where various rotations of the space spanned by factors 2 and 3 could be studied interactively by dial manipulations.

The Q-Mode Computer Algorithm. The full mathematical development and basis for the new Q-mode computational algorithm is given in Appendix B. A few brief details of the method will be presented here.

Basically the method is based on:

- (1) the formation of the new matrix  $Z_Q Z_Q'$  which will be  $n \times n$  in size instead of  $N \times N$  as is the cosine matrix.
- (2) the eigenvectors and eigenvalues of  $Z_Q Z_Q'$  can be shown to coincide with the  $\underline{F}_j$  and  $\lambda_j$  determined from the classical Q-mode procedures presented earlier.

Although the method is surprisingly simple and based on relations following from known theorems in theoretical algebra, a survey of Q-mode studies over the past decade did not uncover any use of this basic idea. Instead, the Q-mode procedure was restricted, in every case, to data sets leading to cosine matrices capable of being handled by the available computer facilities. Thus, it is concluded that the procedure represents a significant advance in making Q-mode analysis more useful for geologic studies.

#### COST BENEFIT ESTIMATES

Accurate cost/benefit analyses cannot be made for most applications of the Skylab data to natural resource studies because most of the benefits are not immediately realized. General geologic mapping, tectonic studies, and mineral exploration may eventually lead to the discovery of mineral deposits. Likewise, sound planning for resource development may save millions of dollars worth of resources that might otherwise be wasted or minimize damage to the environment. Such benefits will only be realized over a period of many years and are largely dependent upon continued use of the Skylab data by industry, governmental agencies, and the public.

Nevertheless, some rough cost/benefit estimates can be made for general mapping projects by estimating the improvement in mapping efficiency resulting from the use of the Skylab photography. Unfortunately, even these estimates consider only the immediate benefit resulting from increased speed and accuracy of the mapping program. The estimates do not provide a measure of the long-term benefits or those benefits resulting from the applications that could not be accomplished without the synoptic view provided from the satellite.

One of the best cost/benefit estimates available from the Wyoming investigation is provided by the Powder River Basin mapping project which is scheduled to produce three different topical maps (land-forms, land-use, and vegetation) of an eight-county area of Wyoming within a two-year period. The project uses Skylab photography as a prime mapping base supplemented by interpretation of 1:120,000 scale aerial photography, field checks, and available published data. The maps will be compiled at 1:100,000 scale and reduced to 1:250,000 scale for final publication. Total cost of the project will be approximately \$100,000.

Estimates of the time and funding required to compile similar maps through standard field-mapping procedures range on the order of six to eight years (with the same level of effort) and would cost almost five times as much. If the field investigation were supplemented only by high-altitude aerial photography, the project would still require almost four years for completion and twice the expenditure. In either case the satellite data allows for a substantial cost-saving, but even more critical is the time factor. The information being compiled in the Powder River Basin mapping project is essential to planning efforts and impact studies which must precede the development of energy resources in the area. Already, a massive effort has been launched by government and industry to tap these resources. Each day saved in the regulation and planning of this development represents an enormous cost saving and brings us closer to the national goal of energy independence. Each contribution to a better development plan makes us better able to achieve this goal without unnecessarily sacrificing environmental quality.

## SUMMARY OF SIGNIFICANT RESULTS

The three manned Skylab missions provided excellent photographic coverage and some S-192 scanner data over the Wyoming test site. High-altitude aerial photography was also obtained over selected areas for correlation with the Skylab data.

The Skylab photography was proven effective in several earth resources applications, including general geologic mapping, structural and tectonic analyses, geomorphology, geohydrology, land-use and vegetation mapping, and mineral exploration. Image resolution is only one of the factors governing the utility of the satellite data. Other controlling factors are imaging geometry, scene illumination and contrast. In some applications the variations in imaging geometry and orbit cycling of the Skylab space station is detrimental to the imagery because the images cannot be readily compared, but in other applications, special effects, such as low-angle illumination, oblique viewing aspect, and variations in sun azimuth, can be used to advantage. Similarly, changes in vegetation cover, soil moisture, and topography are usually difficult to deal with in the interpretation; but they, too, can be used to advantage if they are interpreted as indirect indicators of the condition of the earth's surface.

Comparisons of the different S-190 photographs reveals a direct relationship between image resolution and the amount of interpretive information that can be derived from it. Also, the information content of the photography increases noticeably with color or false-color presentation and with a stereoscopic view.

Comparison of Skylab photography with LANDSAT imagery and aerial photography in both land-use and geologic applications shows that the information detail increases progressively from LANDSAT imagery, Skylab photography, to aerial photography, but so does the time required for interpretation. In both geologic and land-use applications the Skylab S-190B photography provided sufficient detail for mapping at a scale suitable for regional planning (1:62,500 or 1:100,000). The Skylab photography also retains much of the synoptic view essential to regional resource studies. Aerial photography provides additional detail but lacks the synoptic overview and is more expensive to obtain and interpret. LANDSAT imagery is adequate for reconnaissance mapping (1:250,000 or smaller, but lacks the necessary resolution for some sensors.

In all, the most efficient mapping approach found, was to use the LANDSAT data for regional reconnaissance, then use the Skylab photography for compiling the regional interpretation, and, finally, to supplement this with essential detail from aerial photography and field-checks.

The relatively small amount of Skylab S-192 scanner data available provided some very important information regarding the relative utility of different spectral bands. The most significant results of our evaluation of the S-192 data were the implementation of the more efficient procedures for Q-mode Factor analysis and the determination that near infrared bands, most of which lie beyond the spectral sensitivity of the LANDSAT scanner and beyond the photographic range, provide more data for rock discrimination than any of the bands in the visible range.

In brief, our evaluations of the Skylab data and other earth resources satellite systems indicate that none of those presently available are optimum for geologic work. LANDSAT provides repetitive and world-wide coverage but lacks stereoscopic presentation and provides the wrong spectral bands. Skylab S-190 photography demonstrates the advantages of high spatial resolution but lacks good spectral resolution and complete coverage. The Skylab S-192 data hint of better combinations of spectral bands, but lack resolution and have extremely limited coverage. But, together, these three systems provide the background necessary to define the critical parameters for a dedicated geology satellite and for other dedicated earth resources satellites.

Our experience (which is largely limited to arid and semi-arid regions) suggests that dedicated satellite for geology, soils, and geo-hydrology should have the following parameters:

1. Image resolution capability in the range of 10-30 meters.
2. Stereoscopic image presentation.
3. Spectral resolution in the visible, near infrared, and thermal infrared bands (six bands may be adequate if they are selected carefully to bracket important mineral absorption maxima).
4. Repetitive coverage four to six times per year.
5. Synoptic image presentation (50-100 miles square).

Similarly, it might be argued that a better sensing system for vegetation mapping and land-use planning could be designed. Our work indicates that the visible and near infrared bands provided by LANDSAT and Skylab



are generally adequate but that higher resolution ( $< 10$  meters) and stereoscopic presentation are needed. For monitoring vegetation and land-use changes, a relative rapid ( $\approx 1$  wk.) imaging repetition rate is needed. The synoptic view is not essential to these applications but availability of the data in digital form is very important, because it allows for automated identification of change and map updating.

The EREP experiments have indicated a great potential for the use of satellite systems management and development of earth resources systems. However, these results probably represent only a very small portion of the value that will eventually be realized from the earth resources satellite programs and from the EREP data. Many of the data applications tested briefly in these experiments are only minor in their significance compared to some of the operational use of the data that will undoubtedly follow. Other applications that have not yet been considered will undoubtedly grow out of the efforts to use the EREP data.

#### SELECTED REFERENCES

- Andrews, D. A., Pierce, W. G., and Eargle, D. H., 1947, Geologic map of the Bighorn Basin, Wyoming and Montana; U.S. Geological Survey, Oil and Gas Investigations Preliminary Map 71.
- Barnes, H., 1974, U.S. Geological Survey; personal communication.
- Chow, Tse-Sun, 1974, Matrices and linear algebra; in Pearson, Carl, Handbook of Applied Mathematics; Van Nostrand-Reinhold Co., Princeton, New Jersey, p. 912 (no. 9).
- Duhling, William H., 1970, Oxide facies iron formation in the Owl Creek Mountains, Northeastern Fremont County, Wyoming; University of Wyoming, unpublished M.S. thesis, 92 p.; also 17th Ann. Mt. Lake Superior Geology, Tech. Sessions, 1971, abs., p. 18.
- Earle, J., 1975, A re-evaluation of the tectonics of Wyoming and adjacent areas using photo linear elements mapped from LANDSAT-1 and Skylab imagery; Special Report under contract NAS 5-21799, available from National Technical Information Service, Springfield, Virginia, 85 p.
- Eastman Kodak Company, 1972, Kodak aerial films and plates; Manual M-61, Rochester, New York, p. D-23.
- Friedman, B., 1956, Fundamentals and techniques of applied mathematics; John Wiley and Sons, New York, p. 67-69.
- Gordon, R. C., 1974, Multispectral imagery for range vegetation type mapping and estimation of above-ground green biomass; Special Report for contract NAS 9-13298, available from National Technical Information Service, Springfield, Virginia.
- Hammerling, S. J., 1970, Latent roots and latent vectors; University of Toronto Press, Toronto, p. 16 (ex. lib).
- Houston, R. S., 1973a, Multilevel sensing as an aid in mineral exploration - iron formation example; University of Wyoming, Contributions to Geology, vol. 12, no. 2, p. 43-60.
- Houston, R. S., 1973b, Geologic mapping using space images; University of Wyoming, Contributions to Geology, vol. 12, no. 2, p. 77-97.
- Houston, R. S., 1974, Geologic mapping using space images; in Houston and others, 1974, Some illustrations of the advantages of improved resolution in geologic studies; National Technical Information Service, Springfield, Virginia, report E74-10628, p. 4-27.
- Houston, R. S., Marrs, R. W., and Borgman, L. E., 1975, Analysis of ERTS-1 imagery of Wyoming and its application to evaluation of Wyoming's natural resources; type III Final Report under Contract NAS 5-21799, available from National Technical Information Service, Springfield, Virginia, 290 p.

- Keefer, W. R., Dunrud, T. D., and Koogle, R. L., 1970, Structural Geology of the Wind River Basin, Wyoming; U.S. Geological Survey, Professional Paper 495-D.
- Klován, J. E., 1975, R- and Q-mode factor analysis; in McCammon, R. B., Concepts in Geostatistics, Springer-Verlag, New York, p. 21-69.
- Klován, J. E., and Imbrie, J., 1971, An algorithm and Fortran IV program for large-scale Q-mode factor analysis and calculation of factor scores; Jour. Internatl. Assoc. for Mathematical Geology, v. 3, no. 1, p. 61-77.
- Kolm, K. E., 1975a, Mapping of seleniferous vegetation and soils in the lower Wasatch Formation, Powder River Basin, Wyoming; Special report under NASA contract NAS 9-13298 available from National Technical Information Service, Springfield, Virginia, 20 p.
- Kolm, K. E., 1975b, Selenium in soils of the lower Wasatch Formation, Campbell County, Wyoming: Geochemistry, distribution, and environmental hazards; Special Report for contract NAS 9-13298, available from National Technical Information Service, Springfield, Virginia, 97 p.
- Lauer, W., Vanderpoel, P., and Marrs, R. W., 1975, Diazo Composites from LANDSAT Multispectral Imagery; unpublished report, University of Wyoming, Department of Geology, Laramie, Wyoming.
- Love, J. D., Weitz, J. L., and Hose, R. K., 1955, Geologic map of Wyoming, U.S. Geol. Survey map.
- Marrs, R. W., 1974a, Progress report 3-Multidisciplinary study of Wyoming test sites; available from National Technical Information Service, Springfield, Virginia, 33 p.
- Marrs, R. W., 1974b, Progress report 4 - Multidisciplinary study of Wyoming test sites; available from National Technical Information Service, Springfield, Virginia, report E74-10762, 19 p.
- Marrs, R. W., 1975, Land-use in the Moorcroft and Keyhole Reservoir areas, Crook County, Wyoming; Special Report under NASA contract NAS 9-13298, available from National Technical Information Service, Springfield, Virginia, 17 p.
- Noble, B., 1959, Applied linear algebra; Prentice-Hall, Salt Lake City, Utah, p. 307 (ex. 934) and p. 500.
- Phillips, D. P., 1958, Geologic map and cross sections of the Sheep Ridge area, Hot Springs and Fremont Counties, Wyoming (unpublished thesis map), University of Wyoming.
- Schell, Elmer E., 1973 (editor), Guidebook for the 25th field conference; Wyoming Geological Association, Casper, Wyoming 247 p.

Sharp, W. N., and Gibbons, A. B., 1964, Geology and uranium deposits of the southern part of the Powder River Basin, Wyoming; U.S. Geological Survey Bulletin 1147-D, 60 p.

Short, Nicholas M., and Lowman, Paul D., 1973, Earth observations from space; outlook for the geological sciences; NASA/Goddard Space Flt. Center, Greenbelt, Maryland, No. X-650-73-316, 115 p.

Tomes, B. J., 1975, The use of Skylab and ERTS in a geohydrologic study of the lower Paleozoic section, west-central Bighorn Mountains, Wyoming; Special Report for NASA contract NAS 9-13298, available from National Technical Information Service, Springfield, Virginia, 19 p.

Wenderoth, Sandra, and Yost, Edward, 1974, Multispectral photography for earth resources; Science Engineering Research Group, Greenvale, New York.

APPENDICES

## APPENDIX A

Field notes that evaluate boundaries between rock-vegetation units as displayed on Skylab S-190A green band and red band photographs. For locations see plates 10 and 11.

### Green Band

1. Triassic red beds can be distinguished at this locality by dark tone.
2. Cretaceous Cloverly, Thermopolis, Mowry, and Frontier Formations cannot be distinguished -- all rock units fall into one remote sensing unit that cannot be distinguished in other areas.
3. Boundaries of pediment surface poorly shown -- better map of surface than pediment gravel - rock-vegetation unit.
4. Approximate base of Mesaverde Formation - rock-vegetation unit -- characteristic vegetation on basal sandstone of Mesaverde Formation.
5. Oxidized sandstone in Fort Union Formation can be distinguished on photograph, but unit does not correspond to standard geologic formation or member. This type of unit can be traced over large areas and is useful in delineating structure.
6. Distribution of pediment surfaces shown in general, but contacts with other rock units not well shown.
7. Poor detail of contacts for large pediment surface.
8. Geological detail poor but key reversal can be mapped in stereo.
9. Good display of the contact between the Bighorn Dolomite and Gallatin Formation.
10. Very poor display of geologic units as compared with other bands.
11. Major faults and folds can be mapped in stereo but very poor detail.

#### Red Band

1. Triassic red beds and alluvium are accurately mapped in this area.
2. Remote sensing unit includes Cretaceous Cloverly, Thermopolis, and Mowry Formations. Base of Frontier Formation can be traced.
3. Outline of pediment surface that can be detected only on this band.
4. Basal contact of Mesaverde Formation cannot be detected.
5. Oxidized sandstone in Fort Union Formation can be detected and used as a marker bed in mapping.
6. Surface present but detail poor - mix-up of terrace and pediment and failure to distinguish bare rock within surface area.
7. Best mapping of pediment surfaces, but map does not correspond to geologic map because geologist maps pediment gravel on surface rather than surface proper. The surface is expressed by higher biomass.
8. Extent of pediment surface and alluvium exaggerated, but adequate for reconnaissance map.
9. Accurate map of pediment surface. Contacts shown more accurately than on geologic maps at 1/250,000.
10. Accurate map of pediment surface.
11. Lines approximate contacts with rock units, but dips are too low for accurate structural study.
12. Poor pick of geologic contacts.
13. Contacts between red beds and other units generally well located, alluvium well mapped.
14. Gross structure shown, but very poor detail.
15. Best pick of base of Cambrian with the exception of S-190B.

## APPENDIX B FACTOR ANALYSIS FOR LARGE DATA SETS

In conventional, principle-component (factor) analysis (these two terms will be used interchangeably in the following), the standard analysis proceeds by first determining the eigenvalues and eigenvectors for the correlation matrix (in R-mode) or the cosine matrix (in Q-mode). This procedure is quite satisfactory if the rank of the matrix involved is not too large for computer manipulation. However, cases arise in applications where the data array is very large.

Consider, for example, the problems which involve reflectance data from the Skylab S-192 multispectral scanner. Thirteen channels of information pertaining to various radiation frequencies and resolutions are available for 106,000 locations in a "small" test region in the Big Horn Basin of Wyoming. R-mode factor analysis produces a  $13 \times 13$  correlation matrix which can be handled easily. However, for subjective, geological reasons, the Q-mode factor analysis seems more appropriate; since it looks at site-by-site comparisons rather than variable-by-variable comparisons. However, the dimensions of the cosine matrix would be  $(106,000) \times (106,000)$ . Just to store it would require over 11,200,000k memory. Thus, the standard, straightforward procedure is untenable for the S-192 data.

However, indirect procedures are available, based on a variation of a procedure suggested by Klován and Imbrie (1971) which make Q-mode easy to execute in the above case. The indirect procedures are based on inter-relationships between R- and Q-mode factor analysis which enable Q-mode analysis to be done in the same manner as a sort of R-mode analysis. Analogously, R-mode analysis could be done with a type of Q-mode format if that technique provided some advantages in a particular case.



### Summary of Factor Analysis Procedure

Let D be the matrix of data, consisting of n rows (variables) and N columns (locations). Conventionally, D is modified to produce a normed data matrix,  $Z_i$ , before factor analysis proceeds. In R-mode, the rows of D are made to have mean zero and unit variance by the equations

$$\bar{d}_i = \frac{1}{N} \sum_{j=1}^N d_{ij} \quad (1)$$

$$s_i^2 = \frac{1}{N-1} \sum_{j=1}^N (d_{ij} - \bar{d}_i)^2 \quad (2)$$

$$Z_{ij} = (d_{ij} - \bar{d}_i) / (N s_i) \quad (3)$$

where

$d_{ij}$  = (i-row, j-column) element of D.

Conversely, in Q-mode, the columns of D are adjusted to unit length.

$$(\text{length col. } j) = \left( \sum_{i=1}^N d_{ij}^2 \right)^{1/2} \quad (4)$$

$$Z_{ij} = d_{ij} / (\text{length col. } j) \quad (5)$$

In either mode, a basic normed matrix,  $Z_i$ , is produced which is the basis for further analysis.

The correlation matrix, R, would be given by  $ZZ'$  (using Z from the R-mode norming) while the cosine matrix, C, would result from the matrix multiplication  $Z'Z$  (based on Z from the Q-mode norming). The eigenvectors and eigenvalues for  $ZZ'$  (R-mode) and  $Z'Z$  (Q-mode) provide the starting point for the factor analysis. In both cases, an approximation for Z of the form

$$\hat{Z} = \sum_{k=1}^K \sqrt{\lambda_k} \tilde{F}_k \tilde{W}_k = \tilde{F} L^{1/2} \tilde{W} \quad (6)$$

where  $L^{1/2}$  is a diagonal matrix with the square root of the eigenvalues down the main diagonal and zeros elsewhere,  $\tilde{F}_k$  and  $\tilde{W}_k$  is the k-th row of  $\tilde{W}$ . Also,

the columns of  $\tilde{F}$  are of unit length and are orthogonal to each other. Similarly, the rows of  $\tilde{W}$  are of unit length and orthogonal to each other. In order to be useful,  $K$  should be small. In any case,  $K \leq \text{minimum}(n, N)$ .

In the R-mode analysis, the columns of  $F$  are the eigenvectors of  $ZZ'$  and  $\tilde{W}$  is determined from

$$\tilde{W} = L^{-1/2} \tilde{F}' Z \quad (7)$$

In the Q-mode procedures, the rows of  $\tilde{W}$  are the transposed eigenvectors of  $Z'Z$  and  $\tilde{F}$  is developed from

$$\tilde{F} = Z \tilde{W}' L^{-1/2} \quad (8)$$

In both cases, the eigenvectors (columns of  $\tilde{F}$  for R-mode and rows of  $\tilde{W}$  for Q-mode) are ordered according to the magnitudes of the eigenvalues  $\lambda_1 \geq \lambda_2 \geq \dots \lambda_K$ . In most practical cases, the  $\lambda_i$  will be distinct. If there are some multiple eigenvalues, the corresponding generalized eigenvectors are taken to be an orthogonal basis for that eigenspace by standard procedures. (Friedman, 1956).

#### Generalized R- and Q-mode Analysis

For a given method of norming  $D$  to obtain  $Z$ , define generalized R-mode analysis as the techniques proceeding from the eigenvectors and eigenvalues of  $ZZ'$  and generalized Q-mode analysis as the procedures starting with the eigenvectors and eigenvalues of  $Z'Z$ . This differs from the preceding definitions in that R-mode analysis is not necessarily done on a correlation matrix, nor does Q-mode analysis necessarily start with the cosine matrix. For any system of norming, there will be both a generalized R-mode (based on  $\tilde{R} = ZZ'$ ) and a generalized Q-mode (based on  $\tilde{C} = Z'Z$ ) procedure.

Interrelations between generalized R- and Q-mode analysis: The eigenvectors and eigenvalues of  $ZZ'$  (a  $n \times n$  matrix) and of  $Z'Z$  (a  $N \times N$  matrix) are interrelated.

Theorem: Let  $Z$  be a  $n \times N$  matrix. (1) The matrices  $\tilde{R} = ZZ'$  and  $\tilde{C} = Z'Z$  have the same eigenvalues except that the product which is of larger order has  $|N-n|$  extra zero eigenvalues. (2) Let  $\lambda$  be a non-zero eigenvalue for  $\tilde{R}$  with eigenvector  $\underline{u}$ . Then  $Z'\underline{u}$  will be an eigenvector for  $\tilde{C}$  corresponding to  $\lambda$ . (3) Similarly, let  $\lambda$  be a non-zero eigenvalue for  $\tilde{C}$  with eigenvector  $\underline{v}$ . Then  $Z\underline{v}$  will be an eigenvector for  $\tilde{R}$  corresponding to  $\lambda$ .

Source: The above relation in one form or another is stated in various books on linear algebra (Noble, 1969; Hammerling, 1970; and Chow, 1974).

Proof: By definition,  $ZZ'\underline{u} = \lambda\underline{u}$ . Hence  $Z'Z(Z'\underline{u}) = \lambda(Z'\underline{u})$  upon right-multiplication by  $Z'$ . Consequently,  $\underline{v} = Z'\underline{u}$  is an eigenvector of  $Z'Z$  with eigenvalue  $\lambda$ . Conversely,  $Z'Z\underline{v} = \lambda\underline{v}$  implies  $ZZ'(Z\underline{v}) = \lambda(Z\underline{v})$  and so  $Z\underline{v}$  is an eigenvector of  $ZZ'$  with eigenvalue  $\lambda$ . This proves (2) and (3). It remains to show that the non-zero eigenvalue  $\lambda$  common to  $ZZ'$  and  $Z'Z$  has the same multiplicity in the two cases. That is, the eigenspace for  $\lambda$  in both cases is of the same dimension. The procedure followed is that suggested by Noble (1969). Let  $\tilde{R}$  and  $\tilde{S}$  have  $r$  and  $s$  eigenvectors, respectively, corresponding to  $\lambda \neq 0$ . Let  $(\underline{u}_1, \underline{u}_2, \dots, \underline{u}_r)$  be the  $r$ -eigenvectors orthogonally spanning the eigenspace of  $\lambda$  relative to  $\tilde{R}$ .  $(\underline{u}_1, \dots, \underline{u}_r)$  are linearly independent and so there is no  $(\alpha_1, \alpha_2, \dots, \alpha_r)$ , not all zero, such that  $\sum_{i=1}^r \alpha_i \underline{u}_i = 0$ . But

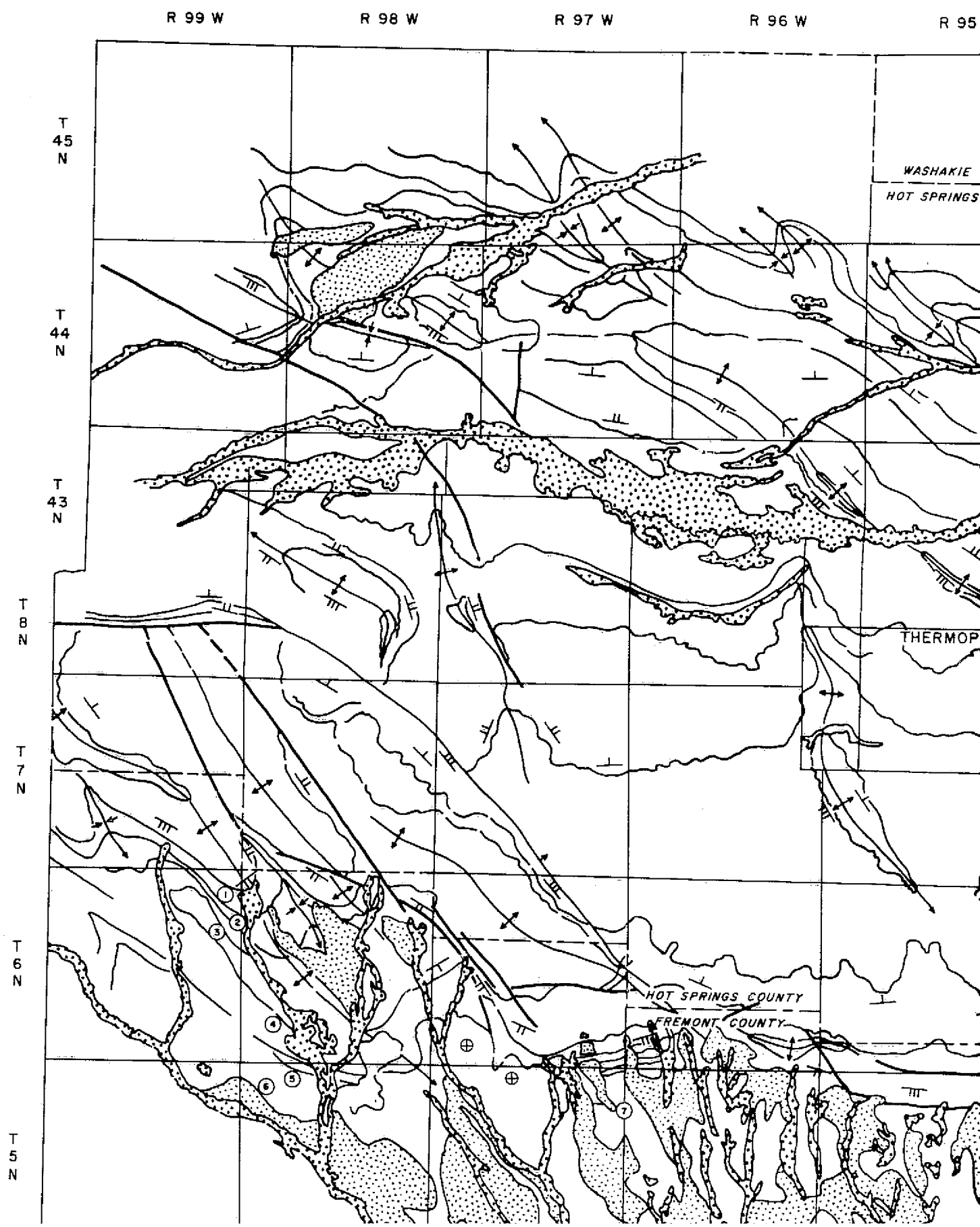
$$R \sum_{i=1}^r \alpha_i \underline{u}_i = Z \sum_{i=1}^r \alpha_i Z' \underline{u}_i = \lambda \sum_{i=1}^r \alpha_i \underline{u}_i$$

It follows that  $Z'\underline{u}_i$ , each an eigenvector for  $\tilde{C}$  by previous argument, are all linearly independent. If they were not, there would exist  $(\alpha_1, \alpha_2, \dots, \alpha_r)$ , not all zero, such that  $\sum_{i=1}^r \alpha_i Z'\underline{u}_i = 0$ . But then, by the above equation, the  $\lambda \sum_{i=1}^r \alpha_i \underline{u}_i = 0$ . Since  $\lambda \neq 0$ , it would follow that  $\sum_{i=1}^r \alpha_i \underline{u}_i = 0$ , which

contradicts the assumed linear independence of the  $\underline{u}_i$ . Thus, there are at least  $r$  linearly independent eigenvectors in the eigenspace for  $\lambda$  relative to  $\tilde{C}$ ; and the dimension,  $s$ , of the eigenspace must be greater than or equal to  $r$ . Exactly reversing the argument, with  $(\underline{v}_1, \underline{v}_2, \dots, \underline{v}_s)$  linearly independent eigenvectors for  $\tilde{C}$  within the eigenspace corresponding to  $\lambda$ , shows that  $r \geq s$ . Hence  $r = s$  and the same number of linearly independent eigenvectors correspond to the non-zero eigenvalue for  $\tilde{R}$  and  $\tilde{C}$ . The eigenspace for  $\lambda$  is of the same dimension for  $\tilde{R}$  and  $\tilde{C}$ .

Application of the interrelation: The application is straightforward. If in Q-mode analysis,  $n$  (the number of variables) is moderate in size while  $N$  (the number of locations) is too large for convenient computation, then the eigenvalues,  $\lambda_i$ , and eigenvectors,  $\underline{u}_i$ , for  $R$  (an  $n \times n$  matrix) are computed after obtaining  $Z$  by Q-mode norming. The  $Z'\underline{u}_i$  would be exactly the eigenvectors for  $\tilde{C}$  that would have been produced if the analysis could have been carried out with  $\tilde{C}$ . In terms of the factor notation in eqs. (6) and (8),  $\underline{u}_i$  would provide the columns of  $\tilde{F}$ . Thus, all the essential elements of Q-mode are obtainable from the corresponding generalized R-mode matrix,  $\tilde{R}$ .

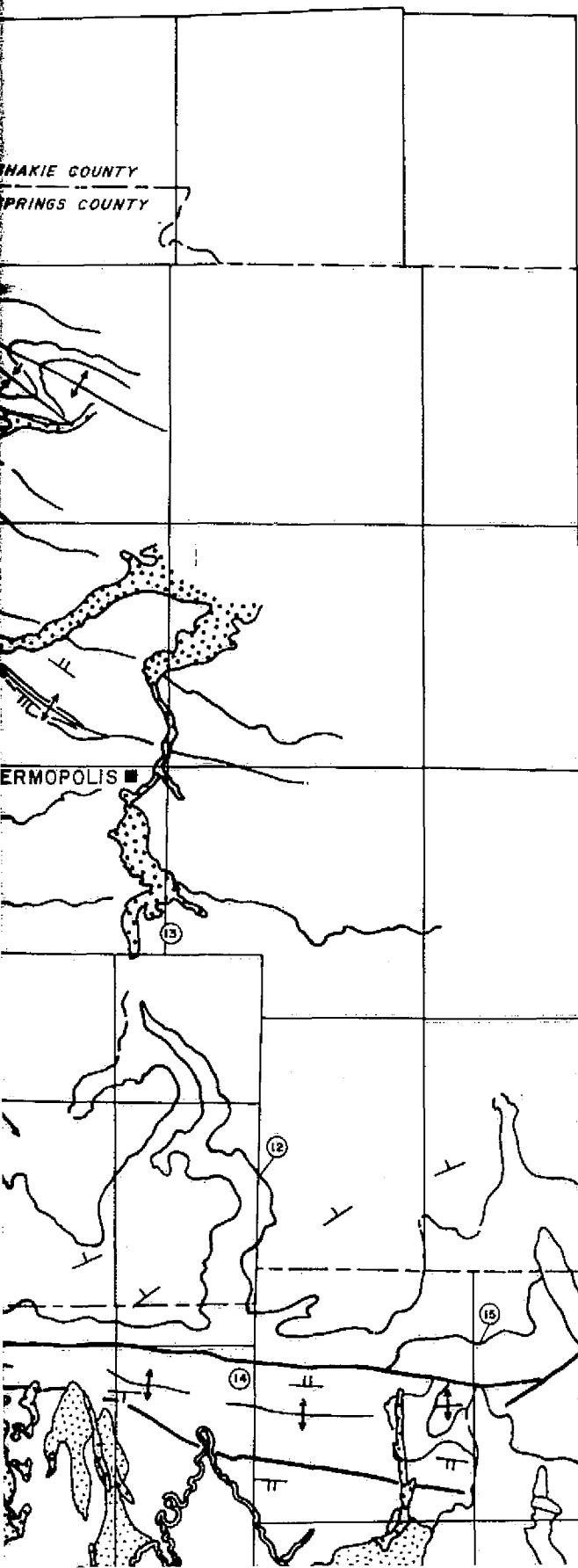
If the vector of attributes had many components (i.e.,  $n$  very large), while the number of locations,  $N$ , was relatively small, the procedure may be reversed. In this case R-mode type norming is carried out to get  $Z$  and the correlation matrix  $R = ZZ'$  is of very large order while the generalized cosine matrix,  $\tilde{C}$ , is of moderate order. The eigenvectors  $(\underline{v}_1, \underline{v}_2, \dots, \underline{v}_N)$  and eigenvalues  $(\lambda_1, \lambda_2, \dots, \lambda_N)$  for  $\tilde{C}$  may be modified to provide the eigenvectors  $\underline{u}_i = Z\underline{v}_i$ .



R 95 W R 94 W R 93 W

SHAKIE COUNTY  
SPRINGS COUNTY

ERMOPOLIS

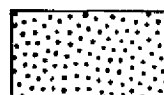


# GEOLOGIC MAP OF A PART OF CENTRAL ARIZONA PREPARED WITH SKYLAB S RED BAND\*

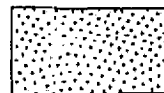
## EXPLANATION

See plate 8 for explanation of symbols

① Location of geologic feature  
discussed in text



Alluvium



Pediment Surface

T  
45  
N

T  
44  
N

T  
43  
N

T  
42  
N

T  
41  
N

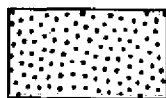
T  
40  
N

GEOLOGIC MAP OF A PART OF CENTRAL WYOMING  
PREPARED WITH SKYLAB S-190A  
RED BAND\*

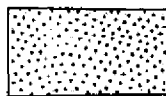
*EXPLANATION*

See plate B for explanation of symbols

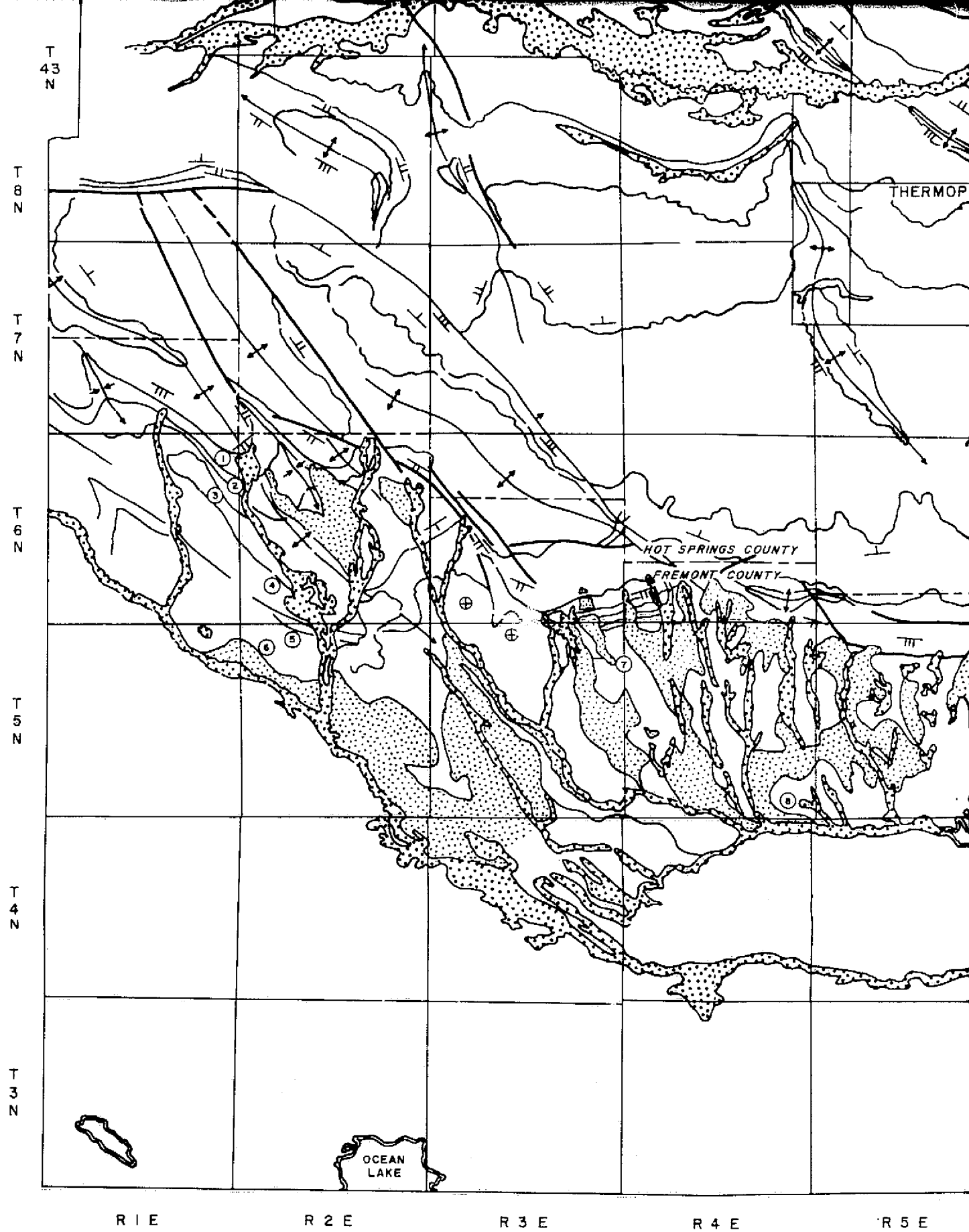
- ① Location of geologic feature  
discussed in text



Alluvium



Pediment Surface

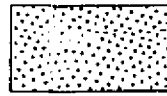


\*STEREO-PAIRS, DATA TRANSFERRED WITH KERN PG-2 STEREO-PLOTTER

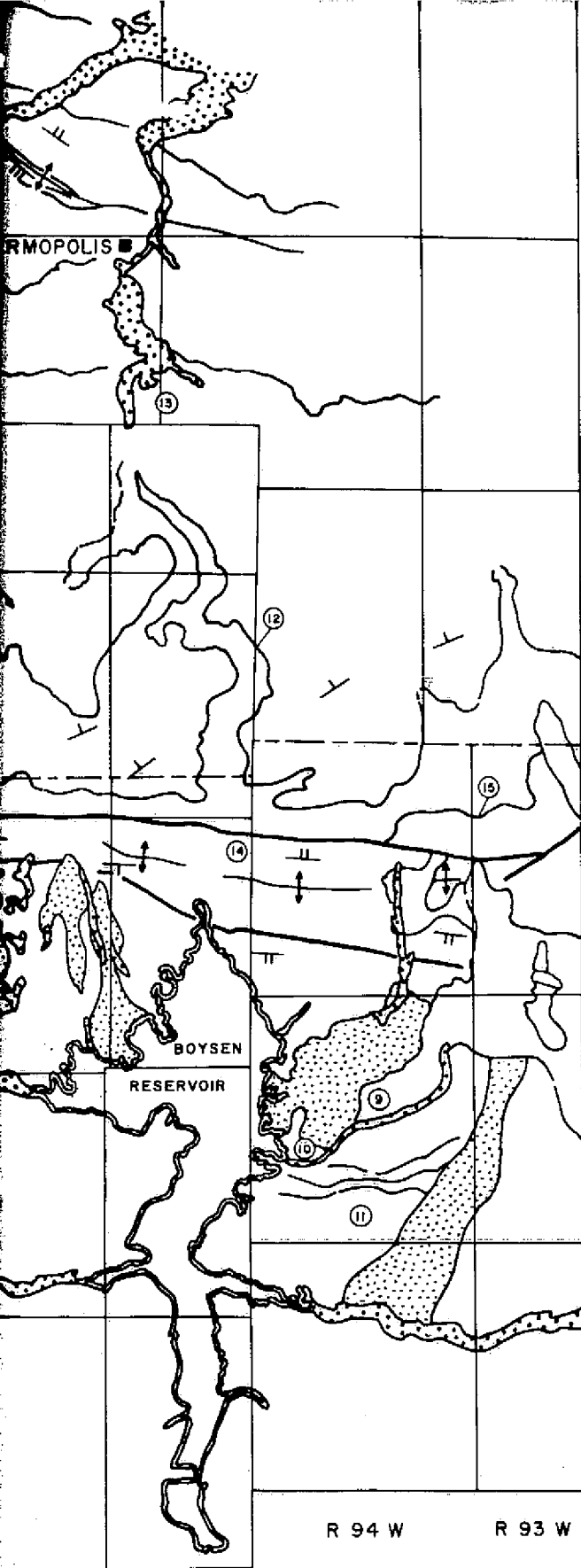
FOLDOUT FRAME 4



Alluvium



Pediment Surface



T  
43  
N

T  
42  
N

T  
41  
N

T  
40  
N

T  
39  
N

T  
38  
N

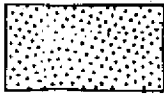
R 94 W

R 93 W

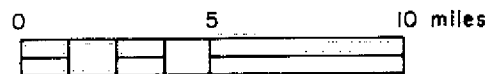
R 92 W



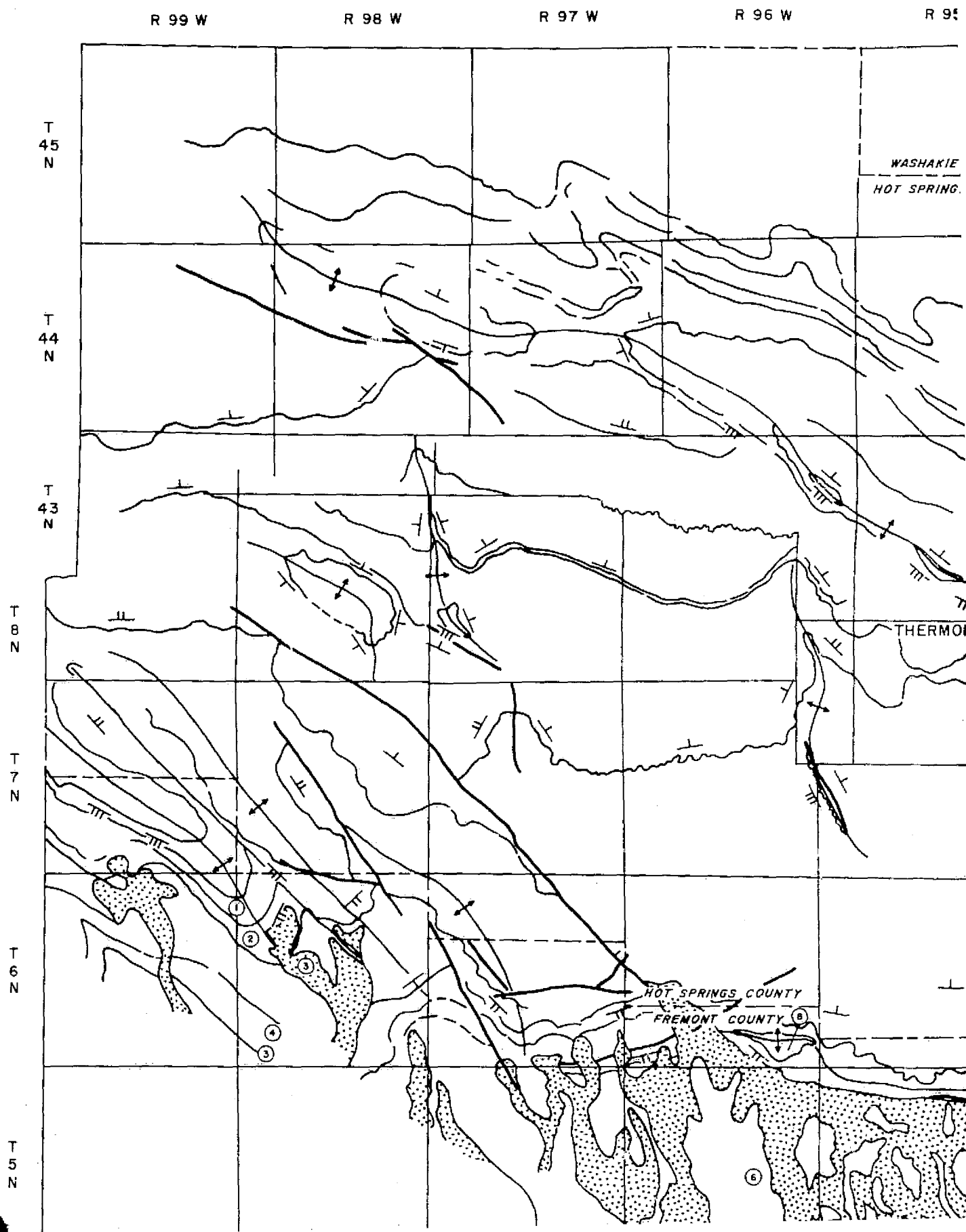
Alluvium

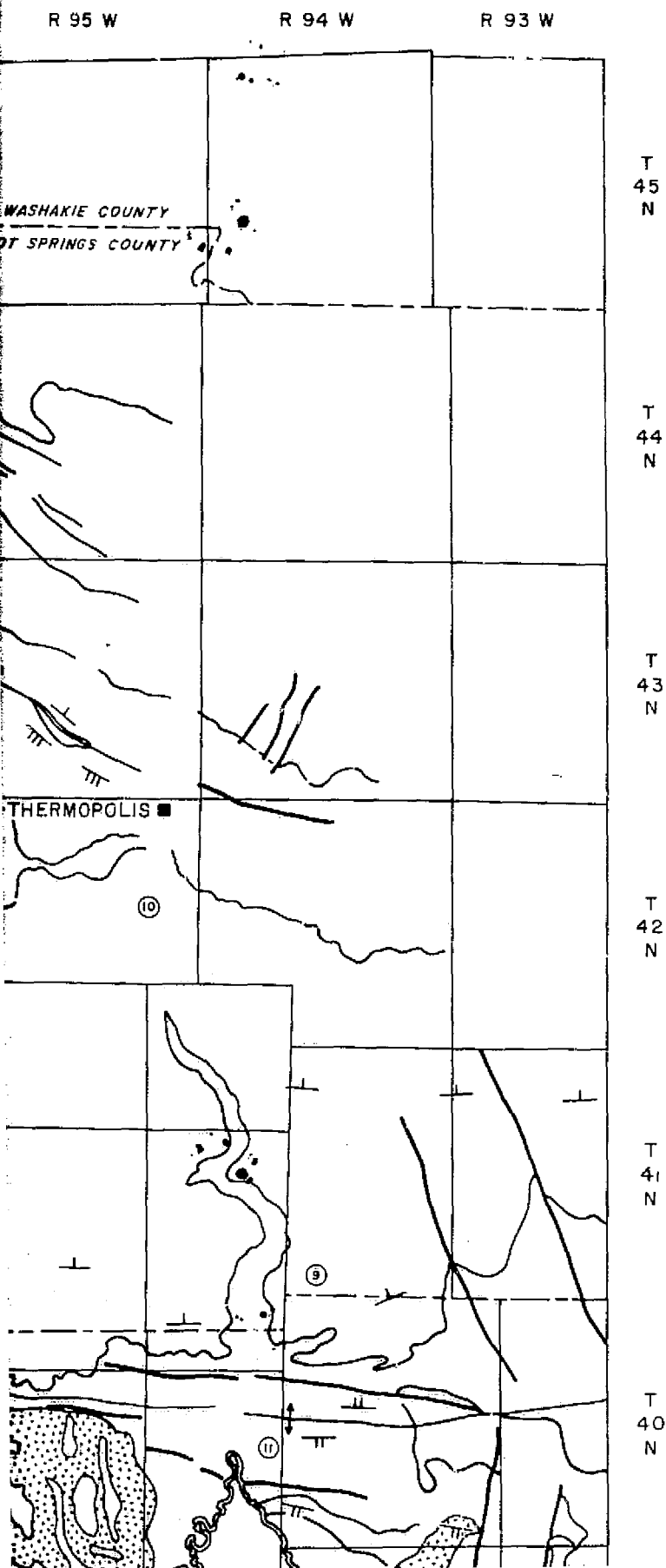


Pediment Surface



FOLDOUT



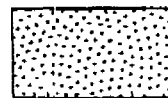


# GEOLOGIC MAP OF A PART OF CEI PREPARED WITH SKYLAB GREEN BAND\*

## EXPLANATION

See plate 8 for explanation of symbols

- ① Location of geologic feature  
discussed in text



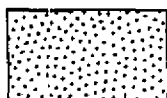
Pediment Surface

GEOLOGIC MAP OF A PART OF CENTRAL WYOMING  
PREPARED WITH SKYLAB S-190A  
GREEN BAND\*

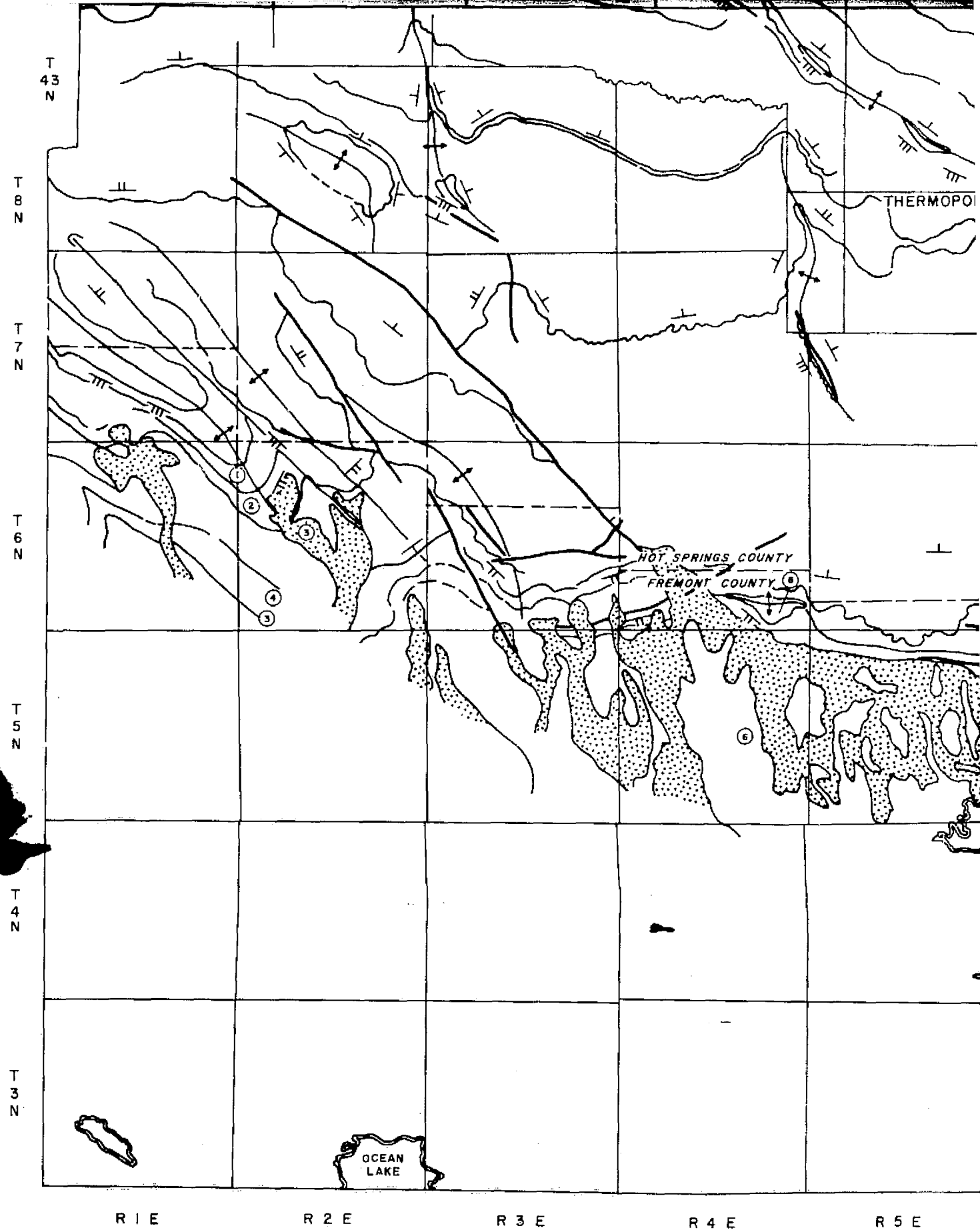
*EXPLANATION*

See plate 8 for explanation of symbols

- ① Location of geologic feature  
discussed in text



Pediment Surface

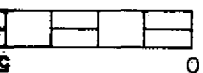
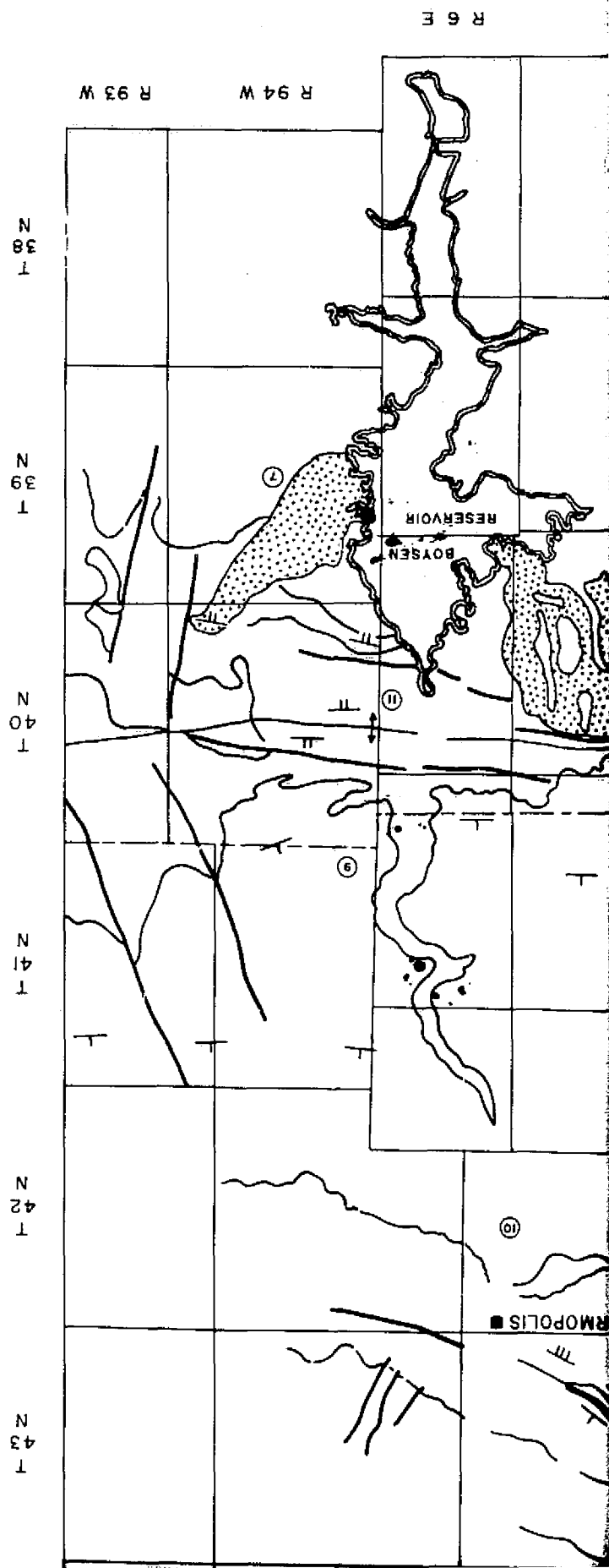



\*STEREO-PAIRS, DATA TRANSFERRED WITH KERN PG-2 STEREO-PLOTTER

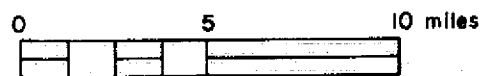
FOLLOUT FRAM

FOLD

Pediment Surface



 Pediment Surface

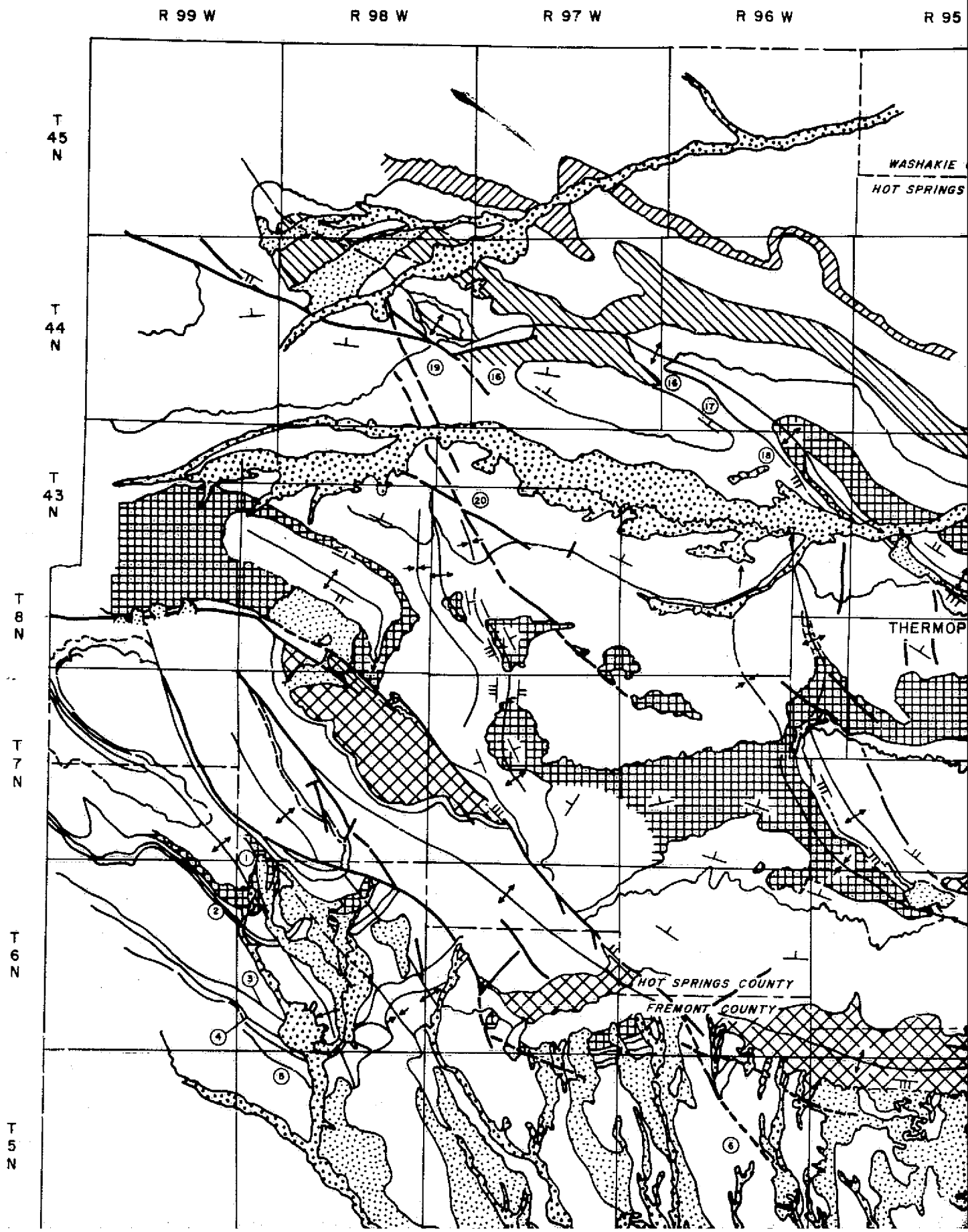


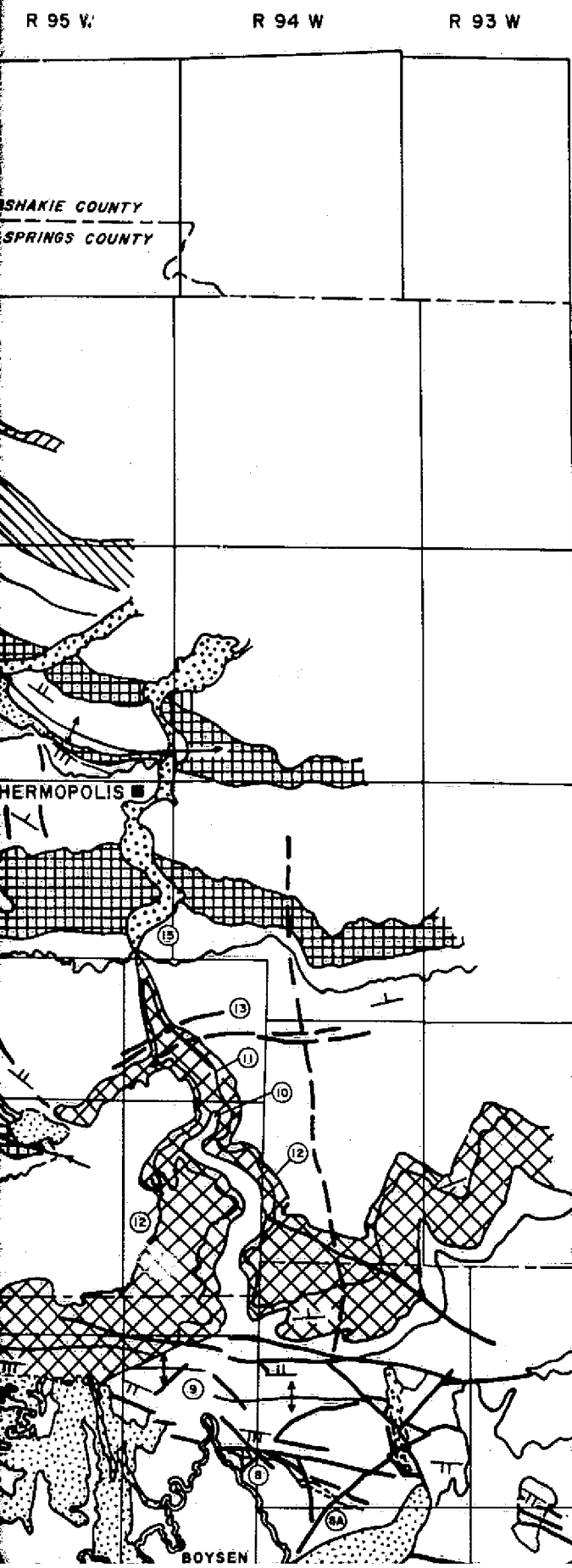
FOLDOUT FRAME 

C-3



FOLDOUT FRAME



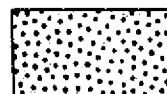


# GEOLOGIC MAP OF A PART OF CENTRAL COLORADO PREPARED WITH SKYLAB COLOR\*

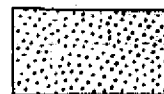
## EXPLANATION

See plate 8 for explanation of symbols

- ① Location of geologic feature discussed in text



Alluvium



Pediment Surface



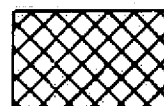
Basal sandstones of the Mesaverde Formation



Shale facies of the Cody Shale



Red sandstone, siltstone, and shale.  
Permo-Triassic



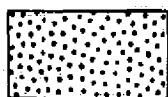
Limestone, dolomite, sandstone unit.  
Includes Blighorn Dolomite, Madison

# GEOLOGIC MAP OF A PART OF CENTRAL WYOMING PREPARED WITH SKYLAB S-190A COLOR\*

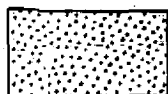
## EXPLANATION

See plate 8 for explanation of symbols

- ① Location of geologic feature  
discussed in text



Alluvium



Pediment Surface



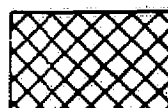
Basal sandstones of the Mesaverde  
Formation



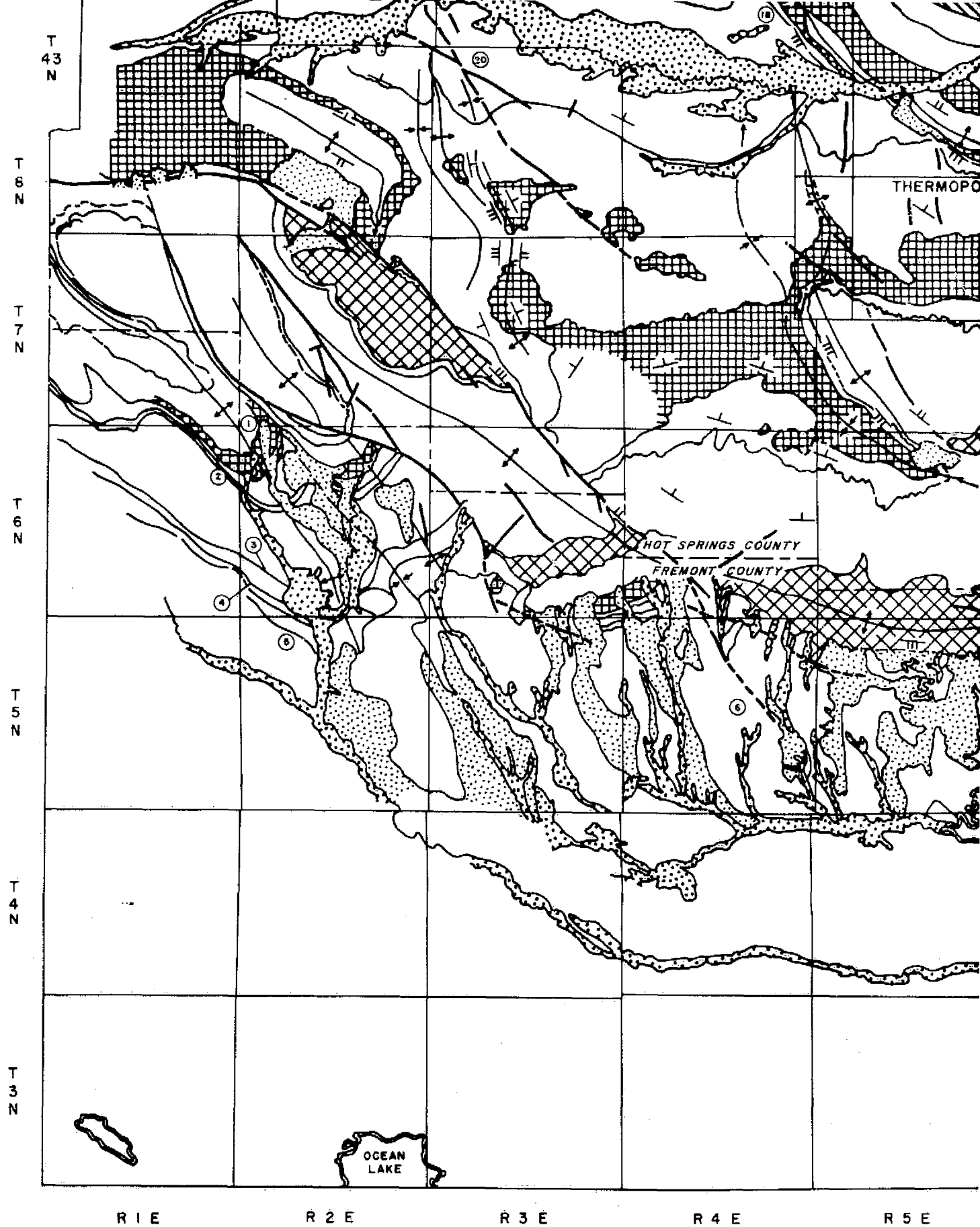
Shale facies of the Cody Shale



Red sandstone, siltstone, and shale.  
Permo-Triassic



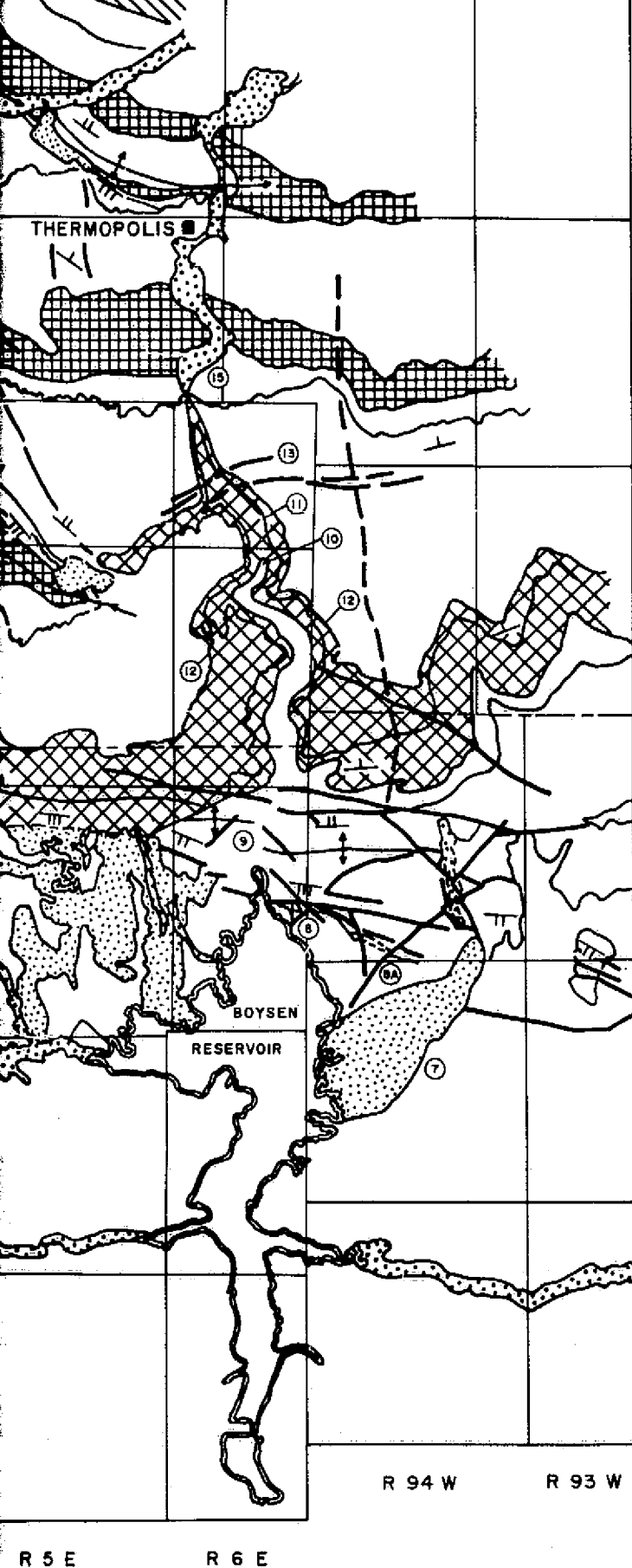
Limestone, dolomite, sandstone unit.  
Includes Bighorn Dolomite, Madison



\*STEREO-PAIRS, DATA TRANSFERRED WITH KERN PG-2 STEREO-PLOTTER

FOLDOUT FRAME

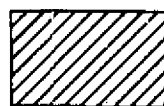
FOLDOUT



Alluvium



Pediment Surface



Basal sandstones of the Mesaverde Formation



Shale facies of the Cody Shale



Red sandstone, siltstone, and shale.  
Permo-Triassic

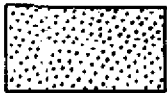


Limestone, dolomite, sandstone unit.  
Includes Bighorn Dolomite, Madison Limestone, and Tensleep Sandstone

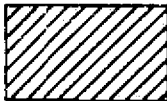
0



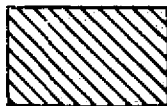
**Alluvium**



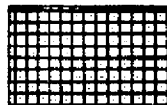
**Pediment Surface**



**Basal sandstones of the Mesaverde  
Formation**



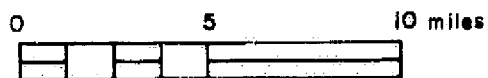
**Shale facies of the Cody Shale**



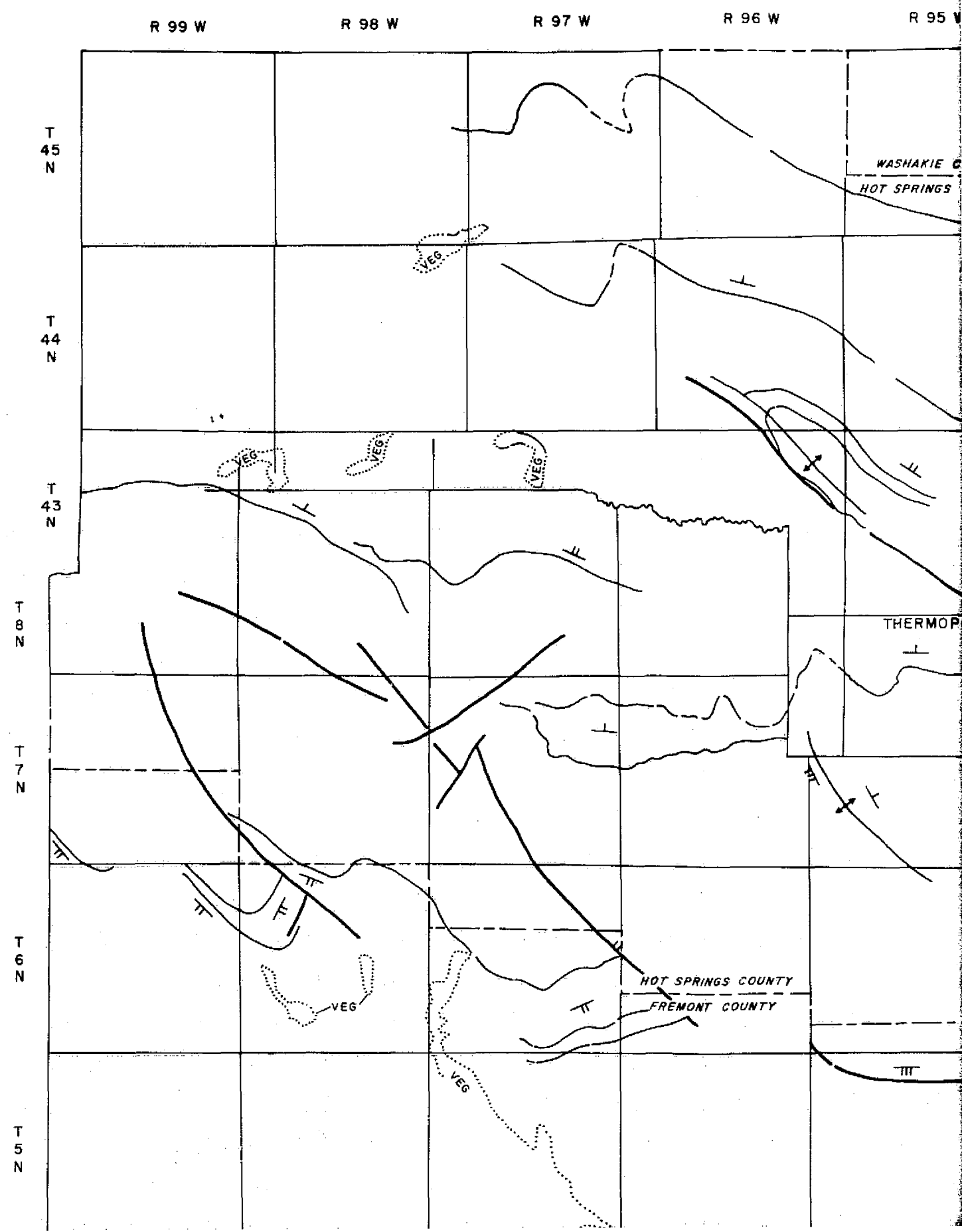
**Red sandstone, siltstone, and shale.  
Permo-Triassic**



**Limestone, dolomite, sandstone unit.  
Includes Blighorn Dolomite, Madison  
Limestone, and Tensleep Sandstone**



FOLDOUT FRAME



R 95 W

R 94 W

R 93 W

WASHAKIE COUNTY  
HOT SPRINGS COUNTY

THERMOPOLIS ■

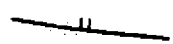
BOYSEN

# GEOLOGIC MAP OF A PART OF PREPARED WITH SKYLAB BANDS\*

## EXPLANATION



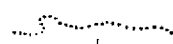
Contact between remote sensing units



Linear feature or fault showing direction of dip

⊕	⊥	⊥	⊥
Horizontal	Low Dip	Moderate Dip	Steep Dip

Strike and dip of planar feature



Outline of water saturated area

Rock units or rock vegetation units cannot be distinguished

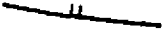
Out  
ous  
alf



# GEOLOGIC MAP OF A PART OF CENTRAL WYOMING PREPARED WITH SKYLAB S-190A IR BANDS\*

## EXPLANATION

 Contact between remote sensing units

 Linear feature or fault showing direction of dip

⊕      /      //      ///

Horizontal      Low Dip      Moderate Dip      Steep Dip

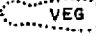
Strike and dip of planar feature

 Outline of water saturated area

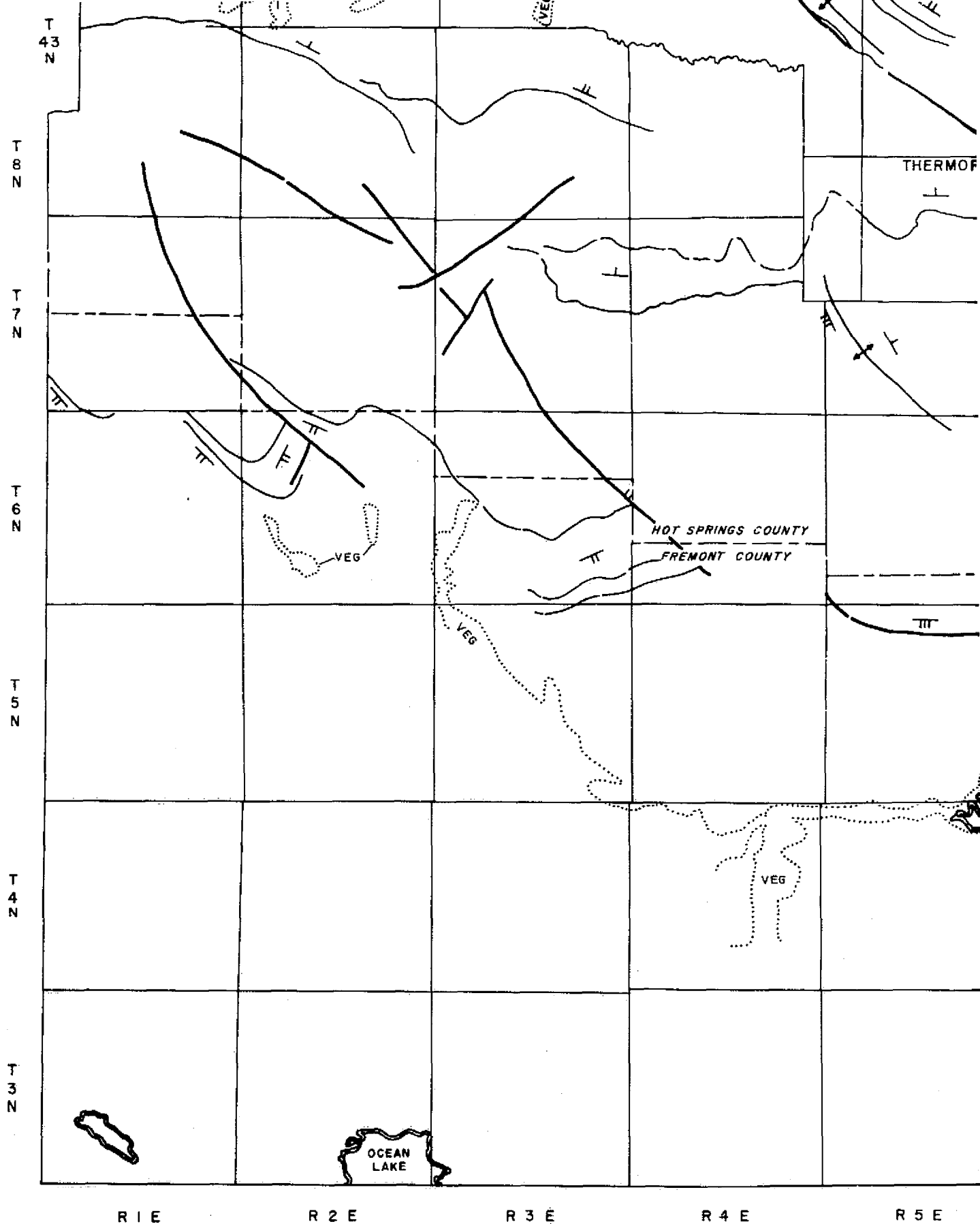
Rock units or rock vegetation units cannot be distinguished

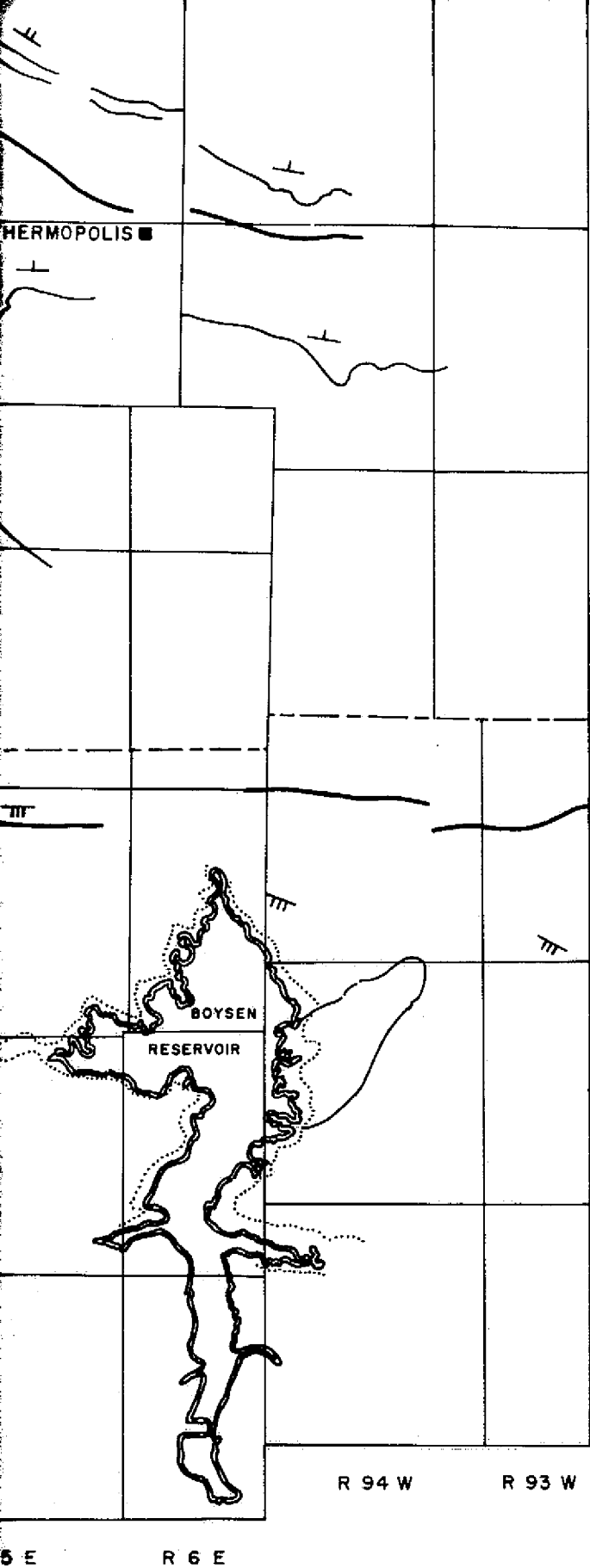
 Syncline

 Anticline

 VEG

Outline of area having especially vigorous vegetation for September (probably alfalfa)





⊕

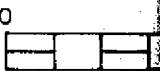
Horizontal Low Dip Moderate Dip Steep Dip

Strike and dip of planar feature

Outline of water saturated area

Rock units or rock vegetation units cannot be distinguished

ous vegeta  
alfaifa)



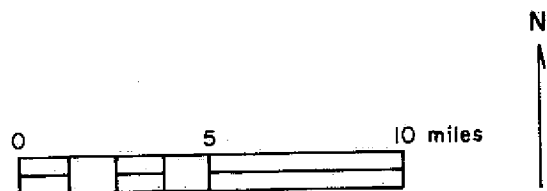
FOLDOUT FRAME

ous vegetation for September (probably  
alfalfa)

⊕  
Horizontal Low Moderate Steep  
Dip Dip Dip  
Strike and dip of planar feature

  
Outline of water saturated area

Rock units or rock vegetation units  
cannot be distinguished



FOLDOUT FRAME 6

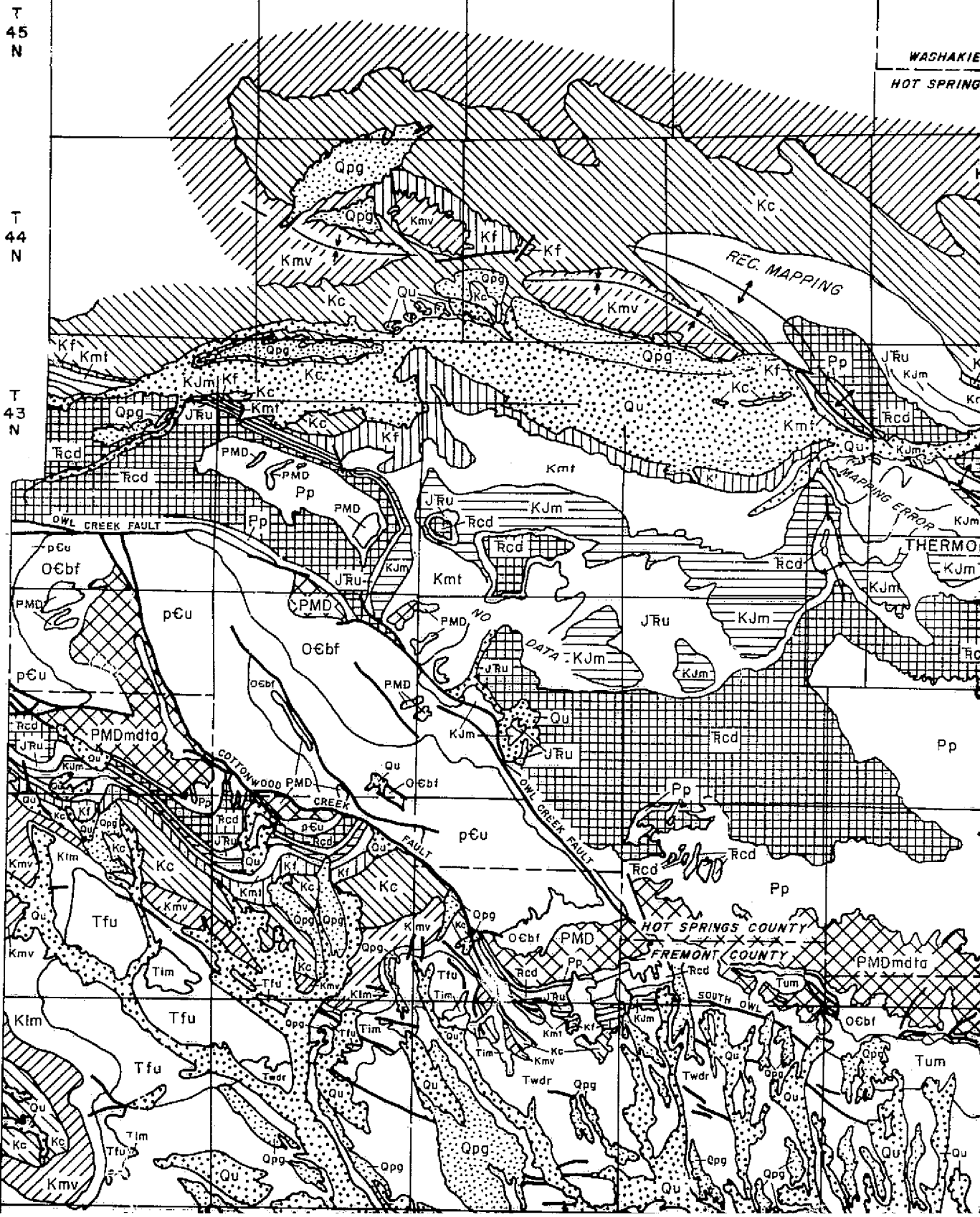
R 99 W

R 98 W

R 97 W

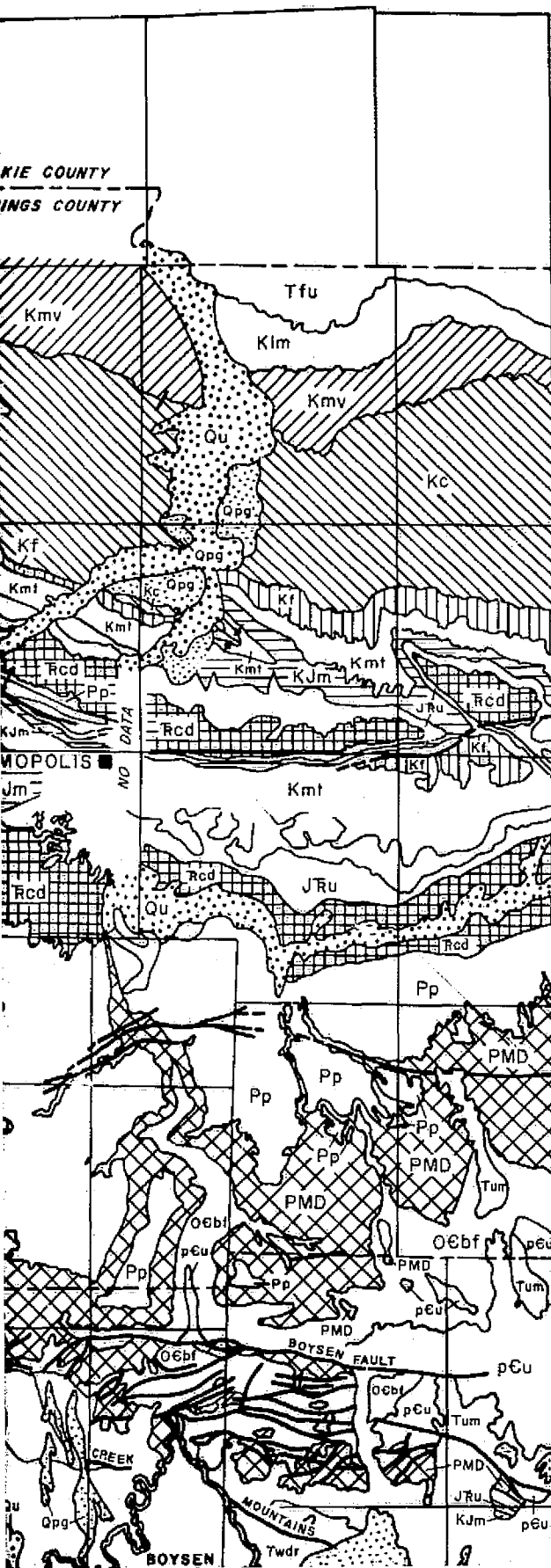
R 96 W

R 95 W



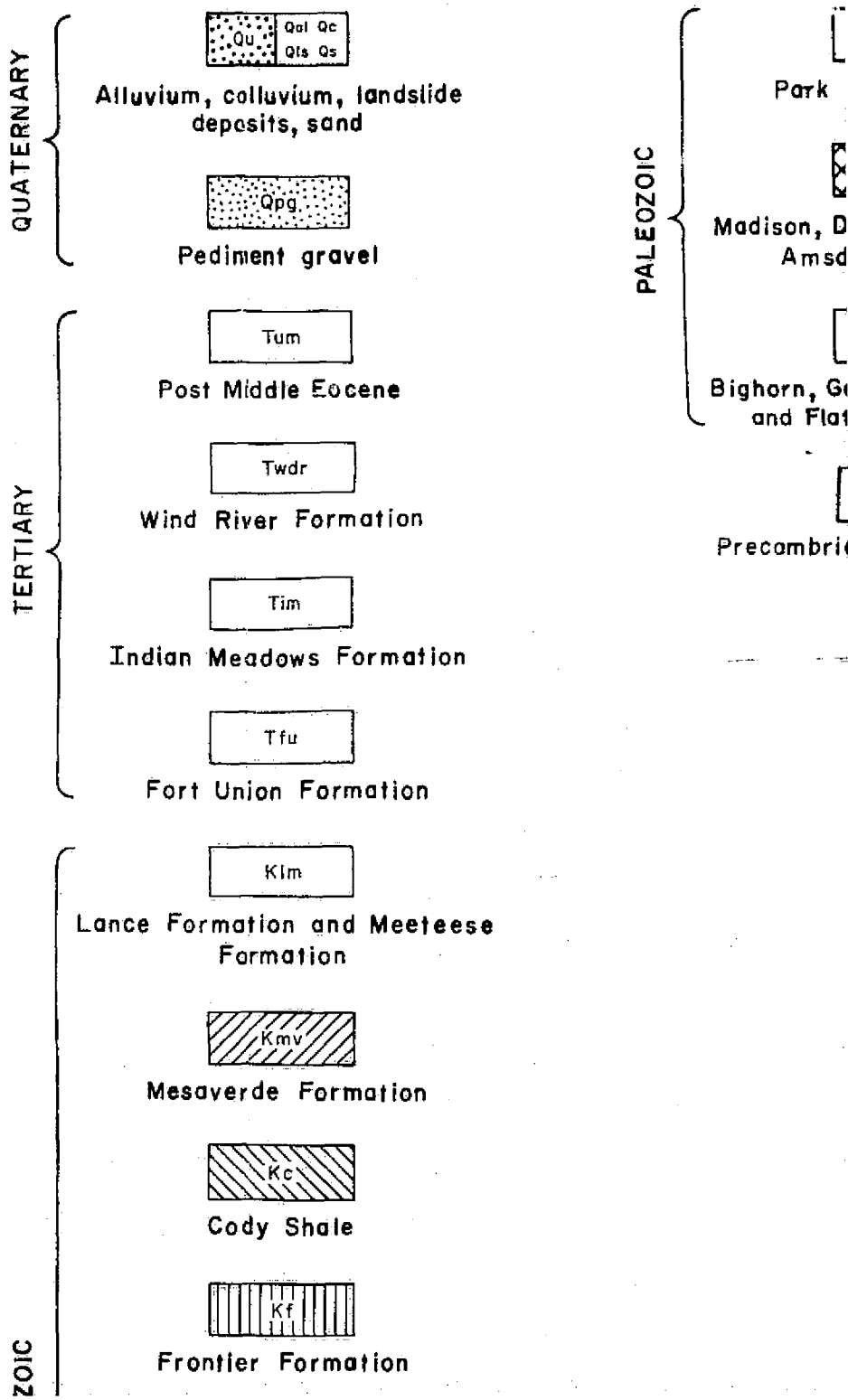
95 W R 94 W R 93 W

KIE COUNTY  
INGS COUNTY



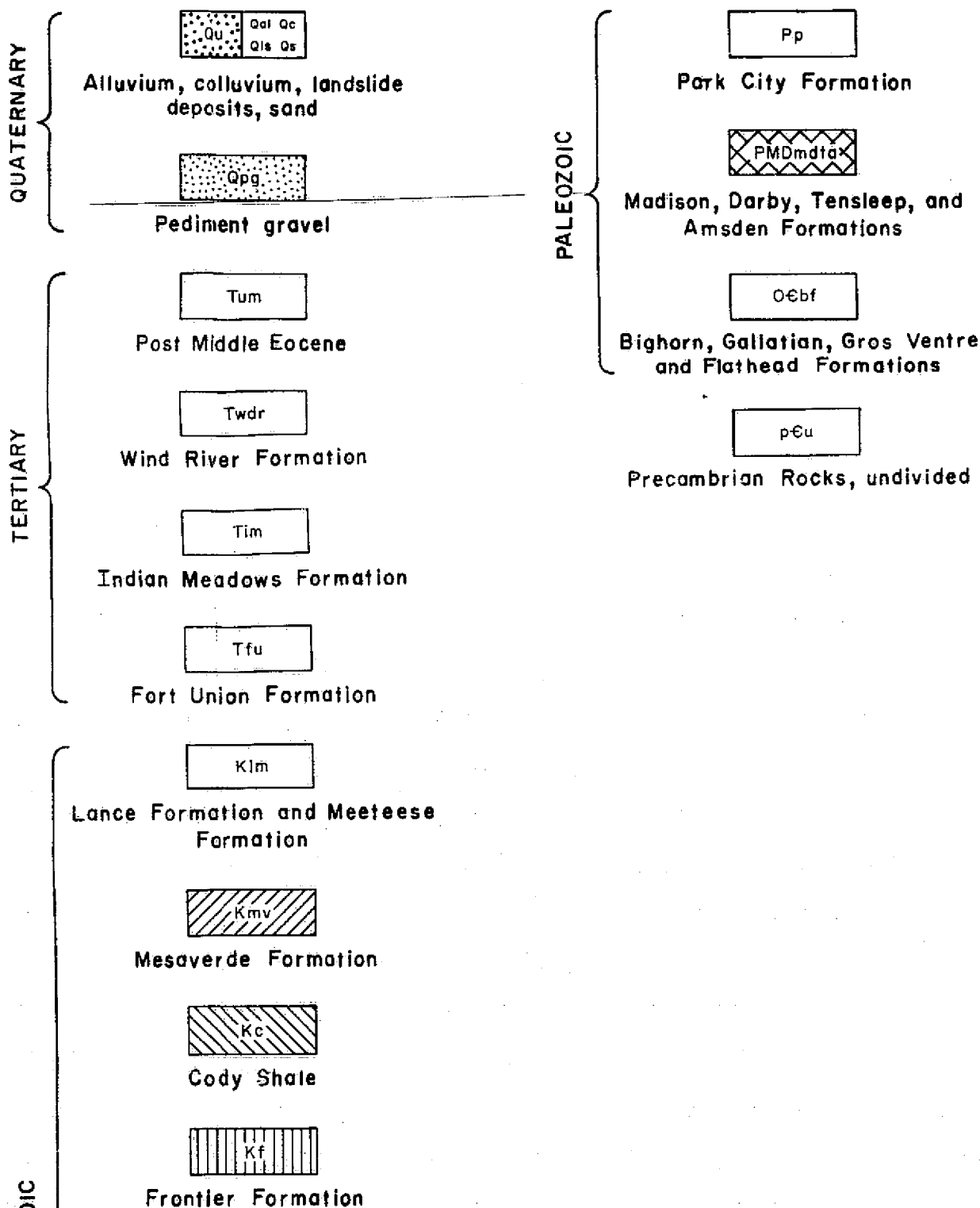
# GEOLOGIC MAP OF A PART OF CENTRAL WYOMING SHOWING ACTUAL MAPPING AND EXTRAPOLATION\*

## EXPLANATION



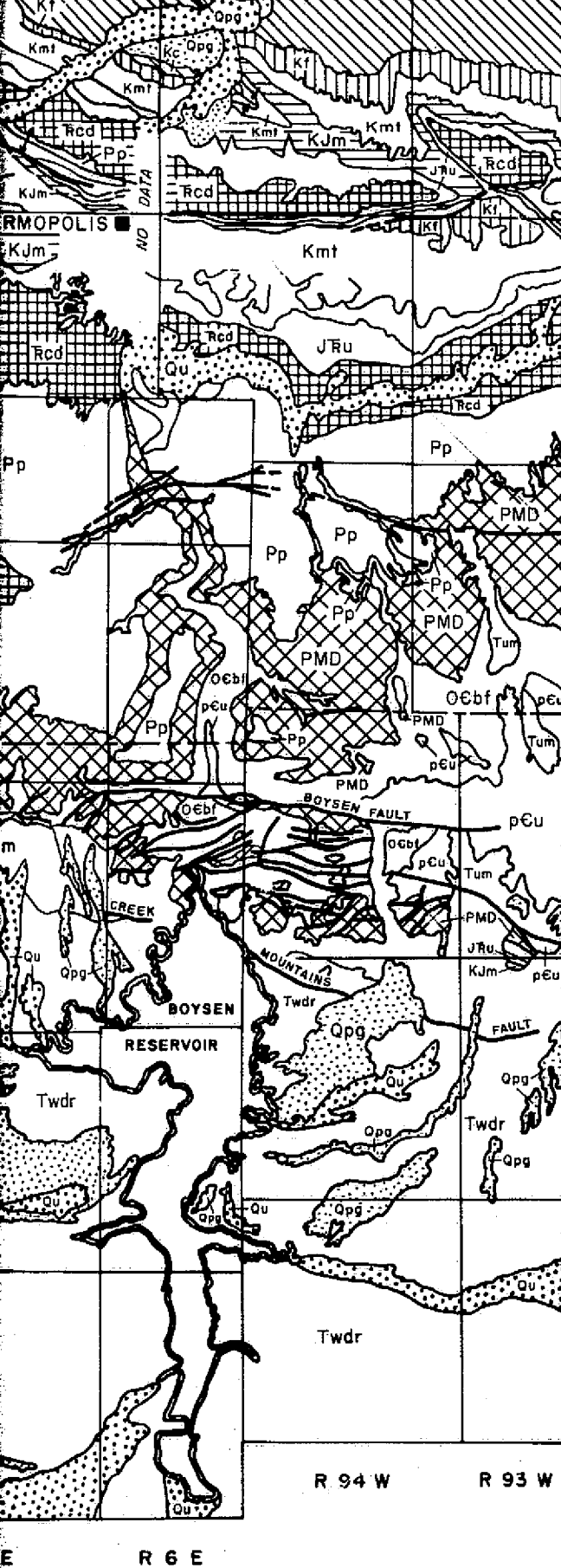
# GEOLOGIC MAP OF A PART OF CENTRAL WYOMING SHOWING ACTUAL MAPPING WITHOUT EXTRAPOLATION\*

## EXPLANATION









TERTIARY

Post Middle Eocene

Twdr

Wind River Formation

Tim

Indian Meadows Formation

Tfu

Fort Union Formation

Kim

Lance Formation and Meeteese Formation

Kmv

Mesaverde Formation

Kc

Cody Shale

Kf

Frontier Formation

Kmt

Mowry and Thermopolis Shales

KJm

Cloverly and Morrison Formations

JRu

Sundance, Gypsum Springs, and Nugget Formations

Rcd

Chugwater and Dinwoody Formations

Bighorn, and F

Precamb

and Rucker (1969); Weitz and Lore (1952 extrapolated Andrews, Pierce, and Eargle (1947)

OUT FRAME

TERTIARY

Tum  
Post Middle Eocene

Twdr  
Wind River Formation

Tim  
Indian Meadows Formation

Tfu  
Fort Union Formation

Oebf  
Bighorn, Gallatian, Gros Ventre  
and Flathead Formations

pCu  
Precambrian Rocks, undivided

MESOZOIC

Klm  
Lance Formation and Meeteese  
Formation

Kmv  
Mesaverde Formation

Kc  
Cody Shale

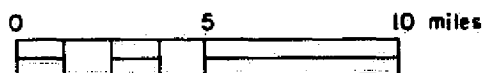
Kf  
Frontier Formation

Kmt  
Mowry and Thermopolis Shales

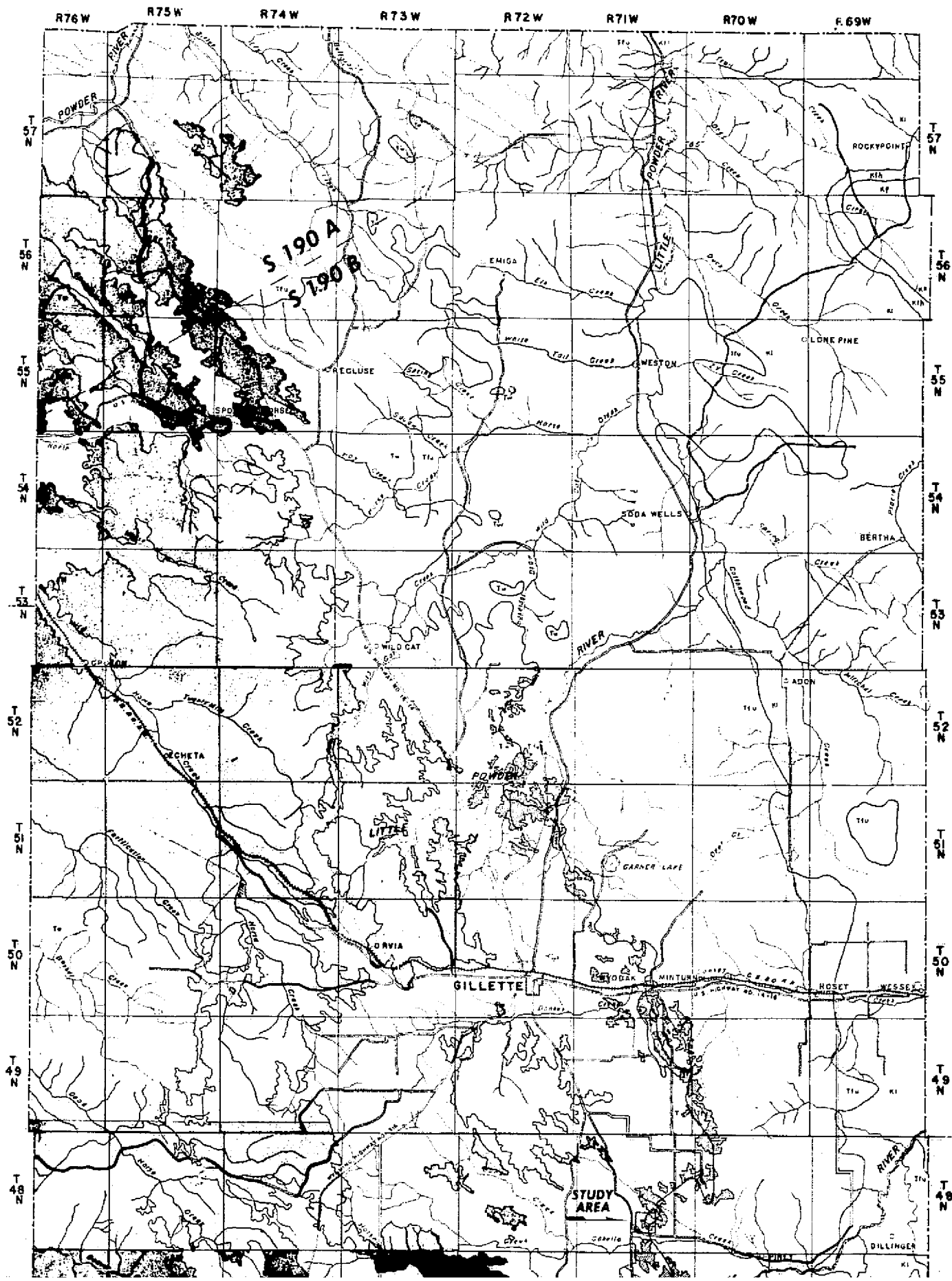
Kjm  
Cloverly and Morrison Formations

JRu  
Sundance, Gypsum Springs, and  
Nugget Formations

Rcd  
Chugwater and Dinwoody  
Formations



**FOLDOUT FRAME**





FOLDOUT FRAME

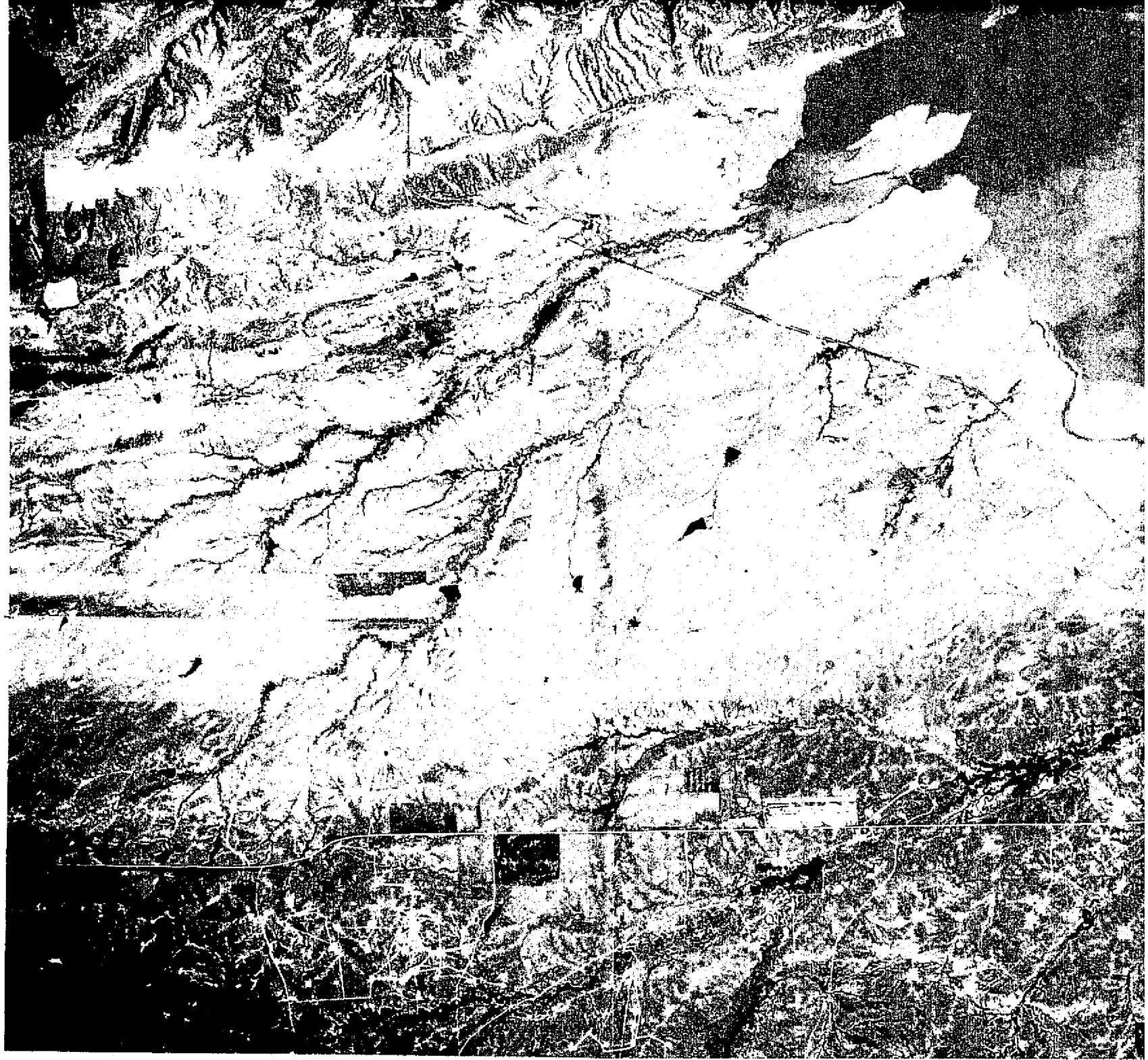
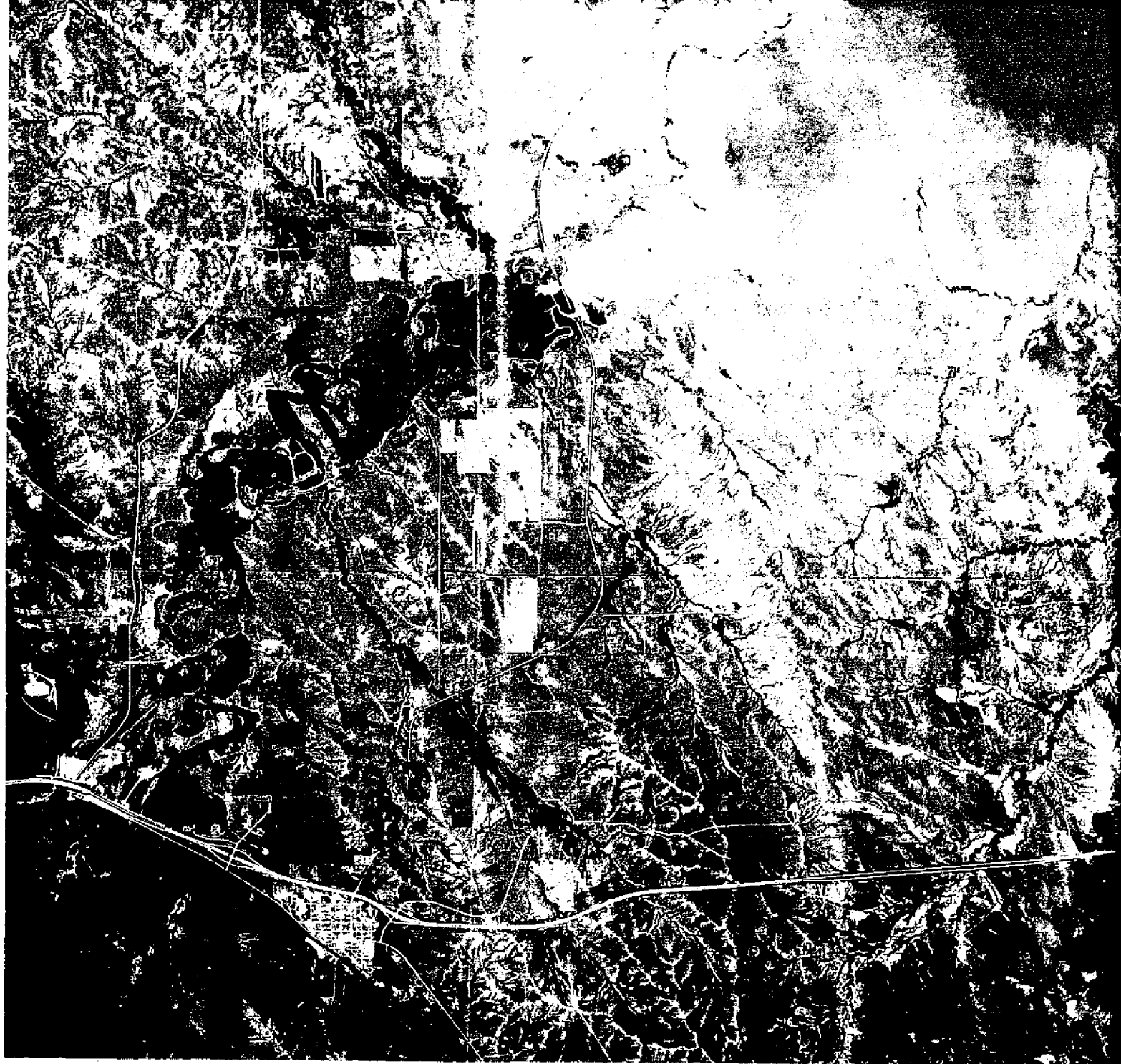


PLATE 6

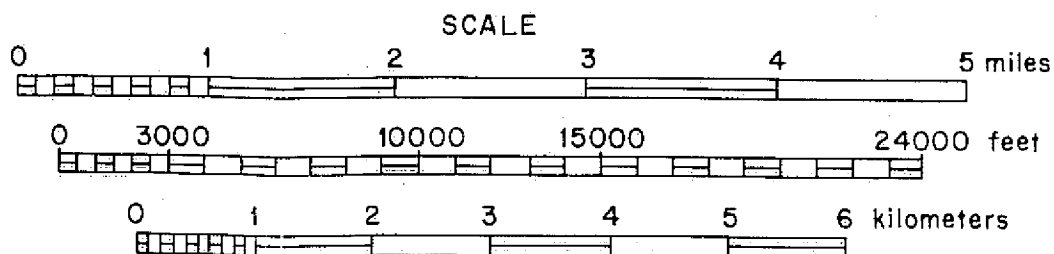
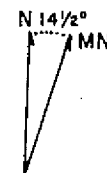
LOLLOUT FRAMES





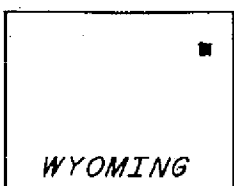
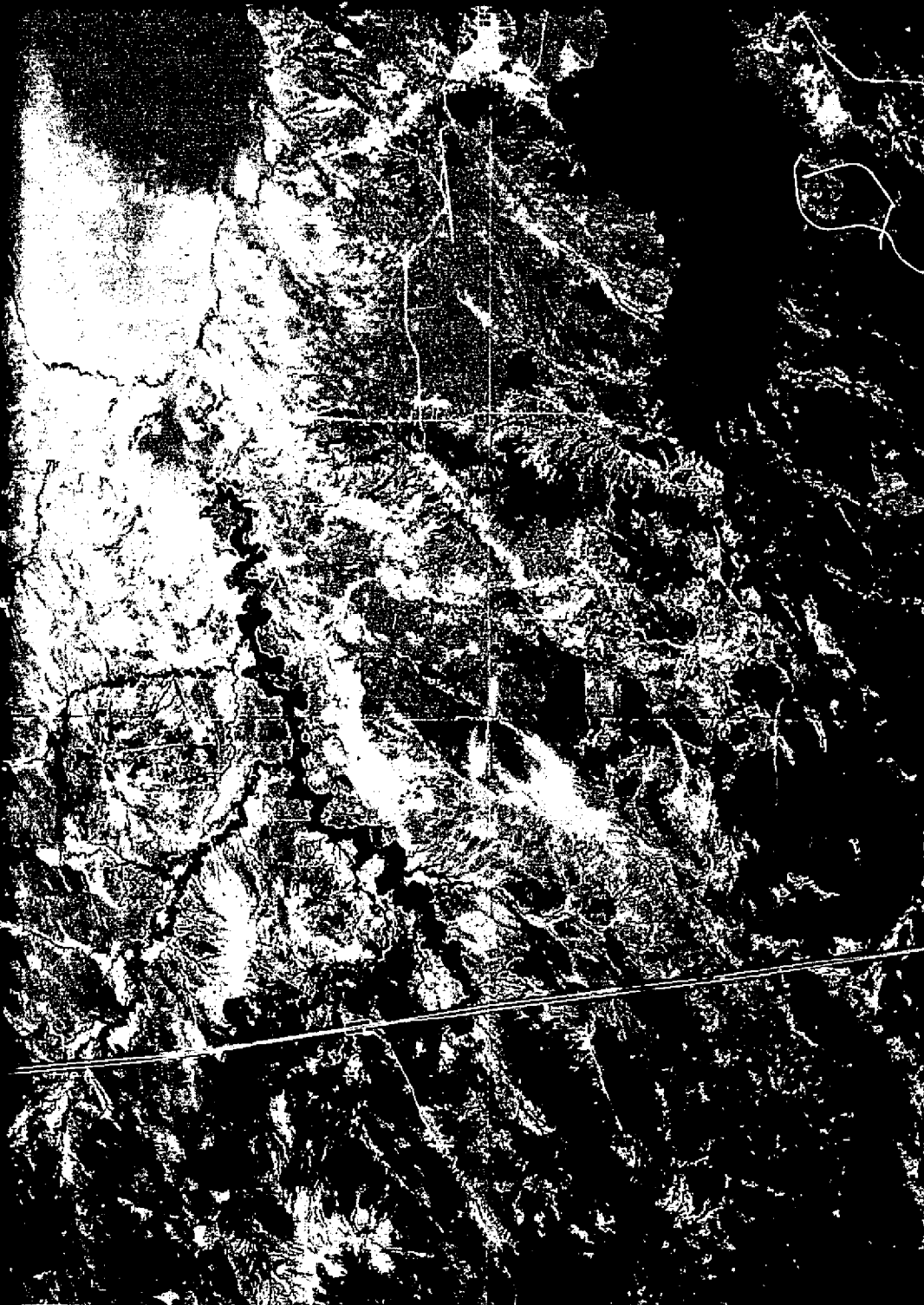


Note: The original aerial photograph (1:120,000 scale; NASA/AMES Flight 72-135, August 9, 1972) was enlarged to 1:62,500 scale for interpretation (see Figure 8). The map shown in Figure 8 is the combined result of field checks and interpretation of Flight 72-135 photography and of similar photography flown June 20, 1973 (NASA/JSC Mission 239).



ORIGINAL PAGE IS  
OF POOR QUALITY

ORIGINAL PAGE  
OF POOR QUALITY



AREA LOCATION

5 miles

1000 feet

0 meters

# HIGH-ALTITUDE AERIAL PHOTOGRAPH MOORCROFT/KEYHOLE AREA

Crook County, Wyoming

FOLDOUT FRAME



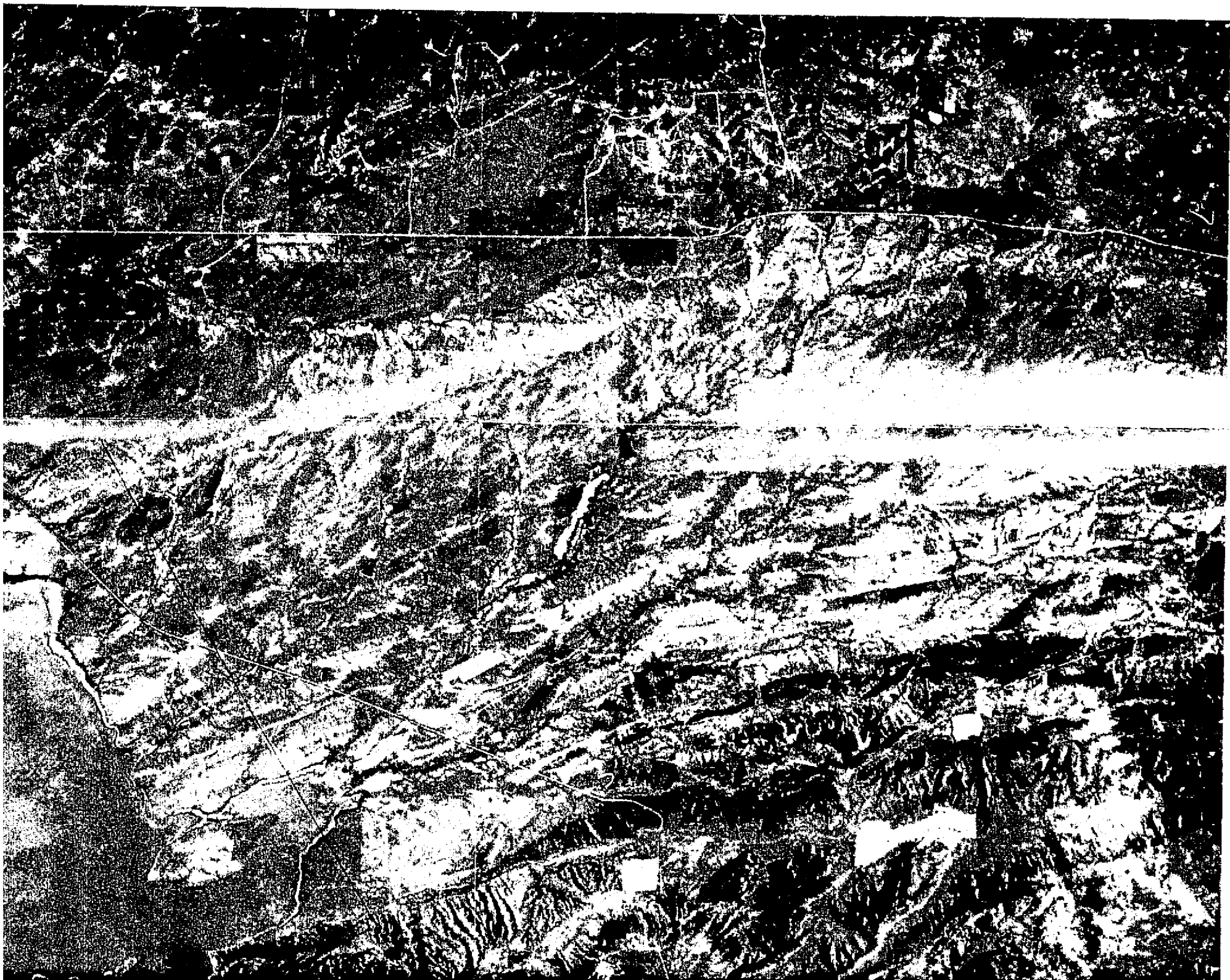
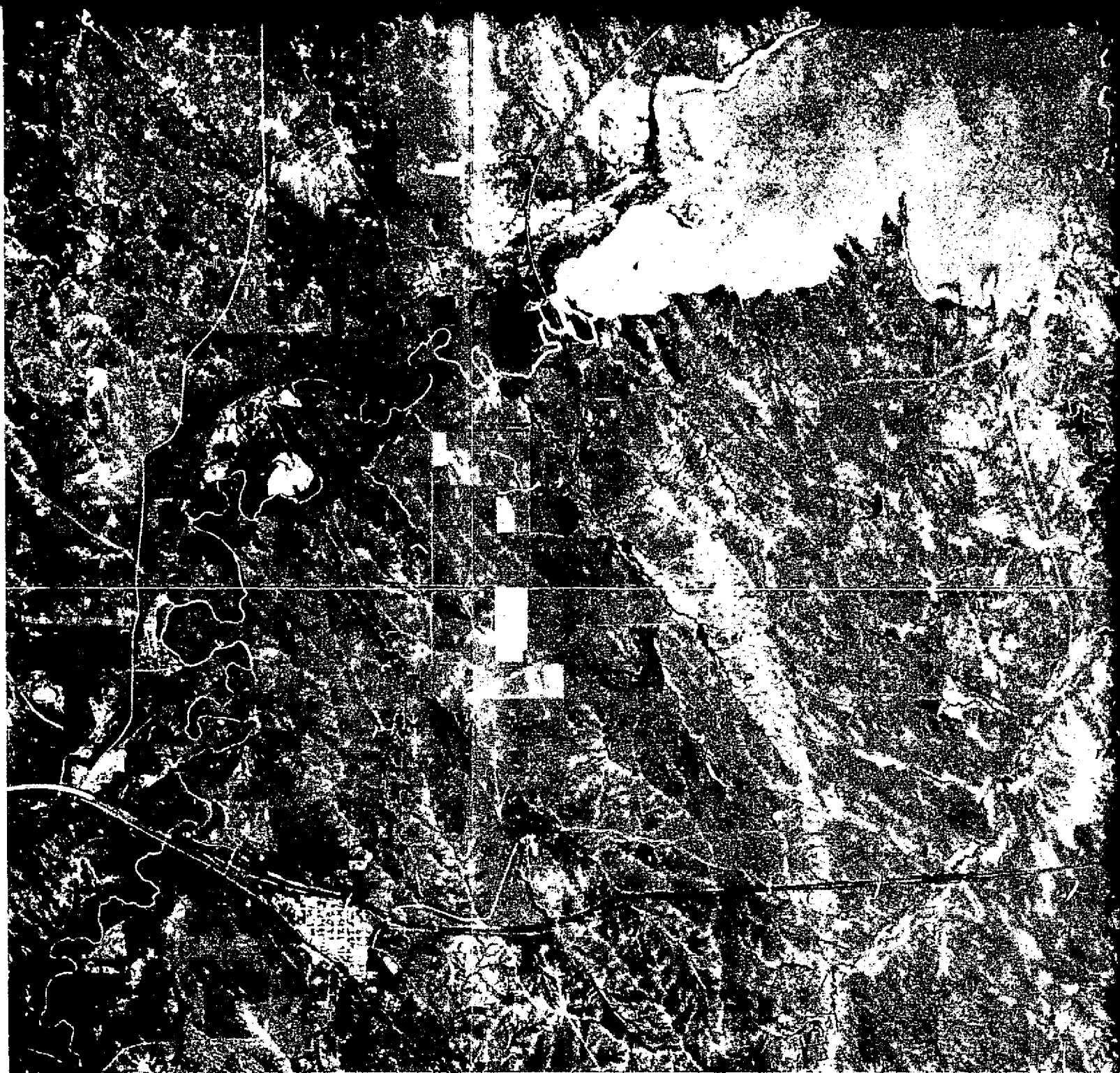


PLATE 5

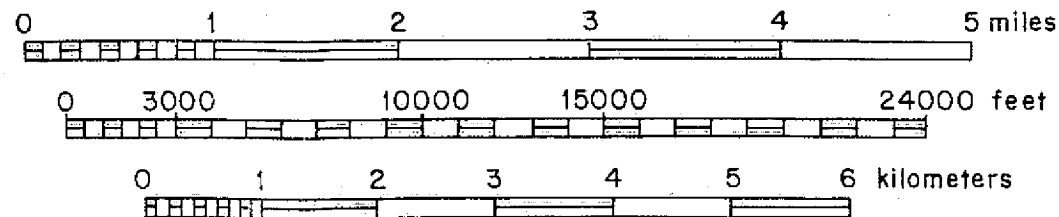




Note: The original color photograph (track 5, pass 28, frame 21, September 13, 1973) was enlarged to 1:62,500 scale for interpretation (see Figure 7).



SCALE

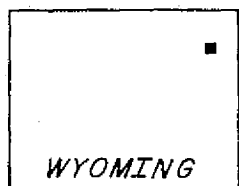
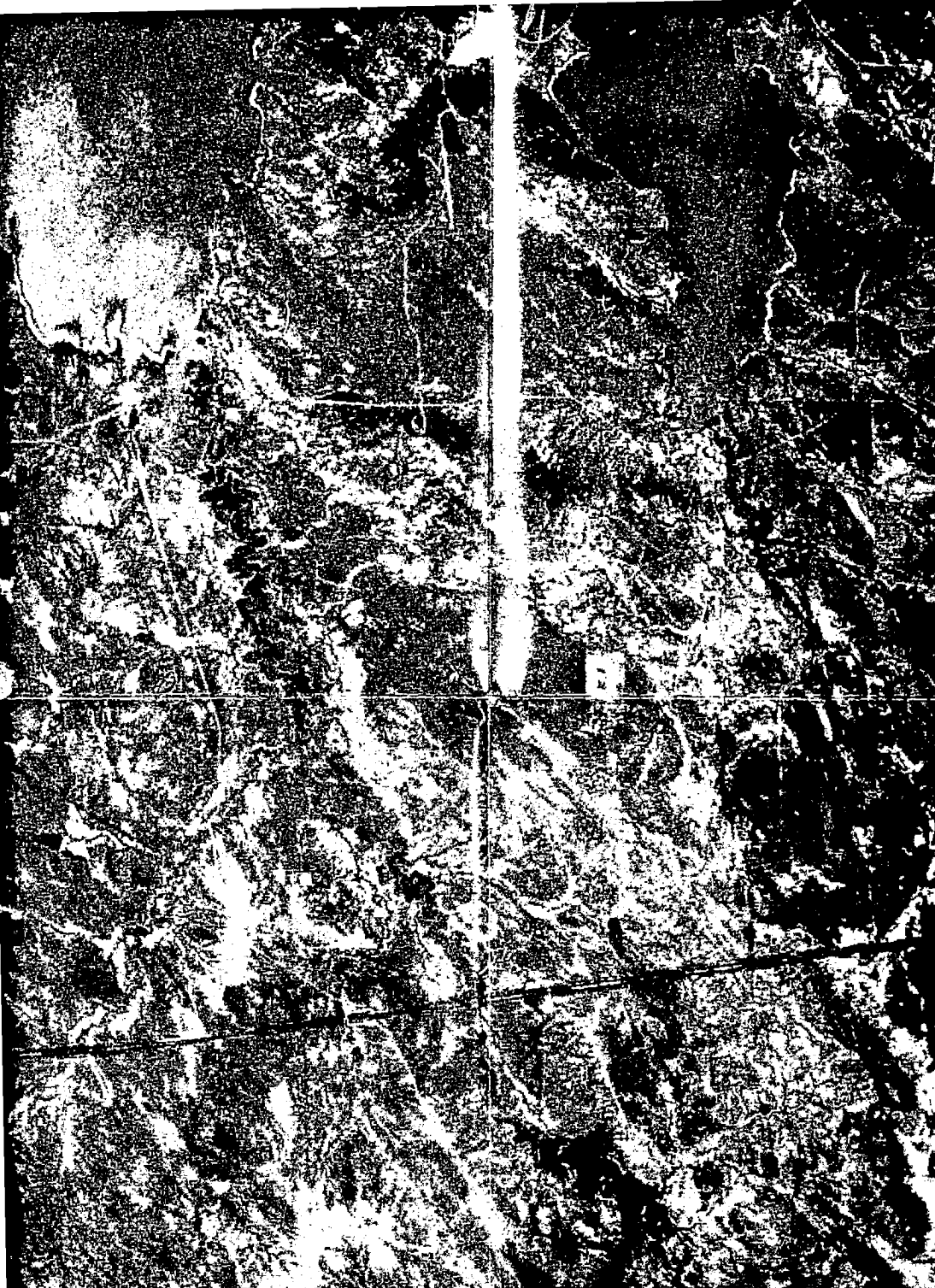


ORIGINAL PHOTOGRAPH  
OF POOR QUALITY

FOLDOUT FRAME

WYO  
AREA L





AREA LOCATION

5 miles



1000 feet



1 meters

**SKYLAB S-190B**  
**PHOTOGRAPH**  
**MOORCROFT/KEYHOLE AREA**  
**Crook County, Wyoming**

FOLDOUT FRAME

ORIGINAL PAGE IS  
OF POOR QUALITY

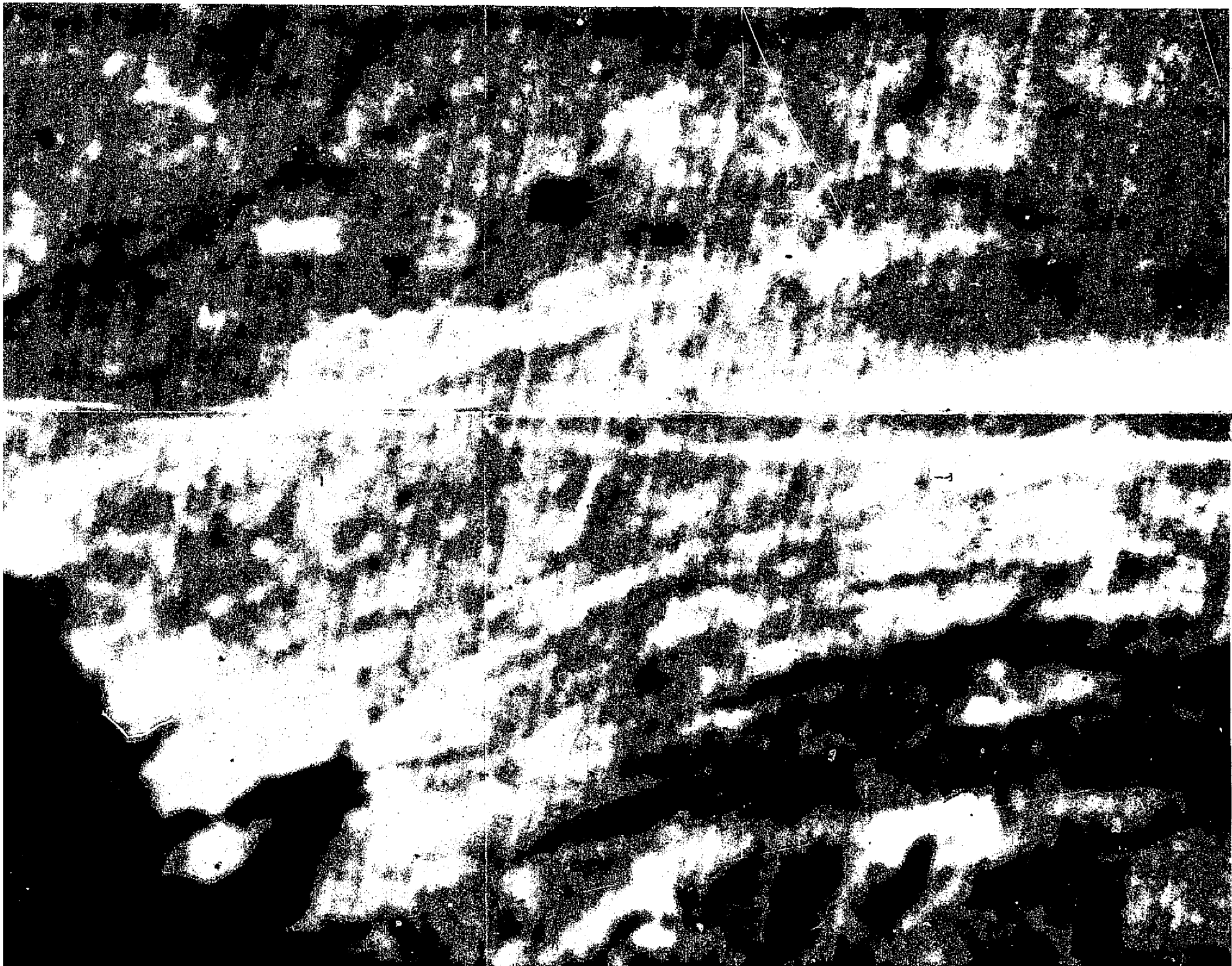
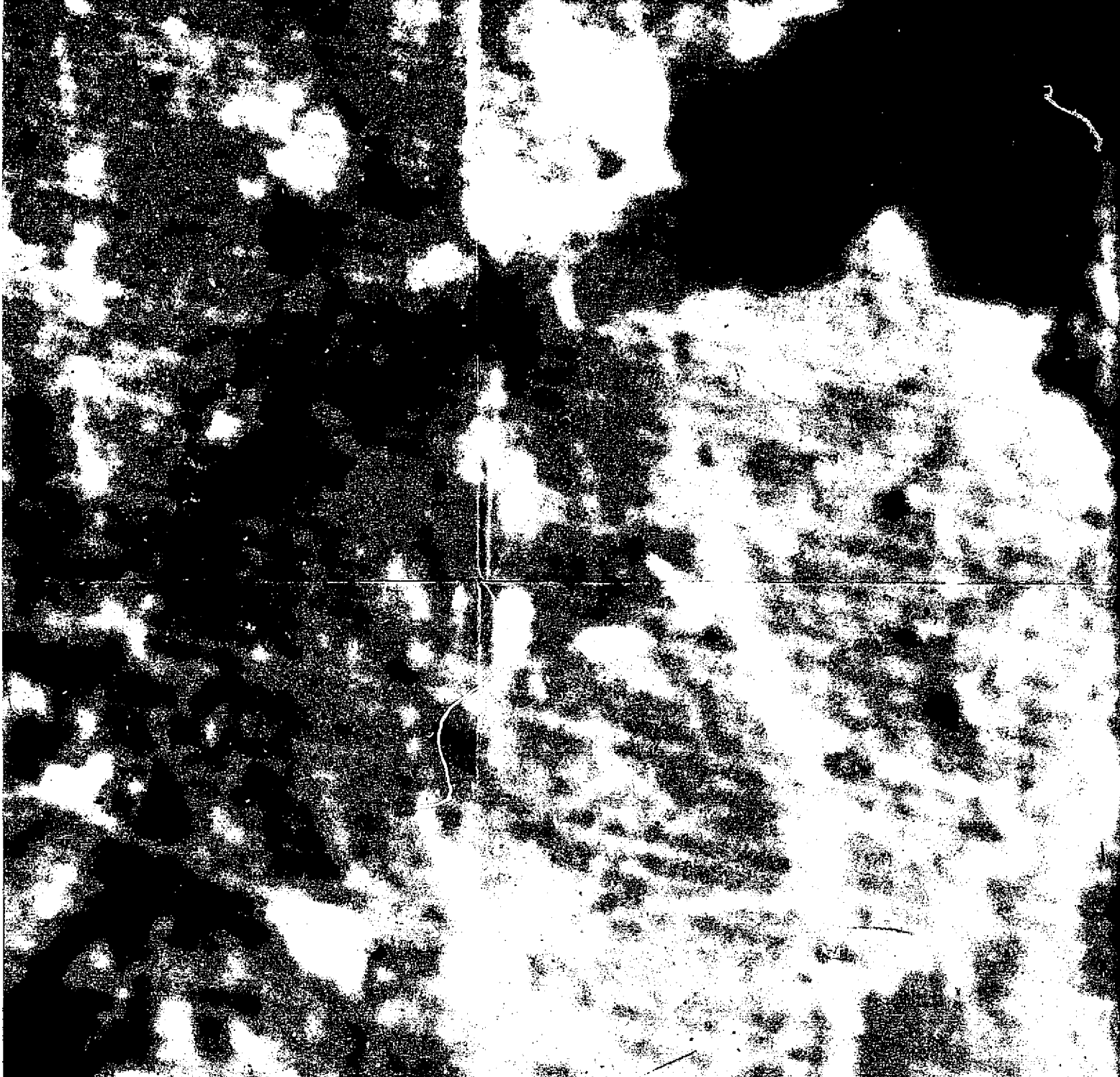
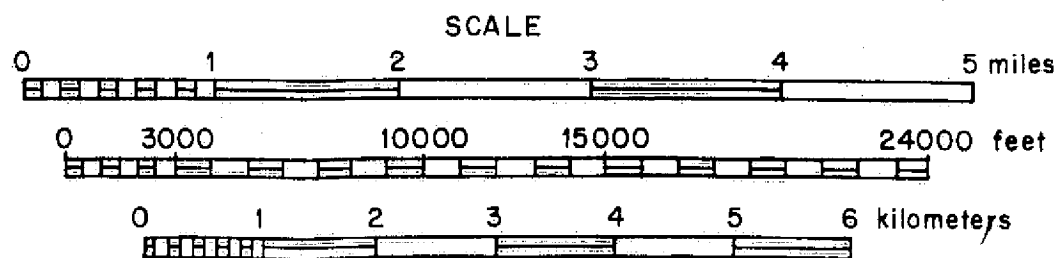


PLATE 4



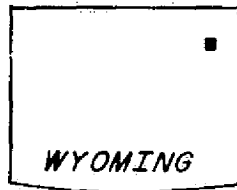


Note: The original composite (image 1353-17183, July 11, 1973) was constructed from the four LANDSAT multispectral scanner bands (band 4 = yellow, band 5 = red, bands 6 and 7 = cyan) using the diazo technique. The diazo composite was enlarged to 1:62,500 scale for interpretation (see Figure 6).



FOLDOUT FRAME





AREA LOCATION

**LANDSAT FALSE-COLOR  
COMPOSITE IMAGE  
MOORCROFT/KEYHOLE AREA  
Crook County, Wyoming**

5 miles

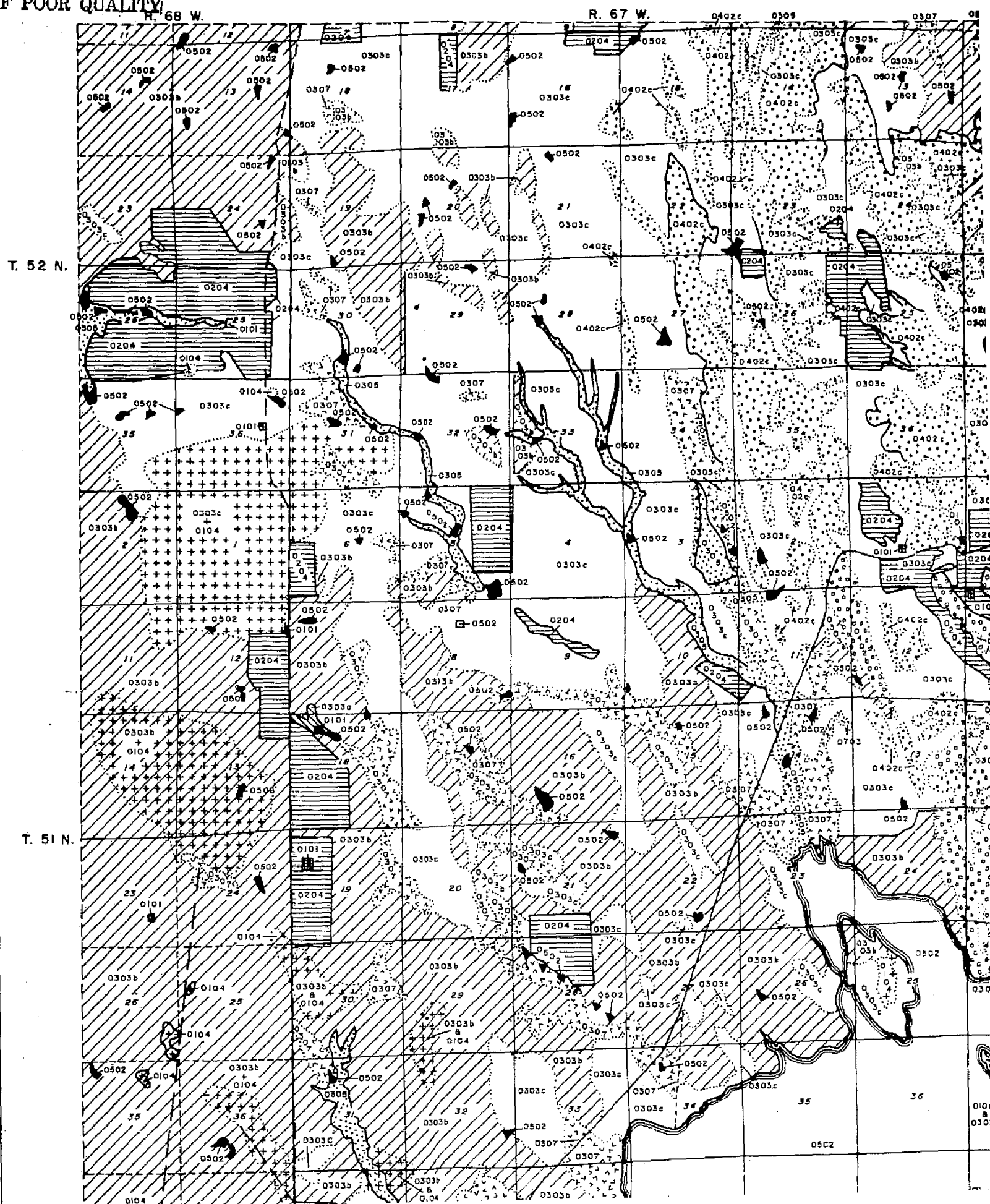
00 feet

meters

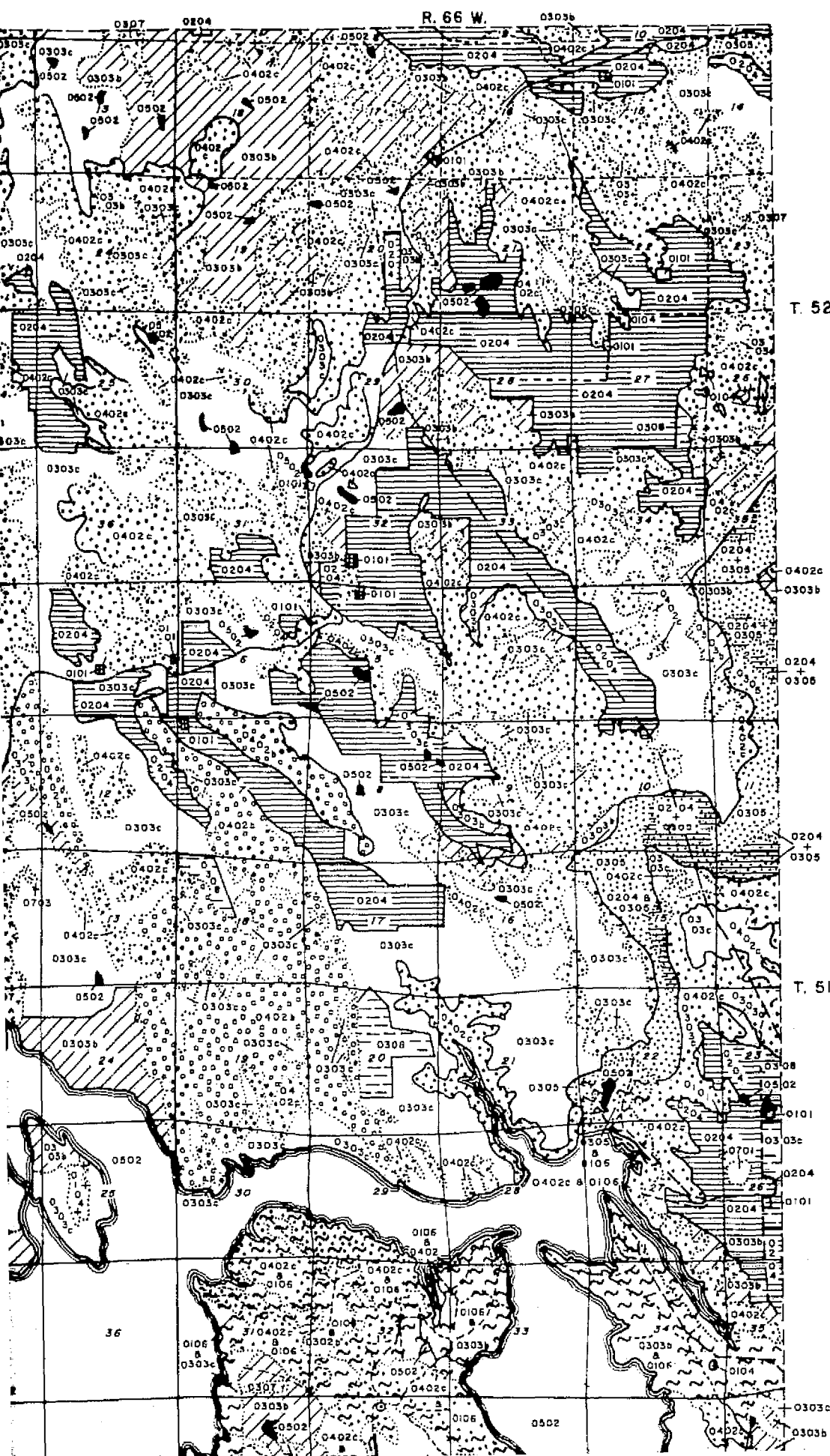
EXDOUT FRAME



ORIGINAL PAGE IS  
OF POOR QUALITY

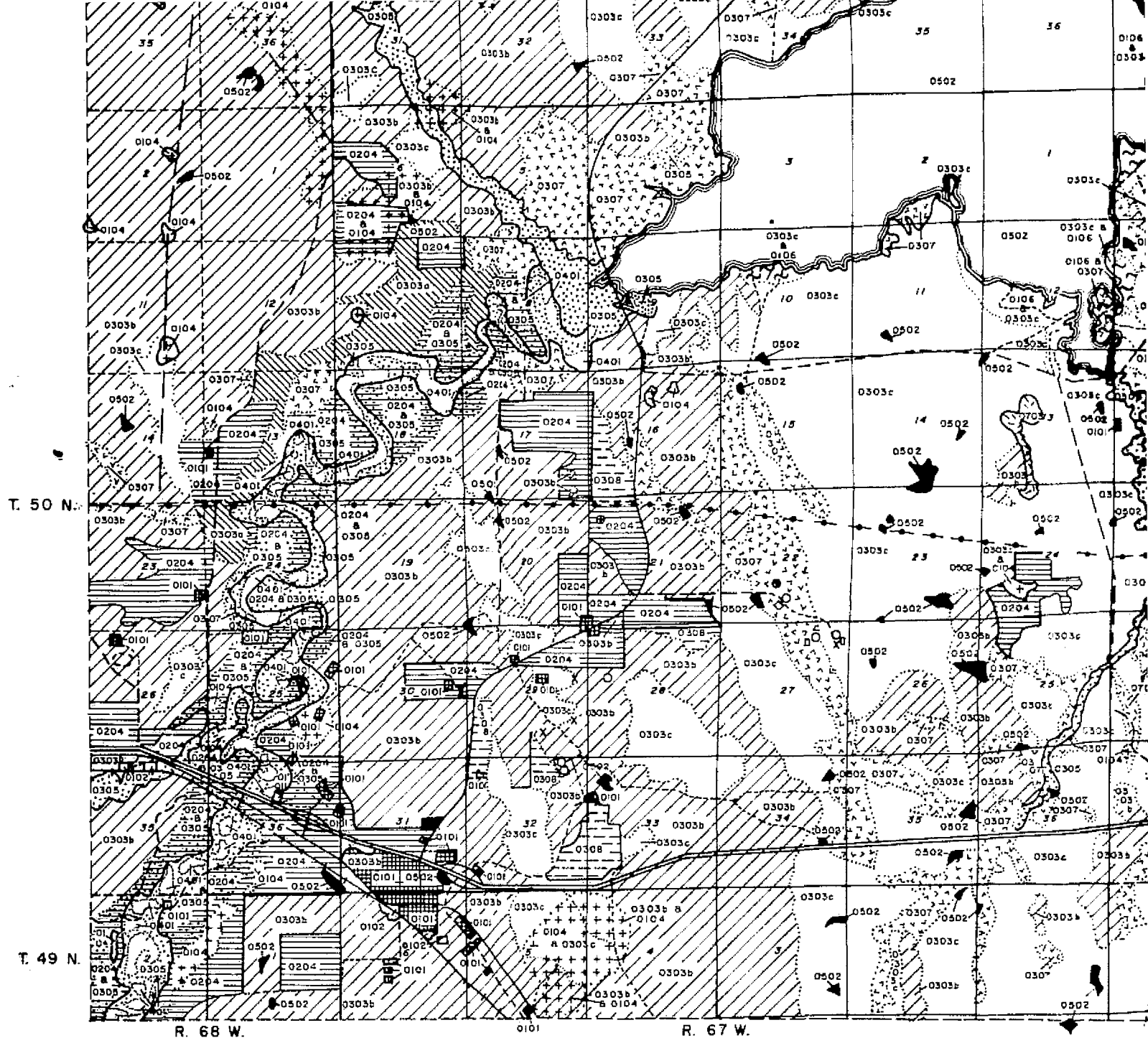


# PLATE 3

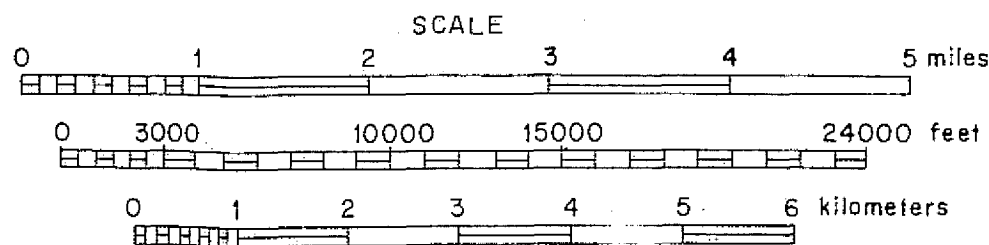
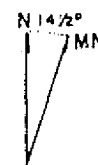


## EXPLANATION

- Urban and Residential
- Industrial, Commercial, and Institutional
- Extractive
- Power line
- Pipeline
- Oil pump jack
- Oil tank
- Dry hole (drill site)
- Waste pond
- Well being drilled
- Transportation
  - 4-lane highway
  - Improved road
  - Unimproved road
  - Trail
  - Airstrip
  - Railroad
- Recreation
- Croplands
- Rangeland
  - 0303a good
  - 0303b moderate
  - 0303c poor
- Floodplains
- Actively eroding areas

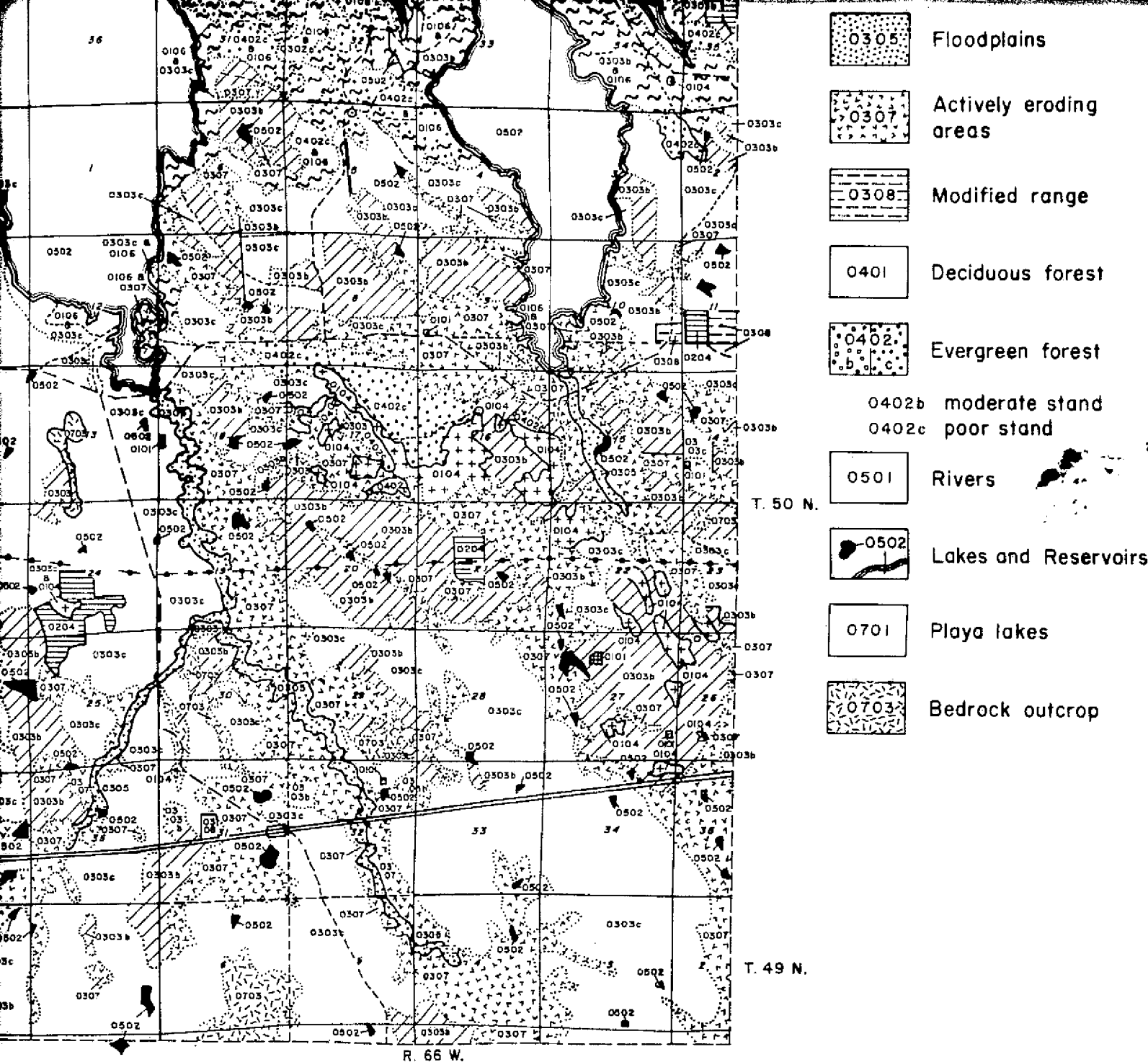


Note: Land-use data was interpreted from 1:120,000 scale aerial photographs (NASA/AMES Flight 72-135, NASA/JSC mission 239) using a Kern PG-2 Stereo-plotter. The interpretation was field checked in June and July, 1975. Map compiled on land grid taken from U.S. Geological Survey 15-minute topographic quad-range map, Moorcroft, Wyoming (1957).



WY  
AREA

FOLDOUT FRAME 3



## LAND-USE MAP

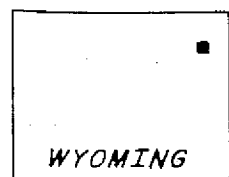
MOORCROFT/KEYHOLE AREA

Crook County, Wyoming

Interpreted from  
aerial photography and field checked

R.W. Marrs

1975



AREA LOCATION

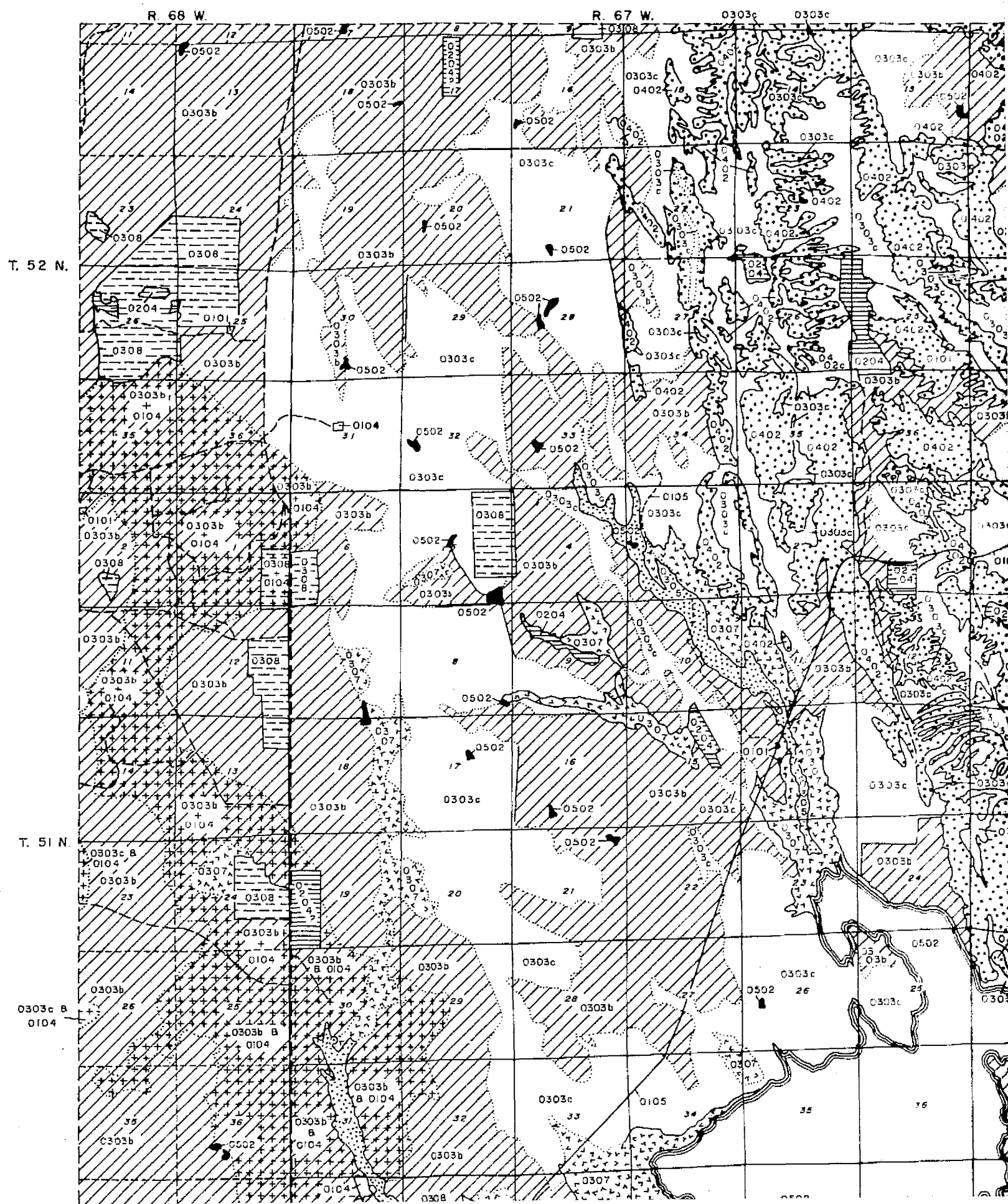
5 miles

0000 feet

ometers

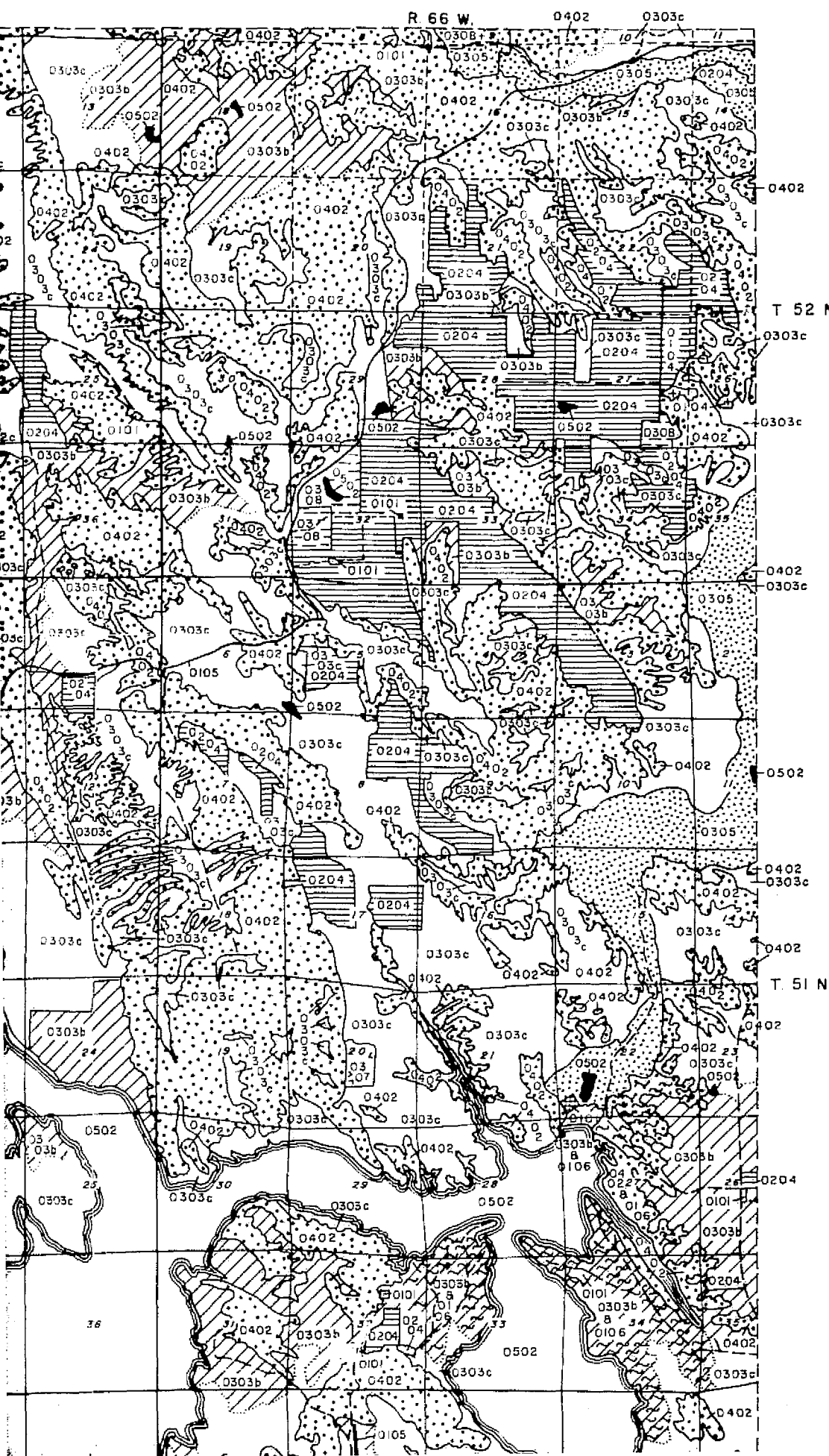
FOLOUT FRAMES 4

ORIGINAL PAGE IS  
OF POOR QUALITY

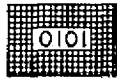
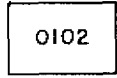
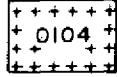
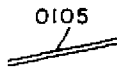
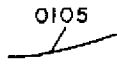
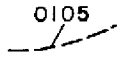
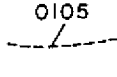
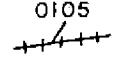
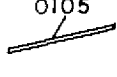
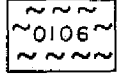
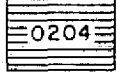
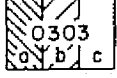
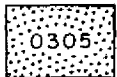
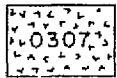
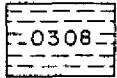




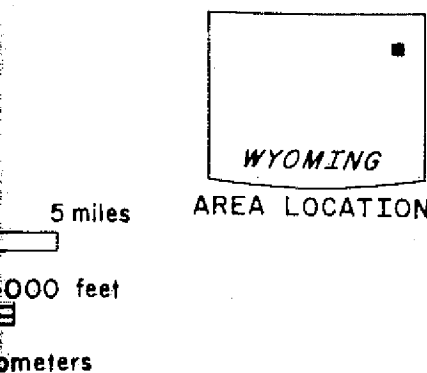
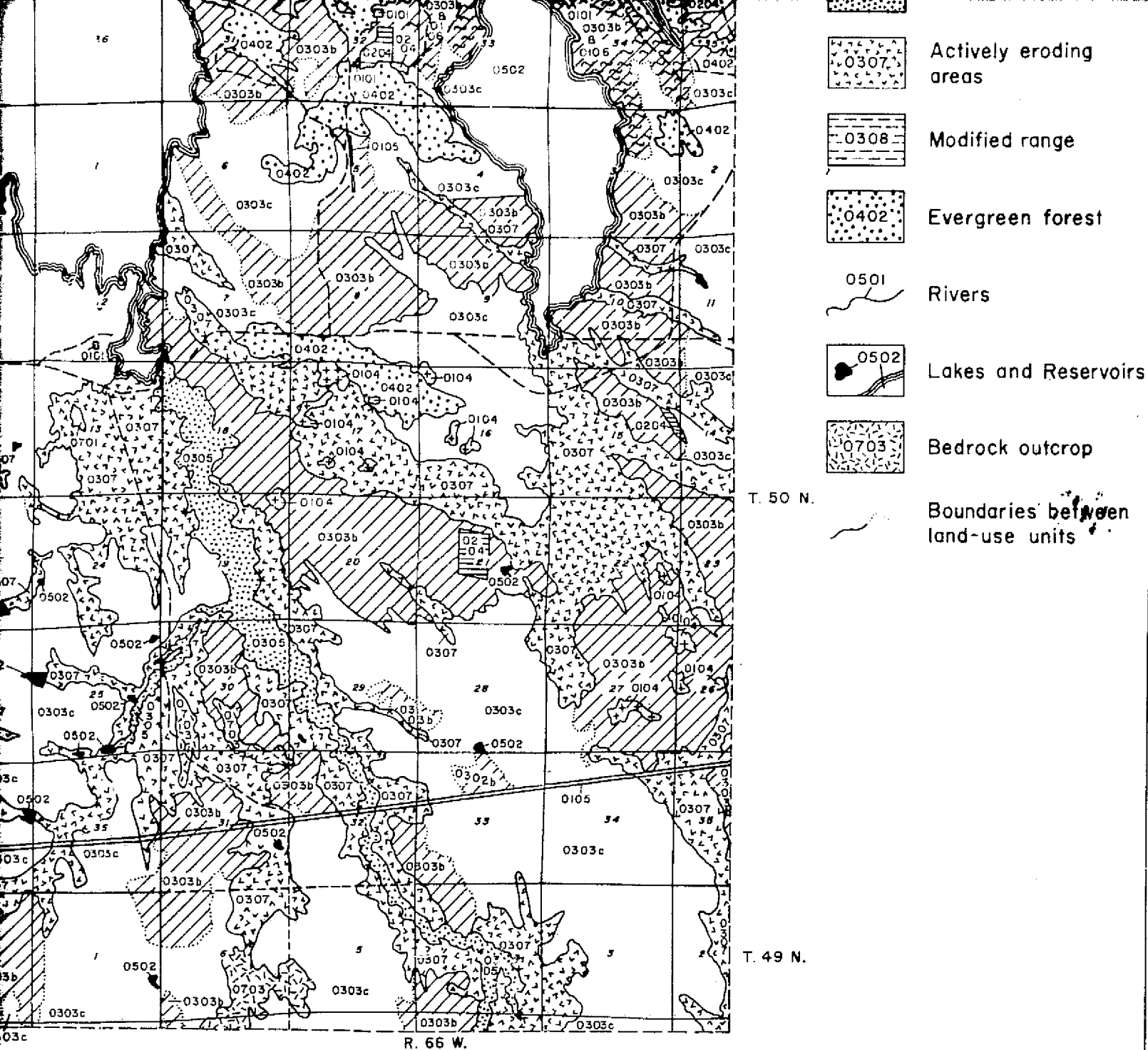
# PLATE 2



## EXPLANATION

-  Urban and Residential
-  Commercial and Institutional
-  Extractive
-  4-lane highway
-  Paved road
-  Improved gravel road
-  Unimproved gravel road
-  Railroad
-  Airfield
-  Recreation
-  Cropland or improved meadow
-  Rangeland
  - 0303a good
  - 0303b moderate
  - 0303c poor
-  Floodplains
-  Actively eroding areas
-  Modified range

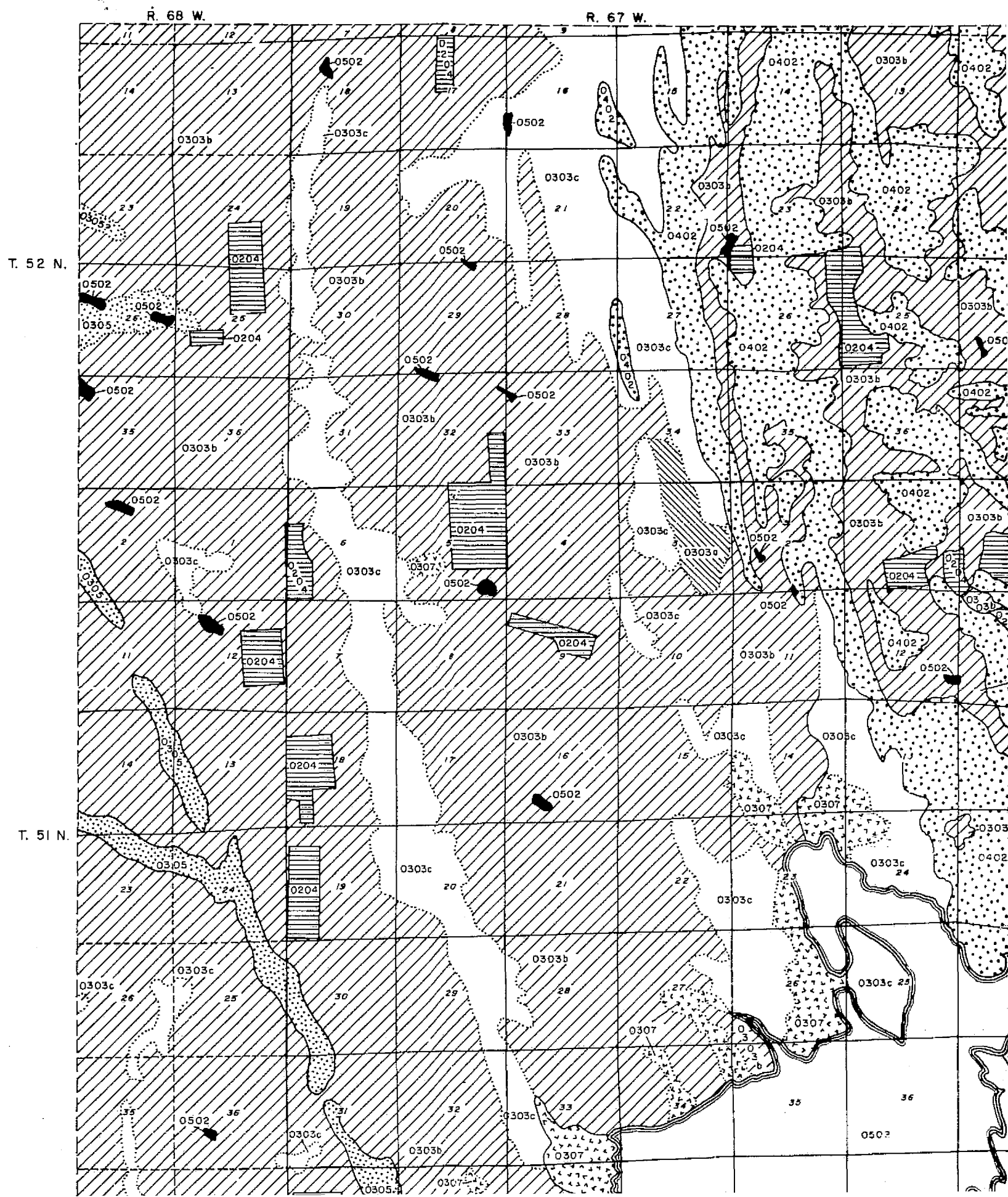




FOLDOUT FRAME

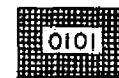


ORIGINAL PAGE IS  
OF POOR QUALITY

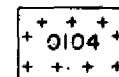


# PLATE I

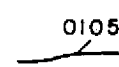
## EXPLANATION



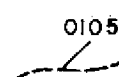
Urban



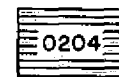
Extractive



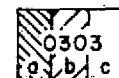
Major transportation route well defined



Probable location of major transportation routes

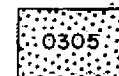


Cropland or improved meadow

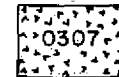


Rangeland

- 0303a good
- 0303b moderate
- 0303c poor



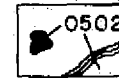
Major floodplains



Barren



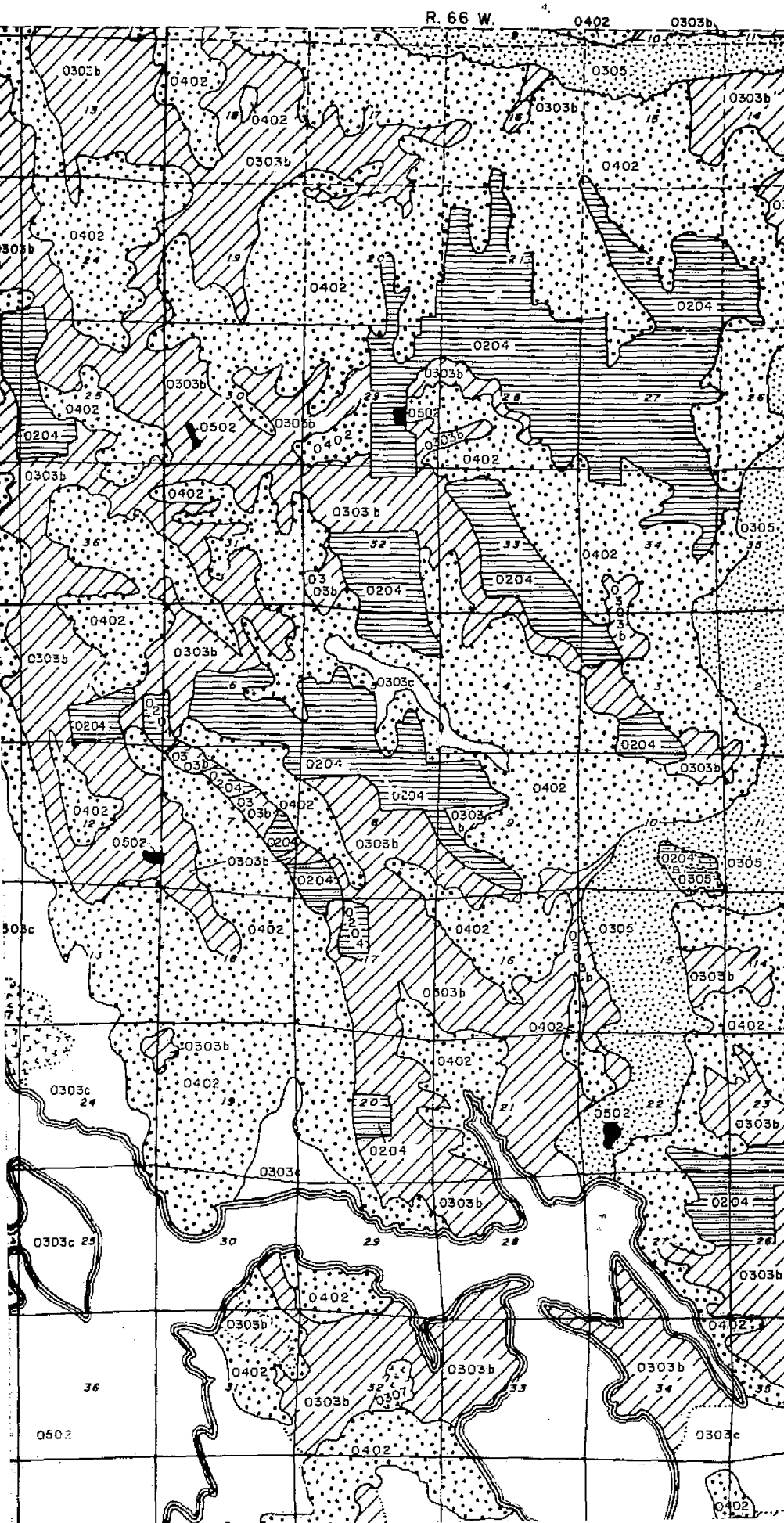
Evergreen forest

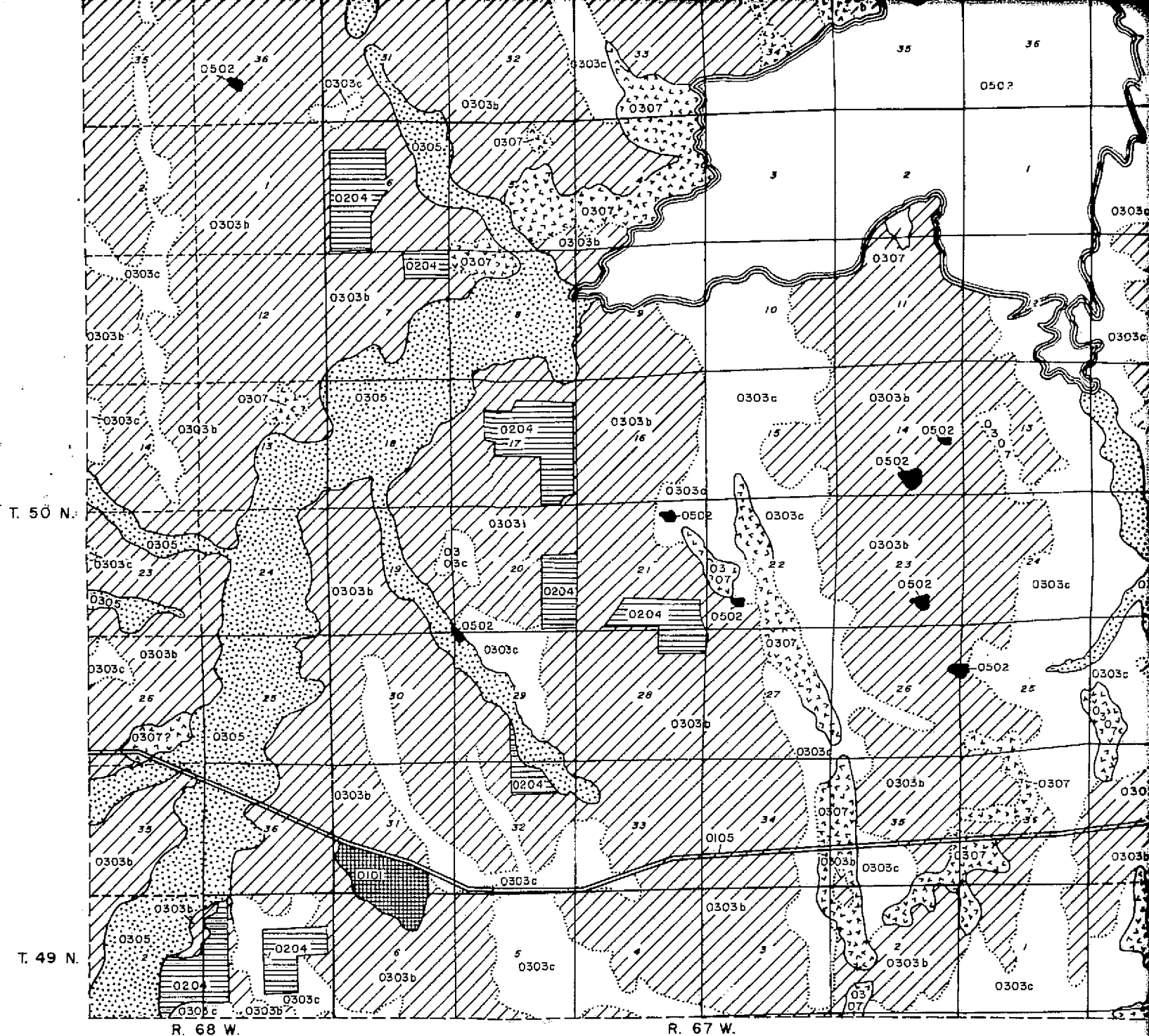


Stockponds and Reservoirs

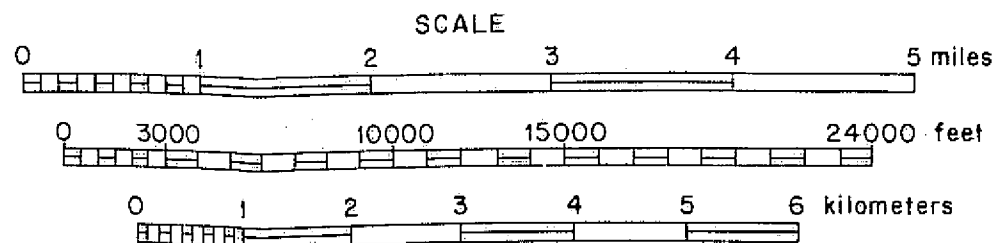
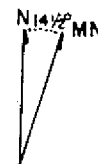


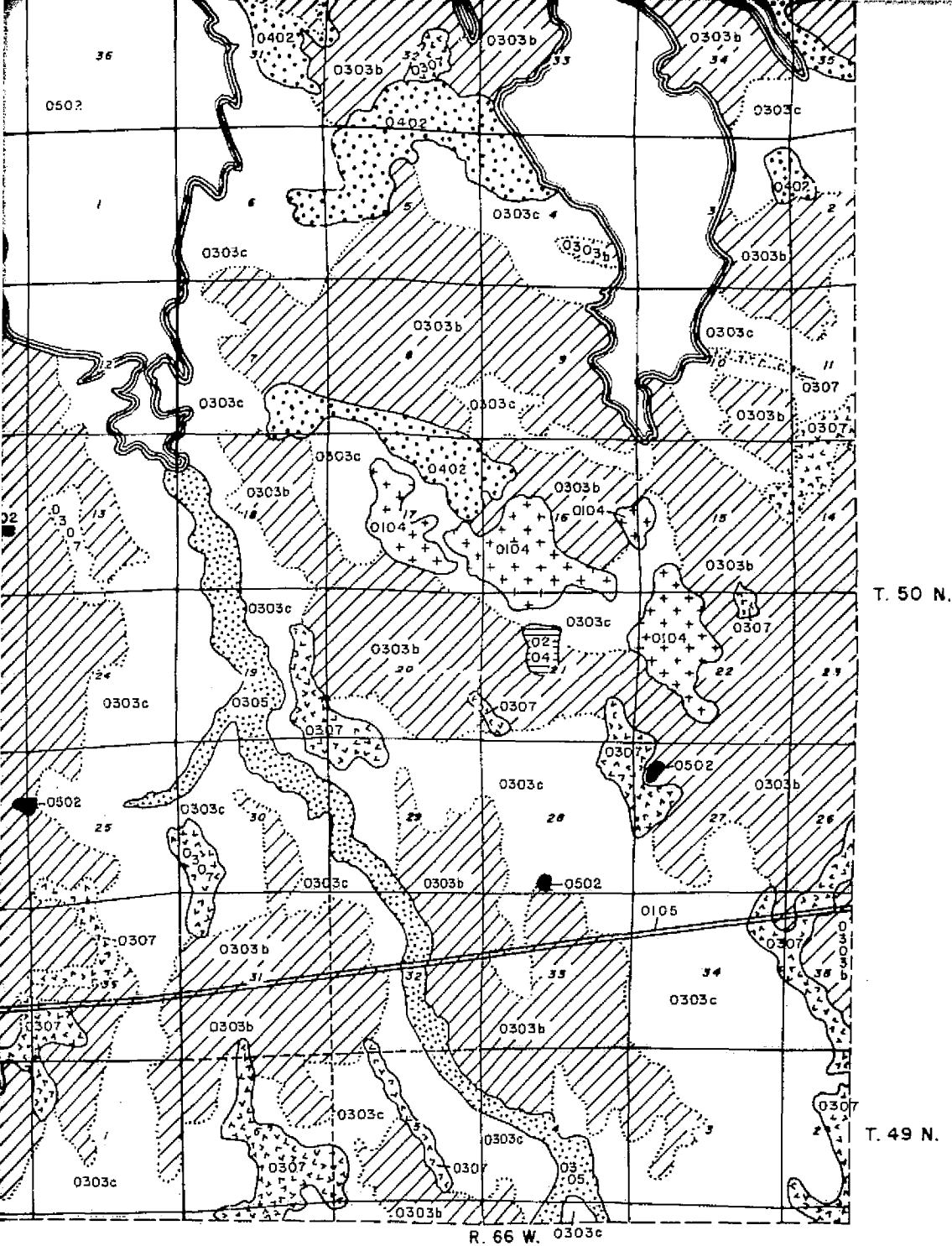
Boundaries between land-use units





**Note:** Land-use data interpreted from diazo color composite image 1353-17183 (11 July, 1973) enlarged to 1:62,500 scale. Map compiled on land grid taken from U.S. Geological Survey 15-minute topographic quadrangle map, Moorcroft, Wyoming (1957).





# **LAND-USE MAP**

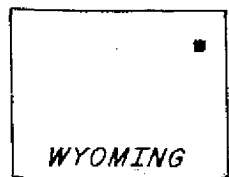
**MOORCROFT/KEYHOLE AREA**

**Crook County, Wyoming**

**Interpreted from LANDSAT Data**

**R.W. Marrs**

**1975**



**AREA LOCATION**

5 miles

1000 feet

0 meters

FOLDOUT FRAME 4